Fisheries and Oceans Canada | Pêches et Océans Canada
Ecosystems and Oceans Science | Sciences des écosystèmes et des océans

Canadian Science Advisory Secretariat (CSAS)

Research Document 2026/003

National Capital Region

Assessment of Port Ocean Prediction System Developed Under Canada's Oceans Protection Plan: Kitimat Fjord

Hauke Blanken[1], Michael Dunphy[1], Maxim Krassovski[1], Stephanne Taylor[2], Rachel Horwitz[2], Simon St-Onge Drouin[3], Adam Drozdowski[2]

[1] Fisheries and Oceans Canada
Institute of Ocean Sciences
9860 West Saanich Road
Sidney, British Columbia V8L 4B2

[2] Fisheries and Oceans Canada
Bedford Institute of Oceanography
1 Challenger Drive
Dartmouth, Nova Scotia B2Y 4A2

[3] Fisheries and Oceans Canada
Maurice Lamontagne Institute
850 route de la Mer
Mont-Joli, Quebec G5H 3Z4

February 2026

Canada

Foreword

This series documents the scientific basis for the evaluation of aquatic resources and ecosystems in Canada. As such, it addresses the issues of the day in the time frames required and the documents it contains are not intended as definitive statements on the subjects addressed but rather as progress reports on ongoing investigations.

Published by:

Fisheries and Oceans Canada
Canadian Science Advisory Secretariat
200 Kent Street
Ottawa ON K1A 0E6

http://www.dfo-mpo.gc.ca/csas-sccs/
DFO.CSAS-SCAS.MPO@dfo-mpo.gc.ca

ISSN 1919-5044
ISBN 978-0-660-79956-8 Cat. No. Fs70-5/2026-003E-PDF

Correct citation for this publication:

Blanken, H., Dunphy, M., Krassovski, M., Taylor, S., Horwitz, R., St-Onge Drouin, S., and Drozdowski, A. 2026. Assessment of Port Ocean Prediction System Developed Under Canada's Oceans Protection Plan: Kitimat Fjord. DFO Can. Sci. Advis. Sec. Res. Doc. 2026/003. xii + 142 p.

Aussi disponible en français :

Blanken, H., Dunphy, M., Krassovski, M., Taylor, S., Horwitz, R., St-Onge Drouin, S. et Drozdowski, A. 2026. Évaluation des modèles portuaires de prévisions océaniques élaborés dans le cadre du Plan de protection des océans du Canada : système de fjords de Kitimat. Secr. can. des avis sci. du MPO. Doc. de rech. 2026/003. xiv + 147 p.

TABLE OF CONTENTS

LIST OF TABLES

LIST OF FIGURES

ABSTRACT

Canada's Ocean Protection Plan (OPP) was launched in 2016 to support initiatives aimed at protecting our marine environment from anthropogenic pressures. To this end, the oceanography sub-initiative of OPP developed six high-resolution port-scale hydrodynamic models, to improve safe navigation, and provide operational emergency response to events such as marine oil spills. The models were downscaled from the Coastal Ice-Ocean Prediction Systems East and West (CIOPS- E, CIOPS-W). Atmospheric forcing was provided by the High-Resolution Deterministic Prediction System (HRDPS).

Model evaluation is an integral part of this development and here the port models are evaluated against available observational data and the parent model using a multiyear hindcast. Evaluations of 48-hour forecasts are performed during a two month period. Additionally, model performance during major storms is examined.

In this report the model evaluation for the hydrodynamic model of the port of Kitimat and the approaches to the port is presented. A hindcast was completed for the years 2016 – 2022 and evaluated against a comprehensive set of observations of water levels, currents, and water properties. This evaluation shows that the port ocean prediction system significantly improves representation of water levels and currents over its parent model, CIOPS-W. Water level predictions are improved by as much as 30% in terms of centered root-mean-square error, predominantly in the tidal domain. The model remained stable during major storms but did not yield significant improvements in the prediction of water levels associated with these storms. Strong non-tidal current events in response to outflow winds were well captured in the model.

Evaluation of the modelled water properties revealed several areas where the model can be improved in future versions. Sub-optimal initialization of deep water masses was found to inhibit the representation of deep water renewal events, and potentially also contribute to a weaker than observed estuarine circulation. Further, a persistent warm bias in sea surface temperatures in the lower reaches of the fjord system requires further evaluation.

Modelled surface currents from the port ocean prediction system were found to improve short-term predictions of the trajectories of drifting objects by as much as 50% in terms of instantaneous prediction skill. Currents from the parent model were found to be better suited for longer-term predictions.

1. INTRODUCTION

Under the Improving Drift Prediction and Nearshore Modelling (DPNM) sub-initiative of Canada's Oceans Protection Plan (OPP), high-resolution models were developed for six Canadian ports and their approaches to enhance the Government of Canada's ocean modelling capabilities in support of environmental protection and marine safety applications (e.g., drift prediction for oil spills) and safety for navigation via a hydrographic e-navigation application. The six ports (three on the east coast and three on the west coast) were selected as at-risk for environmental incidents owing to their high tanker traffic and complex navigational needs. Models have been developed for the west coast ports of Kitimat, Lower Fraser River and Vancouver Harbour, and for the east coast ports of Saint John, the Strait of Canso, and the St. Lawrence estuary.

The models have been developed with both hindcast and forecast capabilities. For each port, a multi-year hindcast is presented with model validation against observations of water levels, velocities, temperature and salinity, as well as a drift experiment conducted using available drifters. Forecast performance is assessed over a two-month period.

The purpose of this document is to review the performance of the model for the port of Kitimat. The design is common to all port models and is presented in Section 2, while Section 3 describes the specifics of the Kitimat port model. The evaluation parameters used to evaluate all models are detailed in Section 4, and Sections 5 and 6 respectively analyze the long hindcast evaluation results and the forecasts evaluation results for the port of Kitimat. The performance of the Kitimat port model is summarized in Section 7, and the main key findings are listed in Section 8.

2. PORT MODEL DESIGN

The port models ("port ocean prediction systems" or POPS) follow a common structure designed to constrain system complexity. We use the same ocean general circulation model and code version, downscaling strategy, preprocessing tools, surface forcing product, and automation suite for all six POPS. The model grids, configuration/tuning, open boundary forcing, and freshwater input sources differ between POPS configurations.

2.1. MODEL SELECTION

The precursor to much of the OPP port modelling effort was conducted using the Finite Volume Community Ocean Model (FVCOM) (Chen, Liu, and Beardsley 2003) under the World Class Tanker Safety System (WCTSS) program, yielding prototype models for ports of Canso, Kitimat, and Vancouver Harbour. Even earlier, there have been modelling efforts based on Backhaus (Backhaus 1983; 1985) yielding models for the St. Lawrence estuary (Saucier and Chassé 2000) and the Gulf of St. Lawrence (Saucier 2003). These were then followed by implementation of an equivalent NEMO model by Environment and Climate Change Canada (ECCC), the Regional Marine Prediction System (RMPS) GSL. The RMPS was operational from 2011 to 2021, though none of these earlier models were considered for use in OPP. The WCTSS FVCOM prototypes used unstructured model meshes to resolve the coastal regions to within tens of metres or less, with resolution gradually decreasing to kilometres to match the parent model grid on the open boundary.

FVCOM has no history of operational deployment in Canada, while NEMO 3.6 (Nucleus of European Modelling of the Ocean) is used operationally by the Canadian Operational Network for Coupled Environmental PredicTion Systems (CONCEPTS). In the early part of OPP, a

comparison exercise between FVCOM 4.1 and NEMO 3.6 (Nudds et al. 2020) informed the decision-making process to select which codebase to use for the POPS models. Both codebases were used to construct models of the Bay of Fundy and the Port of Saint John (Paquin et al. 2020), which was chosen due to the large tides and complex circulation. NEMO 3.6's most significant deficiency in this context is the lack of wetting and drying, so if NEMO 3.6 could provide satisfactory results in the Bay of Fundy, then it would likely be suitable for use in the other regions. The two models were evaluated on how well they matched observations, as well as on computational efficiency, stability, and robustness. Both models were found to be skillful at reproducing observed data: neither model was significantly superior, and the choice of model to use going forward rested more heavily on the other factors.

Ultimately the decision was taken to proceed with NEMO 3.6, despite its structured grid, a somewhat coarser nearshore resolution, and higher demand for computational resources, to facilitate operationalization and align with modelling efforts at ECCC. Additional advantages of NEMO include active development that delivers regular code updates and bug fixes, an international NEMO Consortium group where members steer code development, and a well-established international operational modelling community.

Thus the ocean model used for all port ocean prediction systems is the CONCEPTS code: a fork of NEMO 3.6 (Madec 2016) that has been customized to meet the operational needs of CONCEPTS, for example (Dupont et al. 2015).

2.2. DOWNSCALING STRATEGY

The port models are downscaled solutions driven by larger-scale coastal ocean models currently operational at ECCC:, the Coastal Ice-Ocean Prediction Systems East and West (CIOPS-E, CIOPS-W; Paquin et al. 2021a, Paquin et al. 2021b) have 2-2.5 km resolution, and Salish Sea 500 (~500 m resolution) which is part of the CIOPS-W system. Output from these models forms the boundary conditions for our higher-resolution, smaller-area models. We use two levels of nesting to achieve a resolution fine enough to reach port scale. The nesting is one-way (coarse to fine), so no information is fed back to the larger scale models, allowing the models to run sequentially but otherwise independently of each other. This one-way nesting strategy also enables systematic errors to be corrected at the open boundaries.

We do not employ a dynamic ice model. Instead, we use a NEMO feature called "ice if", which uses input ice fields and the local freezing point to assess where ice cover exists, and in those locations it restores the sea surface temperature to the local freezing point and sets heat fluxes to -4 Wm^{-2} (Madec 2016).

We do not employ data assimilation or spectral nudging; all model runs are free runs.

River discharge data is used where available to supply the most realistic freshwater input to the model, and climatology is used when this is not available. Gauge data is also used in some cases to construct water level boundary conditions.

2.3. SIMULATION SEQUENCING

The port models operate in three configurations: hindcast, pseudo-analysis and forecast. Hindcasts are the most straightforward, using larger-scale model forcing and quality-controlled gauge data to drive the models. The model begins in the past from a cold-start (temperature and salinity interpolated as initial conditions, water at rest) or a hot-start (temperature, salinity, velocity, and sea-surface height interpolated as initial conditions) and reaches a spun-up state after a period of adjustment to the forcing. The model output is considered usable once spun up, and the model can run nearly up to the present in this configuration, provided that forcing data is

available. Pseudo-analysis runs are daily runs that keep the model state caught up to near-real-time, and do not include a direct data-assimilation component. Rather, the state is indirectly driven by data via boundary and surface forcing terms. These runs are used to initialize the first forecast of each day and may use different input than hindcasts depending on what data is available in real-time.

The pseudo-analysis and forecast schedule is chosen to match the schedule of the parent models that we use for forcing. Shortly after 00Z each day, a 24 hour pseudo-analysis simulation runs to catch up the model state to 00Z. This process uses restart files (so no spin up needed) and, where possible, uses gauge data drawn from a near-real-time data feed which receives limited quality control. Following the pseudo-analysis, the POPS generates four forecasts per day, each 48 hours long, which start from 00Z, 06Z, 12Z and 18Z. The daily 00Z forecast starts using the restart file from the daily pseudo-analysis and runs for 48 hours, saving a restart file six hours into the simulation. The 06Z forecast starts from this restart file, also saving a restart file six hours in, and similarly for the 12Z and 18Z forecasts. A schematic of this setup is shown in Figure 1. We focus only on the 00Z forecasts in this evaluation.

While the 00Z forecast simulation is nominally started at 00Z each day, in practice, the initialization of the simulation is delayed as it can not begin until all inputs are available from the larger scale models and the pseudo-analysis completes. At time of writing, this delay is approximately 5 hours, such that upon completion, each forecast simulation has about 43 hours of output that is in the future.

2.4. SURFACE FORCING

Surface forcing is derived from the High-Resolution Deterministic Prediction System (HRDPS) (Milbrandt et al. 2016) that runs operationally at ECCC and provides atmospheric weather forecasts four times per day at 2.5 km resolution. This is the highest-resolution operational atmospheric product available and is chosen to be consistent with the forcing used in CIOPS-E/W. In hindcast and pseudo-analysis mode, we use a time-blended form of the HRDPS forecasts, where hours 06–17 from successive forecasts are combined using weighted averaging to form temporally continuous fields with the same blending schedule as CIOPS-E/W. Additional details are given in the technical documentation for CIOPS-W version 1.5 (Paquin et al. 2022). Time blending is not used for forecasts.

The surface forcing is applied to the NEMO model using the CORE algorithms (Large and Yeager 2004) with modifications by ECCC to (a) read input data from the in-house RPN file format and (b) use the lowest diagnostic level of the atmospheric model rather than the conventional 2 m and 10 m data. Precipitation and sea-level pressure variations are also applied to the surface of the model.

2.5. AUTOMATION SUITE

The hindcast, pseudo-analysis and forecast simulations are all managed using ECCC's Maestro sequencing software. We have constructed a Maestro suite that is based on ECCC's CIOPS-E/W suites, where we use some of ECCC's functionality for the atmospheric forcing preparation and the mechanics of running the NEMO model, including managing restart files and outputs. We augment this baseline with functionality to prepare boundary forcing, extract data from the real-time data feed, generate the runoff forcing and prepare ice-concentration input files for the "ice-if" feature. Fallback strategies for missing data and persistence strategies for forecasts using gauge data are also implemented here.

2.6. ROBUSTNESS AND LIMITATIONS

For an operational model to be useful, it must be robust and not prone to failure. We have not assessed the models exhaustively in this regard; such testing is an ongoing process. However, some aspects have been explored:

- Where gauge data is needed as a model input, fallback mechanisms are implemented to mitigate missing or bad gauge data. Typically, this means we prepare a climatology for each gauge to stand in when the gauge data is unavailable. With these prepared ahead of time and with appropriate tooling to automate the switchover, the models can run despite missing gauge data and experience a graceful degradation through forcing with lower-quality data rather than a failure. Measuring the severity of the degradation under data-loss scenarios is reserved for future work.
- A long hindcast is conducted for model performance assessment. This long simulation demonstrates that the model is stable subject to a multi-year sample of weather/forcing conditions. In some cases, the hindcast period samples some extreme events, which helps bolster the case for model stability.
- Daily demonstration simulations (pseudo-analysis and four forecasts) have run for order one year on the General Purpose Science Cluster (GPSC) on a best-effort basis, to show that the automation suite can run the models routinely and reveal edge cases that can be fixed to improve robustness further. The purpose of running these pre-operational, best-effort simulations is to demonstrate the functionality/stability of the NEMO-based numerical model and the driving automation suite, and identify issues that would impact operational deployment. The dominant source of issues experienced that impede on-schedule daily forecasts are (a) GPSC compute system downtime, both planned and unplanned, and (b) lack of availability of the forcing data from the larger-scale models that are nominally mirrored on schedule from ECCC's systems. These issues are deemed an expected consequence of using a research cluster and would be mitigated using an operational cluster.

The models will have some limitations:

- Intrinsic variability is expected in each model, and this has not been characterized.
- The lack of wetting and drying capability in NEMO 3.6 requires artificial bathymetry deepening in intertidal regions.

3. CURRENT PORT DESCRIPTION

3.1. REGIONAL OCEANOGRAPHY

The Kitimat fjord system spans ~140 km from the Port of Kitimat to the continental shelf ocean at Hecate Strait (Figure 2). The Port of Kitimat primarily serves as a cargo terminal for a local aluminum smelter, as well as a major liquefied natural gas (LNG) export facility that is under construction at the time of writing. This completion of this facility will result in a large increase in traffic for the port. The primary shipping lanes accessing the port, running from Principe and Squally Channel into Douglas Channel, contain a multitude of critical manoeuvres. A major ferry route, utilized by both Canadian and US passenger vessels, also runs through the fjord system via Princess Royal and Grenville Channel, which is less than 500m wide at the narrowest point. For these reasons the port was selected as a primary candidate for implementation of e-Navigation and enhanced environmental emergency response.

Douglas Channel, the primary channel in the system, is between 3 and 5 km wide, however many of the adjacent channels are narrower than this. The bathymetry slopes steeply off the sides of the mountains adjacent to the fjords. At the deepest point in the fjord system in southern Squally Channel, the water depth reaches 680m, and depths of 300 – 400 m are common even into the immediate vicinity of the docks. The shallowest point of the system, barring isolated rocks, is at the junction of Verney Passage and Ursula Channel where a sill spanning across the channel reaches to within 25 m of the water surface.

In an absolute sense, water levels and currents in the system are dominated by the M2, lunar semi-diurnal, tide with an amplitude of 1.65 m at Kitimat. The next most prominent constituents, in order of amplitude, are S2, K1, and O1, and the total combination results in an average tidal range of approximately 4 m (Webster 1980; Shan et al. 2020).

System-wide non-tidal water level fluctuations can be generally attributed to the atmospherically driven inverse barometer effect and wind-generated coastally trapped waves propagating northward along the coast. However, significant smaller scale variations in local water levels can be driven by local wind and freshwater inflow (Wan et al. 2017; Shan et al. 2020).

On seasonal and longer time scales, non-tidal currents are dominated by estuarine circulation driven by the mixing of significant freshwater inflow into the fjord system with ocean water below. Gardner Canal has been identified by (Shan et al. 2019) as the head of the estuarine system, with primary inflow from the Kitlope and Kemano Rivers. The Kemano River and the Kitimat River, at the head of Kitimat Arm, are the only two gauged rivers in the fjord system. However, overland flow is a significant contributor to freshwater influx and total runoff into Gardner Canal has been estimated to be 17 times the Kemano River flow and runoff into Douglas Channel as 3 times the Kitimat River flow (Webster 1980). This estimate was later corroborated by the climatology study of (Morrison et al. 2012). Freshwater inflow peaks with the freshet in June, with a secondary peak in October, attributed to heavy rainfall (Shan et al. 2020). As a result of the significant volume of freshwater, a fresh surface layer (with surface salinities at times <1 PSU at the head of Gardner Canal) is maintained over the upper 8-12 m in the upper reaches of the fjord system (Wan et al. 2017).

Local wind is a significant driver of non-tidal currents in the fjords on time scales of hours to days. In the summertime, the predominant wind is weakly up-channel in Douglas Channel (towards Kitimat) and counteracts, or even reverses, the estuarine outflow in the surface layer. In the winter months, wind is predominantly down-channel and characterized by strong katabatic outflow events. This enhances the surface outflow in Douglas Channel, and results in a multi-layer return flow structure in the deeper water (Wan et al. 2017; Blanken et al. 2020).

For further general information on the physical oceanography of the Kitimat fjord system, the reader is referred to the works collected in (Webster 1980) and (MacDonald 1983). The subtidal circulation in Douglas Channel is detailed by (Wan et al. 2017), and estuarine circulation in the system is further described by (Shan et al. 2019). Surface drift patterns are analysed in (Blanken et al. 2020), and (Shan et al. 2020) provides a detailed study of water levels in the fjord system.

3.2. DOMAIN AND CONFIGURATION

The port model for the Kitimat fjord system consists of a coarser grid, nominally 500m resolution (1/180th degree; KIT500), covering the approaches to the port with boundaries at or near Prince Rupert, Klemtu, and Hecate Strait. The port itself, in the upper reaches of the fjord system, is covered by a finer grid with nominally 100m resolution (1/900th degree; KIT100). The extents of both KIT500 and KIT100 grids are shown in Figure 2.

Both configurations share a vertical grid, which resolves the upper 10m into 1m layers and increases to 28m layer thickness near the sea floor. Fewer vertical layers, 33 rather than 50, are required for the 100m configuration as the maximum depth in this domain is shallower than the maximum depth in the 500m configuration; 413m compared to 864m. Details about parameter choices in both KIT500 and KIT100 configurations are given in Table 1, and further discussed in the following text.

All channels in the model domain are resolved with a minimum horizontal resolution of two grid points. In Douglas Channel and along other parts of the main shipping route into the port of Kitimat a minimum horizontal resolution of seven grid cells is maintained. Note that the resolution across the ferry route through Grenville and Princess Royal Channel is not well enough resolved to produce reliable results. Also, the 2.5km resolution of the applied atmospheric forcing provides at most one full grid point across most of the channels in the upper reaches of the fjord system which likely limits the quality of wind forcing as topographic steering is not properly captured in many parts of the domain.

The Kitimat port model grids are subsets of the CIOPS-W grid (Paquin et al. 2021b; Paquin et al. 2022), and the port models share many of the physics parameterizations employed in the parent model. Momentum advection is processed in vector form, while tracers are advected using the TVD scheme (Zalesak 1979), both using sub-stepping. Diffusion of both momentum and tracers is computed using a Laplacian scheme, with 3D time-varying viscosity according to (Smagorinsky 1993). Bottom friction is represented in a non-linear manner, with log-layer enhancement, while sidewall friction is handled using partial slip with coefficients given in Table 1 (Madec 2016). It is important to note here that, due to the relatively small aspect ratio of the fjords, sidewall friction has a large impact in the Kitimat port model configurations compared to traditional shelf or open ocean NEMO configurations.

3.3. INITIALIZATION

Initial values of temperature, salinity, currents, and water levels for the Kitimat 500m grid (KIT500) are interpolated from CIOPS-W and extrapolated using a flooding algorithm where required, as CIOPS-W does not resolve some smaller channels in the model domain. The Kitimat 100m grid (KIT100) is initialized from the 500m grid in the same manner.

The 500m and 100m simulations were initialized on Dec 16 and 17 2015, respectively. The first 15 days of simulation are considered spin-up, and evaluation against observational data began on Jan 1 2016. It is noted that this spin-up period is likely insufficient to fully initialize deep circulation within the fjords. The choice of spin-up period was necessitated by the availability of atmospheric forcing, and assessment of performance metrics early in the hindcast period is done with this context in mind.

3.4. OPEN BOUNDARY FORCING

Open boundary conditions of sea surface height, currents, temperature, and salinity at the west, south, and east side of the KIT500 domain are provided at an hourly interval by CIOPS-W using the numerical schemes listed in Table 1. Both sea surface height and currents are provided as de-tided values, and supplemented with tidal constituents from WebTide (Foreman et al. 2000), listed in Table 1. This was done to ensure that no tidal errors were propagated into the domain, and to allow fine tuning of the boundary tides to optimize tidal predictions at Kitimat. The phases of the applied constituents were adjusted slightly, by values given in Table 2.

Due to differences in the vertical datum used during bathymetry generation, the final hindcast was completed with 20cm subtracted from the sea surface height forcing applied at the KIT500

open boundary. This offset of -20 cm is an estimate of the difference between CGVD28 and the EGM-DIR-R4 geoid used by CIOPS-W. Revising this estimate is reserved for future work.

Finally, note that hourly currents from CIOPS-W were not available at the eastern boundary of the KIT500 grid, and daily currents were applied here. The impact of this is small, due to the small 'wet' extent of the eastern boundary, but the lack of hourly currents here will be corrected in the next version of CIOPS-W.

3.5. FRESHWATER INPUT

Daily runoff forcing to the port model configurations is determined from the flow gauges on the Kitimat River (ECCC Gauge 08FF001) and the Kemano River (ECCC Gauge 08FE003), with the latter only being applicable to the KIT500 domain. In areas where no real-time information on river flows is available, a runoff climatology for the BC coast (Morrison, Foreman, and Masson 2012) is used to estimate freshwater inputs.

All runoff forcing is applied to the surface cell of the model, with no enhanced mixing, as this was found to best represent the strong surface salinity stratification observed throughout the fjord system. For climatological river runoff (i.e. all sources except for the Kitimat and Kemano rivers), inflow is distributed over a number of model grid points around the central location identified in the climatology since the runoff generally does not enter the ocean in a well-defined stream, but rather as overland flow (Wan et al. 2017). To determine the number of grid points the annual inflow at the point in question is divided by the mean runoff into the system and multiplied by seven. The factor of seven is a tuning parameter that was optimized for representation of the surface fresh layer.

Temperature information for the runoff into the fjord system is taken from a climatology of measurements at the Kitimat River gauge and applied uniformly throughout the model domains. For forecasting, the last measured flow values at the river gauges are assumed to persist for the duration of the forecast.

3.6. ICE MODEL

Sea ice is generally not encountered in in significant volumes in the Kitimat port model domain, though minor sea ice events do occur in some side channels when very fresh surface waters coincide with freezing temperatures. However, these minor events do not warrant the inclusion of a sea ice model here. Treatment of sea ice is limited to the 'ice_if' formulation, described in Section 2.2.

3.7. MODELLING SYSTEM STABILITY

In the described configuration, the models were used to produce a hindcast of ocean conditions from Dec 16, 2015 to Jan 31 2023, as well as a set of forecasts for evaluation between Dec 1, 2021 and Feb 1, 2022. No stability issues were encountered during these simulations.

During model development, the following principal aspects of the domain configuration were identified to be controlling on model stability for the 500m domain:

1. Minimum imposed depth, with stability issues occurring in the islands southwest of Caamaño Sound for values less than 5m;
2. Sub-stepping of momentum advection, with stability issues encountered over the sill at the confluence of Verney Passage and Ursula Channel when sub-stepping was not used;
3. Sidewall friction, with stability issues around the constriction in Grenville Channel for values below 0.2;

4. Time step and eddy viscosity, which were optimized to maximize performance while maintaining stability.

For the 100 m domain, additional control is imposed at the entrance to Foch Lagoon, off upper Douglas Channel, where a slight widening of the entrance and increase of sidewall friction to 0.35 were required to maintain stability.

Instability may be induced by strong water velocity or locally low water level events, which may be a result of strong winds or large volumes of freshwater influx. Based on wind records from ECCC buoy 46181 at Nanakwa Shoal near the port, the 9th strongest wind event on record (since 1988) occurred during the hindcast period, on Jan 6, 2022, with a measured wind speed of 17.6 m/s. This value is representative of common wintertime outflow winds, with a yearly probability of exceedance of 24% based on the full record. However, wintertime outflow winds may be under-represented in the data as the anemometer is prone to failure due to icing in winter storms (Wan et al. 2017; Blanken et al. 2020).

The gauged freshwater influx into the Kitimat fjord system reached the highest levels on record during the hindcast period, for both the Kitimat and Kemano Rivers. Daily average discharges of 1730 m^3/s and 1030 m^3/s were measured on the Kitimat and Kemano on the 24th of October 2017. Record keeping began on August 25, 1964, for the Kitimat River, and November 20, 1971, for the Kemano River.

Based on the ambient environmental conditions during the hindcast period, the port model can be said to be stable during most strong winds as well as extreme runoff events. Systematic stress testing to further delineate the bounds of model stability has not been completed at the time of writing but will be done in the future.

4. EVALUATION METRICS

The model performance is assessed through the analysis of a multi-year hindcast and a shorter set of forecasts, where the dates considered are constrained by available surface and boundary forcing from larger scale models. The hindcast evaluation uses a wide set of observations to analyze the model's representation of ocean conditions, including tidal analysis and model drift that would be difficult to assess on a short model run. Meanwhile, the forecast evaluation focuses on measuring the degradation of model skill as a function of forecast lead time for a smaller set of observations available during the forecast period.

Quality controlled data sources were preferred where possible. We performed additional quality control to some data as needed, including visual inspection, thresholding and automatic de-spiking to eliminate suspect data.

4.1. HINDCAST

Hindcast performance is assessed through comparison with available observational data. For each observation, we extract the corresponding virtual observation from the model. The error is defined as

$$\text{ERROR} = \mathcal{X}_m - \mathcal{X}_o ,$$

where $\mathcal{X}_o$ and $\mathcal{X}_m$ are the observed and modelled values such that a positive/negative value indicates a model over/underestimate. For currents, $\mathcal{X}_o$ and $\mathcal{X}_m$ are taken as complex numbers with the real part representing the eastward and imaginary the northward components of velocity.

We use several scores, the bias, the centered root means square error (hereafter CRMSE) and the root mean square error (hereafter RMSE),

$$\text{bias} = \frac{1}{N}\sum \text{ERROR} = \frac{1}{N}\sum \mathcal{X}_m - \frac{1}{N}\sum \mathcal{X}_o = \overline{\mathcal{X}_m} - \overline{\mathcal{X}_o},$$

$$\text{CRMSE} = \sqrt{\frac{1}{N}\sum (ERROR\text{-}bias)^2},$$

$$\text{RMSE} = \sqrt{\frac{1}{N}\sum ERROR^2} = \sqrt{bias^2 + CRMSE^2},$$

and these measures retain the units of $\mathcal{X}$.

We also use the unitless gamma squared score.

$$\gamma^2 = \frac{CRMSE^2}{\sum(x_o - \overline{x_o})^2},$$

which is the ratio of error variance to observed variance, such that zero indicates perfect agreement between model and observation variance, and unity indicates error variance is as large as the signal variance. A value of unity or larger indicates no skill.

For scalar quantities, we use the unitless sample Pearson correlation coefficient score,

$$\text{PEARSONR} = \frac{\sum (x_m - \overline{x_m})(x_o - \overline{x_o})}{\sqrt{\sum (x_m - \overline{x_m})^2 \sum (x_o - \overline{x_o})^2}}$$

where zero indicates no correlation and unity indicates perfect correlation. For vector quantities (currents) we have the vector correlation coefficient (Kundu 1976; Röhrs and Christensen 2015),

$$\text{VECTORR} = \frac{\sum (x_m - \overline{x_m})^* (x_o - \overline{x_o})}{\sqrt{\sum (x_m - \overline{x_m})^2 \sum (x_o - \overline{x_o})^2}},$$

where the asterisk represents complex conjugation, which is also implied for squaring of complex numbers. This quantity is a complex number, where the magnitude measures the overall correlation and the angle is a measure of the average angle of the modelled current with respect to the observation. Here we compute the angle as positive clockwise to be consistent with the convention of representing the velocity direction as positive clockwise from North. Lastly, the vector correlation angle is only considered meaningful when the correlation magnitude is large (Kundu 1976).

4.1.1. Water level

Water level observations from the Canadian Hydrographic Service (CHS) are transformed from CHS Chart Datum to Canadian Geodetic Vertical Datum of 1928 (CGVD28) by subtracting a station-specific offset. CHS provides these offsets are based on measurements from a GNSS (Global Navigation Satellite System) occupation at each station. Pacific US stations are shifted from the US datum to CGVD28 via NOAA's VDatum and NRCan Vertical Datum Transformations online tools. Atlantic US stations were gathered with a mean low-low water datum and converted to CGVD28 using conversion surfaces provided by CHS. Water level observations from the Water Survey of Canada (WSC) are shifted to CGVD28 using offsets provided by WSC.

Tidal analysis is performed using T_TIDE on one-year segments at an hourly sampling interval. Where data is available at a higher frequency, it is interpolated/subsampled to hourly frequency.

Observations missing more than 10% of the data points are not detided. The tidal analysis enables the decomposition of the total water level into tidal and non-tidal parts as

$$H_{total} = H_{tidal} + H_{nontidal}.$$

The annual (SA) and semi-annual (SSA) constituents are excluded from the tidal analysis; these constituents are subsumed into the non-tidal component. For the present purpose this is adequate as the same process is applied to both model and observations, and the extent to which the models do not reproduce SA or SSA is captured in the non-tidal error scores. Constituents with signal-to-noise ratios below 2 are also subsumed into the non-tidal part. Water level bias is included in the non-tidal component. Scores are reported for the total, tidal and non-tidal components. Owing to a negligible cross-correlation between tidal and non-tidal water levels, to a good approximation, we have

$$\mathrm{CRMSE}^2_{total\ wl} \cong \mathrm{CRMSE}^2_{tidal\ wl} + \mathrm{CRMSE}^2_{nontidal\ wl},$$

which shows how these two errors contribute to the total. Amplitude and phase errors are reported for the significant constituents, as is the tidal error.

$$\text{TIDAL ERROR} = \left[\frac{1}{2}({h_o}^2 + {h_m}^2) - h_o h_m \cos(\phi_o - \phi_m)\right]^{\frac{1}{2}},$$

where h_o and ϕ_o are the observed (subscript *o*) amplitude and Greenwich phase lag for a given tidal constituent, while h_m and ϕ_m are the modeled (subscript *m*) amplitude and phase (Cummins and Oey 1997).

4.1.1.1. Storm surge evaluation

To evaluate the port models' performance during storms, a handful of stormy periods are selected for each port. The cyclone database of (Zhang et al. 2019), which provides global storm tracks from 1958 to 2021 (Figure 3 shows a zoom of North America), guides the selection. The database was queried for storms passing within a few hundred kilometres of each port model domain, and it provides a comprehensive list of storm events during the hindcast period. However, this list is quite extensive for some ports (particularly Canso and Saint John), so longer lists are narrowed down by considering minimum central pressure, examining water level gauges, and local media reports of storm impacts. The evaluation follows the residual water level hindcast evaluation in terms of performance scores and plots but is limited to the storm periods.

Storm surge detiding is done using a 40-day window around the storm's peak, i.e., 20 days before to 20 days after. This differs from the typical water level analysis, which is done in yearly spans and as such can include more constituents. However, using a shorter window does a better job removing the tides during each storm, particularly in areas with non-stationary tides.

We note that storm surges may interact non-linearly with tides to impact water levels, but we do not investigate this phenomenon here.

4.1.2. Water velocity

Velocity data is available from ADCPs and some current metres in one of four configurations: mounted on a mooring, buoy mounted (i.e., floating), in a float towed by a ship, or horizontally mounted on a shore structure (HADCP). Only horizontal (east-west / north-south, u/v) velocities are considered here. The horizontal velocity's u/v and speed/direction decompositions are both considered, and directions are calculated as positive clockwise from north.

Model data is extracted to match the observed data's time span and spatial location. Time series longer than 29 days and with less than 10% of data points missing are detided using

T_TIDE; hourly data is used for detiding, and where more frequent data is available, it is first down sampled. As with water level, the SA and SSA constituents are excluded from fitting, a Rayleigh value of 2 is used, and the observations and model data are processed the same way.

Currents are noisier, tend to have more missing data, are less stationary, and are impacted by more non-linear processes than water level observations, and these factors make the detiding process less robust. Owing to nonlinear processes such as bottom friction, some tidal (kinetic) energy will spread into adjacent frequencies, so fitting to tidal harmonics does not capture all variability induced by the tides, and some near-tidal variability remains in the residual velocities. We do not apply low-pass or band-stop filters to the residual to reduce the noise. While doing so would provide a more completely de-tided residual time series, some of the total signal would be unaccounted for by either the tidal or non-tidal evaluation. Given these caveats, the tidal component may be more accurately described as "the component of the currents that T_TIDE is able to fit." Currents are evaluated using similar metrics to water level, using complex formulations. Tidal constituents are evaluated using the ellipse error (Cummins and Thupaki 2018)

$$D_u = \left[\frac{1}{2}(A_o^2 + B_o^2 + A_m^2 + B_m^2) - \cos(g_o - g_m)\cos(\theta_o - \theta_m)(A_o A_m + B_o B_m) - \sin(g_o - g_m)\sin(\theta_o - \theta_m)\,(A_o B_m + A_m B_o)\right]^{1/2},$$

where A and B are semi-major and semi-minor axes, respectively, the subscripts *o* and *m* correspond to observed and modelled, g is phase, and θ is angle of inclination. For the non-tidal and total time series, complex formulations of the metrics listed at the beginning of the section are used, including bias, CRMSE, γ^2, and vector correlation.

We note that for single-location instruments, in particular moored current meters and moored and horizontally mounted ADCPs, we expect the scoring to be sensitive to the details of the model run under evaluation. Small errors in bathymetry can adjust the location of deterministic features (eddies, jets, meanders, etc.) and this can lead to large errors in the scoring. Meanwhile, chaotic internal variability can also affect the location of such features. An ensemble of model runs could help mitigate the latter but is beyond the scope of the current effort.

4.1.2.1. Horizontal ADCPs

HADCP data is decomposed into along- and cross-channel components, and evaluation is done primarily with mid-beam data to avoid edge effects. When a long enough time series is available, a tidal analysis is done as with moored instruments. Time series of the first week of data are plotted, regardless of how long the total time series is, to show the daily variability in the signal and how well the model captures it. Scatter plots are used to show the distribution of speed and direction of the total velocity, and the semi-major axis for the tidal ellipses are compared when feasible.

4.1.2.2. Current meters and moored ADCPs

Current meters report velocity at a single depth, so those velocities are evaluated at instrument-specific depths. For ADCPs on moorings or buoys, a standard set of depths at which to evaluate the velocities is selected on a per-port basis, taking into account local bathymetry and data availability; for brevity, statistics may be reported only at some depths for each instrument considered. These levels are defined relative to either a nominal surface (i.e., one with no sea-surface height variation) or the time varying sea surface. For regions with ADCPs in relatively deep water without a large tidal range, using the nominal surface is sufficient. For shallow regions and/or those with large tidal ranges, the evaluation is done relative to the time-varying

sea surface, using the observed total water depth to process the observations and modelled sea surface to process the modelled currents.

The observations are preprocessed to remove any spurious data points: values larger than 10 m/s are discarded and the data points are resampled if needed to be evenly spaced.

Tidal analysis is done on all timeseries of at least 29 days at depths with less than 10% of the data missing. Tidal ellipses are plotted for the largest tidal constituents, including depth profiles of tidal ellipses for the largest constituents. Time series and histograms are plotted for both the non-tidal and total velocities. Analysis of total velocities only is done for shorter time series or time series with missing data. We note that if data is missing at consistent phases of the tide, then the analyzed results may be aliased, and so time series with substantive regular gaps are not analyzed or presented.

4.1.2.3. ADCP transects

ADCP transects are too short for tidal analysis, so only the total velocities are considered. An along-transect / cross-transect decomposition is used, with a constant angle used for decomposition for the entire transect; this is sufficient as the transects are typically short and straight. Along-transect plots of velocities at depth are used for evaluation. Scatter plots of bias vs CRMSE are also plotted, with the statistics calculated at each physical point and integrated over the transect.

4.1.3. Water properties

Conductivity-Temperature-Depth (CTD) profiles are grouped into manually defined subregions based on the geography of each port domain. This enables an aggregate assessment over areas, including bias and CRMSE as a function of depth for each area. Model results are taken from the nearest point to the data location and nearest to the observation time. Vertical profiles are interpolated to the model z-levels to bring all data to consistent depths.

Sea surface temperature buoy and moored CTD measurements are evaluated using the bias, CRMSE, χ^2 and Pearson's *r* scores over the evaluation period. Model values are linearly interpolated to observation locations in the horizontal and vertical dimensions. The observed and modelled time series are interpolated to the largest common data interval.

Ferry thermosalinographs are vessel-mounted temperature and conductivity sensors. They provide a measure of near-surface water temperature and salinity by collecting data through one of the vessel's seawater circuits. Model results for comparison with these data are taken from the point nearest to the observed locations both horizontally and vertically and then linearly interpolated to the observation times. Hovmöller plots of observations, model results and differences, plus basic statistics, are used to assess the model performances relating to near-surface water.

4.1.4. Drift

The models' performance in drift trajectory prediction is assessed by comparing the observed tracks of ocean surface drifters with analogous trajectories modelled using the surface currents output by the port models, in combination with wind forcing from the National HRDPS atmospheric forecast. This comparison is done using the drift evaluation tool developed as part of the DPNM sub-initiative, in the OpenDrift configuration (Soontiens and Holden 2024).

Windage on the surface drifters is applied by computing the wind drag coefficient based on the drifters' drag area ratio (Niiler et al. 1995; Daniel et al. 2002; Röhrs et al. 2012; Hourston 2021; Blanken et al. 2021). This coefficient parameterizes the effect of direct wind drag on the parts of

the drifter exposed above the water surface and varies with drifter geometry. To account for wave-induced Stokes' drift, an additional 1% of the wind speed is added (Sutherland et al. 2020), and this sum is applied as the windage in the trajectory prediction.

This method of applying windage assumes that currents over the draft of the drifter are known exactly, as are winds directly at the ocean surface. However, in reality, neither of these assumptions is true, since:

1. The representation of surface currents in NEMO is limited by stability restrictions on near-surface vertical resolution and model uncertainty in general; and
2. Wind speed from the HRDPS model is also subject to model uncertainty and given at 10 m where winds are usually ~30% larger than at 1 m but could be as much as five times larger depending on wind speed and atmospheric stability (Smith 1988).

The representation of Stokes' drift as 1% of the wind speed represents a further assumption, as this value was derived by comparing tracks from various types of surface drifters to currents from the Regional Ice-Ocean Prediction System (RIOPS) ocean model and Canadian Arctic Prediction System (CAPS) atmospheric model (Sutherland et al. 2020). As noted in the discussion section of (Sutherland et al. 2020) and references therein, this value can vary widely depending on the combination of ocean and atmospheric forcing, which implies that model uncertainty contributes significantly to the appropriate value here. The authors also note that explicitly including Stokes drift based on a wave prediction system is preferable over parameterization based on wind velocity.

The windage term used here could be optimized by deriving it for each ocean/atmospheric model combination using the procedure in (Sutherland et al. 2020). However, this is beyond the scope of this report: the focus is on improvements to the current forcing for drift simulations without evaluating the suitability of wind predictions in the port model domains for drift prediction or commenting on the potential utility of a port-scale wave prediction system. The windage parameterization used here is merely intended to provide a consistent, deterministic linkage between modelled currents, winds, and the motion of various drifter types. As considerable uncertainty is associated with this windage term, evaluation of surface currents against observations from ADCPs and current meters is deemed the primary determinant of model suitability for drift prediction, rather than analysis of observed and modelled drifter tracks.

Periods where drifters were active in the model domain are identified, and modelled trajectories are started every hour along the drift tracks. The benefits of starting drift tracks in this manner are to reduce the sensitivity to initial conditions and increase the number of tracks available. However, it means that some drift tracks are not independent and thus the errors may be correlated. Modelled trajectories were computed for a user-specified period of 24 hours or more, where possible. However, in some regions, the majority of the observed drifter tracks were less than 24 hours long, and here a shorter modelled trajectory length was chosen.

Observed drifter tracks were truncated to areas covered by the 'wet' cells of the port model domains to avoid launching virtual drifters in 'dry' parts of the domain where observed drifters are near the shoreline, which may not be precisely resolved. In addition, to facilitate interpolation of starting locations for virtual drifters, observed trajectories were split where time gaps between position records exceeded two hours. In the remaining portions, position records were interpolated to a consistent time interval ranging from five minutes to one hour.

For each model – observation pair of trajectories, two statistics are computed to assess the model performance. First is the separation distance, D, which is given by,

$$D(t) = |\dot{x_o}(t) - \dot{x_m}(t)|$$

Here $\dot{x_o}$ and $\dot{x_m}$ are the positions of the observed and modelled drifter, and || denotes the magnitude of the vector difference, i.e., the distance, between them.

Second is the instantaneous skill score, S, following (Molcard et al. 2009), which is given by

$$S(t) = \max\left(0, 1 - \frac{D(t)}{d_o(t)}\right)$$

Here $d_o(t)$ is the displacement of the observed drifter from the starting point of the pair. The rationale for the normalization by $d_o(t)$ is to increase the skill assigned to a trajectory prediction as the trajectory length increases, even if the separation distance remains constant. A separation distance of, for example, 500 m represents a less grievous error in a trajectory that is 10 km long than in one that is 500 m long. A value of S=1 indicates a perfect prediction.

4.2. FORECAST

The forecast evaluation involves running a set of forecasts (here 48 hours long, each starting at 00Z) and evaluating the performance over the independent forecasts as a function of lead time. Forecast evaluation was performed for a set of order 60 consecutive forecasts by comparing the model values with tide gauge, sea surface temperature and horizontal ADCP records. The set of forecasts were taken from winter 2021/22 for logistical reasons. Forecast performance was evaluated as the discrepancy (bias and CRMSE) with observed values as a function of forecast lead time. The error growth curves represent the discrepancy averaged over the set of evaluated forecasts, and we include 95% confidence intervals computed with a bootstrap method.

To detide the forecast and the corresponding hindcast water level series we subtract the tidal signal precalculated based on the hindcast covering the forecast evaluation period. The tidal signal is obtained with a T_TIDE fit with a Rayleigh number as low as 0.1 (overfitting) to ensure maximal energy removal at tidal frequencies. Such strong suppression of tidal energy was implemented to clear the error growth curves of any tidal residual, which otherwise would dominate the curve.

5. HINDCAST EVALUATION RESULTS

5.1. WATER LEVEL GAUGES

Water level results from the hindcast simulation are evaluated against two active tide gauges in the region of interest, one in the Port of Kitimat and the second in the village of Hartley Bay at the mouth of Douglas Channel approximately 45 nm down-fjord from Kitimat. Data from other active tide gauges at Prince Rupert and Bonilla Island is also examined but is not the focus of this report as this area is very close to the model boundary and performance here was not prioritized during model development. Offsets used to shift the data from the tide gauges from chart datum to CGVD28 are given in Table 3.

5.1.1. Mean sea surface height

Mean modelled sea surface height during the hindcast period is shown in Figure 4, for future use by the Canadian Hydrographic Service in provision of electronic navigation products. These results show a clear increase in mean water levels from Hecate Strait into the upper reaches of the fjord system. The differences reach up to 18cm between the entrance to the fjords and the heads of Kitimat Arm and Gardner Canal. Increases in mean sea level in lagoons and side channels off the main channels are also evident, most clearly in Foch Lagoon off upper Douglas

Channel (see top right panel of Figure 4). These localized increases are highly sensitive to the friction parameterizations employed in the port model and have not been validated due to a lack of observational data. Hence these results should be interpreted with extreme caution.

5.1.2. Tidal water level

For clarity in the presentation of tidal analysis, comparison is limited to constituents with amplitude greater than 10 cm at Kitimat, namely M2, S2, K1, N2, O1, P1, and K2 (sorted by amplitude).

Both the 500 m and 100 m configurations of the Kitimat port model produce skillful simulations of the tidal water level changes at Kitimat and Hartley Bay (locations shown in Figure 5). For the most part, amplitude and tidal errors are below one centimeter and phase errors below one degree, as shown in Table 4. It is notable that the coarser 500 m configuration produces a more accurate representation of semi-diurnal constituents, whereas diurnal constituents are more accurately reproduced in the 100 m configuration. Overall, the accuracy of tidal water level prediction in both port model configurations is characterized by a centered root-mean-square error of 9-10cm (left panels of Figure 6 & 7).

Both configurations provide an improvement on the tidal water level prediction in the parent model, CIOPS-W, as shown in Table 4 and the left-hand panels of Figure 6 & 7. One exception to this is the K2 constituent, where the port model shows a ~7 degree phase error. However, this is the smallest analyzed constituent, and the overall impact is minor. In terms of the complete tidal water level picture, characterized by the tidal centered root-mean-square error, the port model improves upon CIOPS-W results by ~30%.

Further comparison of tidal water level representation against constituents calculated from historical water level gauges in the port model domain shows that port model performs well in the Kitimat fjord system, with tidal errors in the millimeter to low centimeter range for all analyzed constituents (Tables 5 – 11 and Figure 8 - 10). It should be noted here that many of the historical tide gauges are located at anchorages with constricted entrances, such as Surf Inlet and Barnard Harbour. All comparison in Tables 5 - 11 is against results from the 500m port model domain, as the only constituent data available in the 100 m domain is at Kitimat, which has already been discussed above. Locations of all historical tide gauges are shown in Figure 5.

Tidal water level results near the boundary of the domain are not as good, in the vicinity of Prince Rupert in the north-west and Klemtu in the south-east. Here the CIOPS-W parent model provides more accurate representation of tidal water levels.

A notable historical tide gauge station is Lowe Inlet, off Grenville Channel which is closed in CIOPS-W but coarsely resolved in the 500m port model. Here tidal constituents corresponding to the nearest wet cell in CIOPS-W more closely represent those calculated from observation than the port model, which resolves the channel, but water level predictions are impacted by the narrow width (<500m at narrowest point) and the sidewall friction required for model stability. The conclusion here is that the accuracy of data from barely resolved channels, such as Grenville Channel, is likely to be limited by model resolution and should be used with extreme caution.

5.1.3. Overall scores

Seasonal cycles, and most significant change events, in non-tidal water levels are well represented in the port model at both Kitimat and Hartley Bay (Figure 11 & 12). Notably, both port model configurations miss an isolated surge event in early 2019, leading to a one-time water level underestimate of ~75cm. The cause of this requires further investigation. Biases are

similar between CIOPS-W and the port model, which indicates that the offset applied at the open boundary to correct for vertical datum differences is performing the intended function. However, all models show a low bias at Hartley Bay, ranging from 12 – 16cm though slightly smaller in the port model than in CIOPS-W (Figure 7). This suggests that the sea surface slope between Kitimat and Hartley Bay is not well captured. The slope is strongly affected by both local winds and surface stratification (Wan et al. 2017; Shan et al. 2020), and the cause of this error will be investigated through detailed verification of applied wind forcing against measurements taken in Douglas Channel as well as the surface stratification in the channel.

The performance of the port models against water level observations at Kitimat, Hartley Bay, Bonilla Island, and Prince Rupert are summarized in Figure 6 & 7, where the left-hand plots show total water level bias plotted against the centered root-mean-square-error (CRMSE) of total water level. The right-hand plots show CRMSE of tidal vs. non-tidal water level. The summary presented in these plots, some details of which have been discussed above, show that the port model configurations provide a clear improvement in water level predictions at Kitimat over their parent model, CIOPS-W, though room for further improvement remains. The year-by-year CRMSE of total water level ranges from 11-14cm, improved from 15-17cm in CIOPS-W. The majority of this improvement stems from improved representation of tidal water levels, where the CRMSE is improved by ~50%. Year-by-year non-tidal CRMSE is consistent at 5 - 7cm across the port model configurations and CIOPS-W, with the port models having outlier years (CRMSE ~10cm) in 2019 due to the missed surge event identified above. This is not unexpected, as much of the non-tidal sea level variability in the port model domain is remotely forced (Shan et al. 2020). Port model performance at Bonilla Island, near the western boundary of the model, is comparable to CIOPS-W. This is likely due to the relatively exposed location of Bonilla Island. At Prince Rupert, further north along the western boundary where the coastline and bathymetry are more tortuous and complicated, port model performance is noticeably worse than CIOPS-W on all metrics except bias. It is also of note that the hydraulic slope of the Skeena River is directed downward away from the ocean, opposite to that of the Kitimat River. This is most likely due to the use of climatological runoff, spread over a large area, along with an imposed minimum depth of 5m resulting in an underestimate of Skeena River water levels. Therefore, the port model is well suited for water level predictions in the Kitimat fjord system, and provides a clear improvement on existing solutions here, but should not be used for water level prediction in the Prince Rupert area.

Examination of the power spectrum of total water level at Kitimat (Figure 13) suggests that while all models capture energy peaks at the appropriate tidal frequencies, none capture the broadening of the spectral peak around the diurnal frequency which is likely associated with wind forcing of local sea level changes due to summertime sea breezes. This lends further support to the notion that water level changes in Douglas Channel driven by local wind are not fully captured, as noted in the discussion of sea surface slope above. It is also notable that CIOPS-W exhibits the highest energy level of all the models near the Nyquist frequency. This may be due to the increasingly complicated bathymetry near the head of the channel in the port model, with the partial resolution of the tidal flats in the Kitimat River estuary and Minette Bay, causing increased damping of high frequency water level fluctuations.

5.1.4. Storm surge water level

The data collected by these tide gauges is also used to examine the model performance during the ten strongest storms identified during the hindcast period, taken from the database described in Section 4.1.1.1 as the ten events in the model domain with the lowest central pressure.

Statistics summarized over these ten storm events indicate similar performance between CIOPS-W and the port model, with CRMSE being within 2 mm for all three configurations at Kitimat (Table 12). These summary statistics indicate that the models reproduce storm surges to within a CRMSE of 3 - 4cm at Kitimat and Hartley Bay, with strong correlation (0.93 - 0.96) between modelled and observed water levels. As noted above, Prince Rupert is an exception here, with the port model underperforming noticeably when compared to CIOPS-W.

Closer inspection of the time series showing the surges associated with the ten chosen storms confirms the general conclusions above (Figure 14 – 16). At Kitimat (Figure 14), the 100m and 500m port model configurations are tightly coupled and visually well correlated with observations. However, most time series show a positive bias between modelled and observed time series, indicating that larger-scale changes in water level may be missed. These offsets are mostly, but not always, consistent with CIOPS-W results. Similar conclusions can be drawn from the comparison between the port model and CIOPS-W results with observations at Hartley Bay (Figure 15). However, here the bias between models and observations is generally negative, likely for the same reason as discussed in Section 5.1.3. At Prince Rupert, the biases are smaller than in the Kitimat fjord system, however the port model overestimates high-frequency water level fluctuations compared to CIOPS-W (Figure 16). This is most likely due to boundary effects, and further illustrates that while the port model provides improvement over existing water level predictions in the Kitimat fjord system, it should not be used for water level prediction at Prince Rupert.

5.2. WATER VELOCITY

Port model representation of currents throughout the water column are verified against a collection of single-point current meters and multi-level acoustic Doppler current profilers mounted on subsurface moorings in the model domain. Two of these moorings (KIT1 in Kitimat Arm and FOC1 in upper Douglas Channel) were in place specifically for this purpose between July 2020 and July 2021, whereas the remaining data stems from the WCTSS observation campaign in 2016 and several moorings installed in Hecate Strait for other science programs between 2016 and 2019 (Figure 17).

To keep the analysis of tidal currents clear and reasonably brief, only constituents with a major axis amplitude above 5 cm/s in Douglas Channel are analyzed, namely: M2, S2, K1, N2, and O1. Figures are generally limited to the M2 constituent, which dominates all others.

5.2.1. Horizontal ADCP

There is no horizontal ADCP data available from the Kitimat port model domains.

5.2.2. Current meters

Data from single-point current meters for most stations is available at 150m and 250m depth as well as 5m off the sea floor. In the Kitimat 100m domain, single-point current meters are only available at station FOC1, from January to July 2016 and July 2020 to July 2021. Tidal analysis is primarily conducted on the 2020/21 period since this represents a full year of data. Here the tidal current results in the 100m configuration consistently outperform the 500m configuration (Tables 13 & 15). Both configurations however underestimate the rotational, i.e., minor-axis, components of tidal motion at 150m and 250m, and produce ellipses that are more rectilinear than the observed values (Figure 18). Contrary to water levels, the representation of diurnal tidal constituents is consistent between both configurations. In general, the CRMSE of tidal currents is improved from 6-7cm/s in 2016 to 4-5 cm/s in 2020 and the 100m configuration improves on the 500m configuration results by up to 40%.

In the broader 500m port model domain, the port model consistently improves representation of tidal currents in the fjord system and produces results comparable to the parent model on the continental shelf. However, representation of tidal currents in more remote parts of the fjord system is not as refined as in the vicinity of the port. The statistics presented in Tables 14, and exemplified in Figure 19, indicate CRMSE values for tidal currents of 5 – 13 cm/s at stations in the fjords (KSK1, DEV1, & CAM2) compared to 10 – 14 cm/s at shelf stations (SRC1 & SRN1). The figures and ellipse errors tabulated in Table 15 suggest that the direction and phase of tidal currents are generally well represented and major axes currents are mostly well captured with some exceptions. As in the 100m domain, the main issue with tidal current representation is the minor-axis values. Compared to CIOPS-W, the 500m port model improves tidal ellipses by up to 75% in the fjords. On the shelf the comparison is less clear, with ellipse errors suggesting an improvement of up to 60%, even though the centered root-mean-square errors in tidal currents at these stations are often slightly smaller in CIOPS-W.

For non-tidal currents, the data from station FOC1 indicates similar performance between both configurations of the port model, with a centered root-mean-square error of 6-7cm/s. No significant changes are evident between the 2016 and 2020 deployments (Table 16). Outside of the 100m domain, these errors increase to 5-18cm/s both in the fjords and on the continental shelf. In the fjords this represents a significant improvement over the parent model, while on the shelf the performance between the models is similar (Table 17).

In terms of total currents these results equate to a consistent improvement from the 100m port model configuration over the 500m configuration, which in turn improves results over the parent model within the fjord system and provides similar performance on the continental shelf (Tables 18 & 19). In general, representation of currents is better at 150m below the surface than at depths below this level. Centered root-mean-square errors are improved to 8-9cm/s in the 100m configuration compared to 11-18cm/s in the 500m configuration, at station FOC1 (10-20cm/s outside the fjords). Here biases are on the order of mm/s at 150m depth but increase to 2-4cm/s at 250m and 359m (sea floor). The latter suggests that the estuarine inflow is too weak in the model. However, the bias improves noticeably (by ~1cm/s) between the 2016 and 2020 deployments, which indicates that the estuarine circulation may not be fully spun up in the 2016 comparison. In general, biases of currents in the fjords are reduced compared to the parent model, indicating that the representation of mean circulation is improved.

5.2.3. Moored ADCPs

Measurements of currents are also available from ADCPs on the same moorings, and some additional ones, as those presented in the previous section. Most of these instruments were arranged in a configuration of one 600kHz ADCP at ~40m depth to capture near-surface currents (presenting results from 8m and 15m below surface here), along with one or more 150kHz or 300kHz ADCP at 5m off the sea floor, and intermediate depths as required, to provide full water column coverage. For deeper currents, results are presented at 50m, 100, and 250m. To keep the discussion of tidal currents brief, it is limited to the M2 constituent which is the most significant in the domain by an appreciable margin.

A comparison of the modelled baroclinic tidal current structure and the corresponding observations in the 100m port model domain (stations FOC1 and KIT1) is shown in Figure 20 - 23. From these figures it is evident that the 100m configuration improves on the results of the 500m configuration, though both provide reasonably good estimates of the tidal circulation in the port. At KIT1, which is very close to the port and at the head of Douglas Channel, the tidal currents are very small, with M2 having an amplitude of only ~1cm/s near the surface. Both models overestimate this amplitude, ranging from 2-4cm/s in the upper 15m (Figure 20). However, the representation of the tidal amplitude improves with depth, as seen in Figure 21.

This figure also shows that the phase change with depth is well captured away from the surface. Near the surface, results suggest that the phase shift with depth is overestimated from 8m to 15m while a ~10 degree change in current direction is missed (Figure 20). These observed changes occur over the mean halocline between the freshwater layer and the ocean below, and thus should be interpreted with some caution as this strong halocline may also affect ADCP measurements. Representation of tidal currents is markedly improved down-channel at station FOC1, where M2 tidal amplitude is significantly stronger at 14-18cm/s between 8m and 15m depth. However, as noted in the discussion of current meter data above, the modelled tidal ellipses are more rectilinear than their observed counterparts. But in summary, it is evident from the results presented above and the summary statistics in Table 20 that the 100m configuration represents a significant improvement in the representation of tidal currents over its 500m counterpart.

Down-fjord of the 100m domain, data from station KSK1 in lower Douglas Channel (Figure 24 & 25) shows that the port model clearly captures the barotropic and baroclinic tidal dynamics along this main shipping route into Kitimat with reasonable accuracy. Improvements in some aspects of the tidal currents are also evident in Devastation Channel (Station DEV1, Figure 26), however here the tidal amplitude is underestimated near the surface and the phase, while reasonably accurate at 50m depth, is in error by nearly 180 degrees at 15m below the surface. Clearly baroclinic tidal dynamics in the more remote parts of the Kitimat fjord system require further study. At the entrance to the fjords and on the continental shelf, tidal currents are also well represented and improved from the parent model (See Figure 27 and 28 for results from Caamaño Sound (CAM2) and Hecate Strait (SRC1)). These improvements are clearly evidenced by the summary statistics in Table 21, which show consistent improvement of tidal current error metrics for the port model.

The port model also skillfully reproduces strong non-tidal near-surface current events in the 100m domain. Surface current response to a strong outflow wind event in February 2021 is captured well down to 50m depth at both KIT1 and FOC1, as shown in Figure 29 – 31 and 33 – 35. At 100m depth evidence of the signal matching the observations is still present at FOC1 but not at KIT1 (Figure 32 & 36). However, while these lower frequency signals are well captured a point must be made that the kinetic energy in the non-tidal currents is too low in the port model, by a factor of ~2, as seen in the time series as well as the power spectrum of residual currents (Figure 38). The high-frequency energy level improves by about an order of magnitude from the 500m to the 100m configuration, so it is likely that this can be rectified at least in part by implementing higher-resolution configurations in the future. And not all signals at depth are captured, including a prolonged eastward current in the spring/summer that is likely associated with renewal events (Figure 32 & 35 – 37). Evaluation statistics for non-tidal currents are more favourable at FOC1, compared to KIT1, and generally indicate better model performance for deep currents than near the surface. Statistics are generally more favourable for results from the 100m configuration than the 500m configuration (Table 22).

The broader 500m port model also consistently improves on the representation of non-tidal currents, though this improvement is not as drastic as the improvement in the tidal currents (Figure 39 – 41, Table 23). Improvements are evident in the fjords as well as on the continental shelf. The low biases in currents at depth, evident at Stations KSK1, CMP1, and CAM2 (top panels of Figure 39 & 40) suggests that the estuarine inflow may be too slow, as noted above. However, this may also be due to the bias of the observational data towards the beginning of the hindcast period which may result in excessive capture of spinup errors.

In terms of total currents the above results, and summary statistics in Tables 24 & 25 and Figure 39 - 41, show that the port model significantly improves the representation of currents in the Kitimat fjord system from the parent model, CIOPS-W. Further, the 100m zoom on the port of

Kitimat improves representation of currents over the broader 500m configuration. In Kitimat Arm, near the docks, biases are on the order of mm/s, and surface current centered root-mean-square errors are ~10cm/s. Further down-fjord from the port at station FOC1, biases clearly indicate that the modelled estuarine circulation is biased weak with too slow outflow (southwestward) near the surface and too slow inflow (northeastward) at depth. Centered root-mean-square errors from the port model in or near the strong halocline are 17 – 22cm/s however these decrease with depth to <10cm/s below 50m. These centered root-mean-square errors are similar to those observed at the entrance to the fjord system and on the continental shelf, where they range from 12 cm/s at station CAM2 to 25 cm/s at station SRC1.

In summary, tidal currents are generally well represented along the shipping route into the port of Kitimat, and significant non-tidal current events (with magnitudes up to ~50cm/s) are captured skillfully. However, the kinetic energy in more general, smaller non-tidal currents is under-represented by as much as a factor of 2. This can most likely be improved in the future by further increasing the resolution of the port model in critical areas.

5.2.4. ADCP transects

No ADCP transects were completed in the port model domain during the hindcast period.

5.3. WATER PROPERTIES

5.3.1. Sea surface temperature

Comparison of modelled sea surface temperature against observations is limited by data availability in the fjords. The only station with available data near the port itself over the hindcast period is ECCC buoy 46181 (Nanakwa Shoal), located in Douglas Channel approximately 11nm down-fjord from Kitimat. On the continental shelf, ECCC buoy 46185 (South Hecate) is also available for comparison (Figure 42).

The port model provides a very good representation of sea surface temperature at Nanakwa Shoal. For the hindcast period, the 100m configuration is biased by only 0.22 degrees with a CRMSE of 1.10 degrees, while the 500m configuration is even slightly better with a bias of 0.06 degrees and CRMSE of 1.09 degrees. In comparison, CIOPS-W consistently underestimates summertime temperatures resulting in a bias of -1.36 degrees with CRMSE of 2.51 degrees (Table 26 and Figure 43).

At the South Hecate buoy on the continental shelf, modelled sea surface temperatures are very similar between the 500m port model configuration and CIOPS-W. Both indicate a slight low bias -0.77 degrees and -0.68 degrees for CIOPS-W and the port model, respectively. CRMSE is similar at 0.923 degrees (CIOPS-W) and 1.054 degrees (Kitimat 500m) (Table 26). Both models capture the seasonal cycle of sea surface temperature quite well (Figure 44).

5.3.2. Moored CTDs

The modelled temperature and salinity fields in the domain were evaluated against observations collected at many of the same mooring locations discussed in Section 5.2, as well as a couple of additional stations operated by Ocean Networks Canada at Kitamaat Village (KVIP.C2) and Hartley Bay (HBIP). Locations are shown in Figure 42, and the evaluation results are summarized in Tables 27 and 28. A representative set of results is also shown graphically in Figure 45 – 55.

In the vicinity of the port, the port model captures the evolution of the temperature and salinity fields with skill, down to a depth of at least 75m (Figure 45 – 48; Stations KIT1, KVIP.C2, and

FOC1). Temporal patterns are well captured here, and the port model configurations generally perform as well or better than the parent model, CIOPS-W. At depths below 100m however, a primarily salty bias becomes evident along with an underestimate of seasonal temperature fluctuations. Comparisons at station FOC1 from 2016 suggest that the model was initialized with a cool and salty bias. In the 2020 data from FOC1 a clear increase in cool, salty water is observed at depth (likely deep water renewal) however this is not clearly evident in the port model results, though it is captured in CIOPS-W. This suggests that the port model may suffer from sub-optimal initialization, which could also affect the weakened estuarine circulation noted earlier. However, given that CIOPS-W (the source of the initial conditions) accurately captures the renewal event in 2020 it is unlikely that this is the sole cause of the relatively poor representation of water properties at depth. This will be the subject of further investigation. From a statistical perspective, the differences between the port model configurations appears to be minor. Error metrics for CIOPS-W are generally slightly better than the port model, especially at depth as noted above, however this difference is not drastic (Tables 27 & 28). It should be noted that the comparison was made against daily averaged fields from CIOPS-W, while hourly averages were used for the port models. This may affect the CRMSE values given in the tables.

Away from the 100m domain, a similar picture presents itself with the 500m port model providing a suitable representation of the water masses in the upper 100m, but suffering from a persistent cold and salty bias at deeper depths in the fjords (Figure 49 – 52). An interesting scenario arises at the entrance to the fjords, where the bias mentioned above is present at the start of the comparison (which is also the start of the hindcast), but port model temperature and salinity converge with observations during an increase in cool, salty water seen at both 150m and 226m depth at station CAM2 (Figure 53). This suggests that in the port model the mechanism for deep water renewal functions adequately on the continental shelf, but not within the fjords which may be due to initialization with a cool, salty (i.e., high density) bias. On the continental shelf both the port model and CIOPS-W track the water masses well, and there are few notable differences, if any (Figure 54 & 55; Stations HEC1 & SRC1).

5.3.3. CTD profiles

To further the evaluation of modelled water properties, CTD casts (measured vertical profiles of temperature and salinity) were binned into sub-regions throughout the model domains for analysis. The locations of the casts are shown in Figure 56 for the 100m port model domain and Figure 62 for the Kitimat 500m domain.

The plots of mean and CRMSE deviation from this vertical profile in the corresponding model data for the Kitimat 100m domain present a consistent picture of relatively well captured water properties in the port region. For drift prediction and e-Navigation the element of primary importance is the representation of the surface fresh layer (upper 8-12m), which strongly affects surface currents. Here the results show that the port models have a salty bias of 4-5 PSU in Kitimat Arm, which reduces to 2-3 PSU in upper Douglas Channel and Devastation Channel. This represents a major improvement over CIOPS-W, which shows analogous biases of ~9 PSU in Kitimat Arm reducing to ~5 PSU in upper Douglas Channel. At depth the modelled salinities are fairly similar, all exhibiting a mild salty bias below 30m. Temperatures are well represented in the port region, with biases generally below 1 degree (Figure 57 – 61).

Outside of the 100m port model domain, a similar picture presents itself, starting from the head of the estuarine system in Gardner Canal, where a surface salinity bias of ~4 PSU in the port model again represents a significant improvement on the 12 PSU bias in CIOPS-W (Figure 63). This bias again reduces with distance from the head of Gardner Canal (Figure 63), first in Kitimat Arm as discussed above (Figure 64), into Douglas Channel (Figure 65 & 66), and finally into Wright Sound (Figure 68) where the bias is reduced to ~2 PSU. In the lower parts of the

fjord system, Squally and Whale Channel (Figure 69 & 70), the bias is reduced to below 1 PSU. The persistent salty bias of 0.2-0.5 PSU below ~30m remains noticeable throughout the system. This is consistent with the results from moorings discussed above.

Off the main shipping route, in Verney Passage and surrounding channels, the near-surface salty bias is more pronounced than in Douglas Channel. The port model's mean bias is ~10 PSU, improved from ~15 PSU in CIOPS-W. This is accompanied by a warm bias of ~2 degrees in the upper 20m, which decreases to ~0.2 degrees by 100m depth (Figure 67). This near-surface warm bias, which is also seen to a lesser extent in lower Douglas Channel, remains present throughout much of the lower fjord system towards Caamaño Sound and north towards Prince Rupert (Figure 70 – 74). The pattern of improved salinity in the port model continues here, and the near-surface salty bias is reduced to 0.25 PSU in Hecate Strait (Figure 75). These results suggest that the partitioning of water masses at the junction between Gardner Canal, Devastation Channel, and Verney Passage (discussed extensively in (Shan, Hannah, and Wu 2019)) requires further attention in the port model, as do the freshwater inputs into the lower portion of the fjord system.

Regardless, the comparison between CTD casts and model results suggests that the port model improves the representation of water masses from the parent model, especially near the ocean surface. This is consistent with the earlier finding that the port model skillfully represents water masses within the upper 100m of the water column, though accuracy at deeper depths can be further improved.

5.3.4. Ferries

In much of 2018 and 2019, regular measurements of near-surface temperature and salinity were made from the ferry transiting from Bellingham, WA to destinations in Alaska as part of the US Department of Transportation's Marine Highway System. The sensors used to make these measurements were installed and maintained by the Hakai Institute. The portion of the ferry route through the Kitimat 500m domain is shown in Figure 76, and Hovmöller diagrams of the observed temperature and salinity with comparison to results from the Kitimat 500m model and CIOPS-W are shown in Figure 77. Note that CIOPS-W does not include a portion of Grenville Channel, giving rise to the data gap between 130W and 129.5W in the bottom row of Figure 77.

The comparison indicates that summertime sea surface temperatures are biased warm by approximately 2 degrees in the Kitimat 500m model results, consistent with the comparison with CTD casts discussed above. Between October and April, this bias is reversed to a smaller cold bias. CIOPS-W results are generally slightly cooler than observations. Taking the difference between the absolute temperature deviations in results from Kitimat 500m and CIOPS-W reveals that in the wintertime the accuracy of modelled temperatures between the two systems is similar, while in the summertime CIOPS-W provides better estimates along the portions of the channel covered by the model grid (second panel, top row of Figure 77). Statistically, these results translate to a general 0.35 degree warn bias in the Kitimat 500m system with large fluctuations (CRMSE = 1.9 degree). CIOPS-W on the other hand is biased slightly cool overall at 0.1 degrees, with smaller fluctuations (CRMSE = 1.1 degree) (Table 29).

Modelled salinities in the western portion of the transect (Grenville Channel) are generally well represented by the Kitimat 500m, with the exception of large (> 3 PSU) salty biases in the spring of 2018 and 2019. These are likely a result of the Skeena River freshet and under-represented in the discharge climatology used in the model formulation. In Princess Royal Channel, east of Wright Sound, the modelled salinities are however consistently biased fresh. This suggests that freshwater input into this long and narrow channel may be overestimated in the climatology, while wind-driven mixing may be underestimated. Comparison with CIOPS-W

suggests that the port model provides better estimates of near-surface salinity in the portion of the transect west of Wright Sound, while neither model is clearly superior to the east of Wright Sound (fourth panel, top row of Figure 77). This is reflected in the summary statistics, which show a 0.7 PSU fresh bias in the port model with a CRMSE of 2.45 PSU whereas CIOPS-W shows a 0.75 PSU salty bias with CRMSE of 2 PSU (Table 29).

5.4. DRIFT

To further assess the quality of the surface currents provided by the port model, they were used in drift trajectory simulations aimed at replicating the tracks of drifter buoys deployed throughout the domain. Drifters in the 100m model domain were primarily deployed in upper Kitimat Arm, near the docks. In this domain, Surface Circulation Tracker (SCT) drifters were deployed exclusively, though some CODE-Davis drifters entered the domain through Douglas Channel. All drifter tracks in the 100m domain are shown in Figure 78. The various types of drifter buoys used in the analysis are described in (Hourston 2021).

On average, surface currents from the port model lead to improved drift predictions in the 100m domain for approximately 11 hours, as can be seen in the plots of mean instantaneous (Molcard) skill (Figure 79) and mean separation distance (Figure 80) for this set of drifters. Currents from the 100m configuration yield marginally better trajectory predictions than those from the 500m configuration, and both configurations improve on drift predictions made using surface currents from CIOPS-W by up to 50%. After 11 hours, surface currents from CIOPS-W yield better drift predictions. The 11 hour crossover time corresponds well with the average time taken for a drifter in this region to run aground (Blanken et al. 2020). This suggests that the port model gives better predictions of the surface currents encountered normally, while the more coarsely resolved surface currents from CIOPS-W lend themselves to better trajectory predictions during large-scale outflow events where drifters stay afloat for longer than average.

Outside of the 100m domain, OSKER drifters (with and without drogue) and CARTHE-style drifters were employed along with SCT and CODE-Davis buoys. Deployments of OSKER drifters are primarily limited to the continental shelf, as these drifters are more wind-influenced and tend to run aground more rapidly within the fjords (Figure 81). Examination of the skill scores and separation distances corresponding to the simulations of these drifters shows that surface currents from both the port model and CIOPS-W yield relatively low skill scores (Figure 82 & 83). Currents from CIOPS-W lend themselves to marginally better predictions. This is consistent with previous work on wind-influenced drifters which showed that, depending on the degree of susceptibility to wind forcing, more coarsely resolved surface current fields may yield as good, or better, trajectory predictions than surface currents from high-resolution prediction systems (Dagestad and Röhrs 2019). Visual examination of individual pairs of modelled and observed drifter tracks suggests that currents from the port model yield better trajectory predictions in the fjords than those from CIOPS-W, but this has not been confirmed quantitatively at the time of writing.

6. FORECAST EVALUATION RESULTS

6.1. NON-TIDAL WATER LEVEL

The evolution of bias and CRMSE of forecasts of non-tidal water level at Kitimat is shown in Figure 84. Bias in the forecast is steady at ~-4cm in the port models throughout a 48 hour forecast. The 500m configuration exhibits a slightly lesser bias than the 100m configuration. CIOPS-W also does not exhibit a trend in bias over the 48 hour forecast period, however the overall bias is slightly more severe than for the port model, at ~-5cm.

Fluctuating errors in the forecast, summarized by the CRMSE, grow at a rate of ~1cm per 24 hours in the port model, with very similar values for both configurations. Interestingly, CIOPS-W does not exhibit noticeable growth in CRMSE over 48 hours (Figure 84). This may be due to the higher frequency of runoff forcing at the nearby Kitimat River in the port model. Here the last measured value is persisted throughout the forecast, whereas CIOPS-W draws from a monthly climatology and thereby avoids the potential for rapid changes in freshwater input.

Analogous data from the tide gauge at Hartley Bay in the Kitimat 500m domain shows similar patterns. Here biases are higher, as discussed in Section 5.1, though the CRMSE curves exhibit very little change from those for the Kitimat tide gauge (Figure 85).

6.2. HORIZONTAL ADCP

No horizontal ADCP data is available in the port model domain, as there is no suitable location in or around the port to deploy such an instrument.

6.3. SEA SURFACE TEMPERATURE

Sea surface temperatures could not be evaluated as the temperature sensors on both ECCC buoys in the port model domain have been out of service since early 2020.

7. SUMMARY

We have shown that the port model for Kitimat produces skillful simulations of water levels, currents, and water properties in the port of Kitimat and approaches to the port. Results are improved over the parent model of these high-resolution zooms, CIOPS-W. As part of this report, several areas where the next version of the port model can be improved are identified, namely:

1. Re-initialization from optimal interpolation of observations;
2. A detailed study of the effects of spinup time on estuarine circulation;
3. Evaluation, verification, and tuning of the atmospheric forcing against observed weather data in the fjord system;
4. Further investigation of the relationship between the resolution of Minette Bay and the surrounding intertidal areas and high-frequency water level changes in the port of Kitimat.

While further improvements to a modelling system are always possible, the results shown here indicate that the POPS model for the port of Kitimat improves ability to accurately predict water levels and currents for electronic navigation and trajectory prediction.

8. KEY FINDINGS

- Currents and water levels are skillfully modelled, and results improve upon the existing CIOPS-W model.
- Representation of tidal currents and water levels is improved more significantly than non-tidal processes.
- The modelled estuarine circulation is too weak in both the port model and the parent system; further study on initialization of deep-water masses, partitioning of water masses among the channels, and freshwater inputs is needed.

- As a result of the above, deep water renewal processes are not captured accurately which has significant implications for potential application to biophysical studies.
- Results from poorly resolved channels should be interpreted with extreme caution, as the outsized effects of the friction parameterization in the model will lead to poor performance here.
- The increase in accuracy of modelled surface currents in the vicinity of the port leads to improved predictions of object drift trajectories under average circumstances.

9. ACKNOWLEDGEMENTS

The work presented in this report would not have been possible without the support of the OPP Port Leads Team, with particular thanks to Michael Dunphy, Stephanne Taylor, and Maxim Krassovski for their work on developing the Maestro suite used to run the simulations, including the required pre- and post-processing, as well as the software suite used to perform the verification and analysis presented here.

Many thanks to Charles Hannah, David Spear, and Stephen Page for coordinating and conducting observation campaigns to collect the data used in the creation of this report, as well as all the scientists who participated in these campaigns along with the captain and crew of the CCGS *John P. Tully*, CCGS *Vector*, and CCGS *Sir John Franklin*.

The observational data would have been much more difficult to access without the work of Roy Hourston, Di Wan, Lu Guan, and the IOS data team on creating and maintaining waterproperties.ca, and thanks goes to them.

Thanks to Ocean Networks Canada and the Hakai Institute (especially Wiley Evans) for maintaining data collection infrastructure in the Kitimat fjord system and publishing the collected data.

Thanks to Tom Juhasz for his continued work on creating and improving the SCT drifter, which enabled the large-scale drifter data collection presented here.

On the topic of drifters, a special thanks to Bridgeman's Marine Transport of Kitamaat, BC who volunteered their time and resources to deploy drifters in Kitimat Arm in the early months of the COVID-19 pandemic. These drifters were essential to validating the model performance in the port region.

The drift evaluation was done using software developed by Nancy Soontiens and Jennifer Holden of OPP FA3, and they deserve thanks for their thorough work in developing this tool.

A big thanks also to Glenn Cooper, for his tireless guidance and support in developing, deploying, and maintaining a system of weather stations throughout the Kitimat fjord system. Due to time constraints this data was not used in the creation of this report, but it will be invaluable to future efforts to further improve the system presented here.

Finally, many thanks to Jon Chamberlain, Kim Houston, and all managers involved in creating, guiding, and funding the OPP port modelling initiative.

10. REFERENCES CITED

Backhaus, Jan O. 1983. "A Semi-Implicit Scheme for the Shallow Water Equations for Application to Shelf Sea Modelling." *Continental Shelf Research* 2 (4): 243–54. https://doi.org/10.1016/0278-4343(82)90020-6.

———. 1985. “A Three-Dimensional Model for the Simulation of Shelf Sea Dynamics.” *Deutsche Hydrographische Zeitschrift* 38 (4): 165–87. https://doi.org/10.1007/BF02328975.

Blanken, Hauke, Charles Hannah, Jody Klymak M., and Tamás Juhász. 2020. “Surface Drift and Dispersion in a Multiply Connected Fjord System.” *Journal of Geophysical Research: Oceans* 125 (2). https://doi.org/10.1029/2019JC015425.

Blanken, Hauke, Caterina Valeo, Charles Hannah, Usman T. Khan, and Tamás Juhász. 2021. “A Fuzzy-Based Framework for Assessing Uncertainty in Drift Prediction Using Observed Currents and Winds.” *Frontiers in Marine Science* 8 (November):618094. https://doi.org/10.3389/fmars.2021.618094.

Chen, Changsheng, Hedong Liu, and Robert C. Beardsley. 2003. “An Unstructured Grid, Finite-Volume, Three-Dimensional, Primitive Equations Ocean Model: Application to Coastal Ocean and Estuaries.” *Journal of Atmospheric and Oceanic Technology* 20 (1): 159–86. https://doi.org/10.1175/1520-0426(2003)020<0159:AUGFVT>2.0.CO;2.

Cummins, Patrick F., and Lie-Yauw Oey. 1997. “Simulation of Barotropic and Baroclinic Tides off Northern British Columbia.” *Journal of Physical Oceanography* 27 (5): 762–81. https://doi.org/10.1175/1520-0485(1997)027<0762:SOBABT>2.0.CO;2.

Cummins, Patrick F., and Pramod Thupaki. 2018. “A Note on Evaluating Model Tidal Currents against Observations.” *Continental Shelf Research* 152 (January):35–37. https://doi.org/10.1016/j.csr.2017.10.007.

Dagestad, Knut-Frode, and Johannes Röhrs. 2019. “Prediction of Ocean Surface Trajectories Using Satellite Derived vs. Modeled Ocean Currents.” *Remote Sensing of Environment* 223 (March):130–42. https://doi.org/10.1016/j.rse.2019.01.001.

Daniel, Pierre, Gwénaële Jan, Fanch Cabioc’h, Yves Landau, and Erwann Loiseau. 2002. “Drift Modeling of Cargo Containers.” *Spill Science & Technology Bulletin* 7 (5–6): 279–88. https://doi.org/10.1016/S1353-2561(02)00075-0.

Dupont, F., S. Higginson, R. Bourdallé-Badie, Y. Lu, F. Roy, G. C. Smith, J.-F. Lemieux, G. Garric, and F. Davidson. 2015. “A High-Resolution Ocean and Sea-Ice Modelling System for the Arctic and North Atlantic Oceans.” *Geoscientific Model Development* 8 (5): 1577–94. https://doi.org/10.5194/gmd-8-1577-2015.

Foreman, M. G. G., W. R. Crawford, J. Y. Cherniawsky, R. F. Henry, and M. R. Tarbotton. 2000. “A High-Resolution Assimilating Tidal Model for the Northeast Pacific Ocean.” *Journal of Geophysical Research: Oceans* 105 (C12): 28629–51. https://doi.org/10.1029/1999JC000122.

Hourston, Roy A.S. 2021. *Surface Ocean Circulation Tracking Drifter Data from the Northeastern Pacific and Western Arctic Oceans, 2014-2020*. Sidney, B.C.: Fisheries and Oceans Canada = Pêches et Océans Canada.

Kundu, Pijush K. 1976. “Ekman Veering Observed near the Ocean Bottom.” *Journal of Physical Oceanography* 6 (2): 238–42. https://doi.org/10.1175/1520-0485(1976)006<0238:EVONTO>2.0.CO;2.

Large, WIlliam George, and Stephen G. Yeager. 2004. “Diurnal to Decadal Global Forcing for Ocean and Sea-Ice Models: The Data Sets and Flux Climatologies.” NCAR Technical Note NCAR/TN-460+STR. Boulder, CO: Climate and Global Dynamics Division: National Center for Atmospheric Research.

MacDonald, R. W. 1983. “Proceedings of a Workshop on the Kitimat Marine Environment.” Technical Report FS 97-18/18. Canadian Technical Report of Hydrography and Ocean Sciences. Sidney, BC: Institute of Ocean Sciences. https://science-catalogue.canada.ca/record=4086822~S6.

Madec, Gurvan. 2016. *NEMO Ocean Engine*. Note Du Pole de Modelisation de l’Institut Pierre-Simon Laplace 27. NEMO European Consortium.

Milbrandt, Jason A., Stéphane Bélair, Manon Faucher, Marcel Vallée, Marco L. Carrera, and Anna Glazer. 2016. “The Pan-Canadian High Resolution (2.5 Km) Deterministic Prediction System.” *Weather and Forecasting* 31 (6): 1791–1816. https://doi.org/10.1175/WAF-D-16-0035.1.

Molcard, A., P.M. Poulain, P. Forget, A. Griffa, Y. Barbin, J. Gaggelli, J.C. De Maistre, and M. Rixen. 2009. “Comparison between VHF Radar Observations and Data from Drifter Clusters in the Gulf of La Spezia (Mediterranean Sea).” *Journal of Marine Systems* 78 (November):S79–89. https://doi.org/10.1016/j.jmarsys.2009.01.012.

Morrison, J., M. G. G. Foreman, and D. Masson. 2012. “A Method for Estimating Monthly Freshwater Discharge Affecting British Columbia Coastal Waters.” *Atmosphere-Ocean* 50 (1): 1–8. https://doi.org/10.1080/07055900.2011.637667.

Niiler, Pearn P., Andrew S. Sybrandy, Kenong Bi, Pierre M. Poulain, and David Bitterman. 1995. “Measurements of the Water-Following Capability of Holey-Sock and TRISTAR Drifters.” *Deep Sea Research Part I: Oceanographic Research Papers* 42 (11–12): 1951–64. https://doi.org/10.1016/0967-0637(95)00076-3.

Nudds, Shannon, Youyu Lu, Simon Higginson, Susan P. Haigh, Jean-Philippe Paquin, Mitchell O’Flaherty-Sproul, Stephanne Taylor, et al. 2020. “Evaluation of Structured and Unstructured Models for Application in Operational Ocean Forecasting in Nearshore Waters.” *Journal of Marine Science and Engineering* 8 (7): 484. https://doi.org/10.3390/jmse8070484.

Paquin, Jean-Philippe, Youyu Lu, Stephanne Taylor, Hauke Blanken, Guillaume Marcotte, Xianmin Hu, Li Zhai, et al. 2020. “High-Resolution Modelling of a Coastal Harbour in the Presence of Strong Tides and Significant River Runoff.” *Ocean Dynamics* 70 (3): 365–85. https://doi.org/10.1007/s10236-019-01334-7.

Paquin, Jean-Phillipe, François Roy, Gregory C. Smith, Frédéric Dupont, Sarah MacDermid, Yukie Hata, Oleksandr Huizy, et al. 2021a. “Coastal Ice Ocean Prediction System for the East Coast of Canada (CIOPS-E): Update from Version 1.5.0 to 2.0.0.” Canadian Centre for Meteorological and Environmental Prediction Tech. Note. https://collaboration.cmc.ec.gc.ca/cmc/cmoi/product_guide/docs/tech_notes/technote_ciops-east-200_e.pdf.

Paquin, Jean-Phillipe, Gregory C. Smith, Frédéric Dupont, Sarah MacDermid, Yukie Hata, Oleksandr Huizy, Ji Lei, et al. 2021b. “Coastal Ice Ocean Prediction System for the West Coast of Canada (CIOPS-W): Update from Version 1.5.0 to 2.0.0.” Canadian Centre for Meteorological and Environmental Prediction Tech. Note. https://collaboration.cmc.ec.gc.ca/cmc/cmoi/product_guide/docs/tech_notes/technote_ciops-west-200_e.pdf.

Paquin, Jean-Phillipe, Gregory C. Smith, Francois Roy, Frederic Dupont, Sarah MacDermid, Ji Lei, Youyu Lu, Stephanne Taylor, Hauke Blanken, and Li Zhai. 2022. “Coastal Ice Ocean Prediction System for the West Coast of Canada (CIOPS-W): System Description for Versions 1.0.0 and 1.5.0.” Canadian Centre for Meteorological and Environmental Prediction Tech. Note. https://collaboration.cmc.ec.gc.ca/cmc/cmoi/product_guide/docs/tech_notes/technote_ciops-west-100_e.pdf.

Röhrs, Johannes, and Kai H. Christensen. 2015. “Drift in the Uppermost Part of the Ocean.” *Geophysical Research Letters* 42 (23). https://doi.org/10.1002/2015GL066733.

Röhrs, Johannes, Kai Håkon Christensen, Lars Robert Hole, Göran Broström, Magnus Drivdal, and Svein Sundby. 2012. “Observation-Based Evaluation of Surface Wave Effects on Currents and Trajectory Forecasts.” *Ocean Dynamics* 62 (10–12): 1519–33. https://doi.org/10.1007/s10236-012-0576-y.

Saucier, François J. 2003. “Modeling the Formation and Circulation Processes of Water Masses and Sea Ice in the Gulf of St. Lawrence, Canada.” *Journal of Geophysical Research* 108 (C8): 3269. https://doi.org/10.1029/2000JC000686.

Saucier, François J., and Joël Chassé. 2000. “Tidal Circulation and Buoyancy Effects in the St. Lawrence Estuary.” *Atmosphere-Ocean* 38 (4): 505–56. https://doi.org/10.1080/07055900.2000.9649658.

Shan, Shiliang, Charles G. Hannah, and Yongsheng Wu. 2019. “Coupling of Estuarine Circulations in a Network of Fjords.” *Journal of Geophysical Research: Oceans* 124 (10): 6809–30. https://doi.org/10.1029/2018JC014924.

———. 2020. “Response of Sea Level to Tide, Atmospheric Pressure, Wind Forcing and River Discharge in the Kitimat Fjord System.” *Estuarine, Coastal and Shelf Science* 246 (November):107025. https://doi.org/10.1016/j.ecss.2020.107025.

Smagorinsky, J. 1993. “Some Historical Remarks on the Use of Non-Linear Viscosities.” In *Large Eddy Simulation of Complex Engineering and Geophysical Flows*, edited by Boris Galperin and Steven A. Orszag. Cambridge: Cambridge University Press.

Smith, Stuart D. 1988. “Coefficients for Sea Surface Wind Stress, Heat Flux, and Wind Profiles as a Function of Wind Speed and Temperature.” *Journal of Geophysical Research* 93 (C12): 15467. https://doi.org/10.1029/JC093iC12p15467.

Soontiens, Nancy, and Jennifer Holden J. 2024. “A framework for evaluation and characterization of drift prediction in the marine environment.” Can. Tech. Rep. Hydrogr. Ocean Sci. 383: ix + 45 p. https://waves-vagues.dfo-mpo.gc.ca/library-bibliotheque/41252287.pdf.

Sutherland, Graig, Nancy Soontiens, Fraser Davidson, Gregory C. Smith, Natacha Bernier, Hauke Blanken, Douglas Schillinger, et al. 2020. “Evaluating the Leeway Coefficient of Ocean Drifters Using Operational Marine Environmental Prediction Systems.” *Journal of Atmospheric and Oceanic Technology* 37 (11): 1943–54. https://doi.org/10.1175/JTECH-D-20-0013.1.

Wan, Di, Charles G. Hannah, Michael G. G. Foreman, and Stan Dosso. 2017. “Subtidal Circulation in a Deep-silled Fjord: Douglas Channel, British Columbia.” *Journal of Geophysical Research: Oceans* 122 (5): 4163–82. https://doi.org/10.1002/2016JC012022.

Webster, Ian. 1980. “Kitimat Physical Oceanographic Study 1977-1978.” Technical Report 80–3. Contractor Report Series. Sidney, BC: Institute of Ocean Sciences. https://science-catalogue.canada.ca/record=1092851~S6.

Zalesak, Steven T. 1979. “Fully Multidimensional Flux-Corrected Transport Algorithms for Fluids.” *Journal of Computational Physics* 31 (3): 335–62. https://doi.org/10.1016/0021-9991(79)90051-2.

Zhang, Minghong, William Perrie, and Zhenxia Long. 2019. “Springtime North Pacific Oscillation and Summer Sea Ice in the Beaufort Sea.” *Climate Dynamics* 53 (1–2): 671–86. https://doi.org/10.1007/s00382-019-04627-1.

11. TABLES

Table 1. Model parameters for Kitimat 100/500 m NEMO configurations.

Parameter	Outer grid (KIT500)	Inner grid (KIT100)
Grid dimensions, NX × NY × NZ	519 × 869 × 50	899 × 639 × 33
Horizontal resolution, ΔX × ΔY	Approx. 354 × 278 m	Approx. 70 × 54 m
Vertical resolution	1 m surface, 28 m bottom	1 m surface, 24 m bottom
Baroclinic / barotropic time step	30 s / auto w/ Courant=0.75	10 s / auto w/ Courant=0.75
Open boundary update frequency	1 h (W, S, E surface), 24 h (E 3d currents)	1 h
Open Boundary SSH offset	-20 cm (W, S, E)	0 cm
Tidal constituents source	WebTide	Directly from KIT500
Tidal constituents forced	M2, S2, N2, K1, O1, Q1, K2, P1	N/A
Equation of state	EOS-80	EOS-80
Free surface	Variable volume	Variable volume
Light penetration	Two band	Two band
Lateral boundary condition	Partial slip (shlat=0.2)	Partial slip (shlat=0.35)
Momentum advection	Vector form, 5 sub-steps for vertical advection	Vector form, 5 sub-steps for vertical advection
Momentum lateral diffusion	Horizontal Laplacian and Smagorinsky	Horizontal Laplacian and Smagorinsky
Tracer advection	Total Variance Dissipation, 5 vertical advection sub-steps	Total Variance Dissipation, 5 vertical advection sub-steps
Tracer lateral diffusion	Iso-neutral Laplacian and Smagorinsky	Iso-neutral Laplacian and Smagorinsky
Vertical diffusion	k-ε	k-ε
Bottom friction	Log-layer	Log-layer

Table 2. Adjustment of tidal phase from WebTide at 500 m grid open boundary.

Tidal Constituent	Phase Adjustment from WebTide (degrees)
M2	-8
S2	-8
N2	-7
O1	-0.6
Q1	+1

Table 3. Offsets to shift water levels at continuous tide gauges from chart datum to CGVD28.

Station	Offset, Chart Datum to CGVD28 (m)
Kitimat	3.209
Hartley Bay	2.922
Bonilla Island	3.531
Prince Rupert	3.854

Table 4. Tidal water level statistics at continuous tide gauges in 2021.

Model			Amplitude Error (m)			Phase Error (º)			Tidal Error (m)		
Station	Amp	Phase	CIOPS-W	KIT 500	KIT 100	CIOPS-W	KIT 500	KIT 100	CIOPS-W	KIT 500	KIT 100
M2 Constituent											
Kitimat	1.659	258.11	0.120	-0.002	-0.053	3.370	-0.270	-1.140	0.111	0.006	0.044
Hartley Bay	1.592	256.57	0.079	-0.025	n/a	3.970	-0.130	n/a	0.097	0.018	n/a
S2 Constituent											
Kitimat	0.535	289.10	0.040	0.004	-0.013	4.650	-0.010	-0.900	0.043	0.003	0.011
Hartley Bay	0.512	287.55	0.025	-0.005	n/a	5.060	-0.040	n/a	0.037	0.003	n/a
K1 Constituent											
Kitimat	0.484	255.22	0.009	0.012	0.006	0.600	0.670	0.410	0.008	0.009	0.005
Hartley Bay	0.476	254.92	0.007	0.009	n/a	0.410	0.550	n/a	0.006	0.007	n/a
N2 Constituent											
Kitimat	0.341	234.36	0.021	0.002	-0.008	3.230	0.850	0.010	0.020	0.004	0.006
Hartley Bay	0.327	232.56	0.015	-0.001	n/a	3.980	0.940	n/a	0.020	0.004	n/a
O1 Constituent											
Kitimat	0.292	239.16	0.003	0.002	-0.001	0.030	-0.450	-0.670	0.002	0.002	0.002
Hartley Bay	0.290	239.04	-0.001	-0.002	n/a	-0.340	-0.670	n/a	0.001	0.003	n/a
P1 Constituent											
Kitimat	0.158	251.86	0.005	0.001	-0.001	-0.700	0.250	-0.050	0.004	0.001	0.001
Hartley Bay	0.153	251.030	0.006	0.002	n/a	-0.440	0.570	n/a	0.004	0.002	n/a
K2 Constituent											
Kitimat	0.147	281.93	0.005	-0.002	-0.007	2.160	7.420	6.600	0.005	0.013	0.013
Hartley Bay	0.141	280.30	0.001	-0.005	n/a	2.730	7.650	n/a	0.005	0.014	n/a

Table 5. Comparison of M2 tidal statistics at historical (constituent-only) tide gauge locations.

			Ampl Error (m)		Phase Error (º)		Tidal Error (m)	
Station	Ampl	Phase	CIOPS-W	KIT 500	CIOPS-W	KIT 500	CIOPS-W	KIT 500
Aero Trading	1.898	267.96	+0.098	-0.212	+1.70	+8.75	0.081	0.244
Barnard Harbour	1.574	255.37	+0.079	-0.029	+3.21	-0.18	0.085	0.021
Beauchemin Channel	1.453	253.91	+0.043	-0.048	+2.55	-1.89	0.055	0.047
Block Islands	1.573	257.92	+0.032	-0.047	+2.91	-0.33	0.061	0.034
Bonilla Island	1.738	259.81	+0.070	+0.003	+3.85	-0.68	0.098	0.015
Butedale	1.558	256.44	+0.067	+0.017	+3.10	+0.40	0.077	0.015
Claxton	1.930	269.76	+0.151	-0.273	+5.59	+15.13	0.175	0.385
Clear Passage	1.733	259.12	+0.109	-0.040	+4.98	+0.76	0.134	0.032
Griffin Passage	1.333	251.52	+0.123	-0.121	+2.82	-0.66	0.100	0.086
Griffith Harbour	1.816	261.87	+0.074	-0.050	+1.98	+0.93	0.069	0.041
Haysport	1.960	282.57	+0.073	-0.434	+3.49	+17.33	0.101	0.480
Higgins Passage West	1.316	250.11	+0.029	-0.086	+3.06	-2.83	0.054	0.075
Inverness Passage	1.933	270.32	+0.072	-0.234	-0.75	+8.52	0.054	0.252
Kemano Bay	1.726	258.47	+0.145	+0.009	+3.90	-0.05	0.134	0.007
Khyex Point	1.810	302.87	+0.359	-0.770	-19.36	+26.94	0.535	0.708
Kitkatla	1.886	264.35	+0.094	-0.037	+2.48	+5.04	0.089	0.119
Klemtu	1.338	250.94	+0.069	-0.135	+4.02	-4.14	0.084	0.115
Larsen Island	1.764	260.87	+0.134	+0.006	+3.75	+3.52	0.127	0.077
Lawyer Islands	1.901	266.01	+0.098	-0.089	+3.43	+2.15	0.107	0.080
Lowe Inlet	1.669	258.77	-0.009	+0.101	+1.50	+10.68	0.031	0.237
McKenney Islands	1.378	255.07	+0.052	-0.019	+1.63	-2.73	0.047	0.048
Meyers Narrows	1.377	252.87	-0.007	-0.030	+1.04	+3.55	0.018	0.063
Milne Island	1.339	250.76	+0.021	-0.115	+3.43	-2.77	0.059	0.092
Northland Terminal	1.948	267.86	+0.069	-0.416	+2.50	+21.66	0.078	0.545
Oswald Bay	1.489	255.49	+0.035	-0.029	+3.19	-1.00	0.064	0.027
Patterson Inlet	1.673	257.94	+0.074	-0.034	+3.68	+0.43	0.094	0.025
Port Blackney	1.298	249.41	+0.045	-0.120	+3.20	-3.37	0.061	0.099
Price Island	1.300	249.96	+0.015	-0.144	+3.25	-3.11	0.053	0.112
Prince Rupert Roro	1.920	267.05	+0.081	-0.115	+2.76	+1.53	0.088	0.089
Seabreeze Point	1.886	265.76	+0.143	-0.023	+2.07	+3.72	0.113	0.088
Smithers Island	1.439	253.66	+0.049	-0.058	+3.56	-0.85	0.073	0.044
Stryker Island	1.266	248.38	+0.032	-0.118	+3.39	-14.50	0.058	0.231
Surf Inlet	1.414	255.87	+0.137	+0.034	+1.38	-1.63	0.100	0.037
Tom Bay	1.325	253.87	+0.086	-0.101	-5.55	-10.87	0.112	0.185
Wainwright Basin	1.560	292.86	+0.448	-0.217	-23.14	+21.68	0.594	0.414

Table 6. Comparison of S2 tidal statistics at historical (constituent-only) tide gauge locations.

			Ampl Error (m)		Phase Error (°)		Tidal Error (m)	
Station	Ampl	Phase	CIOPS-W	KIT 500	CIOPS-W	KIT 500	CIOPS-W	KIT 500
Aero Trading	0.625	299.96	+0.042	-0.102	+2.93	+11.11	0.038	0.106
Barnard Harbour	0.482	286.87	+0.036	-0.008	+14.03	+9.44	0.090	0.056
Beauchemin Channel	0.458	284.48	+0.021	-0.006	+3.90	-1.40	0.027	0.009
Block Islands	0.477	288.20	+0.032	-0.002	+13.89	+9.33	0.087	0.055
Bonilla Island	0.567	291.04	+0.026	+0.005	+5.64	-0.23	0.044	0.004
Butedale	0.478	285.65	+0.086	+0.062	+14.55	+11.57	0.111	0.085
Claxton	0.641	303.77	+0.170	-0.032	+10.11	+23.00	0.150	0.178
Clear Passage	0.538	289.74	+0.044	-0.013	+12.31	+6.35	0.091	0.043
Griffin Passage	0.452	285.18	-0.082	-0.147	-7.67	-10.48	0.070	0.114
Griffith Harbour	0.585	292.00	+0.091	+0.018	+14.99	+13.82	0.133	0.102
Haysport	0.575	324.70	-0.092	-0.312	+5.30	+20.27	0.074	0.241
Higgins Passage West	0.399	279.82	+0.011	-0.026	+7.42	-0.26	0.038	0.018
Inverness Passage	0.610	299.91	+0.074	-0.087	+9.02	+23.49	0.089	0.174
Kemano Bay	0.554	289.00	+0.057	+0.016	+6.18	+1.52	0.060	0.015
Khyex Point	0.566	347.00	+0.217	-0.311	-11.37	-300.96	0.179	0.344
Kitkatla	0.619	295.67	+0.037	-0.004	+4.48	+6.82	0.044	0.052
Klemtu	0.422	281.00	+0.023	-0.042	+5.42	-4.50	0.033	0.037
Larsen Island	0.576	293.00	+0.019	-0.003	-6.26	-8.31	0.047	0.059
Lawyer Islands	0.608	297.24	+0.044	-0.027	+7.39	+5.05	0.065	0.042
Lowe Inlet	0.521	289.72	-0.007	+0.035	+6.65	+16.74	0.043	0.114
McKenney Islands	0.412	285.80	-0.002	-0.019	+2.28	-4.33	0.012	0.025
Meyers Narrows	0.432	285.00	-0.046	-0.057	+10.64	+12.96	0.063	0.076
Milne Island	0.395	282.55	+0.002	-0.045	+12.87	+4.11	0.063	0.037
Northland Terminal	0.644	299.81	+0.031	-0.183	+3.95	+28.27	0.039	0.229
Oswald Bay	0.452	286.31	+0.001	-0.021	+7.60	+1.59	0.042	0.017
Patterson Inlet	0.507	288.55	+0.025	-0.015	+9.72	+4.42	0.065	0.029
Port Blackney	0.387	279.09	+0.019	-0.033	+7.01	-1.72	0.037	0.024
Price Island	0.382	279.26	+0.033	-0.024	+13.72	+5.48	0.071	0.030
Prince Rupert Roro	0.644	295.13	+0.043	-0.022	+2.85	+0.84	0.038	0.017
Seabreeze Point	0.595	296.22	+0.195	+0.121	+9.90	+13.05	0.161	0.136
Smithers Island	0.435	283.93	+0.007	-0.032	+13.09	+7.24	0.071	0.044
Stryker Island	0.370	277.03	+0.037	-0.004	+13.36	-7.78	0.069	0.035
Surf Inlet	0.475	285.00	-0.035	-0.073	+14.24	+9.32	0.084	0.072
Tom Bay	0.426	285.00	+0.149	+0.070	+3.26	-1.85	0.107	0.050
Wainwright Basin	0.418	333.70	+0.166	-0.088	-35.52	+20.92	0.244	0.114

Table 7. Comparison of K1 tidal statistics at historical (constituent-only) tide gauge locations.

			Ampl Error (m)		Phase Error (º)		Tidal Error (m)	
			CIOPS-W	KIT 500	CIOPS-W	KIT 500	CIOPS-W	KIT 500
Station	**Ampl**	**Phase**						
Aero Trading	0.509	260.27	+0.010	-0.010	-0.97	+9.70	0.009	0.061
Barnard Harbour	0.473	254.59	+0.098	+0.093	+13.86	+12.86	0.112	0.105
Beauchemin Channel	0.471	253.25	+0.003	+0.005	+0.30	+0.59	0.003	0.005
Block Islands	0.470	255.97	+0.085	+0.082	+12.08	+12.14	0.097	0.096
Bonilla Island	0.500	255.78	+0.005	+0.013	-0.08	-0.21	0.003	0.009
Butedale	0.474	254.53	+0.012	+0.011	+17.49	+16.95	0.104	0.100
Claxton	0.484	262.28	-0.098	-0.124	+11.58	+21.44	0.093	0.140
Clear Passage	0.479	256.62	+0.080	+0.078	+6.54	+6.03	0.070	0.067
Griffin Passage	0.440	253.68	+0.151	+0.125	-11.55	-4.40	0.129	0.093
Griffith Harbour	0.521	259.33	-0.006	-0.006	+17.11	+17.52	0.109	0.112
Haysport	0.458	269.53	+0.285	+0.156	-5.84	+10.72	0.206	0.131
Higgins Passage West	0.455	253.09	+0.047	+0.039	+3.42	+3.64	0.039	0.035
Inverness Passage	0.492	261.98	+0.045	+0.013	+7.94	+19.84	0.059	0.122
Kemano Bay	0.489	255.43	+0.013	+0.017	+1.39	+0.83	0.013	0.013
Khyex Point	0.448	281.33	+0.110	-0.119	+8.31	+47.99	0.093	0.236
Kitkatla	0.498	258.45	+0.018	+0.032	-0.30	+4.61	0.013	0.037
Klemtu	0.460	252.86	+0.008	-0.003	+1.01	+1.59	0.008	0.009
Larsen Island	0.484	258.33	+0.082	+0.099	-19.62	-17.78	0.139	0.136
Lawyer Islands	0.499	259.95	+0.049	+0.056	+1.71	+4.57	0.036	0.050
Lowe Inlet	0.473	255.40	+0.068	+0.097	+4.82	+11.76	0.057	0.102
McKenney Islands	0.446	253.93	+0.101	+0.101	-2.51	-2.49	0.073	0.073
Meyers Narrows	0.475	253.33	+0.128	+0.123	+10.77	+13.57	0.115	0.125
Milne Island	0.444	253.81	+0.134	+0.115	+10.80	+10.46	0.116	0.104
Northland Terminal	0.513	260.10	+0.009	-0.036	-0.47	+19.82	0.007	0.123
Oswald Bay	0.456	254.89	+0.086	+0.084	+2.64	+2.14	0.063	0.061
Patterson Inlet	0.476	255.63	+0.089	+0.089	+4.61	+4.51	0.069	0.069
Port Blackney	0.449	252.67	+0.059	+0.051	+2.82	+3.53	0.045	0.042
Price Island	0.450	253.72	+0.060	+0.045	+12.62	+12.37	0.086	0.079
Prince Rupert Roro	0.510	259.11	-0.013	-0.009	-7.55	-3.84	0.048	0.025
Seabreeze Point	0.502	258.72	-0.095	-0.091	+15.94	+19.46	0.111	0.126
Smithers Island	0.454	254.19	+0.109	+0.100	+9.79	+9.77	0.098	0.093
Stryker Island	0.444	252.62	+0.059	+0.009	+12.44	+11.79	0.084	0.065
Surf Inlet	0.454	253.33	+0.164	+0.154	+10.78	+10.61	0.135	0.129
Tom Bay	0.481	251.33	-0.165	-0.161	+10.73	+10.56	0.127	0.125
Wainwright Basin	0.413	286.07	+0.211	+0.138	-34.25	+5.33	0.259	0.102

Table 8. Comparison of N2 tidal statistics at historical (constituent-only) tide gauge locations.

			Ampl Error (m)		Phase Error (°)		Tidal Error (m)	
			CIOPS-W	KIT 500	CIOPS-W	KIT 500	CIOPS-W	KIT 500
Station	**Ampl**	**Phase**						
Aero Trading	0.378	244.21	+0.028	-0.052	+1.97	+12.24	0.022	0.064
Barnard Harbour	0.316	230.92	+0.015	-0.005	+4.87	+3.74	0.022	0.015
Beauchemin Channel	0.295	228.41	+0.011	-0.007	+4.06	+0.88	0.017	0.006
Block Islands	0.326	232.61	+0.007	-0.006	+4.26	+3.23	0.018	0.014
Bonilla Island	0.349	235.14	+0.019	+0.006	+4.73	+1.65	0.025	0.008
Butedale	0.321	231.46	+0.009	+0.005	+5.06	+4.21	0.021	0.017
Claxton	0.327	236.66	+0.087	-0.007	+18.94	+35.72	0.106	0.140
Clear Passage	0.349	235.12	+0.027	-0.001	+5.66	+3.97	0.032	0.017
Griffin Passage	0.377	242.52	+0.006	-0.013	-1.04	+1.84	0.006	0.012
Griffith Harbour	0.246	232.63	+0.032	+0.009	-3.10	-7.32	0.025	0.024
Haysport	0.386	246.73	+0.021	-0.065	+0.41	+17.46	0.015	0.088
Higgins Passage West	0.357	236.42	+0.024	-0.002	+2.27	+0.08	0.020	0.001
Inverness Passage	0.371	286.52	+0.068	-0.169	-16.24	+66.67	0.094	0.244
Kemano Bay	0.382	240.02	+0.018	-0.010	+3.72	+7.21	0.022	0.034
Khyex Point	0.277	225.64	+0.013	-0.028	+5.72	-1.00	0.022	0.020
Kitkatla	0.353	235.52	+0.025	+0.003	+5.42	+6.72	0.030	0.029
Klemtu	0.378	242.23	+0.026	-0.018	+4.53	+5.19	0.029	0.027
Larsen Island	0.340	235.37	-0.002	+0.021	+1.22	+14.07	0.005	0.062
Lawyer Islands	0.281	229.12	+0.009	-0.004	+4.09	+1.61	0.016	0.006
Lowe Inlet	0.310	227.52	-0.029	-0.033	+2.02	+7.24	0.022	0.035
McKenney Islands	0.277	226.27	+0.006	-0.021	+3.92	-0.54	0.014	0.015
Meyers Narrows	0.386	244.21	+0.023	-0.095	+2.80	+28.24	0.021	0.134
Milne Island	0.297	231.77	+0.015	+0.005	+3.13	+0.43	0.016	0.004
Northland Terminal	0.333	234.58	+0.024	+0.003	+3.67	+2.60	0.023	0.011
Oswald Bay	0.260	225.22	+0.015	-0.017	+3.54	-1.29	0.016	0.013
Patterson Inlet	0.261	226.17	+0.012	-0.019	+3.33	-1.16	0.014	0.014
Port Blackney	0.349	242.07	+0.064	+0.010	+3.96	+3.50	0.049	0.017
Price Island	0.389	237.11	+0.024	-0.018	+7.31	+14.21	0.040	0.068
Prince Rupert Roro	0.294	228.94	+0.009	-0.011	+4.38	+2.28	0.017	0.011
Seabreeze Point	0.269	224.06	-0.004	-0.032	+4.78	-12.35	0.016	0.045
Smithers Island	0.323	231.52	-0.003	-0.025	+1.81	+0.28	0.008	0.018
Stryker Island	0.284	270.37	+0.126	-0.031	-23.73	+34.17	0.133	0.113
Surf Inlet	0.378	244.21	+0.028	-0.052	+1.97	+12.24	0.022	0.064
Tom Bay	0.316	230.92	+0.015	-0.005	+4.87	+3.74	0.022	0.015
Wainwright Basin	0.295	228.41	+0.011	-0.007	+4.06	+0.88	0.017	0.006

Table 9. Comparison of O1 tidal statistics at historical (constituent-only) tide gauge locations.

			Ampl Error (m)		Phase Error (°)		Tidal Error (m)	
			CIOPS-W	KIT 500	CIOPS-W	KIT 500	CIOPS-W	KIT 500
Station	**Ampl**	**Phase**						
Aero Trading	0.308	244.54	+0.001	-0.016	-0.66	+12.92	0.003	0.049
Barnard Harbour	0.299	238.70	-0.009	-0.008	-0.14	-1.02	0.007	0.007
Beauchemin Channel	0.290	237.86	-0.004	-0.007	-0.19	+0.33	0.003	0.005
Block Islands	0.293	239.05	-0.003	-0.003	-0.35	-0.06	0.002	0.002
Bonilla Island	0.305	240.07	-0.001	0	+0.60	+0.15	0.002	0.001
Butedale	0.294	238.28	+0.002	+0.002	+0.76	+0.74	0.003	0.003
Claxton	0.300	247.09	+0.032	+0.019	-1.55	+14.06	0.024	0.055
Clear Passage	0.301	239.54	-0.003	-0.004	+1.04	+0.05	0.004	0.003
Griffin Passage	0.289	236.46	+0.003	-0.017	-2.48	+6.43	0.009	0.025
Griffith Harbour	0.295	240.55	+0.021	+0.018	-2.70	-1.36	0.018	0.014
Haysport	0.313	256.25	+0.036	-0.024	+5.23	+33.29	0.033	0.123
Higgins Passage West	0.282	237.06	+0.004	+0.002	-0.01	+0.41	0.003	0.002
Inverness Passage	0.311	245.66	+0.001	+0.011	-1.59	+15.38	0.006	0.060
Kemano Bay	0.299	240.95	-0.001	-0.002	+0.36	0	0.002	0.001
Khyex Point	0.313	272.55	+0.085	-0.001	-25.02	+29.07	0.124	0.111
Kitkatla	0.310	241.44	+0.001	+0.004	+0.15	+5.82	0.001	0.023
Klemtu	0.281	236.56	+0.002	-0.005	+1.50	+1.99	0.005	0.008
Larsen Island	0.301	244.55	+0.018	+0.022	-3.59	-3.17	0.019	0.020
Lawyer Islands	0.310	243.81	-0.003	+0.001	+0.16	+3.33	0.002	0.013
Lowe Inlet	0.300	238.34	-0.004	+0.014	+2.58	+9.44	0.010	0.037
McKenney Islands	0.276	238.05	+0.013	+0.015	-1.77	-2.35	0.011	0.013
Meyers Narrows	0.277	236.55	+0.014	+0.018	-0.41	+3.62	0.010	0.018
Milne Island	0.288	236.60	-0.015	-0.019	-0.53	-0.78	0.011	0.013
Northland Terminal	0.311	244.44	0	-0.025	-0.26	+24.89	0.001	0.093
Oswald Bay	0.288	238.65	0	0	-0.55	-1.46	0.002	0.005
Patterson Inlet	0.299	239.95	+0.002	+0.002	0	-0.56	0.001	0.002
Port Blackney	0.276	236.23	+0.001	-0.001	+1.74	+2.06	0.006	0.007
Price Island	0.289	237.16	-0.011	-0.015	-1.70	-1.57	0.010	0.012
Prince Rupert Roro	0.308	244.08	-0.003	-0.001	-0.89	+3.26	0.004	0.012
Seabreeze Point	0.303	243.97	+0.007	+0.007	-1.93	+3.06	0.009	0.013
Smithers Island	0.288	238.30	-0.005	-0.008	-0.26	-0.16	0.004	0.005
Stryker Island	0.282	236.00	+0.001	-0.025	+2.05	+2.77	0.007	0.020
Surf Inlet	0.277	237.55	+0.022	+0.022	+0.13	-0.34	0.016	0.016
Tom Bay	0.262	242.55	+0.037	+0.032	-8.02	-6.38	0.038	0.032
Wainwright Basin	0.243	278.19	+0.070	+0.035	-37.23	+7.70	0.134	0.035

Table 10. Comparison of P1 tidal statistics at historical (constituent-only) tide gauge locations.

			Ampl Error (m)		Phase Error (º)		Tidal Error (m)	
Station	Ampl	Phase	CIOPS-W	KIT 500	CIOPS-W	KIT 500	CIOPS-W	KIT 500
Aero Trading	0.160	257.63	+0.006	-0.014	-2.12	+11.11	0.006	0.023
Beauchemin Channel	0.147	249.47	+0.005	-0.002	-0.73	+0.72	0.004	0.002
Bonilla Island	0.159	251.84	+0.001	-0.002	-0.98	-0.10	0.002	0.001
Kemano Bay	0.151	251.57	+0.009	+0.004	-0.03	+0.56	0.007	0.003
Kitkatla	0.155	255.93	+0.009	+0.007	-2.42	+3.55	0.008	0.009
Klemtu	0.142	247.98	+0.006	-0.002	+0.45	+1.40	0.004	0.003
Northland Terminal	0.161	257.42	+0.005	-0.022	-1.83	+22.63	0.005	0.044

Table 11. Comparison of K2 tidal statistics at historical (constituent-only) tide gauge locations.

			Ampl Error (m)		Phase Error (º)		Tidal Error (m)	
Station	Ampl	Phase	CIOPS-W	KIT 500	CIOPS-W	KIT 500	CIOPS-W	KIT 500
Aero Trading	0.166	292.92	+0.014	-0.014	-0.12	+15.63	0.010	0.032
Beauchemin Channel	0.127	277.84	+0.001	-0.004	+0.46	+4.53	0.001	0.007
Bonilla Island	0.155	284.07	+0.006	+0.005	+1.67	+5.05	0.005	0.010
Kemano Bay	0.158	281.46	+0.006	-0.002	+3.28	+8.77	0.008	0.017
Kitkatla	0.172	288.66	+0.004	-0.007	+1.22	+14.14	0.004	0.030
Klemtu	0.116	275.37	+0.003	-0.013	+0.96	+1.57	0.002	0.009
Northland Terminal	0.172	292.64	+0.010	-0.036	+0.95	+33.49	0.008	0.067

Table 12. Storm surge performance statistics calculated over ten strongest storm events during hindcast period.

Metric	CRMSE (m)			χ^2			Pearson Correlation		
Model	**CIOPS-W**	**KIT500**	**KIT100**	**CIOPS-W**	**KIT500**	**KIT100**	**CIOPS-W**	**KIT500**	**KIT100**
Station									
Hartley Bay	0.028	0.031	n/a	0.073	0.094	n/a	0.967	0.964	n/a
Kitimat	0.037	0.039	0.038	0.158	0.188	0.174	0.933	0.933	0.937
Prince Rupert	0.033	0.067	n/a	0.111	0.464	n/a	0.946	0.82	n/a

Table 13. Comparison of error statistics for tidal currents measured by current meters in the Kitimat 100 m domain.

			CRMSE (m/s)		χ^2	
Station	**Time**	**Depth (m)**	**KIT500**	**KIT100**	**KIT500**	**KIT100**
FOC1	201601 – 201606	150	0.071	0.070	0.771	0.75
		250	0.068	0.056	0.597	0.405
	202008 – 202106	150	0.049	0.042	0.331	0.24
		250	0.057	0.051	0.352	0.281
		359	0.055	0.051	0.427	0.371

Table 14. Comparison of error statistics for tidal currents measured by current meters in the Kitimat 500 m domain.

			CRMSE (m/s)		χ^2	
Station	**Time**	**Depth (m)**	**CIOPS-W**	**KIT500**	**CIOPS-W**	**KIT500**
CAM2	20160101 – 2010708	150	0.105	0.136	0.469	0.782
CMP1	20160127 – 20160520	250	0.191	0.129	1	0.455
DEV1	20160101 – 2016517	152	0.152	0.107	1.691	0.844
KSK1	20160101 – 20160519	150	0.135	0.049	2.354	0.312
SRC1	20160709 – 20170710	150	0.103	0.122	0.753	0.8
		204	0.276	0.284	0.652	0.918
	20170711 – 20180821	153	0.09	0.138	0.439	1.025
		205	0.09	0.106	0.379	0.522
SRN1	20170709 – 20180822	150	0.086	0.098	0.304	0.263
		192	0.095	0.088	0.272	0.358

Table 15. Comparison of ellipse error for tidal currents measured by current meters.

Station	Dates	Depth (m)	Constituent	Ellipse Error CIOPS-W	KIT500	KIT100
FOC1	20160101 – 20160608	150	M2	n/a	0.048	0.047
			S2	n/a	0.017	0.016
			K1	n/a	0.009	0.010
			N2	n/a	0.007	0.006
			O1	n/a	0.003	0.003
		250	M2	n/a	0.046	0.032
			S2	n/a	0.018	0.010
			K1	n/a	0.005	0.005
			N2	n/a	0.009	0.005
			O1	n/a	0.003	0.002
	202008 – 202106	150	M2	n/a	0.032	0.021
			S2	n/a	0.013	0.009
			K1	n/a	0.005	0.004
			N2	n/a	0.007	0.005
			O1	n/a	0.004	0.004
		250	M2	n/a	0.037	0.030
			S2	n/a	0.016	0.012
			K1	n/a	0.010	0.007
			N2	n/a	0.010	0.008
			O1	n/a	0.008	0.006
		359	M2	n/a	0.034	0.029
			S2	n/a	0.016	0.012
			K1	n/a	0.010	0.009
			N2	n/a	0.008	0.005
			O1	n/a	0.008	0.008
CAM2	20160101 – 2010708	150	M2	0.132	0.091	n/a
			S2	0.045	0.037	n/a
			K1	0.034	0.023	n/a
			N2	0.030	0.014	n/a
			O1	0.023	0.021	n/a
CMP1	20160127 – 20160520	250	M2	0.157	0.078	n/a
			S2	0.052	0.039	n/a
			K1	0.036	0.034	n/a
			N2	0.030	0.018	n/a
			O1	0.015	0.016	n/a
DEV1	20160101 – 2016517	152	M2	0.162	0.053	n/a
			S2	0.059	0.013	n/a
			K1	0.038	0.012	n/a
			N2	0.032	0.009	n/a

Station	Dates	Depth (m)	Constituent	Ellipse Error CIOPS-W	KIT500	KIT100
			O1	0.024	0.008	n/a
KSK1	20160101 – 20160519	150	M2	0.097	0.034	n/a
			S2	0.038	0.011	n/a
			K1	0.025	0.009	n/a
			N2	0.021	0.010	n/a
			O1	0.018	0.006	n/a
SRC1	20160709 – 20170710	150	M2	0.108	0.073	n/a
			S2	0.041	0.018	n/a
			K1	0.028	0.018	n/a
			N2	0.021	0.016	n/a
			O1	0.017	0.011	n/a
		204	M2	0.086	0.099	n/a
			S2	0.040	0.030	n/a
			K1	0.036	0.036	n/a
			N2	0.019	0.027	n/a
			O1	0.021	0.028	n/a
	20170711 – 20180821	153	M2	0.122	0.093	n/a
			S2	0.045	0.017	n/a
			K1	0.028	0.017	n/a
			N2	0.021	0.018	n/a
			O1	0.019	0.010	n/a
		205	M2	0.103	0.064	n/a
			S2	0.038	0.030	n/a
			K1	0.019	0.013	n/a
			N2	0.011	0.009	n/a
			O1	0.013	0.009	n/a
SRN1	20170709 – 20180822	150	M2	0.044	0.057	n/a
			S2	0.020	0.024	n/a
			K1	0.012	0.016	n/a
			N2	0.010	0.011	n/a
			O1	0.011	0.012	n/a
		192	M2	0.053	0.043	n/a
			S2	0.019	0.015	n/a
			K1	0.009	0.019	n/a
			N2	0.011	0.008	n/a
			O1	0.004	0.011	n/a

Table 16. Comparison of error statistics for non-tidal currents measured by current meters in the Kitimat 100 m domain.

Station	Time	Depth	CRMSE (m/s) KIT 500	CRMSE (m/s) KIT 100	χ^2 KIT 500	χ^2 KIT 100	Vector Correlation (Magnitude @ Direction) KIT 500	Vector Correlation (Magnitude @ Direction) KIT 100
FOC1	20160101 – 20160608	150m	0.057	0.060	1.122	1.273	0.422 @ 0.3	0.365 @ 3.4
		250m	0.062	0.067	0.848	0.870	0.022 @ -62.4	0.027 @ -87.9
	202008 – 202106	150m	0.065	0.065	0.917	0.915	0.291 @ 2.6	0.320 @ 3.0
		250m	0.065	0.064	0.893	0.867	0.327 @ 1.9	0.373 @ -3.0
		359m	0.069	0.068	0.960	0.954	0.212 @ 10.4	0.214 @ 3.1

Table 17. Comparison of error statistics for non-tidal currents measured by current meters in the Kitimat 500 m domain.

Station	Time	Depth (m)	CRMSE (m/s) CIOPS-W	CRMSE (m/s) KIT 500	χ^2 CIOPS-W	χ^2 KIT 500	Vector Correlation (Magnitude @ Direction) CIOPS-W	Vector Correlation (Magnitude @ Direction) KIT 500
CAM2	20160101 – 2010708	150	0.239	0.14	2.973	1.017	0.373 @ 119.6	0.351 @ 2.5
CMP1	20160127 – 20160520	250	n/a	0.175	n/a	0.953	n/a	0.228 @ 14.4
DEV1	20160101 – 2016517	152	0.171	0.163	1.786	1.051	0.171 @ -14.0	0.057 @ -166.4
KSK1	20160101 – 20160519	150	0.178	0.049	8.133	0.919	0.224 @ -160.8	0.317 @ 24.1
SRC1	20160709 – 20170710	150	0.129	0.144	0.985	1.207	0.047 @ 53.7	0.183 @ 22.3
		204	0.641	0.634	1.002	0.981	0.444 @ 25. 5	0.458 @ 54.8
	20170711 – 20180821	153	0.104	0.117	0.838	1.068	0.433 @ 16.5	0.212 @ -17.1
		205	0.085	0.094	0.827	0.97	0.501 @ 17.7	0.352 @ 40.7
SRN1	20170709 – 20180822	150	0.078	0.098	0.964	1.43	0.232 @ 9.3	0.074 @ -21.7
		192	0.064	0.073	0.766	0.994	0.511 @ 17.1	0.202 @ 18.1

Table 18. Comparison of error statistics for total currents measured by current meters in the Kitimat 100 m domain.

Station	Period	Instrument Depth (m)	Bias (m/s, u + vj) KIT 500	Bias (m/s, u + vj) KIT 100	CRMSE (m/s) KIT 500	CRMSE (m/s) KIT 100	χ^2 KIT 500	χ^2 KIT 100	Vector Correlation (Magnitude @ Direction) KIT 500	Vector Correlation (Magnitude @ Direction) KIT 100
FOC1	201601 – 201606	150m	-0.0058-0.0086j	-0.0002-0.0013j	0.178	0.093	3.301	0.912	n/a	0.727@9.6
		250m	-0.0028-0.0120j	-0.0208-0.0302j	0.108	0.089	n/a	0.561	0.578@-39.5	0.676@20.1
	202008 – 202106	150m	0.0086-0.0287j	0.0058-0.0028j	0.183	0.078	2.715	0.502	0.538@-45.2	0.725@11.7
		250m	-0.0101-0.0188j	-0.0089-0.0213j	0.12	0.085	n/a	0.481	n/a	0.743@13.9
		359m	-0.0210-0.0305j	-0.0176-0.0271j	0.112	0.087	n/a	0.595	n/a	0.661@-4.7

Table 19. Comparison of error statistics for total currents measured by current meters in the Kitimat 500 m domain.

Station	Period	Instrument Depth (m)	Bias (m/s, u + vj) CIOPS -W	Bias (m/s, u + vj) KIT 500	CRMSE (m/s) CIOPS -W	CRMSE (m/s) KIT 500	χ^2 CIOPS -W	χ^2 KIT 500	Vector Correlation (Magnitude @ Direction) CIOPS -W	Vector Correlation (Magnitude @ Direction) KIT 500
CAM2	201601 – 20107	150m	-0.0229-0.184j	-0.0600-0.0899j	0.262	0.196	1.088	0.846	0.511@26.9	0.714@16.5
CMP1	201601 – 201605	250m	0.0072-0.1218j	0.0191-0.125j	0.259	0.219	1.000	0.608	n/a	0.694@24.7
DEV1	201601 – 201605	152m	0.0816+0.0190j	0.0410+0.108j	0.230	0.196	1.736	0.945	0.297@21.3	0.308@35.8
KSK1	201601 – 201605	150m	0.0293-0.104j	0.0045-0.0110j	0.224	0.070	3.759	0.464	0.382@54.2	0.811@22.4
SRC1	201601 – 201607	204m	0.267+0.0476j	0.259+0.0675j	0.702	0.699	0.946	0.940	0.245@17.2	0.278@-12.3
	201607 – 201707	150m	0.0008-0.0155j	-0.0091+0.0223j	0.168	0.192	0.827	1.072	0.626@23.9	0.549@11.4
	201707 – 201806	205m	0.0044+0.0042j	-0.0042+0.0223j	0.126	0.144	0.517	0.658	0.750@22.1	0.636@-21.4
		153m	-0.0042-0.0284j	-0.0183+0.0251j	0.140	0.183	0.607	1.050	0.731@18.5	0.568@-5.8
SRN1	201707 – 201808	150m	0.0173-0.0125j	0.0244-0.0246j	0.118	0.141	0.406	0.561	0.802@12.6	0.739@10.3
		192m	0.0093+0.0038j	0.0089-0.0088j	0.116	0.116	0.379	0.379	0.857@22.1	0.798@-3.6

Table 20. Comparison of error statistics for tidal currents measured by ADCP in the Kitimat 100 m domain.

Station	Period	ADCP Depth (m)	Depth (m)	CRMSE (m/s) KIT500	CRMSE (m/s) KIT100	γ^2 KIT500	γ^2 KIT100
FOC1	201601 – 201606	37	8	0.148	0.133	1.472	1.192
			15	0.104	0.104	0.954	0.938
		356	50	0.056	0.054	0.676	0.625
			100	0.053	0.050	0.543	0.493
			250	0.056	0.048	0.299	0.214
FOC1	202008 – 202106	36	8	0.104	0.096	0.367	0.312
			15	0.096	0.087	0.490	0.405
		358	50	0.058	0.052	0.423	0.339
			100	0.046	0.041	0.311	0.253
			250	0.043	0.039	0.210	0.173
KIT1	202008 – 202106	41	8	0.054	0.051	1.303	1.164
			15	0.035	0.034	1.024	0.993
		101	50	0.019	0.019	0.923	0.915
		196	100	0.013	0.013	0.688	0.672

Table 21. Comparison of error statistics for tidal currents measured by ADCP in the Kitimat 500 m domain.

Station	Period	ADCP Depth (m)	Depth (m)	CRMSE (m/s) CIOPS-W	CRMSE (m/s) KIT500	γ^2 CIOPS-W	γ^2 KIT500
CAM2	201601 – 201607	227	50	0.237	0.069	1.619	0.138
			100	0.223	0.084	1.288	0.181
CMP1	201601 – 201605	355	100	0.151	0.088	0.483	0.163
			250	0.172	0.092	n/a	0.286
DEV1	201601 – 201604	102	15	0.258	0.113	9.334	1.803
			50	0.269	0.061	8.683	0.447
HEC1	201601 – 201607	39	15	0.209	0.088	1.703	0.299
		125	50	0.188	0.074	1.782	0.275
			100	0.195	0.073	1.726	0.239
KSK1	201601 – 201605	41	15	0.171	0.084	1.343	0.319
		359	50	0.197	0.048	7.293	0.427
			100	0.186	0.039	5.590	0.241
			250	0.064	0.029	n/a	0.209
SRC1	201607 – 201707	203	50	0.170	0.106	0.611	0.237
			100	0.147	0.117	0.639	0.404
SRN1	201908 – 201909	41	8	0.093	0.109	0.092	0.126
			15	0.078	0.088	0.068	0.087
		190	50	0.068	0.100	0.097	0.213
			100	0.070	0.114	0.178	0.474

Table 22. Comparison of error statistics for non-tidal currents measured by ADCP in the Kitimat 100 m domain.

				CRMSE (m/s)		χ^2		Vector Correlation (Magnitude @ Direction)	
				KIT 500	KIT 100	KIT 500	KIT 100	KIT 500	KIT 100
Station	**Period**	**ADCP Depth (m)**	**Depth (m)**						
FOC1	201601 – 201607	37	**8**	0.152	0.144	0.977	1.071	0.305@ 0.0	0.358@ 6.7
			15	0.145	0.124	0.900	0.969	0.345@ -9.0	0.369@ 0.8
		356	**50**	0.060	0.060	0.931	1.113	0.324@ -13.3	0.274@ -14.8
			100	0.064	0.072	0.948	1.005	0.240@ -12.9	0.188@ -18.3
			250	0.069	0.073	0.797	0.780	0.557@ -22.1	0.497@-17.8
	202008 – 202106	36	**8**	0.195	0.181	0.776	0.867	0.51@ -1.6	0.568@ 4.7
			15	0.153	0.145	0.944	1.11	0.358@ 2.0	0.403@ 8.2
		358	**50**	0.079	0.075	1.03	1.051	0.244@ 0.2	0.331@ 0.6
			100	0.069	0.068	0.862	0.883	0.383@ -9.0	0.395@ -9.6
			250	0.059	0.059	0.9	0.902	0.337@ -19.3	0.383@ -22.7
KIT1	202008 – 202106	41	**8**	0.077	0.083	1.138	1.313	0.173@ 3.6	0.234@ -3.4
			15	0.055	0.059	1.097	1.272	0.203@ 6.0	0.211@ 12.6
		101	**50**	0.033	0.033	1.036	1.072	0.137@ -8.0	0.155@ -12.5
		196	**100**	0.027	0.026	0.986	0.952	0.181@ -29.1	0.283@ -24.6

Table 23. Comparison of error statistics for non-tidal currents measured by ADCP in the Kitimat 500 m domain.

Station	Period	ADCP Depth (m)	Depth (m)	CRMSE (m/s) CIOPS -W	CRMSE (m/s) KIT 500	χ^2 CIOPS -W	χ^2 KIT 500	Vector Correlation (Magnitude @ Direction) CIOPS -W	Vector Correlation (Magnitude @ Direction) KIT 500
CAM2	201601 – 201607	227	**50**	0.114	0.094	1.140	0.896	0.381@ -49.7	0.442@ 22.9
			100	0.105	0.101	1.054	1.130	0.215@ 14.3	0.270@ 38.2
CMP1	201601 – 201605	355	**100**	0.118	0.119	0.974	1.114	0.416@ -52.8	0.238@ 6.2
			250	0.150	0.149	n/a	0.922	n/a	0.284@ -9.5
DEV1	201601 – 201604	102	**15**	0.131	0.092	1.678	1.127	0.078 @ -35.6	0.087 @ 38.3
			50	0.096	0.077	1.586	1.038	0.068@ -24.1	0.046@ 80.4
HEC1	201601 – 201607	39	**15**	0.183	0.180	0.891	0.870	0.346@ -8.5	0.414@ -5.7
		125	**50**	0.147	0.139	0.921	0.816	0.335@ -21.2	0.490@ -0.6
			100	0.128	0.129	0.966	0.882	0.251@ -25.6	0.418@ -12.3
KSK1	201601 – 201605	41	**15**	0.204	0.145	1.532	0.978	0.038@ -125.9	0.226@ -7.1
		359	**50**	0.103	0.079	1.975	1.065	0.192@ -75.9	0.046@ -82.1
			100	0.071	0.061	1.328	1.039	0.343@ -56.9	0.057@ -17.0
			250	0.038	0.037	n/a	0.996	n/a	0.133@ -7.2
SRC1	201607 – 201707	203	**50**	0.221	0.223	0.839	0.977	0.413@ -12.8	0.267 @ 13.6
			100	0.192	0.173	0.900	0.842	0.384@ -34.6	0.470@ 27.9
SRN1	201908 – 201909	41	**8**	0.124	0.149	0.866	1.106	0.408 @ -5.2	0.359@ -14.8
			15	0.124	0.143	0.991	1.249	0.316@ -13.5	0.240@ -22.2
		190	**50**	0.107	0.098	1.136	1.164	0.301 @ 56.0	0.136@ 58.0
			100	0.064	0.076	1.009	1.376	0.134@ -32.7	0.166@ 158.3

Table 24. Comparison of error statistics for total currents measured by ADCP in the Kitimat 100 m domain.

Station	Period	ADCP Depth (m)	Depth (m)	Bias (m/s, u+vj) KIT 500	Bias (m/s, u+vj) KIT 100	CRMSE (m/s) KIT 500	CRMSE (m/s) KIT 100	χ^2 KIT 500	χ^2 KIT 100	Vector Correlation (Magnitude @ Direction) KIT 500	Vector Correlation (Magnitude @ Direction) KIT 100
FOC1	201601 – 201607	37	**8**	0.0694 +0.0153j	0.0274 -0.0085j	0.214	0.198	1.191	1.123	0.508@ -10.6	0.521 @ -8.5
			15	0.0916 +0.0352j	0.0514 +0.0212j	0.18	0.163	0.93	0.961	0.497 @ -6.8	0.485 @ -2.3
		356	**50**	-0.0282 -0.0094j	-0.0182 -0.0060j	0.083	0.082	0.777	0.816	0.61 @ -3.9	0.585 @ -5.6
			100	0.0113 +0.0177j	0.0260 +0.0253j	0.083	0.088	0.72	0.716	0.644 @ -5.1	0.625 @ -6.5
			250	-0.0219 -0.0258j	-0.0255 -0.0330j	0.089	0.087	0.452	0.389	0.786 @ -9.8	0.793 @ -6.8
	202008 – 202106	36	**8**	0.0992 +0.0680j	0.0619 +0.0526j	0.223	0.207	0.584	0.603	0.662 @ -1.6	0.671 @ 0.6
			15	0.0881 +0.0362j	0.0591 +0.0269j	0.182	0.172	0.699	0.729	0.604 @ -2.4	0.598 @ 1.5
		358	**50**	-0.0370 -0.0166j	-0.0283 -0.0123j	0.099	0.092	0.647	0.602	0.717 @ -2.3	0.722 @ -2.9
			100	-0.0180 -0.0049j	-0.0114 -0.0037j	0.084	0.081	0.554	0.531	0.713 @ -0.6	0.712 @ -1.7
			250	-0.0050 -0.0111j	-0.0057 -0.0113j	0.074	0.072	0.415	0.39	0.78 @ -2.8	0.785 @ -4.8
KIT1	202008 – 202106	41	**8**	0.0098 +000.8j	0.0075 +0.0119j	0.096	0.099	1.188	1.269	0.299 @ 0.2	0.334 @ -3.1
			15	-0.0012 -0.0026j	0.0025 +0.0023j	0.066	0.07	1.08	1.197	0.313 @ 1.0	0.31 @ 4.4
		101	**50**	-0.0053 +0.0020j	-0.0039 +0.0024j	0.038	0.039	1.008	1.033	0.217 @ 0.0	0.219 @ -5.2
		196	**100**	0.0049 +0.0043j	0.0049 +0.0037j	0.03	0.03	0.908	0.882	0.375 @ 1.9	0.405 @ -2.2

Table 25. Comparison of error statistics for total currents measured by ADCP in the Kitimat 500 m domain.

Station	Period	ADCP Depth (m)	Depth (m)	Bias (m/s, u+vj) CIOPS -W	Bias (m/s, u+vj) KIT 500	CRMSE (m/s) CIOPS -W	CRMSE (m/s) KIT 500	χ^2 CIOPS -W	χ^2 KIT 500	Vector Correlation (Magnitude @ Direction) CIOPS -W	Vector Correlation (Magnitude @ Direction) KIT 500
CAM2	201601 – 201607	227	**50**	-0.0059 +0.0406j	-0.0068 +0.0066j	0.264	0.119	1.51	0.311	0.831@-60.6	0.839@-5.7
			100	-0.0486 -0.0182j	-0.0280 -0.0200j	0.247	0.133	1.246	0.349	0.767@-56.6	0.815 @ 0.7
CMP1	201601 – 201605	355	**100**	-0.0157 +0.054j	-0.0189 +0.0358j	0.193	0.149	0.582	0.351	0.842@-34.1	0.814@ 0.6
			250	-0.0243 -0.0873j	-0.013 -0.0943j	0.228	0.176	n/a	0.498	n/a	0.712@ 3.8
DEV1	201601 – 201604	102	**15**	-0.0446 +0.0535j	0.0026 +0.0066j	0.29	0.147	5.327	1.449	0.258@-93.2	0.139@ 143.2
			50	-0.0108 +0.0342j	0.0157 -0.0230j	0.286	0.1	5.948	0.672	0.612@-101.8	0.594@ 9.0
HEC1	201601 – 201607	39	**15**	-0.0131 -0.0234j	-0.0113 -0.0178j	0.28	0.203	1.222	0.64	0.546@-39.8	0.638@-8.0
		125	**50**	0.0059 -0.0083j	-0.003 -0.007j	0.241	0.159	1.318	0.576	0.619@-36.9	0.702@-5.2
			100	-0.0066 +0.0035j	-0.0392 +0.0155j	0.234	0.15	1.394	0.526	0.647@-49.6	0.741@-1.1
KSK1	201601 – 201605	41	**15**	-0.0183 +0.138j	-0.0034 +0.0815j	0.268	0.169	1.422	0.59	0.620@-33.9	0.647@-0.2
		359	**50**	-0.0217 -0.0231j	-0.0119 -0.0291j	0.223	0.093	4.7	0.738	0.632@-39.2	0.580@-5.3
			100	-0.0102 -0.0166j	-0.0053 +0.0045j	0.199	0.073	4.033	0.537	0.721@-41.9	0.705@-8.1
			250	-0.0013 -0.0065j	-0.0037 -0.002j	0.075	0.048	n/a	0.415	n/a	0.781@-5.7
SRC1	201607 – 201707	203	**50**	-0.0740 +0.0672j	0.0060 +0.0667j	0.281	0.249	0.726	0.608	0.685@-30.9	0.653@-9.1
			100	-0.054 +0.0619j	0.0027 +0.0416j	0.244	0.212	0.774	0.631	0.660@-29.8	0.634@-4.7

Station	Period	ADCP Depth (m)	Depth (m)	Bias (m/s, u+vj) CIOPS-W	Bias (m/s, u+vj) KIT 500	CRMSE (m/s) CIOPS-W	CRMSE (m/s) KIT 500	χ^2 CIOPS-W	χ^2 KIT 500	Vector Correlation (Magnitude @ Direction) CIOPS-W	Vector Correlation (Magnitude @ Direction) KIT 500
SRN1	201908 – 201909	41	**8**	0.0657 +0.0235j	0.0861 +0.0405j	0.158	0.188	0.187	0.245	0.897@-0.2	0.885@-1.0
			15	0.0688 +0.0232j	0.0838 +0.0282j	0.148	0.171	0.168	0.214	0.909@0.3	0.898@-1.7
		190	**50**	0.0652 +0.0408j	0.0494 +0.0394j	0.128	0.142	0.2	0.309	0.909@1.3	0.902@-7.7
			100	0.0005 +0.0282j	0.0238 +0.0269j	0.097	0.139	0.276	0.573	0.892@2.7	0.871@ 8.0

Table 26. Comparison of SST error statistics for the hindcast period (Jan 2016 – Feb 2022).

	Bias (º)			CRMSE (º)			χ^2			Pearson		
Station	**CIOPS -W**	**KIT 500**	**KIT 100**	**CIOPS -W**	**KIT 500**	**KIT 100**	**CIOPS -W**	**KIT 500**	**KIT 100**	**CIOPS -W**	**KIT 500**	**KIT 100**
46181	-1.361	0.055	0.221	2.51	1.091	1.102	0.283	0.054	0.055	0.947	0.978	0.978
46185	-0.772	-0.68	n/a	0.923	1.054	n/a	0.097	0.127	n/a	0.951	0.937	n/a

Table 27. Comparison of moored CTD temperature error statistics (continued on next page).

			Bias (º)			CRMSE (º)			χ2			Pearson		
Station	**Dates**	**Depth (m)**	**CIOPS -W**	**KIT 500**	**KIT 100**	**CIOPS -W**	**KIT 500**	**KIT 100**	**CIOPS -W**	**KIT 500**	**KIT 100**	**CIOPS -W**	**KIT 500**	**KIT 100**
KIT1	8/20 - 6/21	40	n/a	0.123	0.189	n/a	0.403	0.344	n/a	0.326	0.237	n/a	0.838	0.882
		100	n/a	-0.018	0.160	n/a	0.385	0.365	n/a	1.035	0.932	n/a	0.343	0.420
KVIP.C2	10/18 - 2/20	46	0.956	-0.393	-0.521	0.317	0.535	0.625	0.716	1.367	1.866	0.825	0.618	0.688
FOC1	1 - 7/16	15	0.074	-0.061	-0.060	0.313	0.396	0.439	0.151	0.222	0.273	0.953	0.903	0.891
		40	0.291	0.315	0.303	0.265	0.425	0.398	1.225	2.717	2.38	0.397	-0.274	-0.284
		51	0.11	0.211	0.207	0.322	0.401	0.388	2.415	3.07	2.875	0.065	-0.299	-0.279
		150	-0.652	-0.576	-0.530	0.183	0.435	0.404	0.756	3.848	3.322	0.548	-0.7	-0.616
		250	-0.815	-0.982	-0.975	0.102	0.219	0.222	0.321	1.058	1.086	0.837	0.413	0.410
		300	-0.786	-1.214	-1.155	0.091	0.025	0.027	4.137	0.25	0.294	0.979	0.872	0.857
		350	-0.632	-1.26	-1.233	0.108	0.143	0.145	0.503	0.875	0.900	0.875	0.36	0.324
	8/20 - 6/21	15	n/a	0.302	0.257	n/a	1.013	1.011	n/a	0.786	0.783	n/a	0.923	0.925
		40	n/a	0.225	0.243	n/a	0.574	0.481	n/a	0.422	0.296	n/a	0.818	0.873
		75	n/a	0.404	0.414	n/a	0.365	0.391	n/a	0.686	0.789	n/a	0.692	0.655
		250	n/a	0.04	0.056	n/a	0.281	0.265	n/a	0.827	0.739	n/a	0.459	0.583
		356	n/a	0.13	0.123	n/a	0.25	0.249	n/a	1.035	1.032	n/a	0.054	0.058
KSK1	1 - 5/16	15	0.029	-0.315	n/a	0.247	0.339	n/a	0.19	0.331	n/a	0.905	0.86	n/a
		40	-0.002	0.285	n/a	0.457	0.682	n/a	1.98	4.315	n/a	-0.39	-0.857	n/a
		150	-0.681	-0.671	n/a	0.144	0.284	n/a	0.725	2.675	n/a	0.533	-0.794	n/a
		362	-1.201	-1.793	n/a	0.064	0.132	n/a	0.141	0.605	n/a	0.972	0.789	n/a
Dev1	1 - 4/16	15	-0.314	-0.213	n/a	0.274	0.52	n/a	0.989	3.238	n/a	0.841	0.805	n/a
		100	-0.042	0.213	n/a	0.152	0.212	n/a	0.364	0.689	n/a	0.798	0.56	n/a
		110	0.01	0.053	n/a	0.182	0.313	n/a	0.349	1.008	n/a	0.947	0.136	n/a
		152	-0.123	-0.103	n/a	0.164	0.307	n/a	0.461	1.534	n/a	0.756	-0.744	n/a
HBIP	10/20 - 6/21	95	n/a	-0.165	n/a	n/a	0.394	n/a	n/a	3.953	n/a	n/a	0.71	n/a
GRC1	8/19 - 8/20	20	n/a	0.645	n/a	n/a	1.017	n/a	n/a	1.379	n/a	n/a	0.859	n/a
PRC1	8/19 - 8/20	15	0.339	0.324	n/a	0.44	1.444	n/a	0.103	0.913	n/a	0.981	0.906	n/a
		150	-0.382	-0.167	n/a	0.131	0.296	n/a	0.153	0.711	n/a	0.976	0.622	n/a
		439	n/a	-0.492	n/a	n/a	0.303	n/a	n/a	1.042	n/a	n/a	-0.014	n/a
CAM1	1 - 7/16	15	-0.02	-0.04	n/a	0.394	0.543	n/a	0.205	0.359	n/a	0.925	0.881	n/a
		40	-0.092	-0.24	n/a	0.25	0.316	n/a	0.318	0.459	n/a	0.865	0.754	n/a
		150	-0.603	-0.436	n/a	0.278	0.469	n/a	0.182	0.516	n/a	0.906	0.782	n/a
		417	n/a	-0.906	n/a	n/a	0.858	n/a	n/a	1.232	n/a	n/a	-0.458	n/a

			Bias (º)			CRMSE (º)			ɣ2			Pearson		
Station	**Dates**	**Depth (m)**	**CIOPS -W**	**KIT 500**	**KIT 100**	**CIOPS -W**	**KIT 500**	**KIT 100**	**CIOPS -W**	**KIT 500**	**KIT 100**	**CIOPS -W**	**KIT 500**	**KIT 100**
CAM2	1 - 7/16	40	-0.089	-0.239	n/a	0.282	0.395	n/a	0.255	0.463	n/a	0.89	0.735	n/a
		150	-0.635	-0.636	n/a	0.221	0.414	n/a	0.264	0.886	n/a	0.858	0.338	n/a
		227	-0.715	-0.712	n/a	0.358	0.624	n/a	0.507	1.543	n/a	0.704	-0.672	n/a
CMP1	1 - 5/16	150	-0.602	-0.664	n/a	0.17	0.207	n/a	1.368	1.702	n/a	0.883	0.26	n/a
		355	-1.448	-1.983	n/a	0.324	0.21	n/a	2.709	1.006	n/a	-0.003	0.118	n/a
HEC1	1 - 7/16	15	-0.181	-0.195	n/a	0.31	0.584	n/a	0.05	0.176	n/a	0.976	0.91	n/a
		39	-0.052	-0.212	n/a	0.41	0.379	n/a	0.663	0.511	n/a	0.825	0.713	n/a
		52	-0.047	-0.184	n/a	0.386	0.297	n/a	1.667	0.868	n/a	0.638	0.569	n/a
		126	-0.212	-0.039	n/a	0.297	0.612	n/a	0.087	0.336	n/a	0.965	0.883	n/a
SRC1	7/16 - 7/17	40	0.632	0.217	n/a	1.017	0.901	n/a	0.943	0.703	n/a	0.776	0.754	n/a
		150	-0.049	-0.409	n/a	0.545	0.733	n/a	0.279	0.488	n/a	0.866	0.716	n/a
		202	0.055	0.019	n/a	0.314	0.393	n/a	0.224	0.344	n/a	0.881	0.819	n/a
SRC1	7/17 - 8/18	43	0.007	-0.452	n/a	0.422	0.808	n/a	0.123	0.402	n/a	0.938	0.778	n/a
		153	0.021	-0.281	n/a	0.481	0.483	n/a	0.72	0.691	n/a	0.547	0.624	n/a
SRN1	7/17 - 8/18	40	n/a	-0.546	n/a	n/a	0.752	n/a	n/a	0.356	n/a	n/a	0.814	n/a
		150	n/a	-0.145	n/a	n/a	0.442	n/a	n/a	0.406	n/a	n/a	0.772	n/a
		189	n/a	0.373	n/a	n/a	0.558	n/a	n/a	0.669	n/a	n/a	0.578	n/a
SRN1	8/18 - 8/19	50	n/a	-0.339	n/a	n/a	0.368	n/a	n/a	0.14	n/a	n/a	0.934	n/a
		150	n/a	-0.325	n/a	n/a	0.649	n/a	n/a	0.513	n/a	n/a	0.771	n/a
		189	n/a	0.389	n/a	n/a	0.33	n/a	n/a	0.791	n/a	n/a	0.626	n/a
CHAT1	8 - 12/18	50	0.152	0.164	n/a	0.205	0.339	n/a	0.078	0.211	n/a	0.981	0.894	n/a
		103	n/a	0.412	n/a	n/a	0.298	n/a	n/a	0.094	n/a	n/a	0.959	n/a

Table 28. Comparison of moored CTD salinity error statistics (continued on next page).

			Bias (psu)			CRMSE (psu)			Ɣ2			Pearson		
Station	**Dates**	**Depth (m)**	**CIOPS -W**	**KIT 500**	**KIT 100**	**CIOPS -W**	**KIT 500**	**KIT 100**	**CIOPS -W**	**KIT 500**	**KIT 100**	**CIOPS -W**	**KIT 500**	**KIT 100**
KIT1	8/20 – 6/21	40	n/a	0.495	0.492	n/a	0.236	0.262	n/a	0.351	0.433	n/a	0.809	0.755
		100	n/a	0.564	0.586	n/a	0.228	0.23	n/a	0.246	0.25	n/a	0.935	0.951
KVIP.C2	10/18 - 2/20	46	0.308	0.35	0.326	0.176	0.251	0.284	0.345	0.552	0.705	0.819	0.674	0.565
FOC1	1 - 7/16	15	0.495	0.358	0.434	0.708	0.878	0.888	0.719	0.693	0.709	0.554	0.573	0.556
		40	0.455	0.571	0.541	0.165	0.178	0.183	0.296	0.275	0.288	0.882	0.886	0.879
		51	0.28	0.403	0.386	0.15	0.249	0.253	0.18	0.439	0.45	0.953	0.753	0.747
		150	0.342	0.657	0.624	0.231	0.333	0.327	0.599	1.129	1.093	0.655	0.208	0.227
		250	0.546	0.72	0.728	0.098	0.198	0.195	0.32	1.011	0.977	0.846	0.342	0.371
		300	0.581	0.833	0.83	0.067	0.02	0.019	6.273	0.428	0.427	0.98	0.785	0.779
		350	0.434	0.919	0.918	0.111	0.111	0.107	1.16	1.159	1.063	0.88	-0.167	0.068
FOC1	8/20 – 6/21	15	n/a	0.59	0.622	n/a	1.306	1.306	n/a	0.8	0.8	n/a	0.611	0.606
		40	n/a	0.626	0.615	n/a	0.339	0.335	n/a	0.54	0.527	n/a	0.684	0.694
		75	n/a	-0.048	-0.066	n/a	0.125	0.129	n/a	0.109	0.116	n/a	0.948	0.946
		250	n/a	0.414	0.411	n/a	0.183	0.179	n/a	0.76	0.723	n/a	0.682	0.735
		356	n/a	0.32	0.329	n/a	0.142	0.145	n/a	0.927	0.968	n/a	0.305	0.179
KSK1	1 - 5/16	15	0.992	0.587	n/a	0.875	0.909	n/a	1.037	0.827	n/a	0.006	0.416	n/a
		40	0.455	0.594	n/a	0.141	0.142	n/a	0.497	0.443	n/a	0.823	0.752	n/a
		150	0.528	0.844	n/a	0.08	0.206	n/a	0.108	0.685	n/a	0.951	0.572	n/a
		362	0.657	1.041	n/a	0.077	0.115	n/a	0.305	0.682	n/a	0.984	0.957	n/a
Dev1	1 - 4/16	15	0.333	-0.136	n/a	0.54	0.617	n/a	0.654	0.692	n/a	0.694	0.616	n/a
		100	0.341	0.699	n/a	0.09	0.129	n/a	0.186	0.369	n/a	0.904	0.795	n/a
		110	0.265	0.696	n/a	0.048	0.075	n/a	0.253	0.573	n/a	0.948	0.728	n/a
		152	0.362	0.929	n/a	0.091	0.155	n/a	0.206	0.581	n/a	0.894	0.656	n/a
HBIP	10/20 - 6/21	95	n/a	0.844	n/a	n/a	0.209	n/a	n/a	0.574	n/a	n/a	0.712	n/a
GRC1	8/19 - 8/20	20	n/a	-1.479	n/a	n/a	0.666	n/a	n/a	2.192	n/a	n/a	0.176	n/a
PRC1	8/19 - 8/20	15	0.876	0.663	n/a	0.507	0.929	n/a	0.478	0.924	n/a	0.782	0.378	n/a
		150	0.333	0.48	n/a	0.034	0.259	n/a	0.06	0.815	n/a	0.973	0.521	n/a
		439	n/a	0.487	n/a	n/a	0.116	n/a	n/a	0.843	n/a	n/a	0.633	n/a
CAM1	1 - 7/16	15	0.196	0.056	n/a	0.226	0.355	n/a	0.655	1.551	n/a	0.588	0.251	n/a
		40	0.24	0.232	n/a	0.206	0.197	n/a	0.491	0.439	n/a	0.809	0.768	n/a
		150	0.456	0.44	n/a	0.117	0.456	n/a	0.033	0.5	n/a	0.983	0.796	n/a
		417	n/a	0.79	n/a	n/a	0.718	n/a	n/a	1.281	n/a	n/a	-0.649	n/a

Station	Dates	Depth (m)	Bias (psu) CIOPS-W	Bias (psu) KIT 500	Bias (psu) KIT 100	CRMSE (psu) CIOPS-W	CRMSE (psu) KIT 500	CRMSE (psu) KIT 100	χ2 CIOPS-W	χ2 KIT 500	χ2 KIT 100	Pearson CIOPS-W	Pearson KIT 500	Pearson KIT 100
CAM2	1 - 7/16	40	0.43	0.404	n/a	0.2	0.22	n/a	0.502	0.531	n/a	0.772	0.685	n/a
		150	0.441	0.572	n/a	0.088	0.395	n/a	0.029	0.583	n/a	0.986	0.693	n/a
		227	0.47	0.531	n/a	0.142	0.439	n/a	0.111	1.055	n/a	0.954	0.071	n/a
CMP1	1 - 5/16	150	0.288	0.552	n/a	0.063	0.234	n/a	0.134	1.397	n/a	0.981	0.289	n/a
		355	0.851	1.144	n/a	0.195	0.179	n/a	1.55	1.015	n/a	0.136	0.033	n/a
HEC1	1 - 7/16	15	0.293	0.166	n/a	0.231	0.356	n/a	0.524	1.217	n/a	0.72	0.46	n/a
		39	-0.006	-0.001	n/a	0.24	0.258	n/a	0.847	0.912	n/a	0.403	0.4	n/a
		52	0.084	0.135	n/a	0.247	0.236	n/a	0.793	0.687	n/a	0.455	0.563	n/a
		126	0.069	0.03	n/a	0.173	0.415	n/a	0.063	0.34	n/a	0.968	0.856	n/a
SRC1	7/16 - 7/17	40	-0.066	-0.097	n/a	0.28	0.257	n/a	0.747	0.607	n/a	0.505	0.629	n/a
		150	0.169	0.239	n/a	0.281	0.31	n/a	0.72	0.819	n/a	0.539	0.425	n/a
		202	0.046	0.063	n/a	0.102	0.12	n/a	0.707	0.926	n/a	0.553	0.33	n/a
SRC1	7/17 - 8/18	43	0.145	0.185	n/a	0.194	0.211	n/a	0.928	0.92	n/a	0.39	0.418	n/a
		153	0.119	0.18	n/a	0.222	0.204	n/a	0.85	0.665	n/a	0.389	0.579	n/a
SRN1	7/17 - 8/18	40	n/a	0.209	n/a	n/a	0.207	n/a	n/a	1.283	n/a	n/a	0.434	n/a
		150	n/a	0.207	n/a	n/a	0.296	n/a	n/a	0.434	n/a	n/a	0.806	n/a
		189	n/a	-0.008	n/a	n/a	0.244	n/a	n/a	0.601	n/a	n/a	0.66	n/a
SRN1	8/18 - 8/19	50	n/a	0.238	n/a	n/a	0.157	n/a	n/a	0.446	n/a	n/a	0.841	n/a
		150	n/a	0.282	n/a	n/a	0.397	n/a	n/a	0.885	n/a	n/a	0.353	n/a
		189	n/a	0.016	n/a	n/a	0.1	n/a	n/a	0.822	n/a	n/a	0.442	n/a
CHAT1	8 - 12/18	50	0.058	0.032	n/a	0.087	0.104	n/a	0.244	0.331	n/a	0.952	0.896	n/a
		103	n/a	-0.041	n/a	n/a	0.107	n/a	n/a	0.176	n/a	n/a	0.925	n/a

Table 29. Comparison of model results from CIOPS-W and the Kitimat 500 m configuration against near-surface temperature and salinity data measured from the Bellingham - Alaska ferry.

		T (°)		S (psu)	
Metric	**Period**	**CIOPS-W**	**KIT500**	**CIOPS-W**	**KIT500**
Bias	**Full Run**	-0.091	0.349	0.759	-0.719
	2017	0.105	-0.508	0.517	-1.158
	2018	0.064	0.656	0.825	-0.661
	2019	-0.385	0.316	0.792	-0.595
CRMSE	**Full Run**	1.073	1.908	1.987	2.45
	2017	0.595	0.78	1.739	1.709
	2018	1.155	2.046	2.03	2.548
	2019	1.045	1.895	2.014	2.566

Table 30. Drift trajectory comparison statistics over 24 hours, for simulations of drifters in the Kitimat 100 m domain.

	Molcard Skill			Separation Distance (km)		
Hour	**CIOPS-W**	**KIT500**	**KIT100**	**CIOPS-W**	**KIT500**	**KIT100**
1	0.2	0.31	0.32	0.9	0.7	0.67
2	0.21	0.32	0.33	1.68	1.27	1.21
3	0.22	0.33	0.34	2.37	1.85	1.77
4	0.23	0.33	0.34	3	2.36	2.27
5	0.2	0.33	0.33	3.69	2.88	2.78
6	0.2	0.33	0.33	4.33	3.43	3.32
7	0.21	0.34	0.34	4.96	3.85	3.7
8	0.21	0.34	0.34	5.51	4.35	4.18
9	0.28	0.31	0.32	5.71	5.51	5.19
10	0.29	0.3	0.32	6.12	6.04	5.69
11	0.3	0.28	0.3	6.65	6.67	6.22
12	0.28	0.25	0.26	5.7	5.57	5.54
13	0.31	0.27	0.27	5.73	5.8	5.73
14	0.3	0.28	0.27	6.03	6.03	6
15	0.35	0.32	0.32	6.08	6.56	6.54
16	0.36	0.34	0.32	6.25	6.76	6.88
17	0.37	0.35	0.33	6.32	6.92	7.12
18	0.38	0.34	0.33	6.33	7.06	7.28
19	0.39	0.34	0.32	6.3	7.2	7.53
20	0.4	0.33	0.3	6.29	7.38	7.78
21	0.41	0.33	0.29	6.32	7.58	8.07
22	0.42	0.32	0.27	6.41	7.83	8.48
23	0.42	0.3	0.26	6.58	8.18	8.83
24	0.41	0.29	0.25	6.78	8.58	9.16

Table 31. Drift trajectory comparison statistics over 24 hours, for simulations of drifters in the Kitimat 500 m domain.

	Molcard Skill		Separation Distance (km)	
Hour	**CIOPS-W**	**KIT500**	**CIOPS-W**	**KIT500**
1	0.25	0.24	0.91	0.95
2	0.26	0.24	1.73	1.79
3	0.26	0.25	2.54	2.64
4	0.27	0.24	3.27	3.45
5	0.32	0.28	3.46	3.87
6	0.32	0.28	3.94	4.48
7	0.32	0.28	4.28	4.89
8	0.31	0.27	4.7	5.4
9	0.3	0.25	4.91	5.81
10	0.3	0.25	5.27	6.31
11	0.29	0.25	5.62	6.73
12	0.29	0.25	5.98	7.16
13	0.3	0.25	6.36	7.62
14	0.3	0.25	6.76	8.1
15	0.32	0.26	7.04	8.42
16	0.33	0.27	7.22	8.86
17	0.33	0.27	7.63	9.3
18	0.33	0.28	7.95	9.58
19	0.33	0.28	8.34	9.97
20	0.33	0.29	8.74	10.34
21	0.33	0.29	9.12	10.69
22	0.32	0.29	9.49	11.08
23	0.32	0.29	9.86	11.44
24	0.27	0.19	8.21	9.59

12. FIGURES

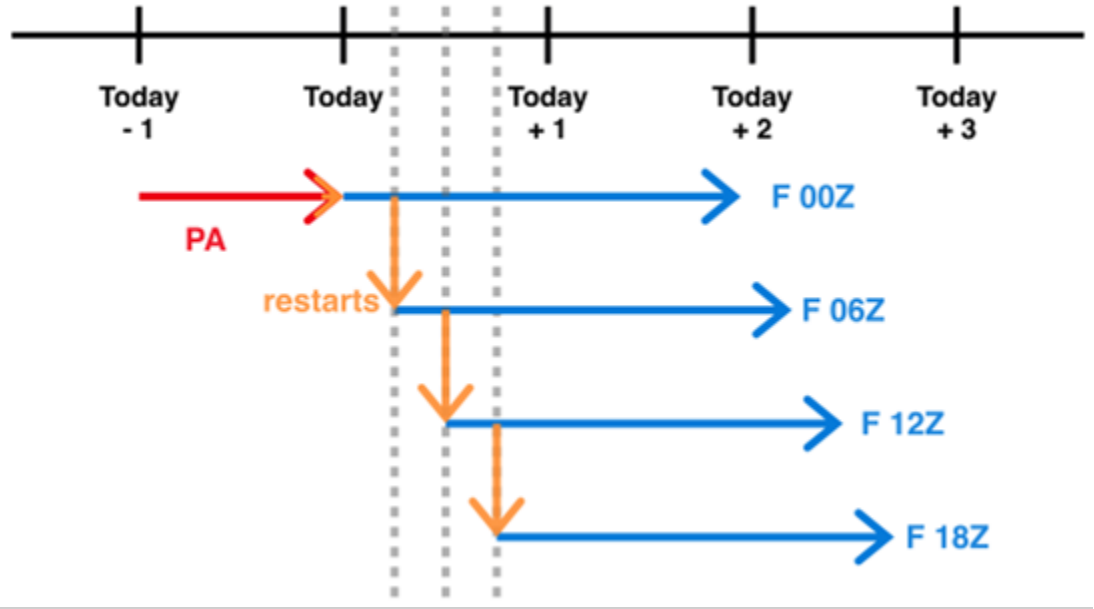

Figure 1: Schematic of one timestamp's set of pseudo-analysis (PA, in red) and forecast (in blue) runs. Grey dashed lines are spaced six hours apart, and orange arrows indicate where a restart file is generated and used to launch the subsequent step. The PA for today+1 will start with the same restart used to start today's 00Z forecast, and the pattern will repeat.

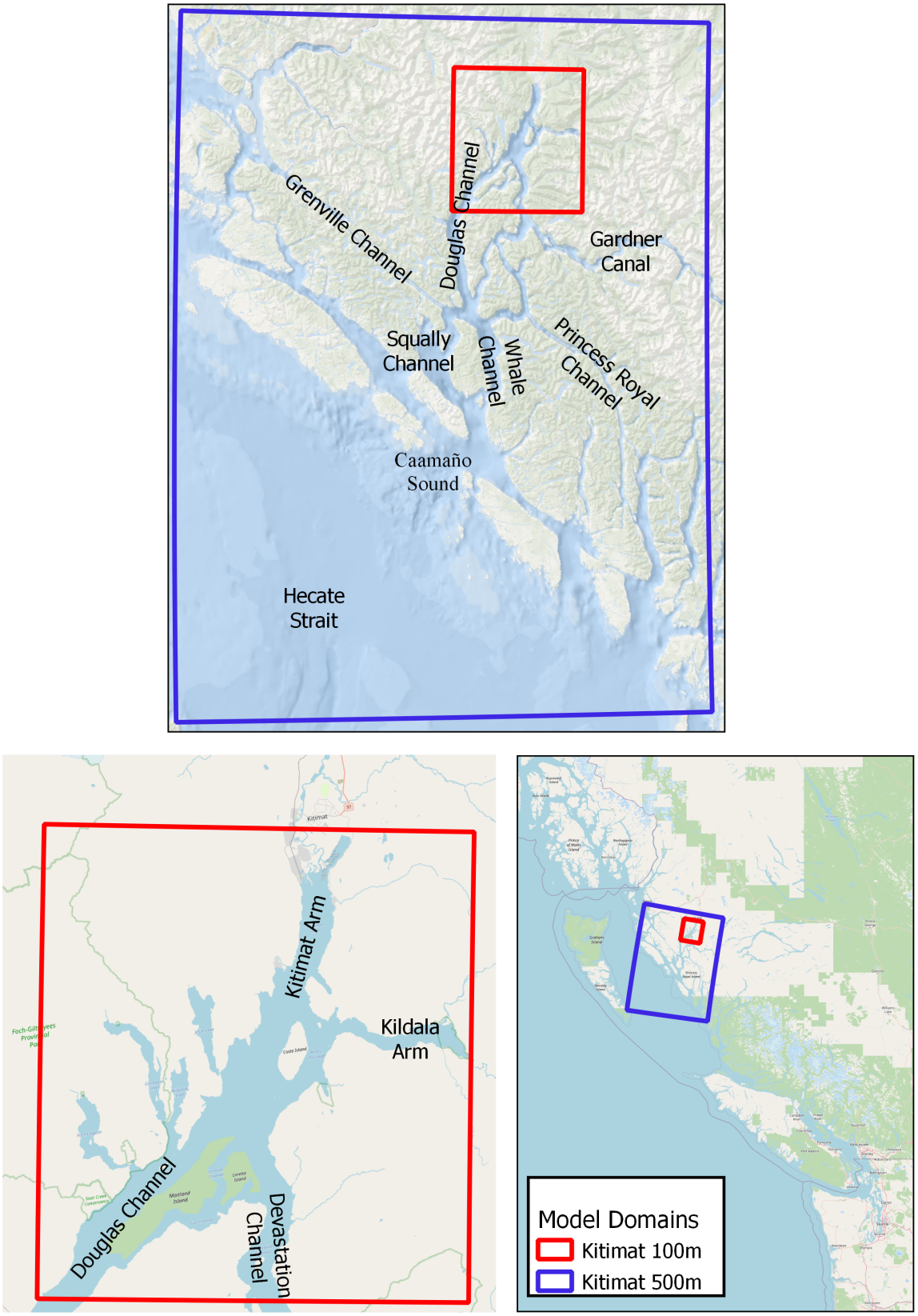

Figure 2. Kitimat domain layout with major channels labelled.

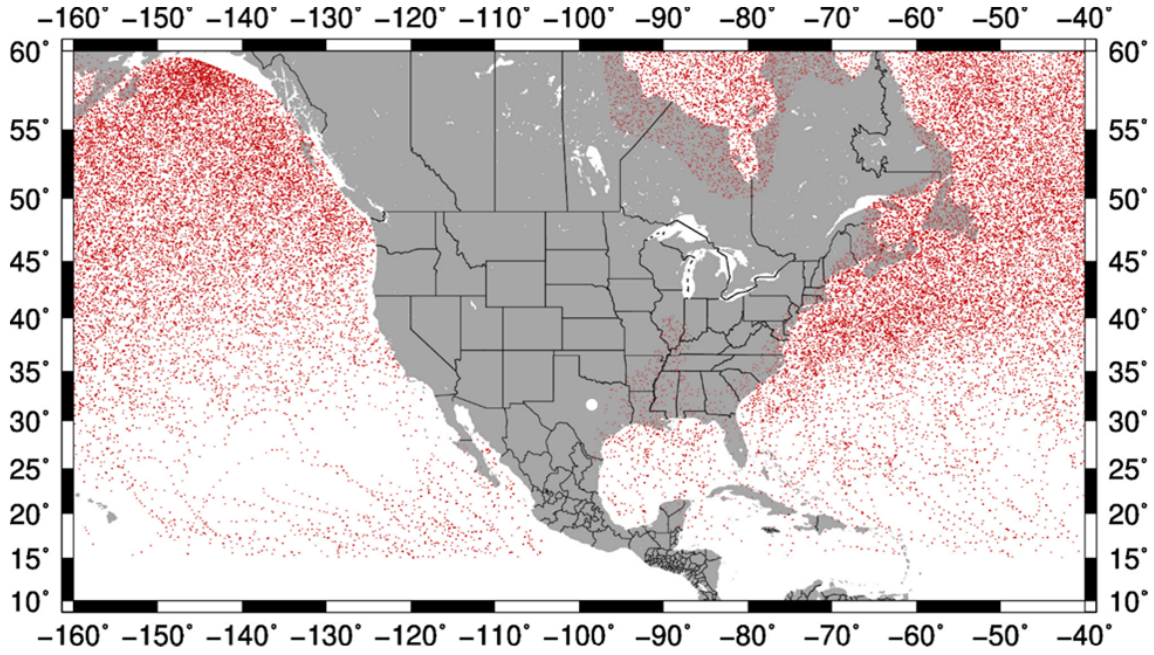

Figure 3. Cyclone locations every 6 hours from 2010-2021.

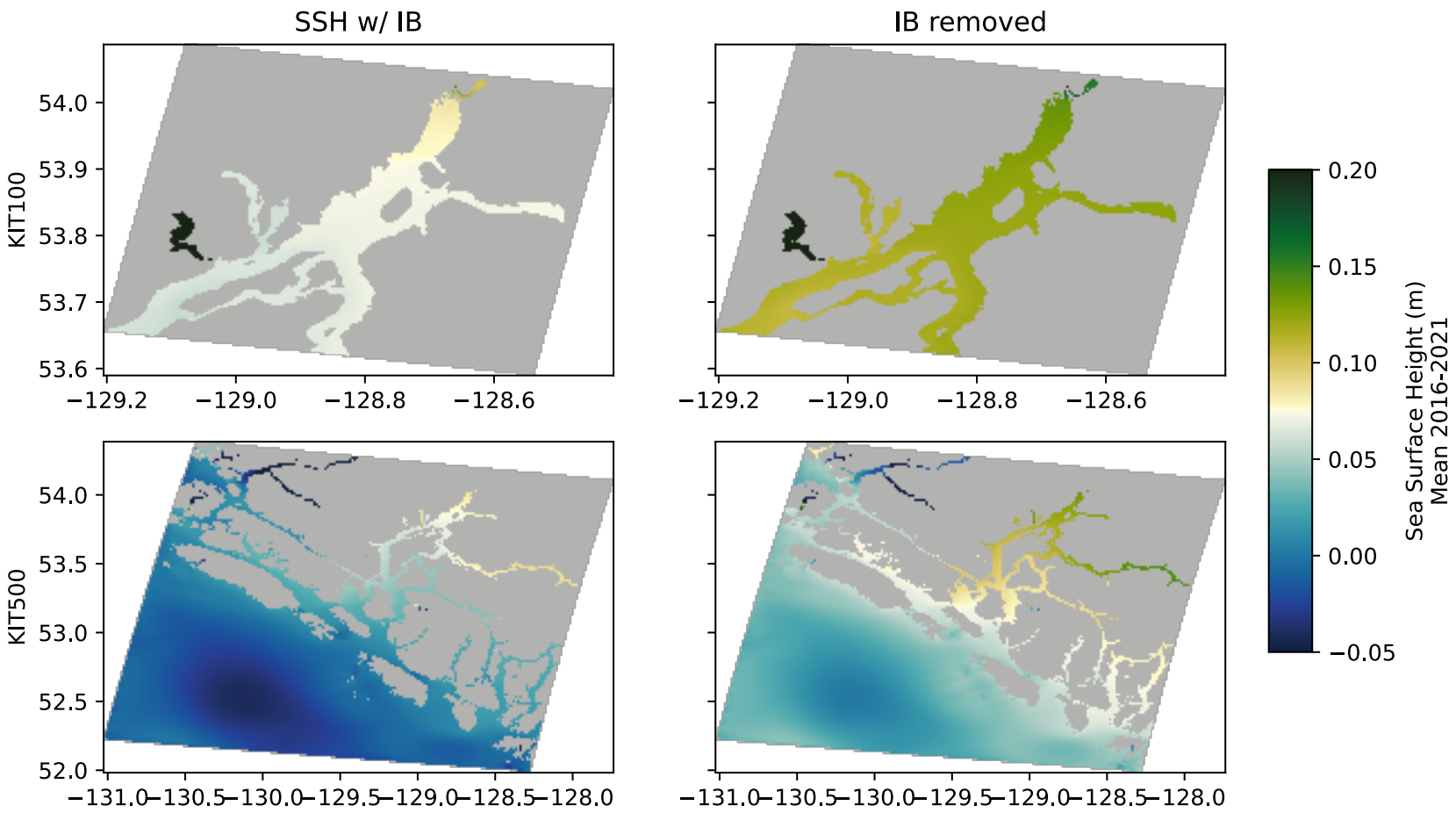

Figure 4. Mean Sea Surface Height from Kitimat port model hindcast, 2016 – 2021.

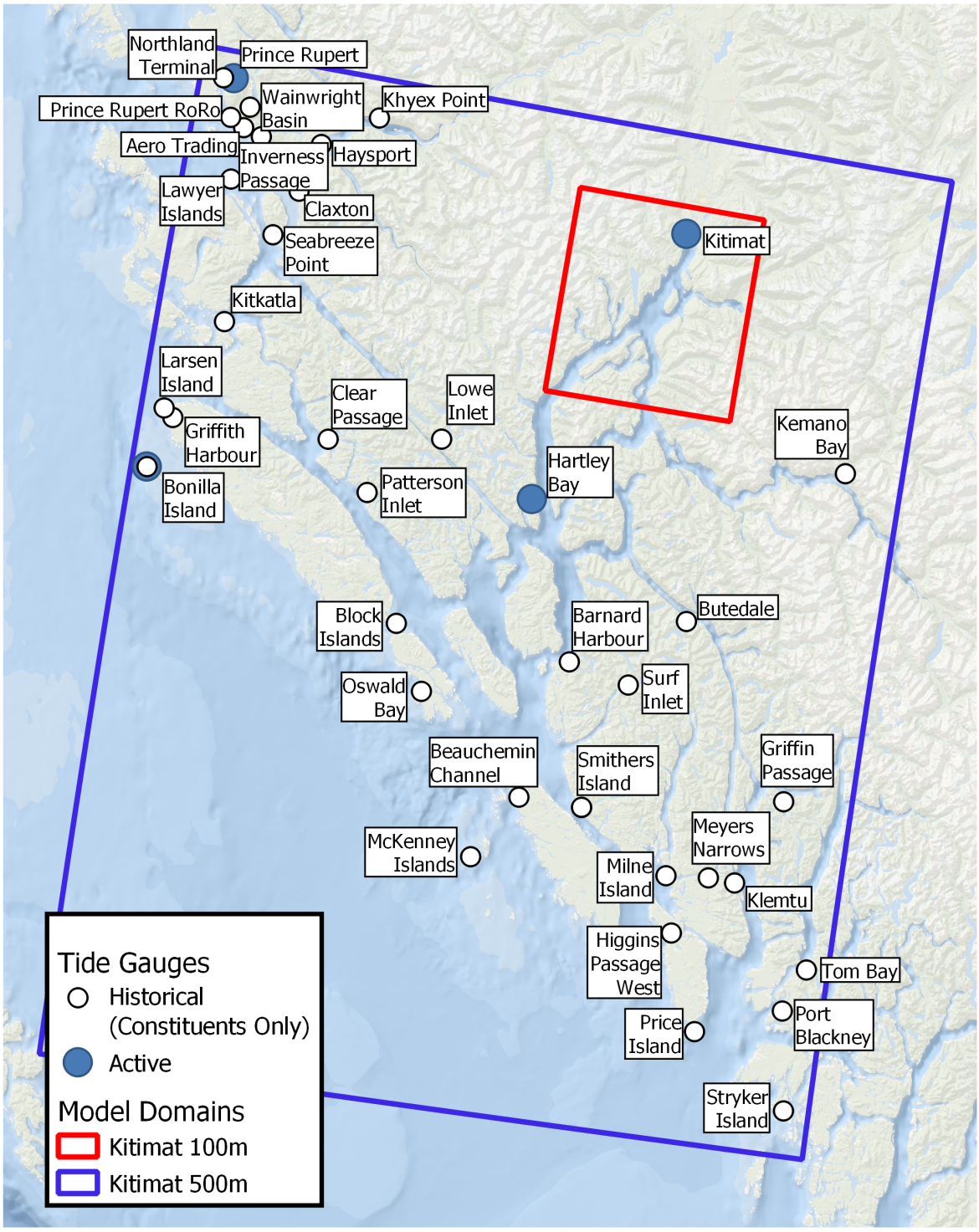

Figure 5. Key plot of active and historical tide gauge locations.

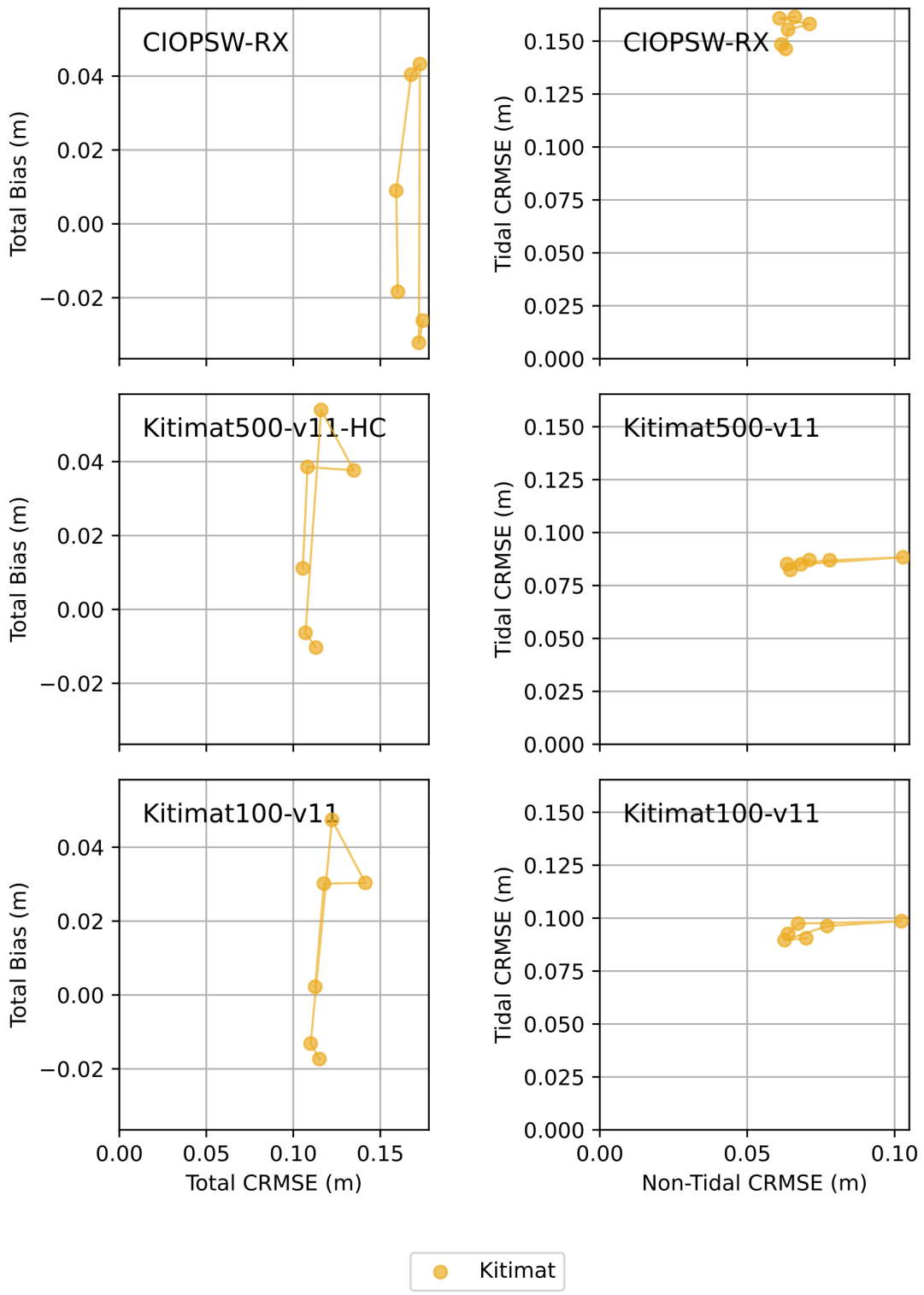

Figure 6. Water level summary scores for CIOPS-W (top), Kitimat 500 m (middle), and Kitimat 100 m (bottom). Left panels are bias against centered RMSE for total water level. Right panels are centered RMSE for tidal against non-tidal component of water level. Each marker represents values for one year between 2016 and 2021. In all cases movement towards the origin indicates model improvement. This plot only contains data from the tide gauge at Kitimat.

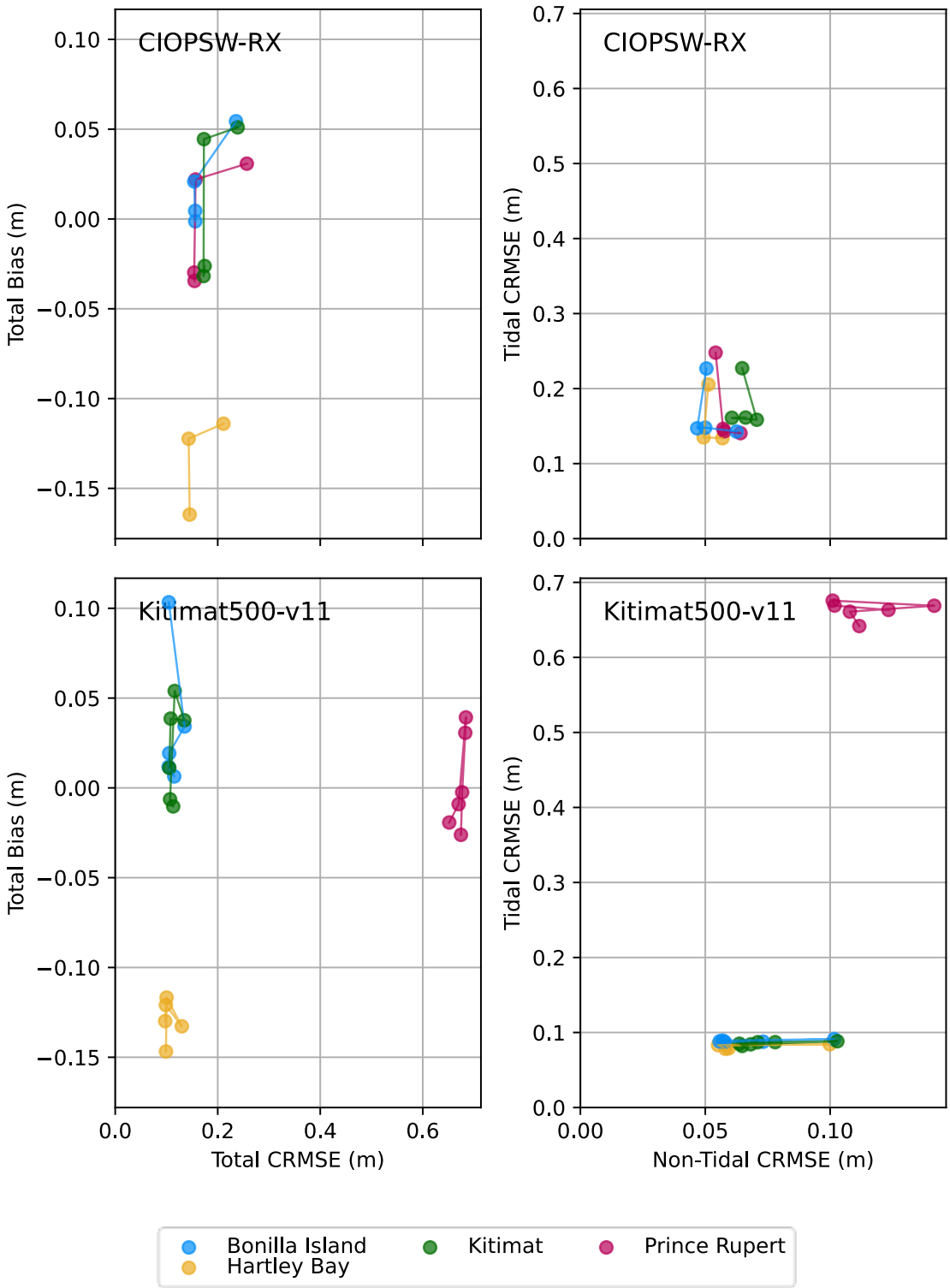

Figure 7. Water level summary scores for CIOPS-W (top) and Kitimat 500 m (bottom). Left panels are bias against centered RMSE for total water level. Right panels are centered RMSE for tidal against non-tidal component of water level. Each marker represents values for one year between 2016 and 2021. In all cases movement towards the origin indicates model improvement. This plot contains data from the tide gauges at Kitimat (green), Hartley Bay (yellow), Bonilla Island (blue), and Prince Rupert (magenta).

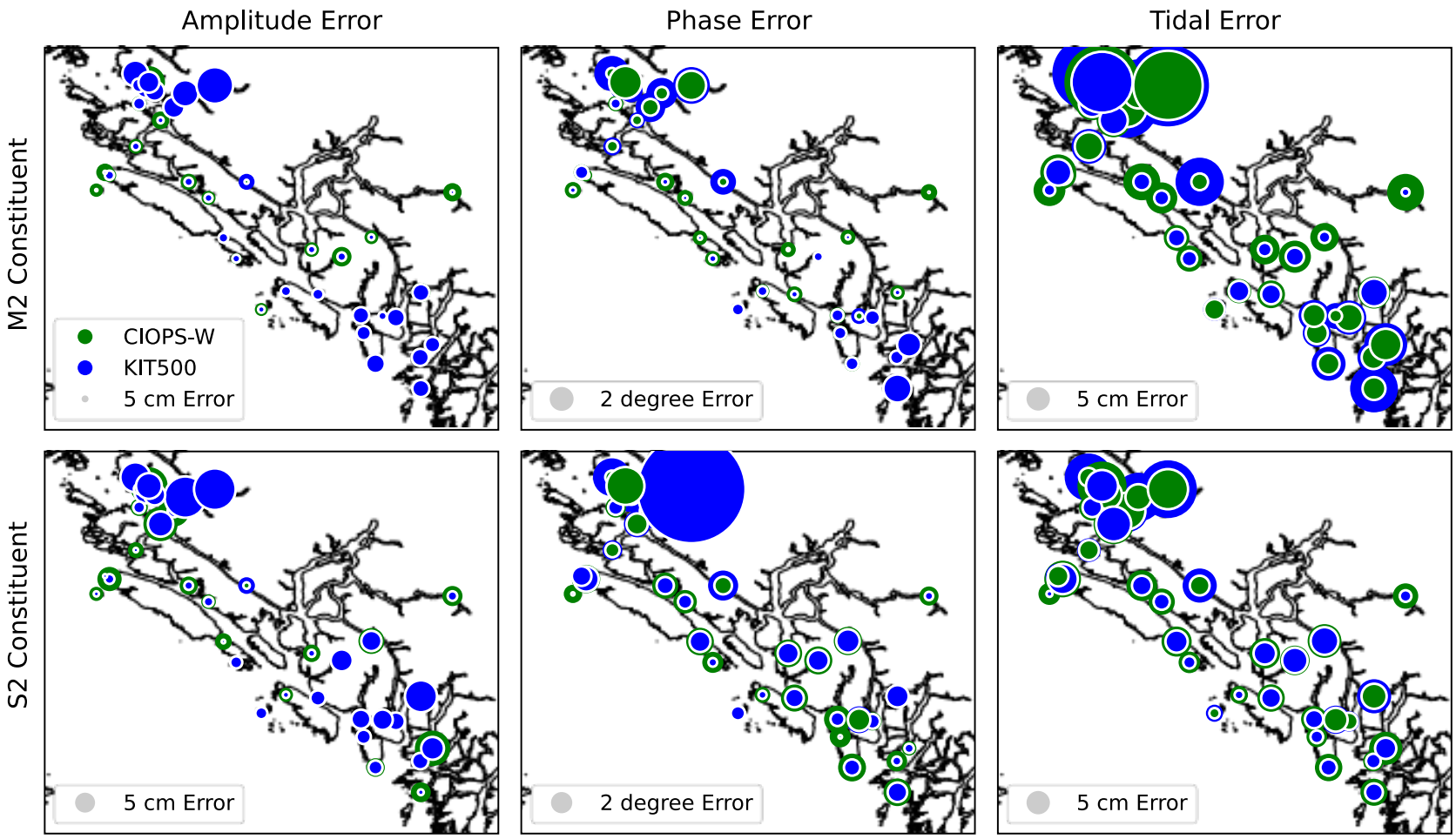

Figure 8. Summary of modelled tidal constituent comparisons against historical tide gauge data for M2 and S2.

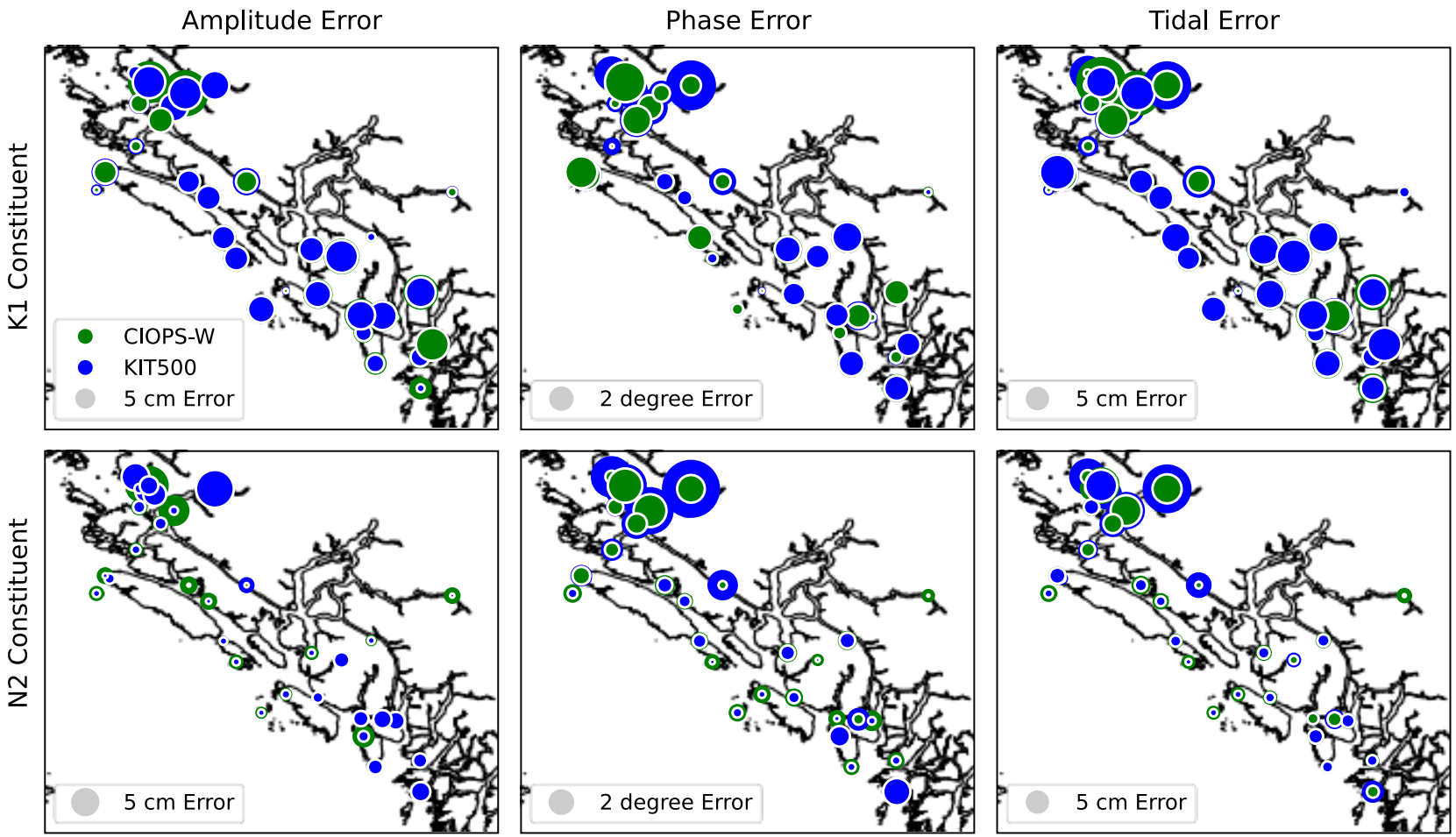

Figure 9. Summary of modelled tidal constituent comparisons against historical tide gauge data for K1 and N2.

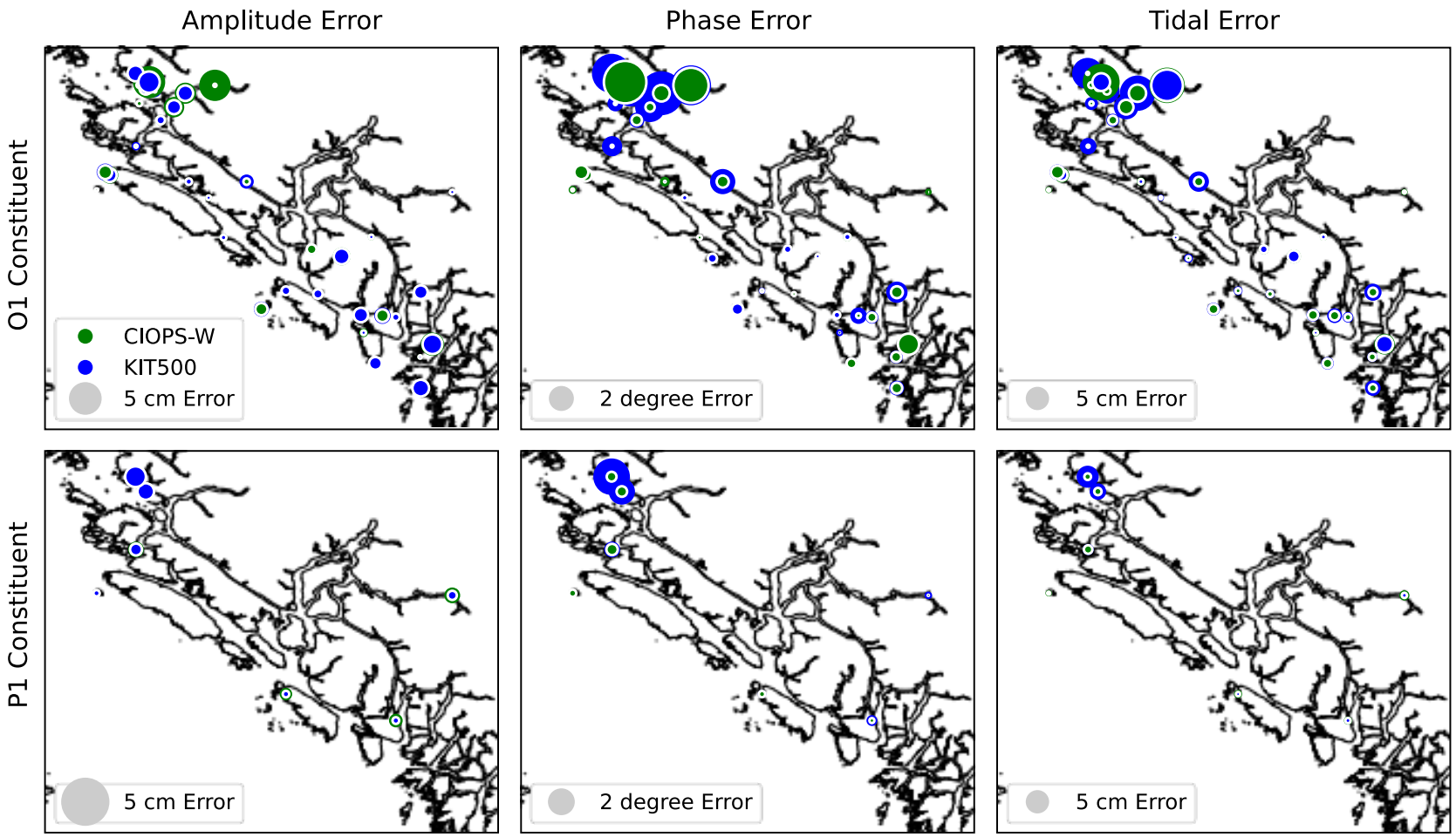

Figure 10. Summary of modelled tidal constituent comparisons against historical tide gauge data for O1 and P1.

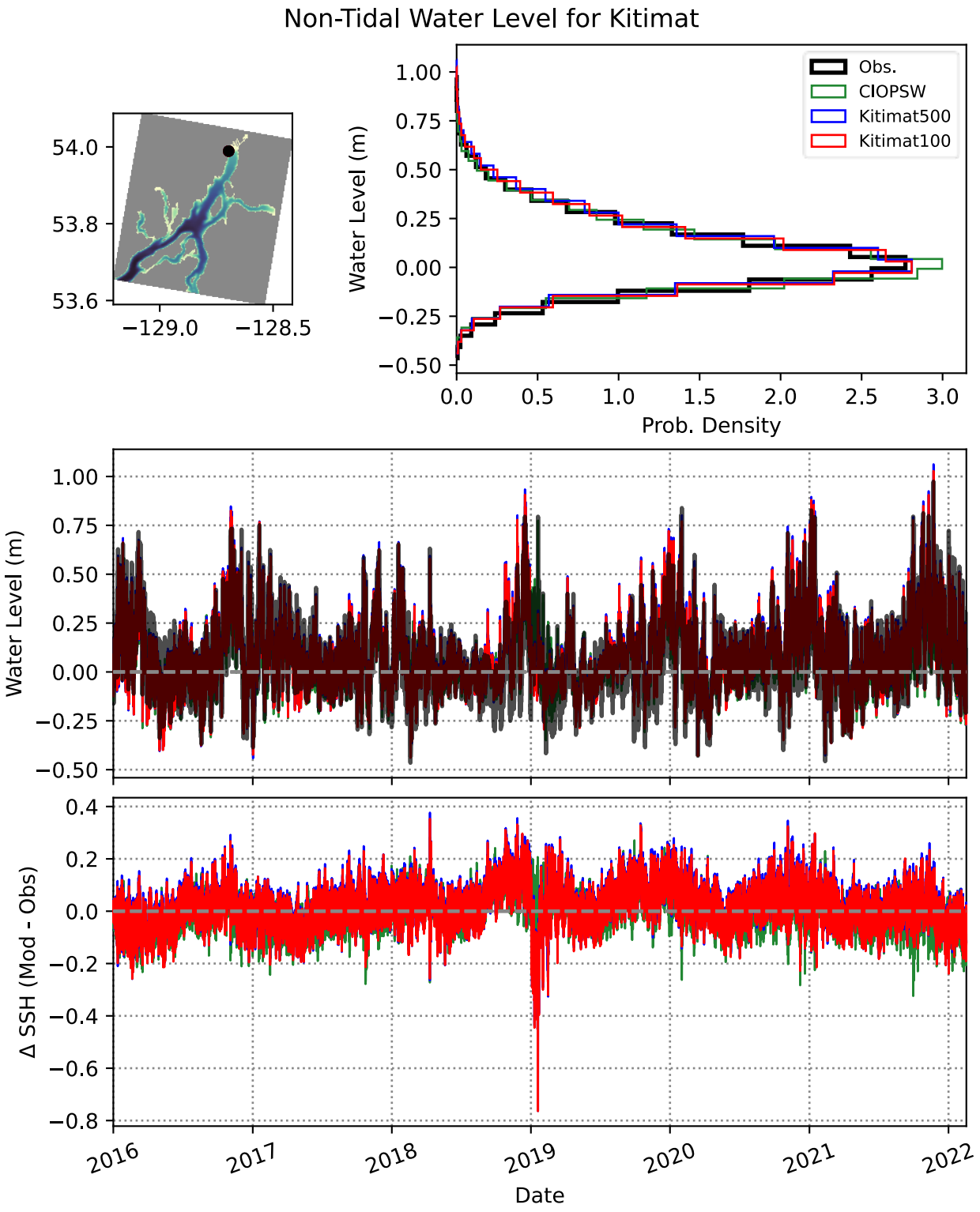

Figure 11. Comparison of non-tidal water level predictions at Kitimat between Kitimat 100 m (red), Kitimat 500 m (blue), and CIOPS-W (green).

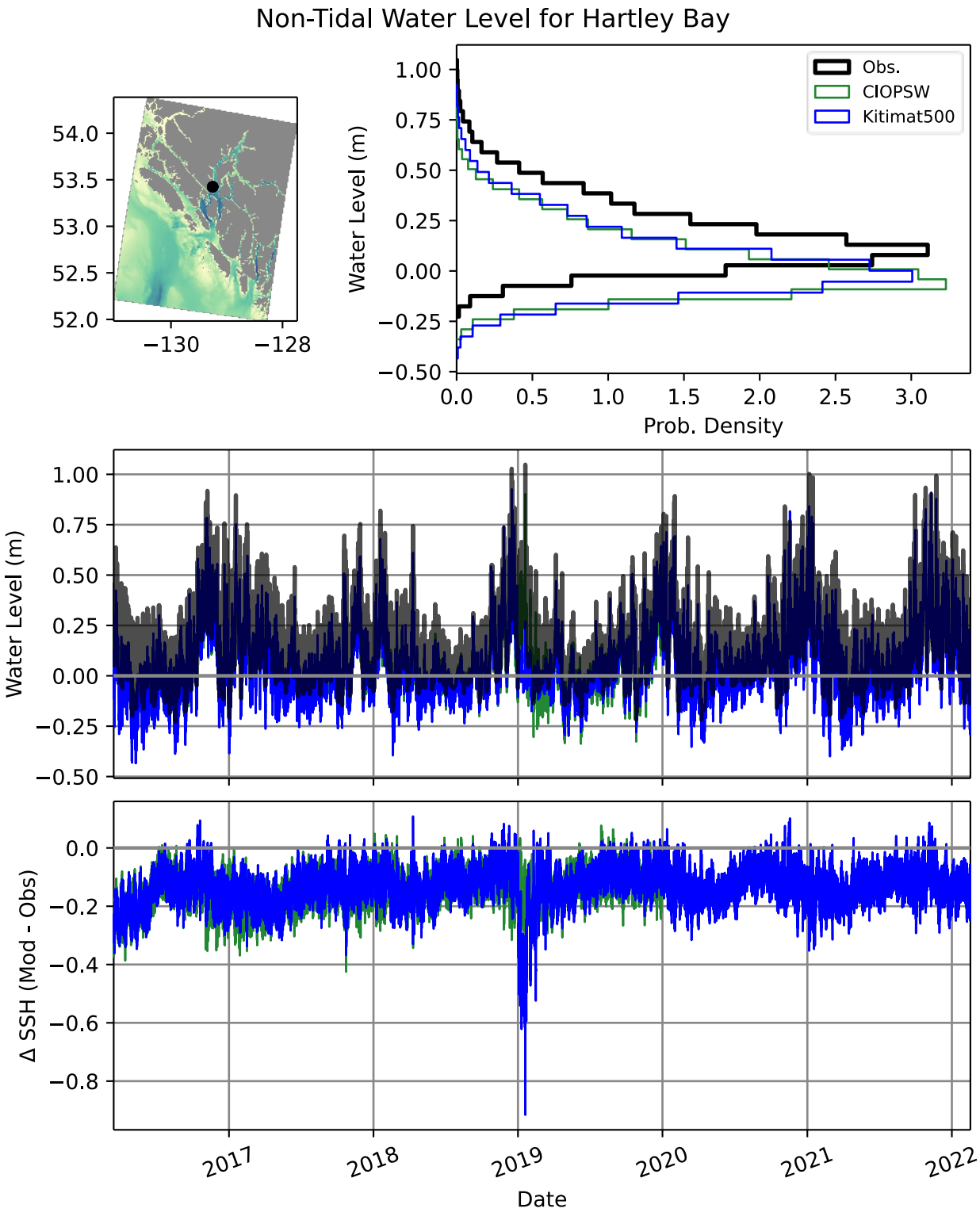

Figure 12. Comparison of non-tidal water level predictions at Hartley Bay between Kitimat 500 m (blue) and CIOPS-W (green).

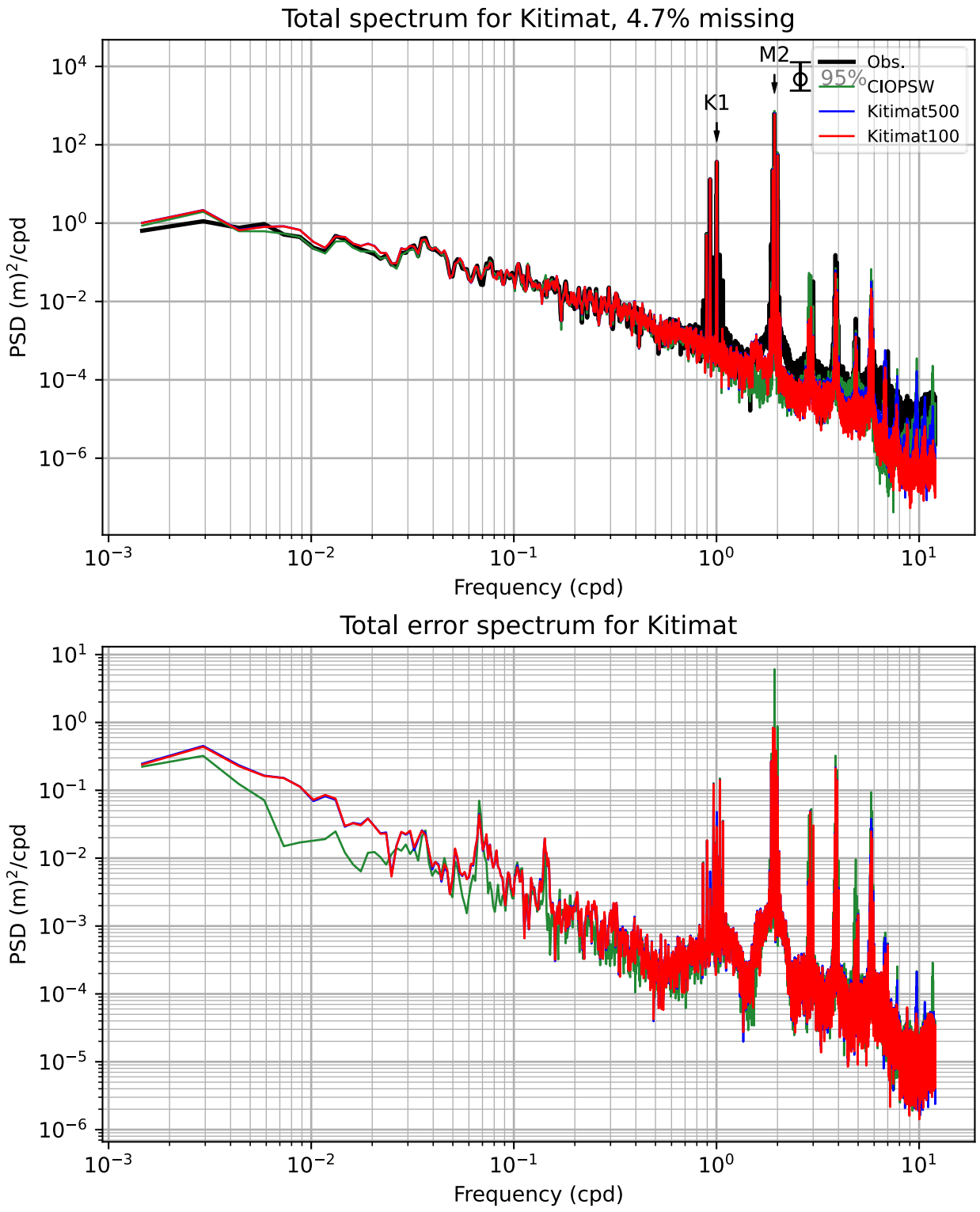

Figure 13. Power spectrum of total water level at Kitimat.

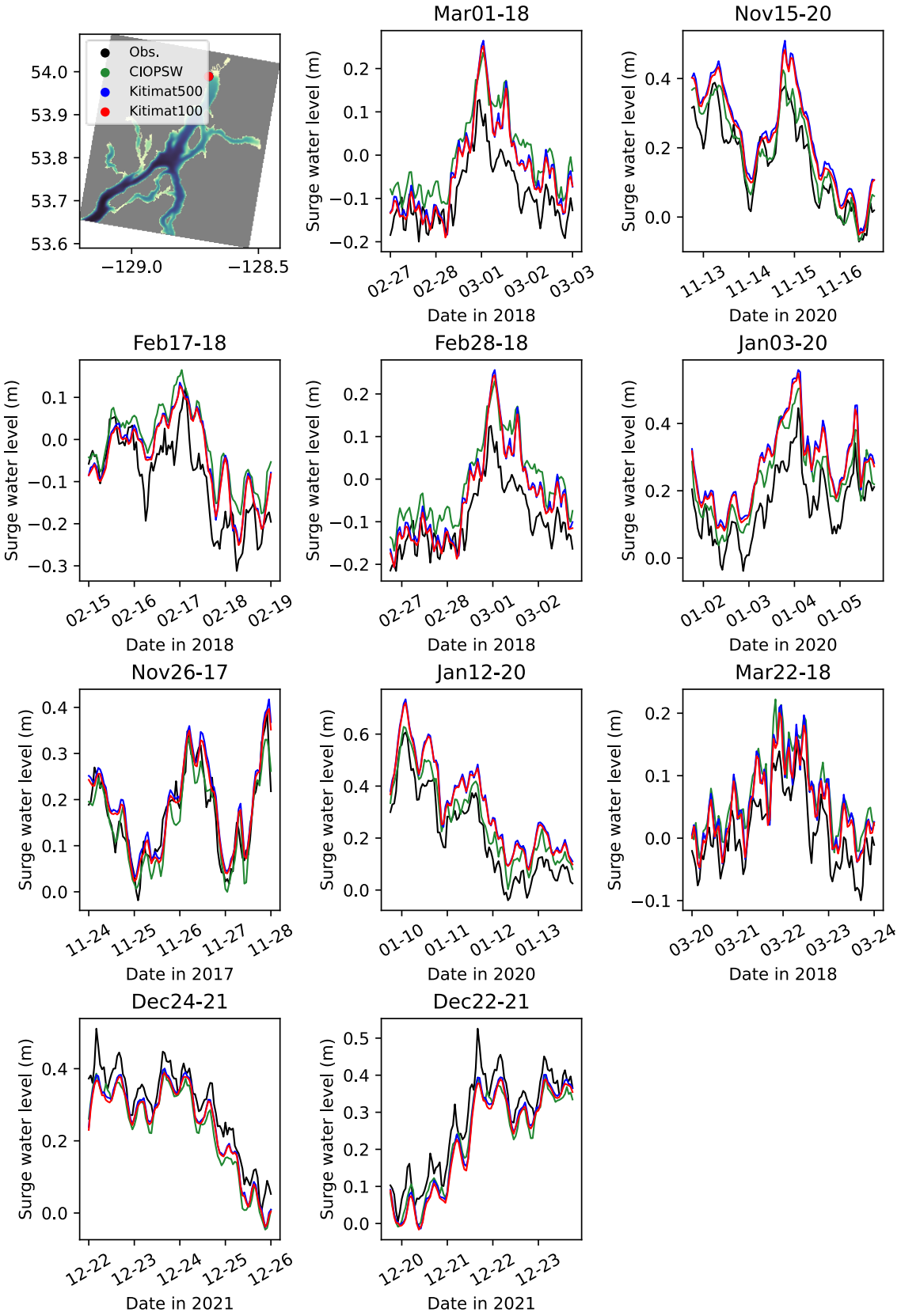

Figure 14. Water level changes at Kitimat during ten strongest storms identified during hindcast period.

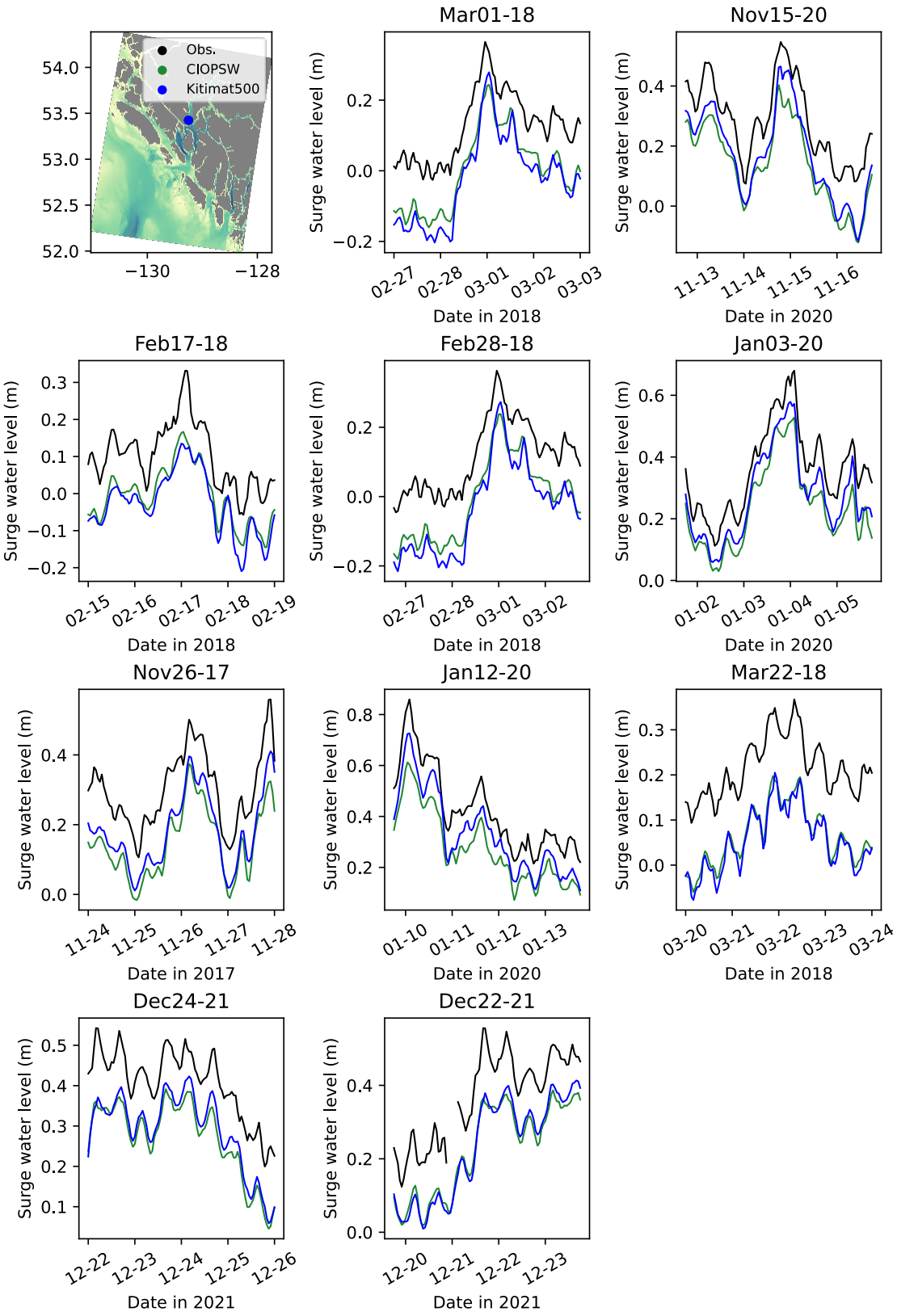

Figure 15. Water level changes at Hartley Bay during ten strongest storms identified during hindcast period.

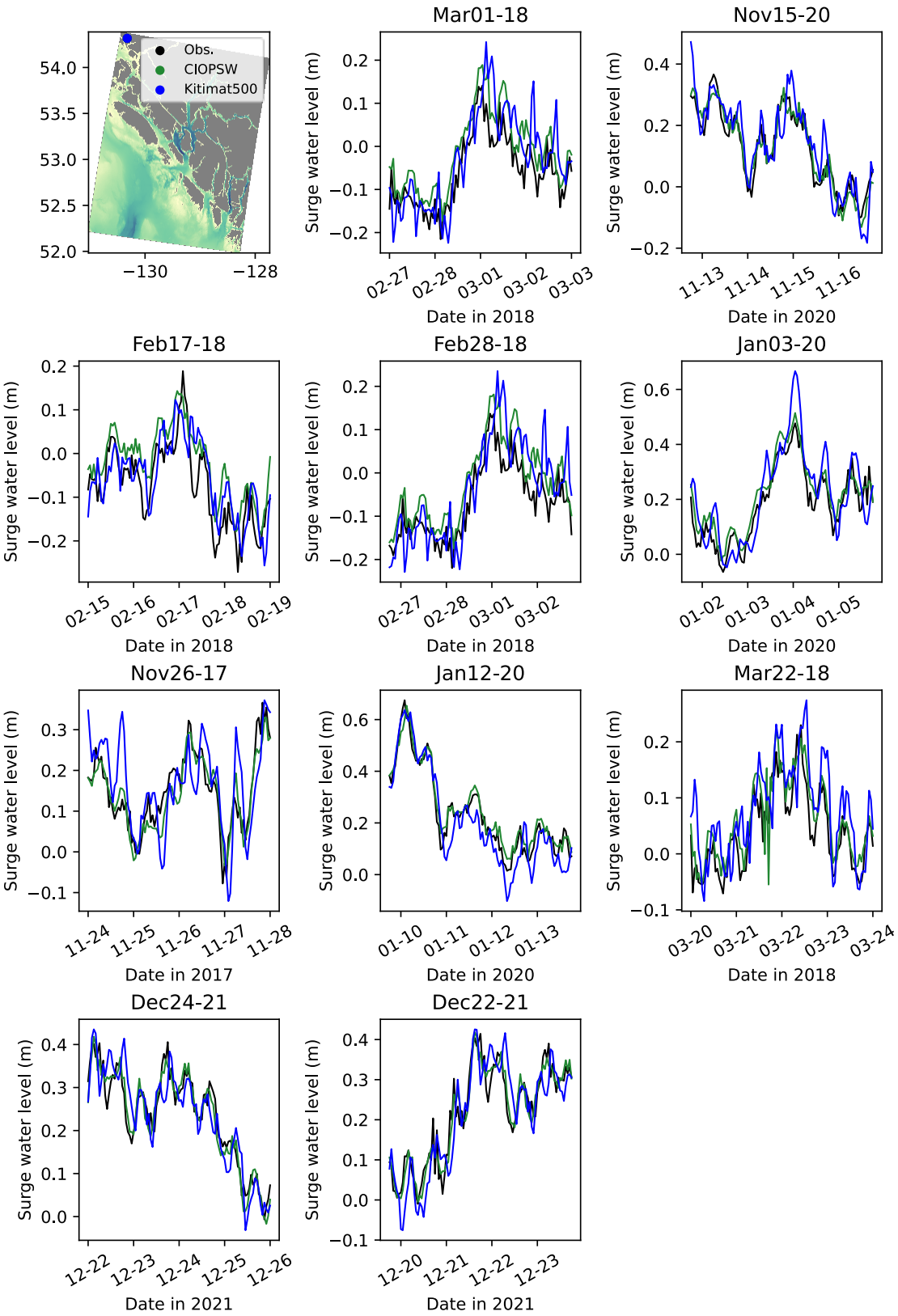

Figure 16. Water level changes at Prince Rupert during ten strongest storms identified during hindcast period.

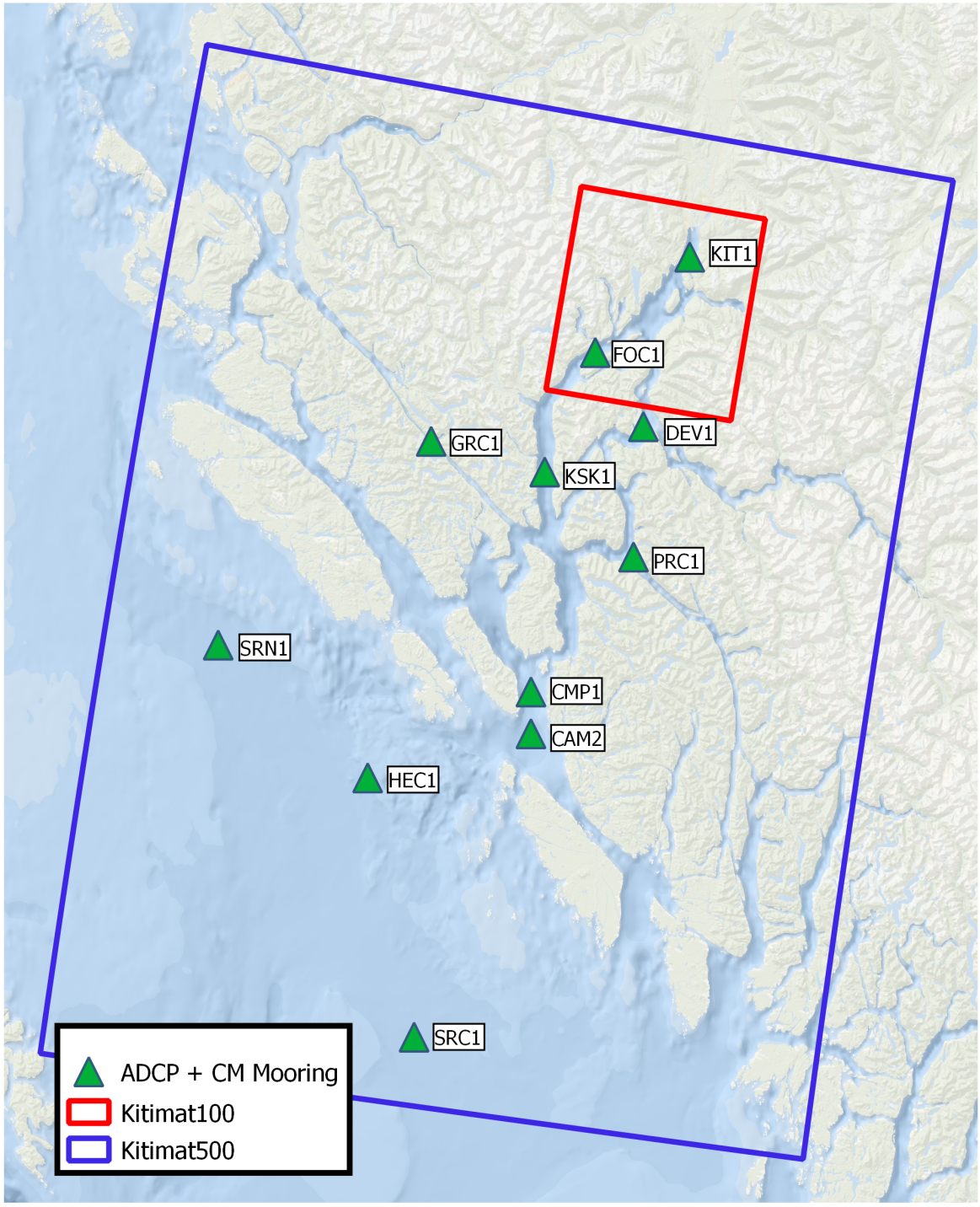

Figure 17. Key plot showing locations of moored current meters and ADCPs in the port model domain during the hindcast period.

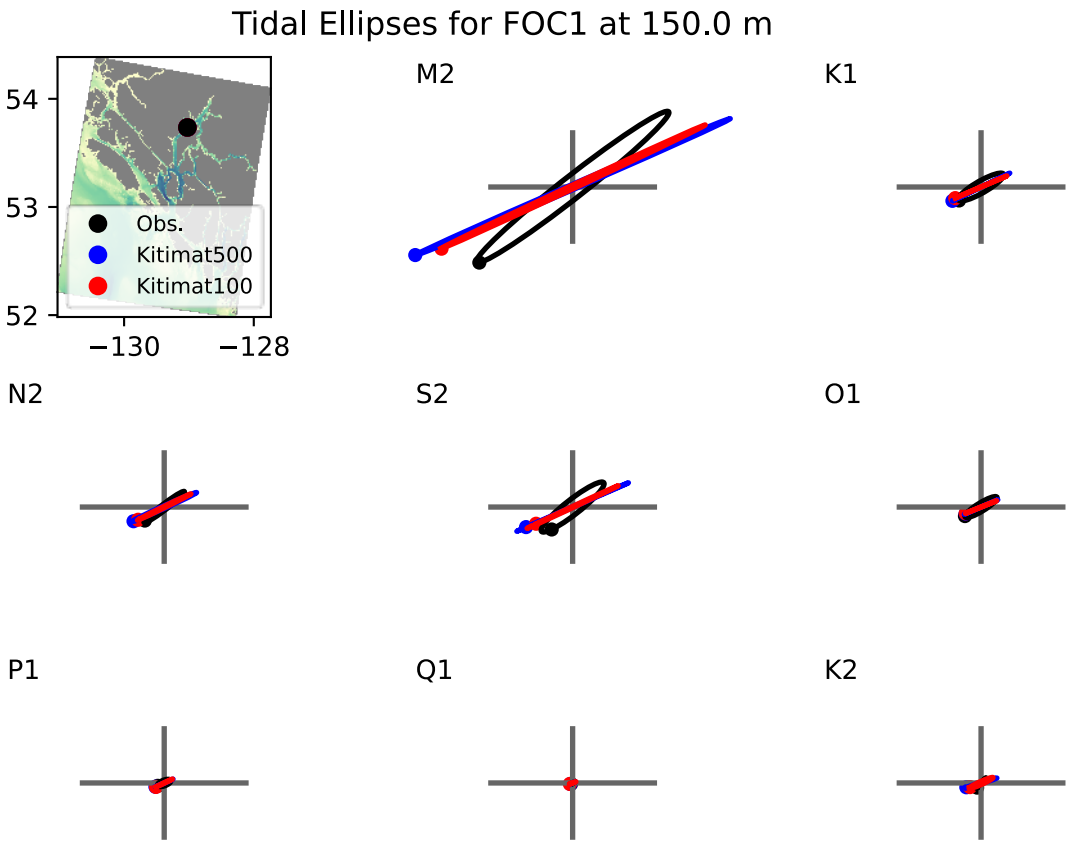

Figure 18. Station FOC1, upper Douglas Channel: Comparison of tidal ellipses between observations from a current meter at 150 m depth (black), and the Kitimat 100 m (red) and 500 m (blue) configurations.

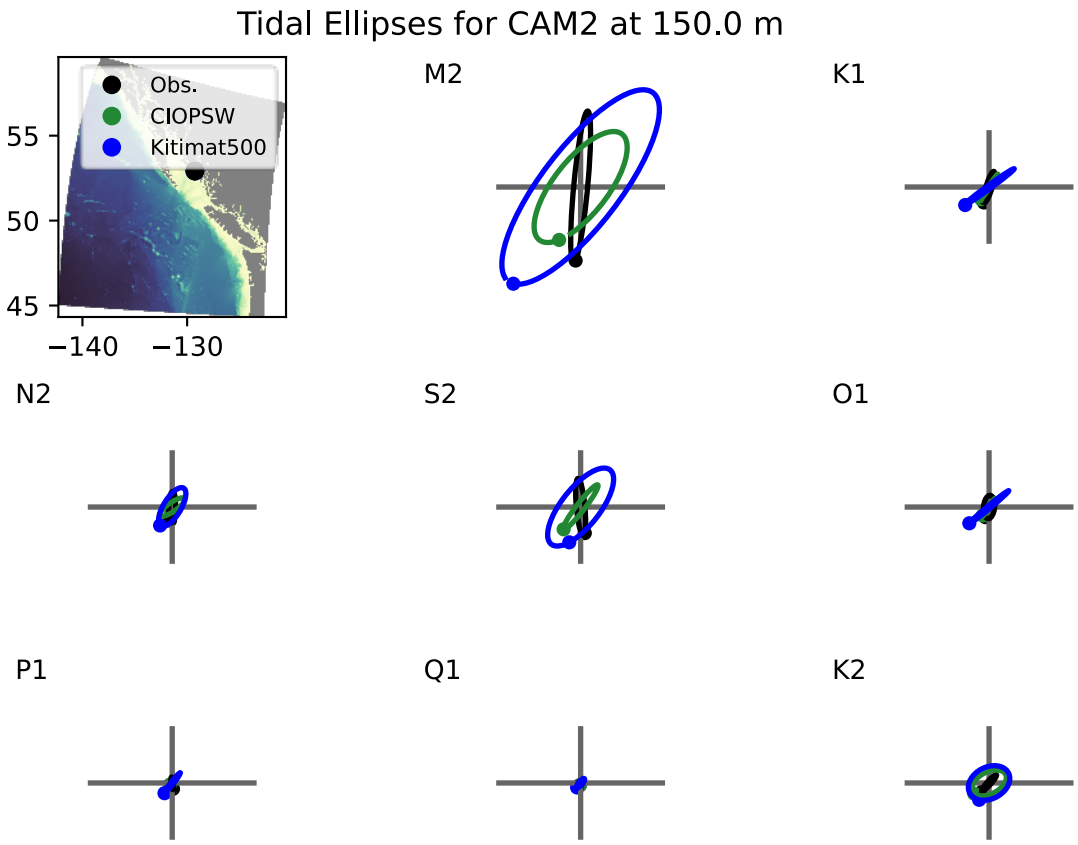

Figure 19. Station CAM2, Caamaño Sound: Comparison of tidal ellipses between observations from a current meter at 150 m depth (black), CIOPS-W (green), and the Kitimat 500 m configuration (blue).

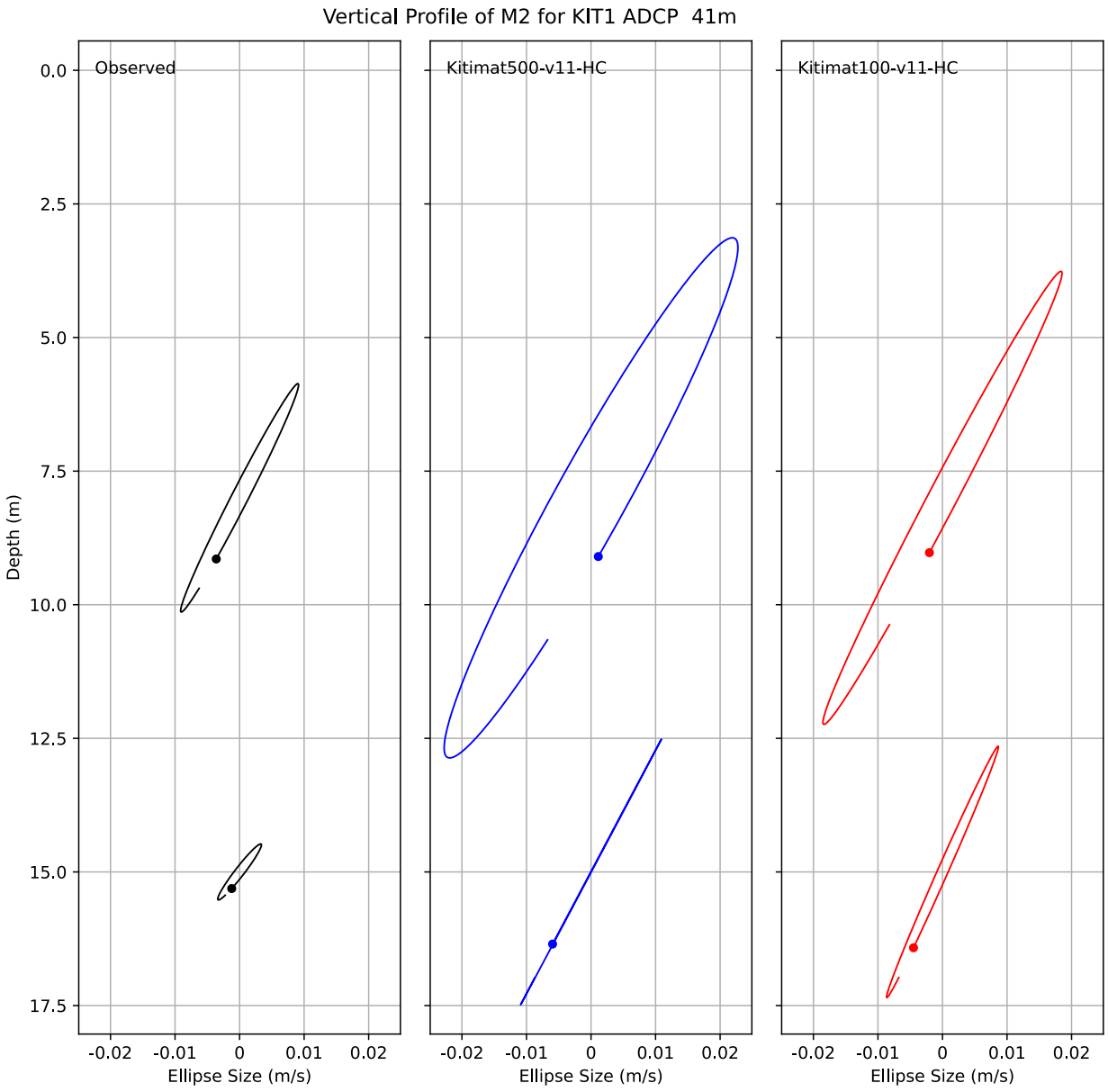

Figure 20. Comparison of M2 tidal ellipses based on data from an ADCP moored at 41 m depth at station KIT1 between July 2020 and July 2021, and results from the 100 m and 500 m port model domains over this period.

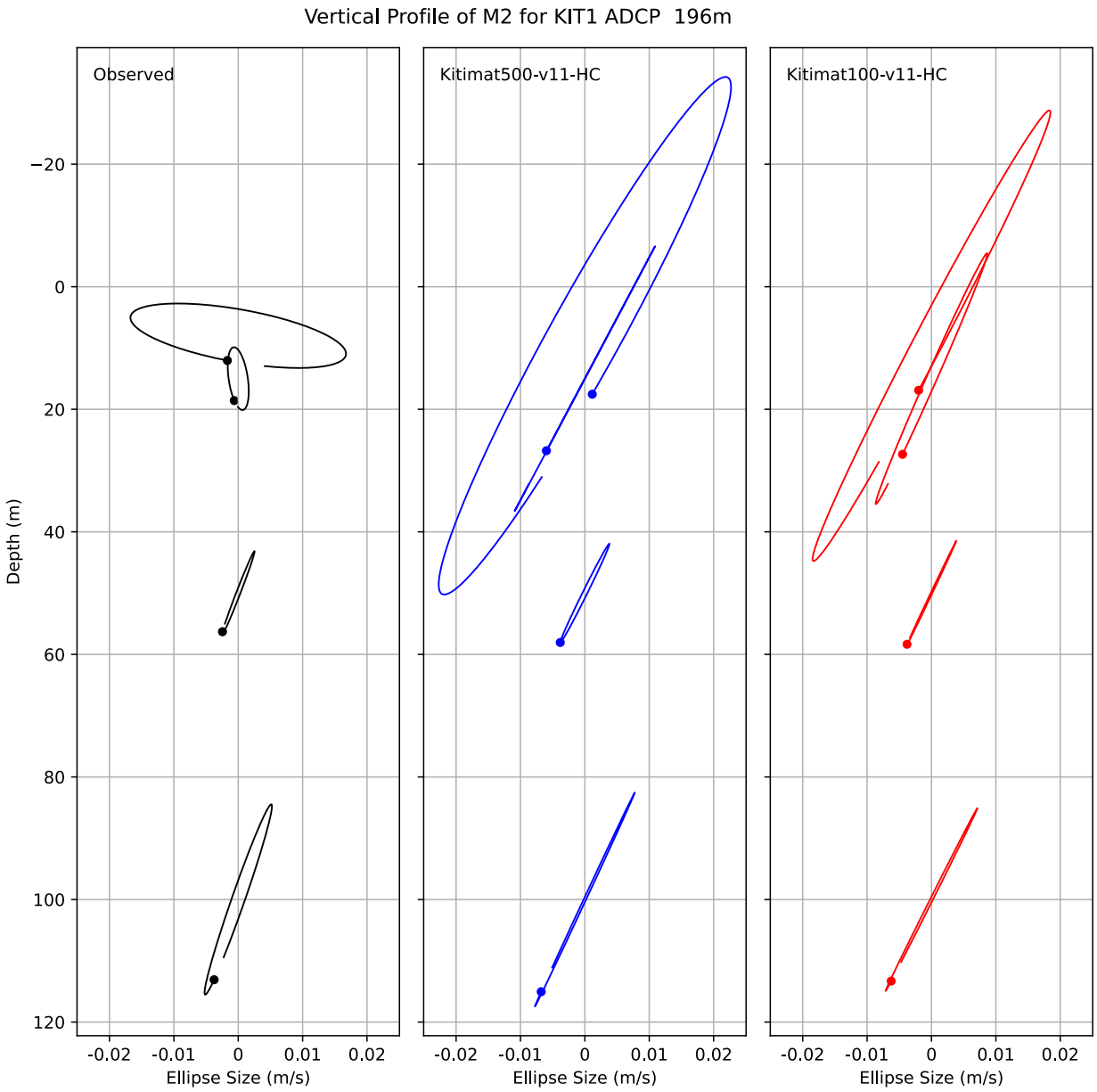

Figure 21. Comparison of M2 tidal ellipses based on data from an ADCP moored at 196 m depth at station KIT1 between July 2020 and July 2021, and results from the 100 m and 500 m port model domains over this period.

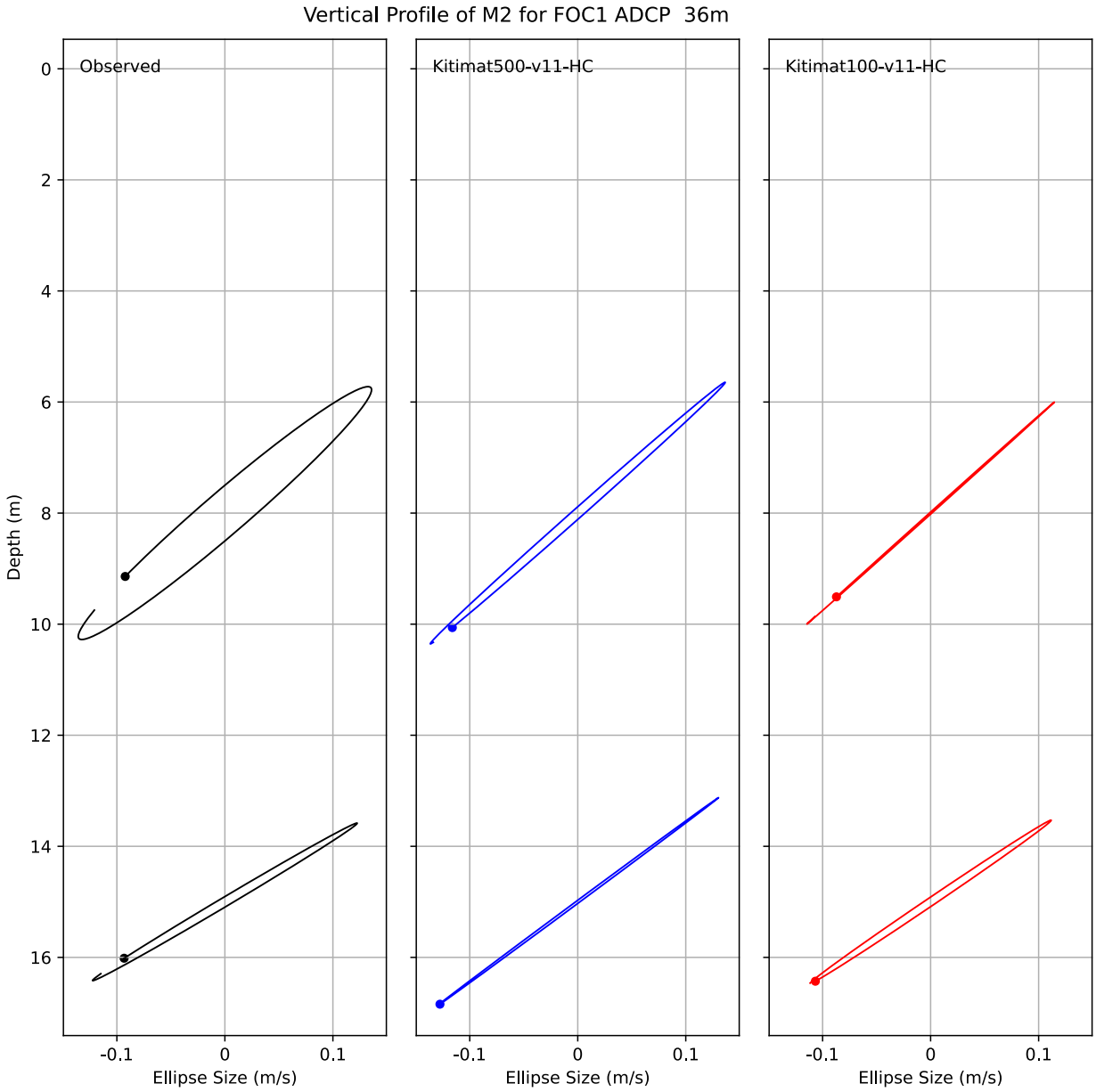

Figure 22. Comparison of M2 tidal ellipses based on data from an ADCP moored at 36 m depth at station FOC1 between July 2020 and July 2021, and results from the 100 m and 500 m port model domains over this period.

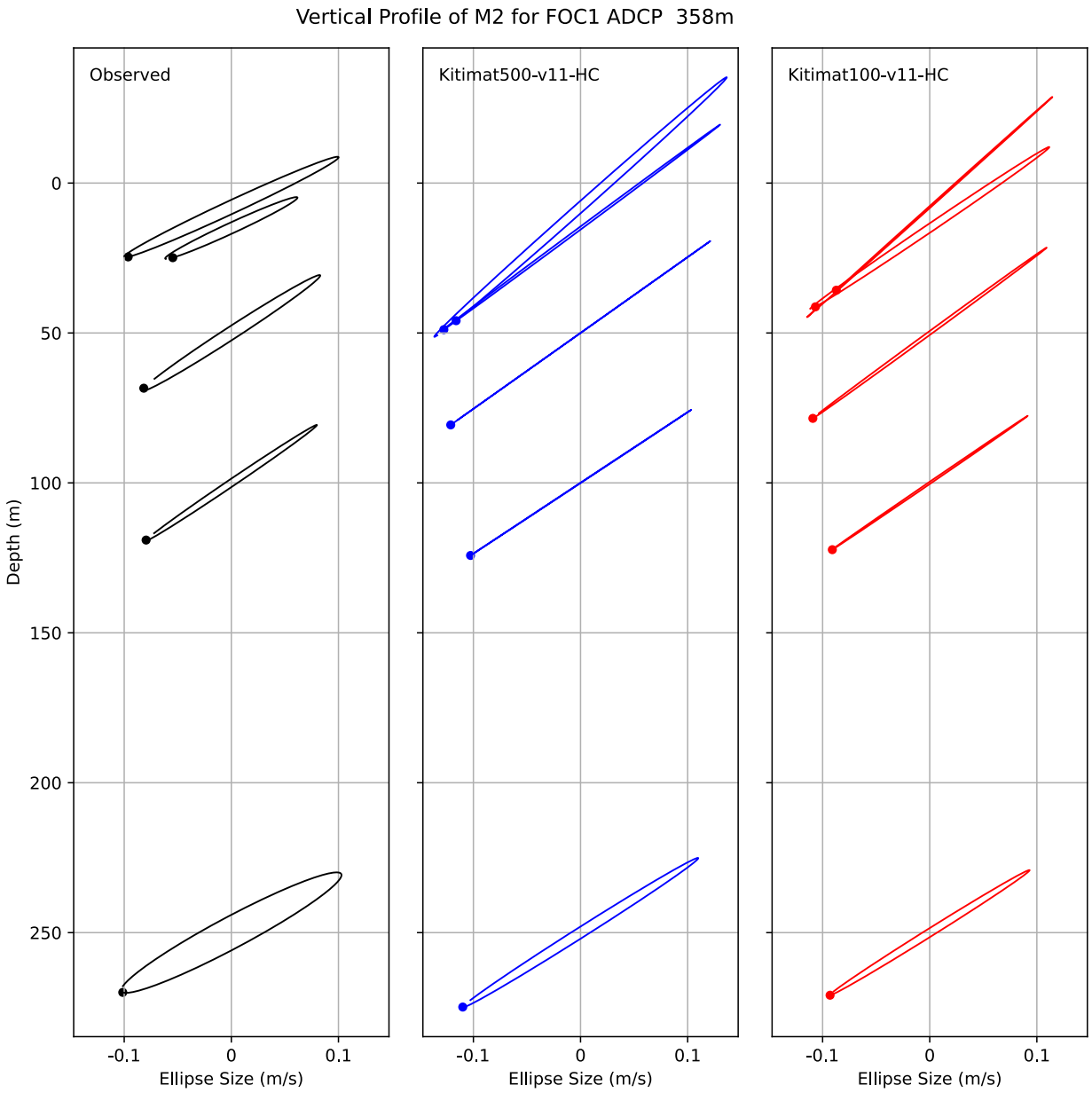

Figure 23. Comparison of M2 tidal ellipses based on data from an ADCP moored at 358 m depth at station FOC1 between July 2020 and July 2021, and results from the 100 m and 500 m port model domains over this period.

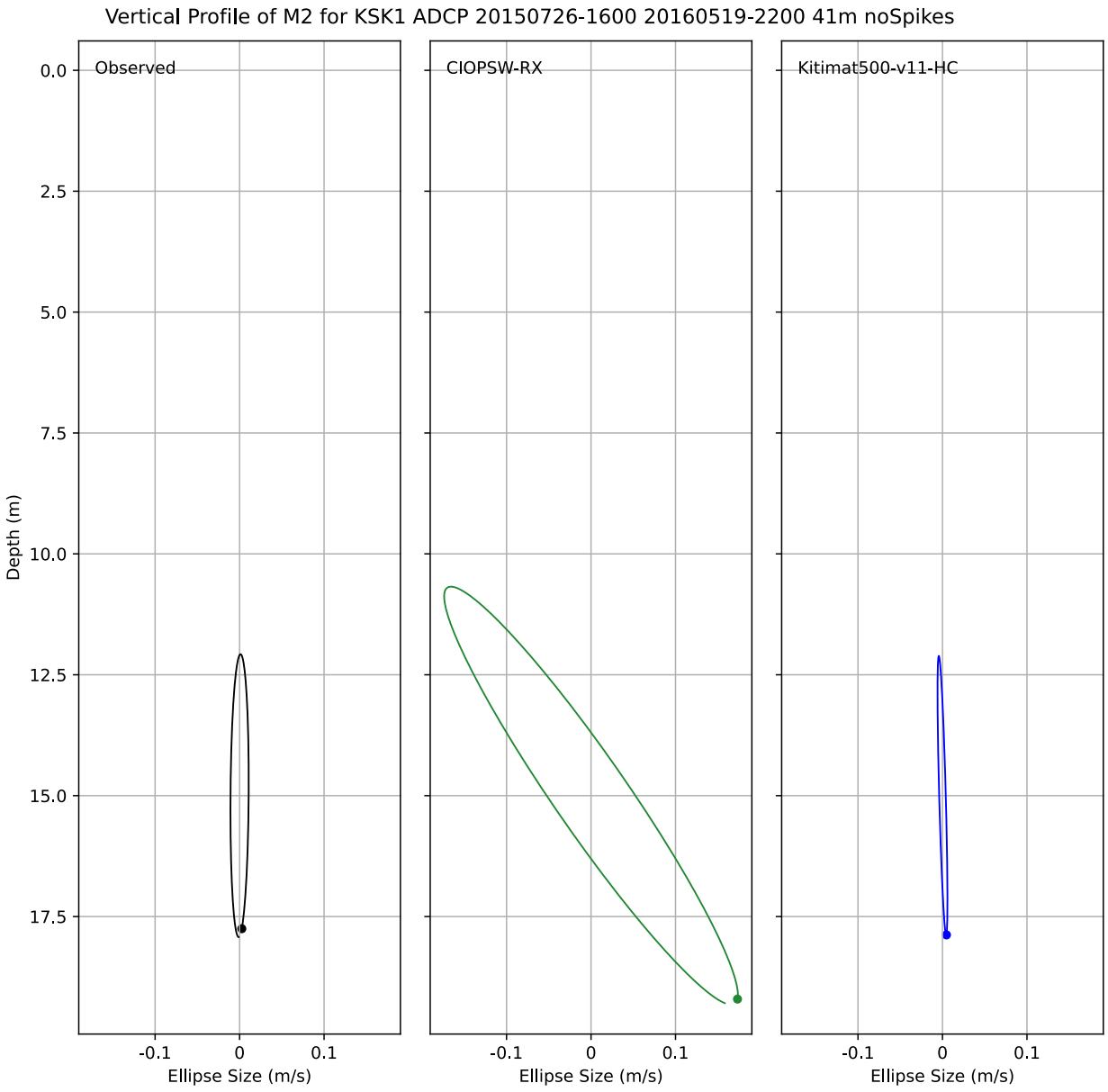

Figure 24. Comparison of M2 tidal ellipses based on data from an ADCP moored at 41 m depth at station KSK1 between January and July 2016, and results from the 500 m port model and CIOPS-W over this period.

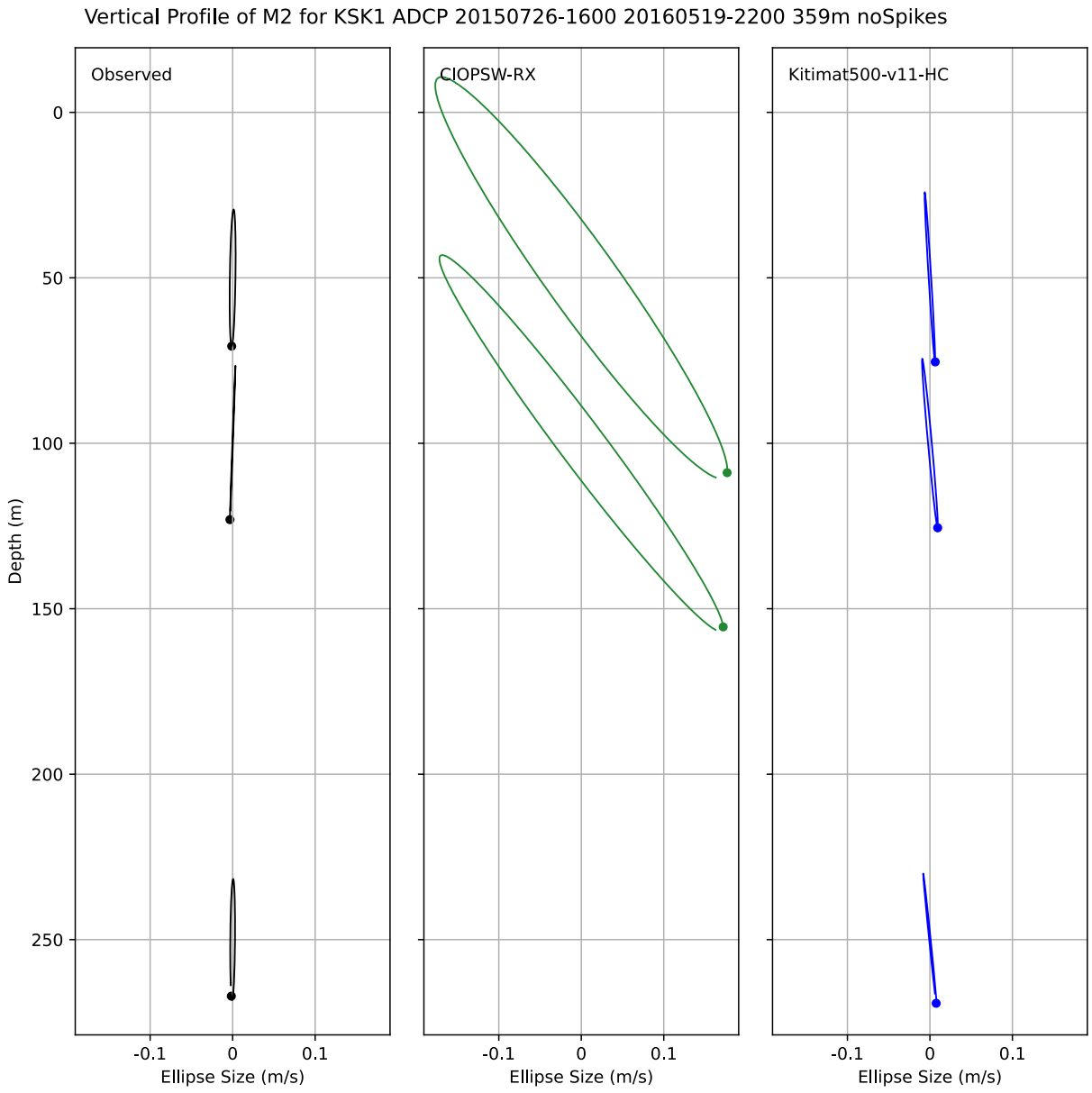

Figure 25. Comparison of M2 tidal ellipses based on data from an ADCP moored at 359 m depth at station KSK1 between January and July 2016, and results from the 500 m port model and CIOPS-W over this period.

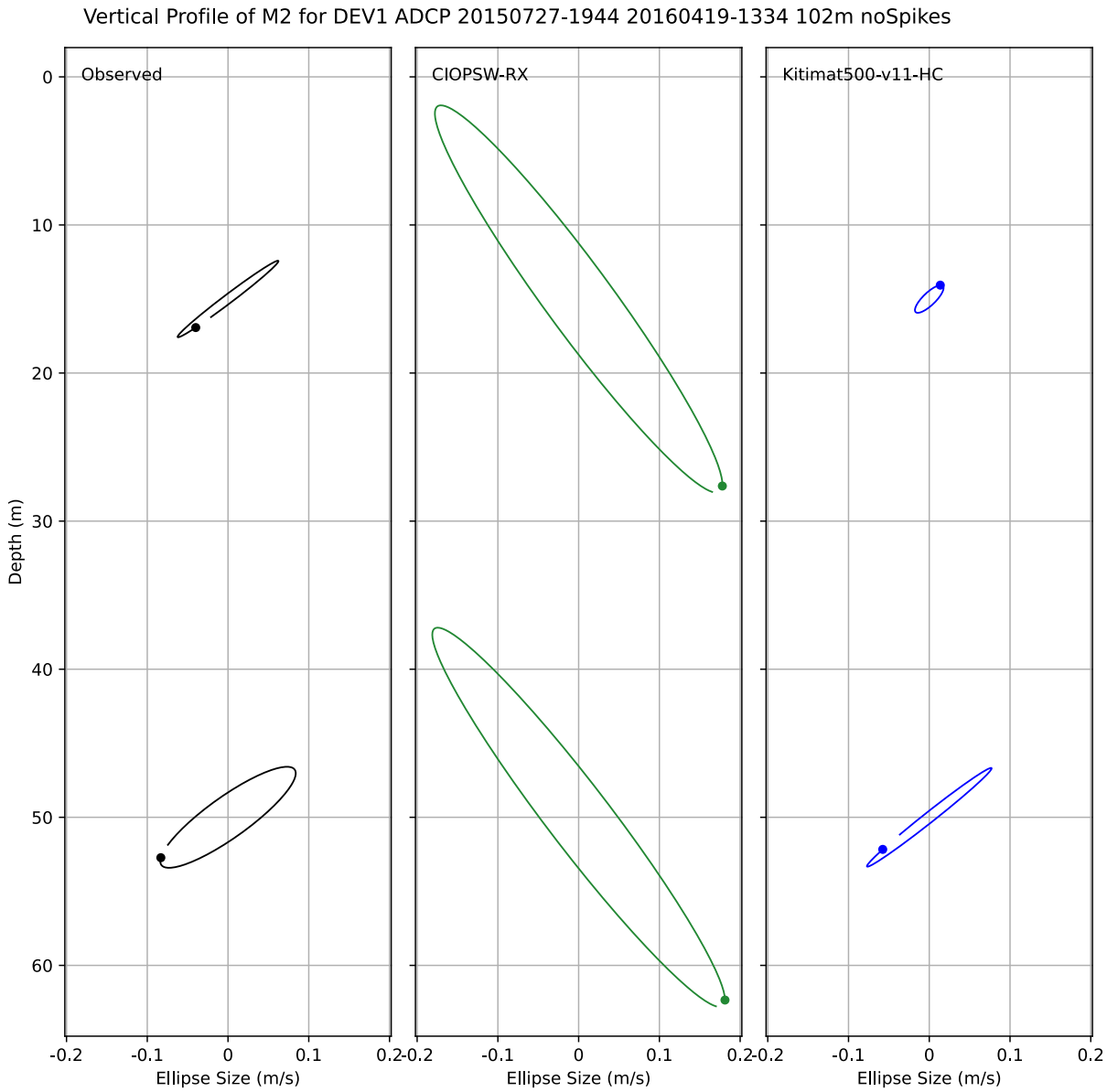

Figure 26. Comparison of M2 tidal ellipses based on data from an ADCP moored at 102 m depth at station DEV1 between January and July 2016, and results from the 500 m port model and CIOPS-W over this period.

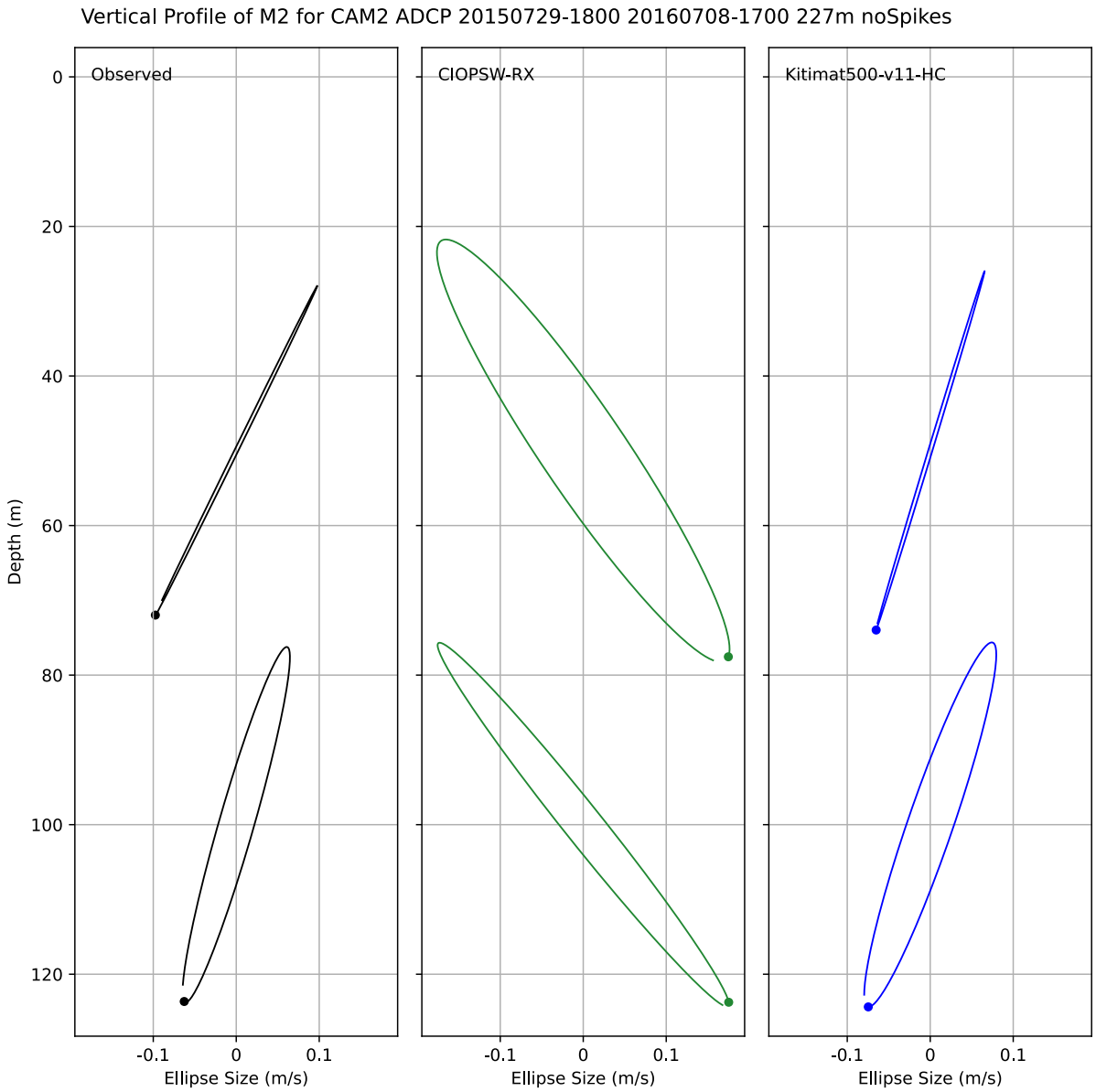

Figure 27. Comparison of M2 tidal ellipses based on data from an ADCP moored at 227 m depth at station CAM2 between January and July 2016, and results from the 500 m port model and CIOPS-W over this period.

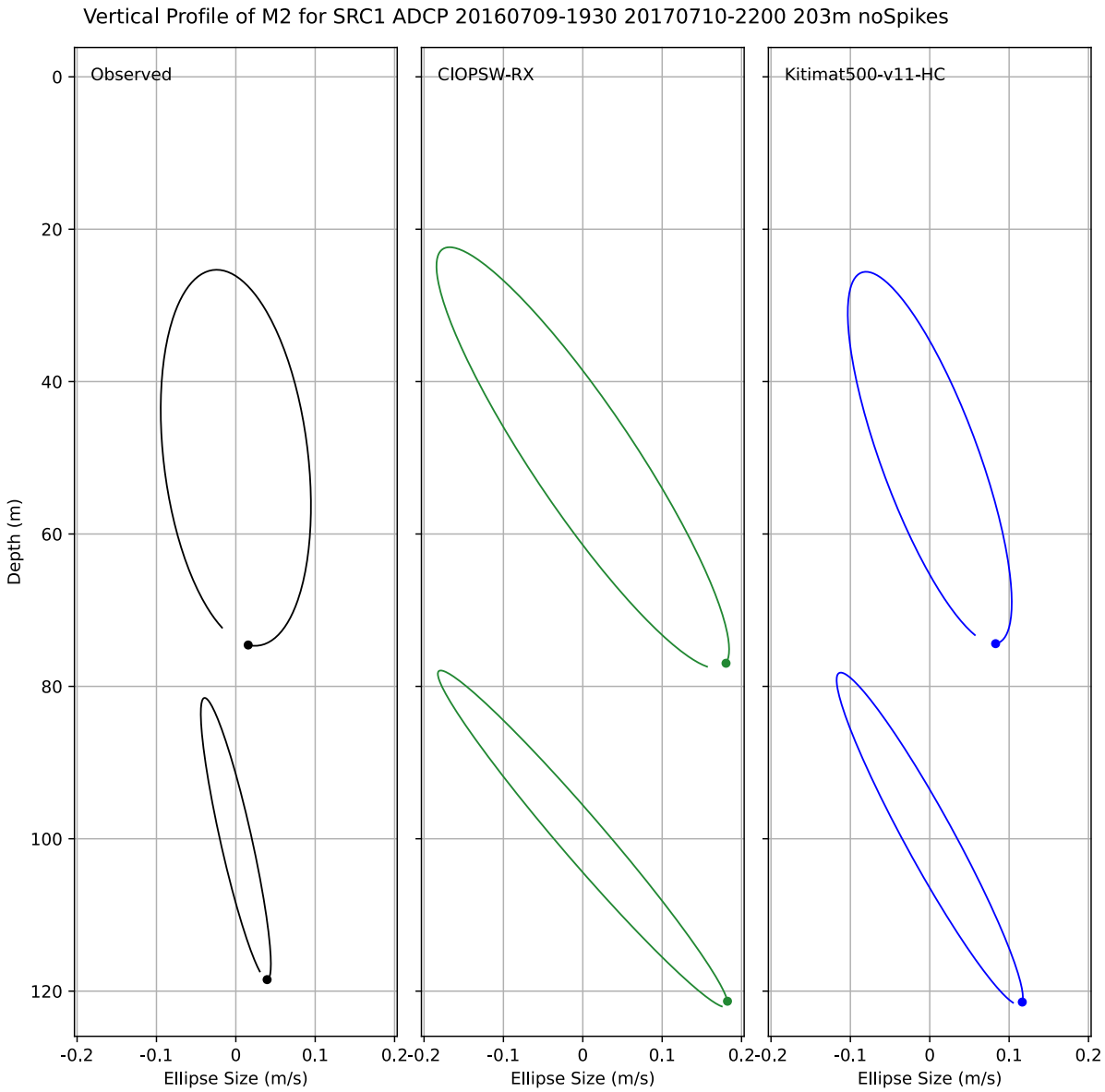

Figure 28. Comparison of M2 tidal ellipses based on data from an ADCP moored at 203 m depth at station SRC1 between July 2016 and July 2017, and results from the 500m port model and CIOPS-W over this period.

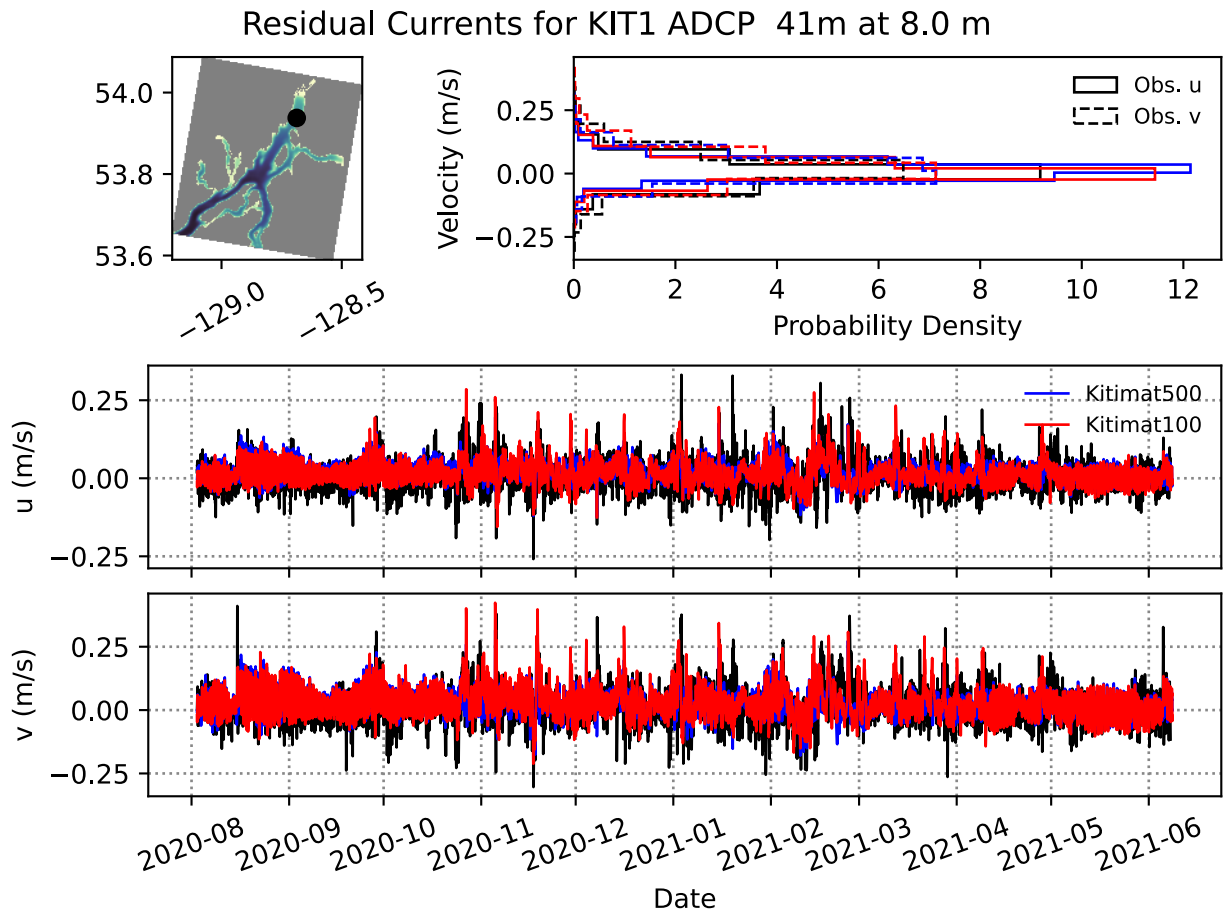

Figure 29. Comparison of currents at 8 m below surface between observations from ADCP (41 m depth) at station KIT1 (Kitimat Arm) and Kitimat port model configurations.

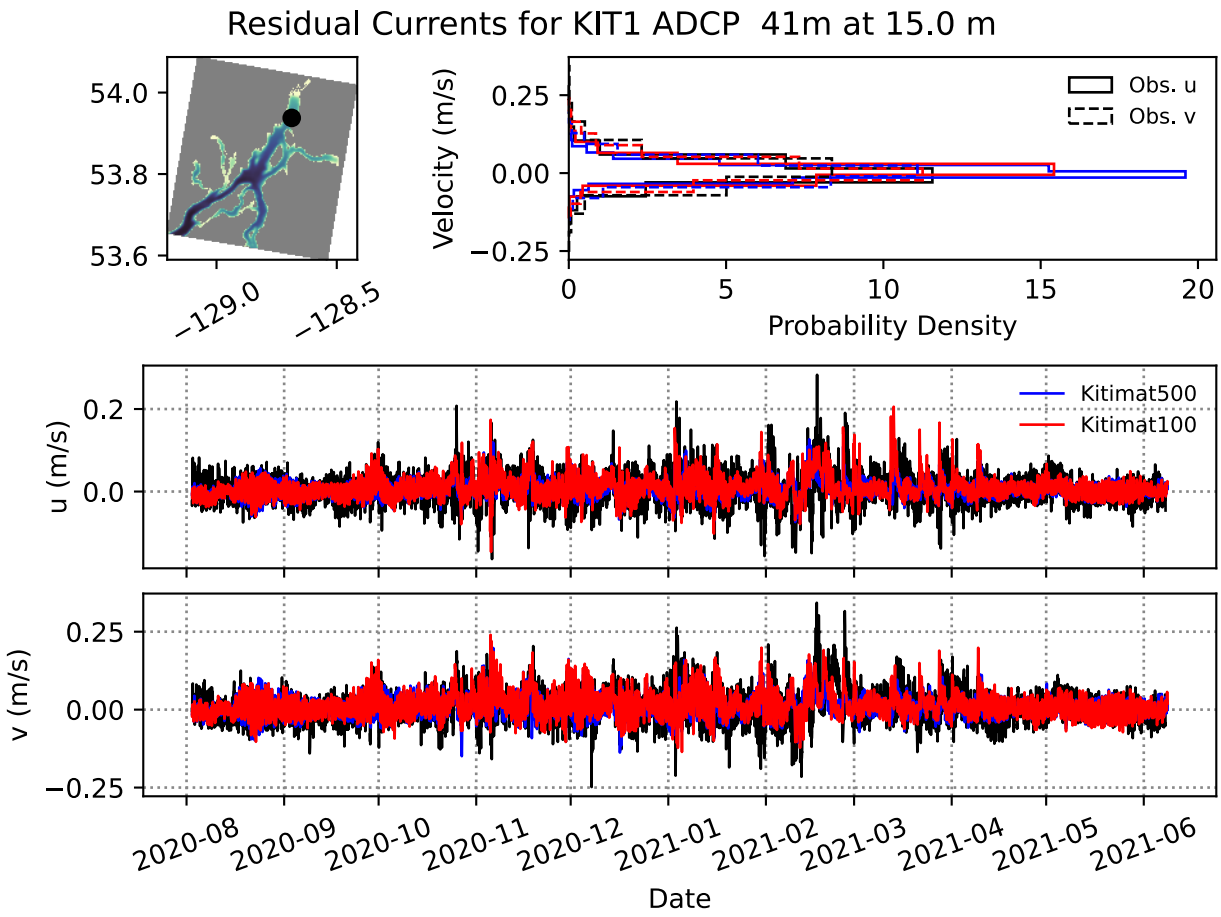

Figure 30. Comparison of currents at 15 m below surface between observations from ADCP (41 m depth) at station KIT1 (Kitimat Arm) and Kitimat port model configurations.

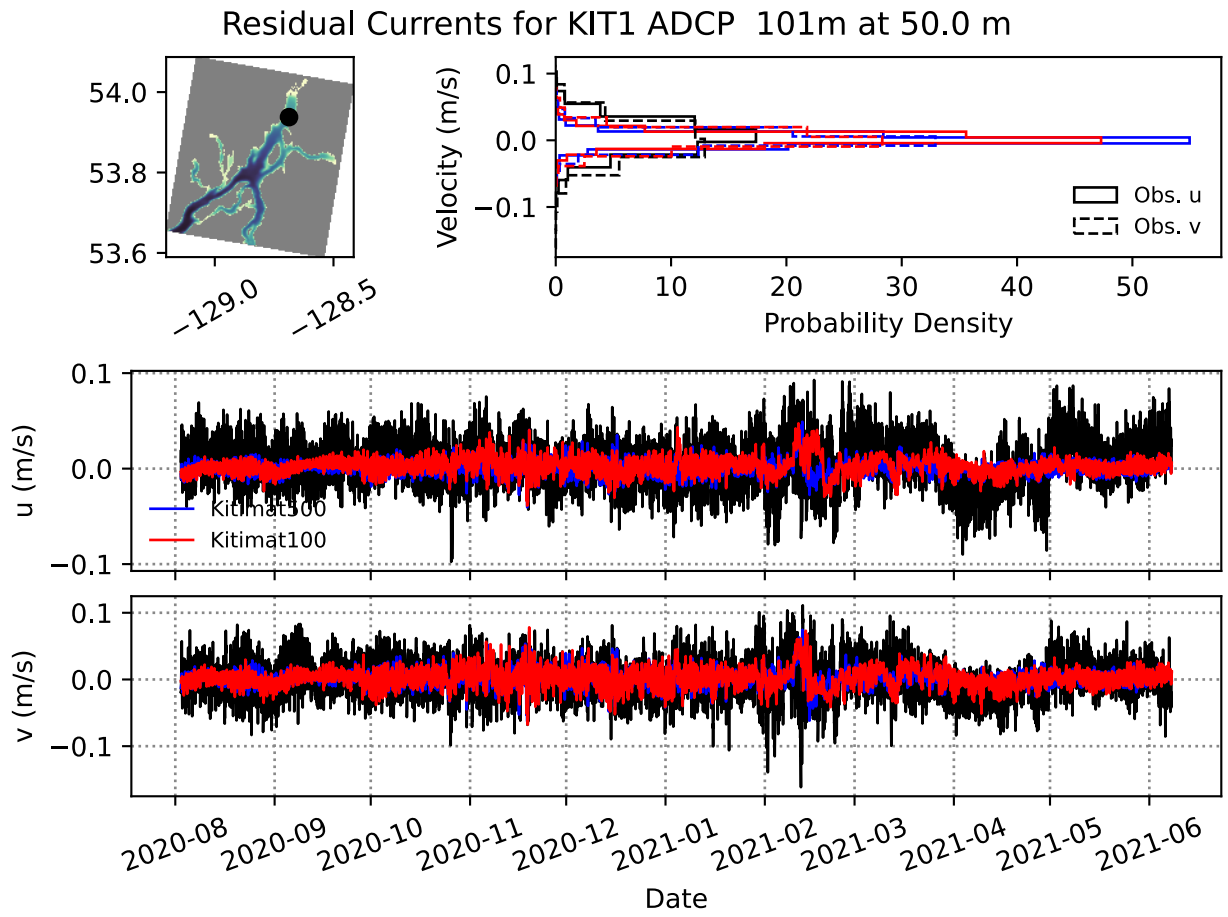

Figure 31. Comparison of currents at 50 m below surface between observations from ADCP (101 m depth) at station KIT1 (Kitimat Arm) and Kitimat port model configurations.

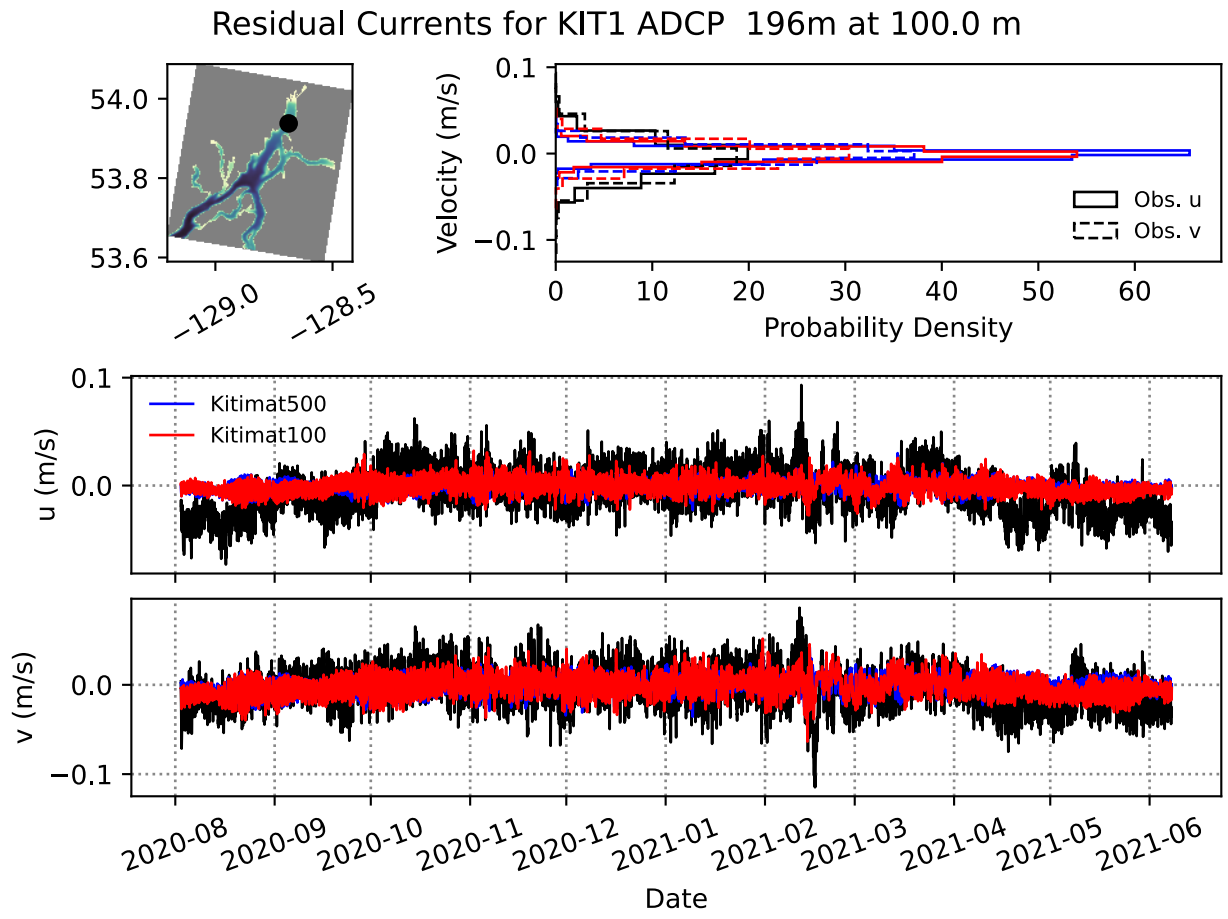

Figure 32. Comparison of currents at 100 m below surface between observations from ADCP (196 m depth) at station KIT1 (Kitimat Arm) and Kitimat port model configurations.

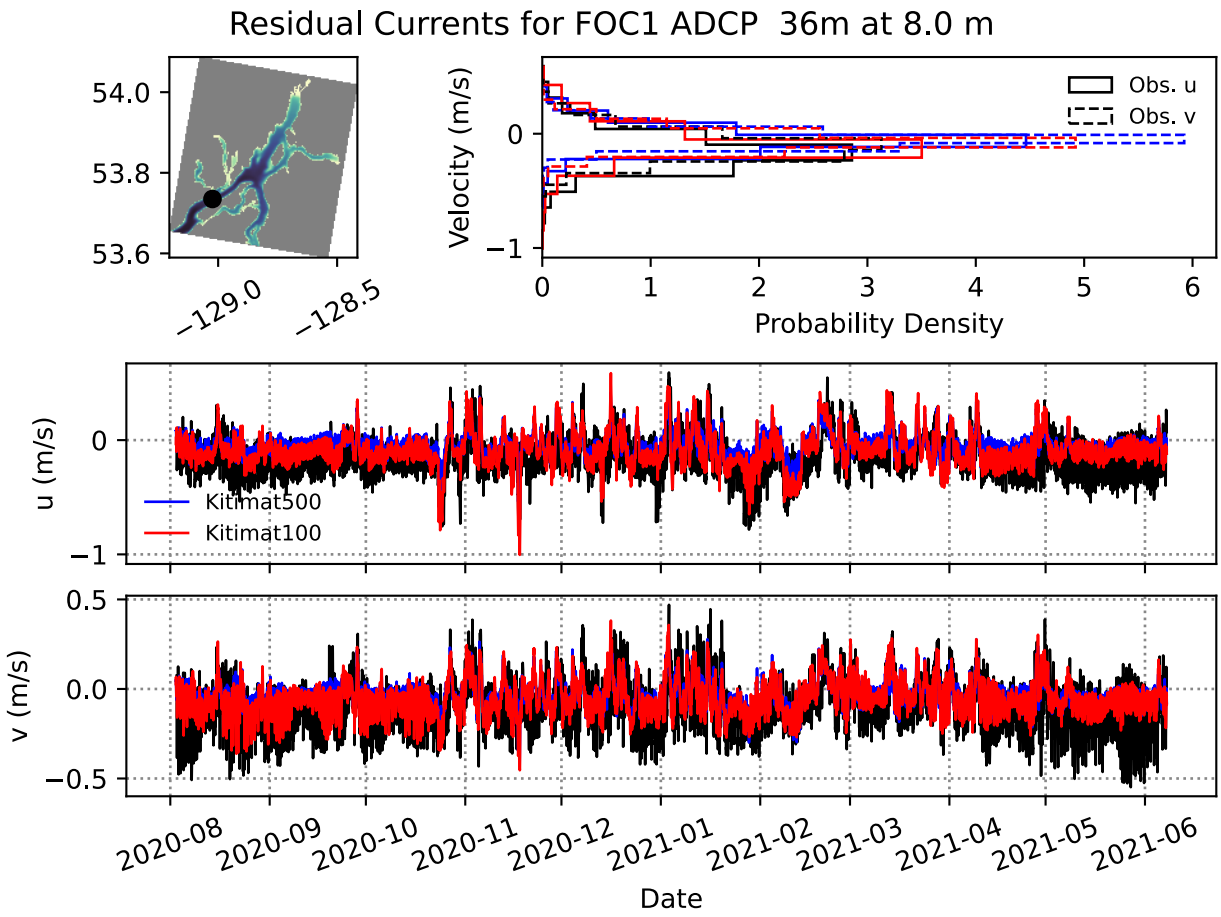

Figure 33. Comparison of currents at 8 m below surface between observations from ADCP (36 m depth) at station FOC1 (upper Douglas Channel) and Kitimat port model configurations.

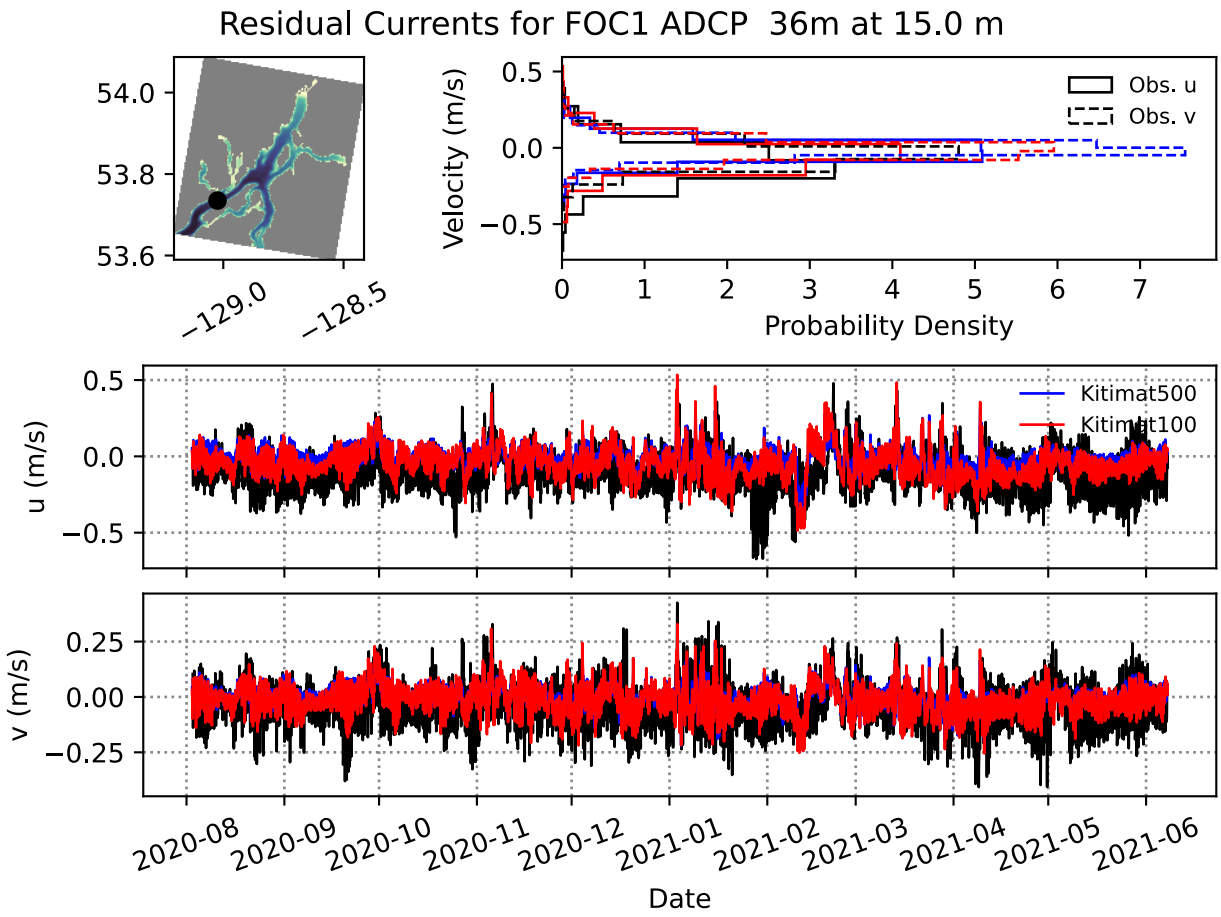

Figure 34. Comparison of currents at 15 m below surface between observations from ADCP (36 m depth) at station FOC1 (upper Douglas Channel) and Kitimat port model configurations.

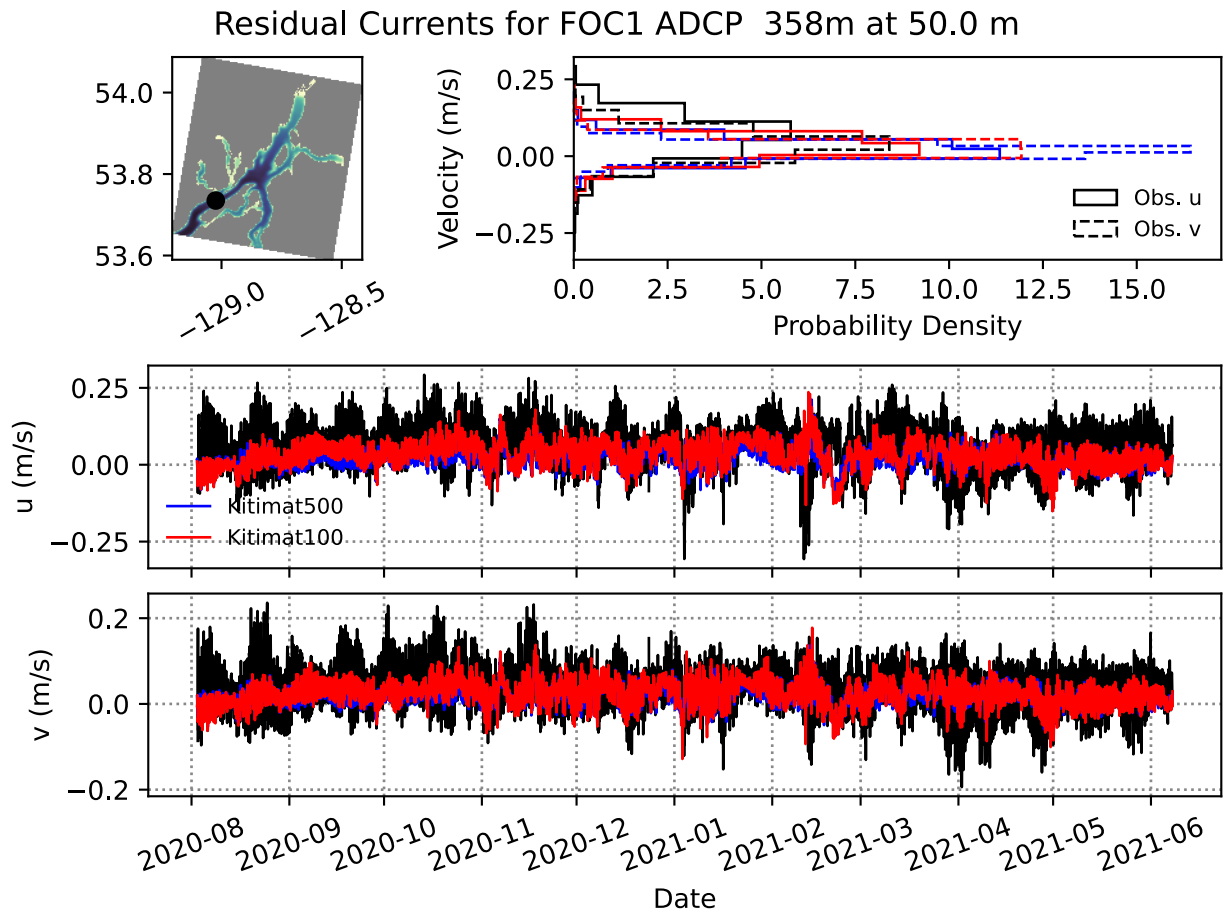

Figure 35. Comparison of currents at 50 m below surface between observations from ADCP (358 m depth) at station FOC1 (upper Douglas Channel) and Kitimat port model configurations.

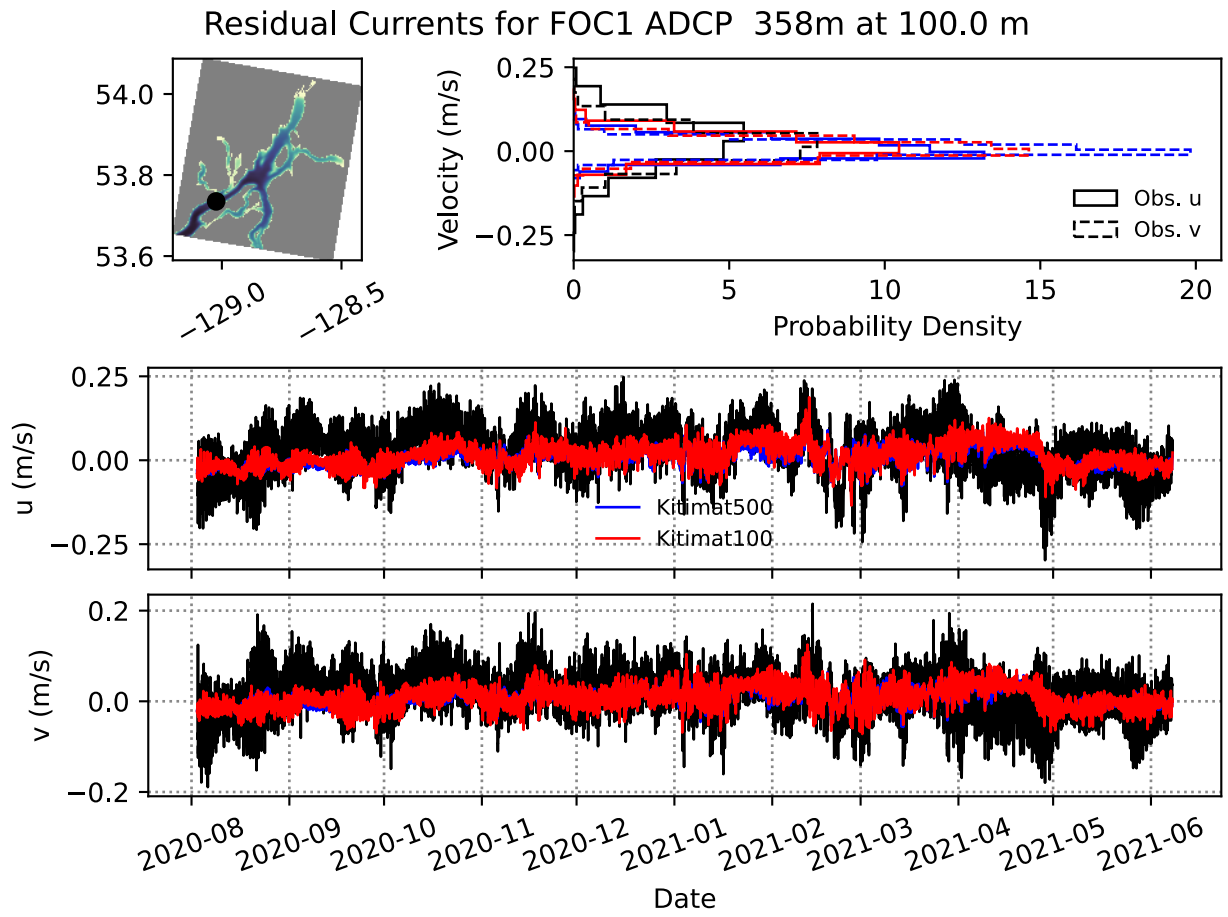

Figure 36. Comparison of currents at 100 m below surface between observations from ADCP (358 m depth) at station FOC1 (upper Douglas Channel) and Kitimat port model configurations.

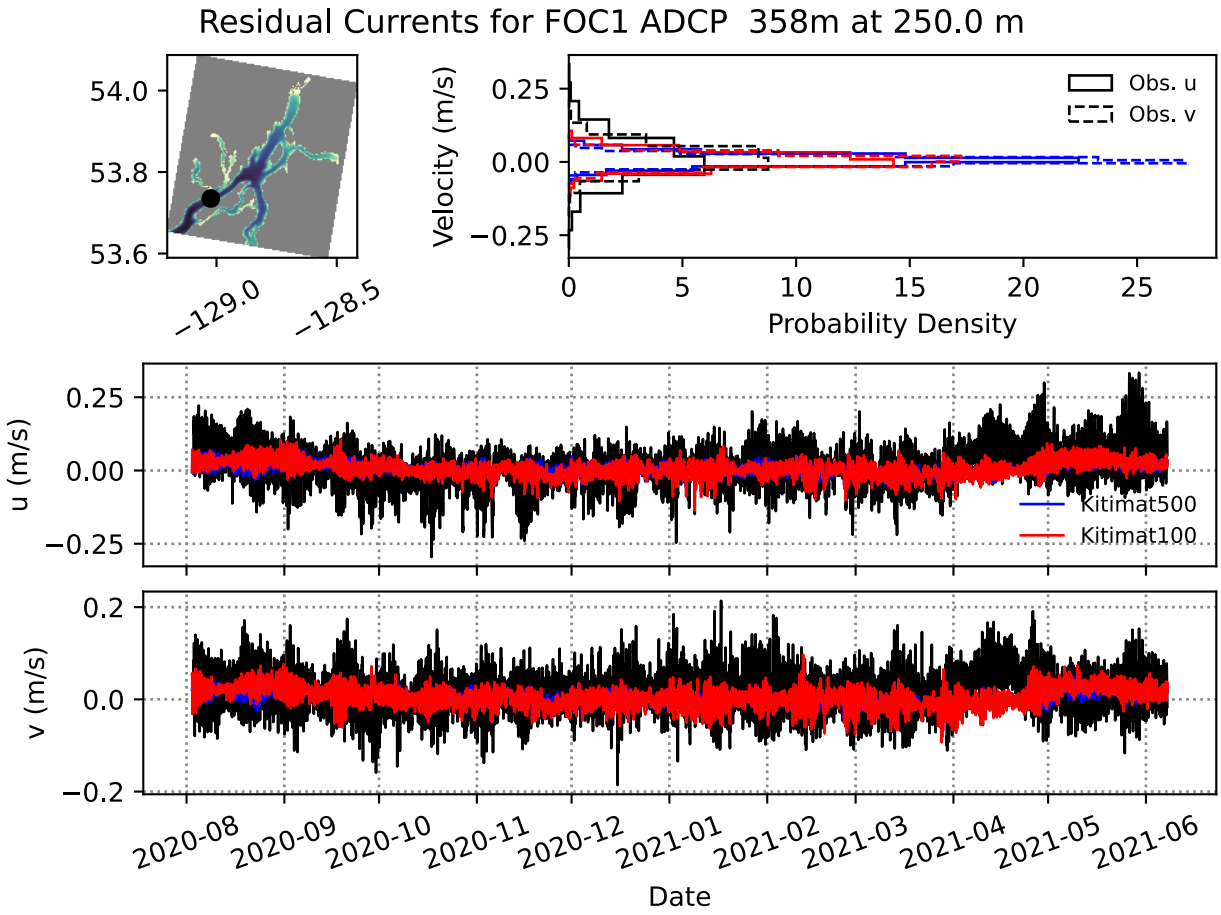

Figure 37. Comparison of currents at 250 m below surface between observations from ADCP (358 m depth) at station FOC1 (upper Douglas Channel) and Kitimat port model configurations.

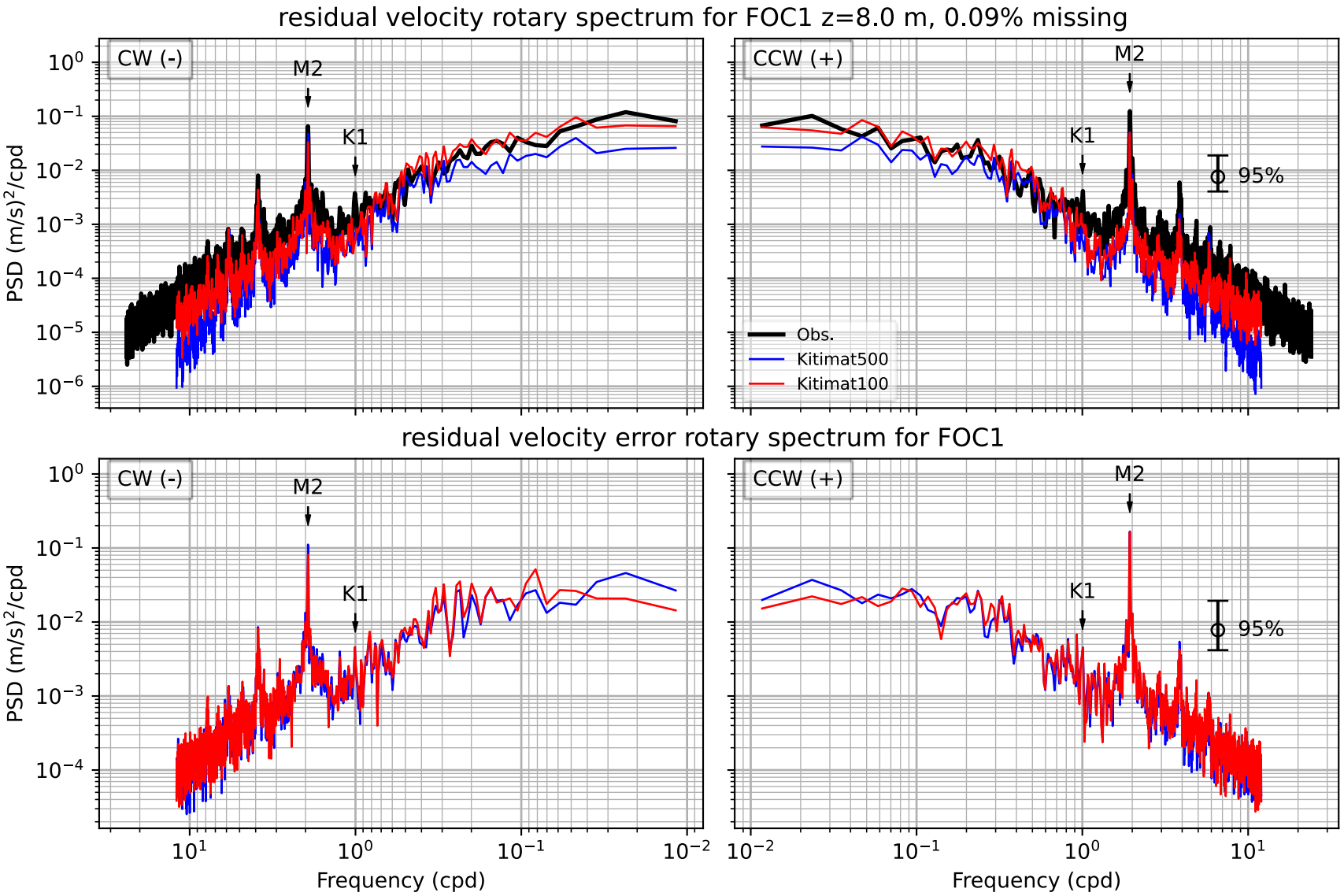

Figure 38. Rotary power spectrum of non-tidal currents at 8 m depth at station FOC1, measured by an ADCP moored at 36 m depth.

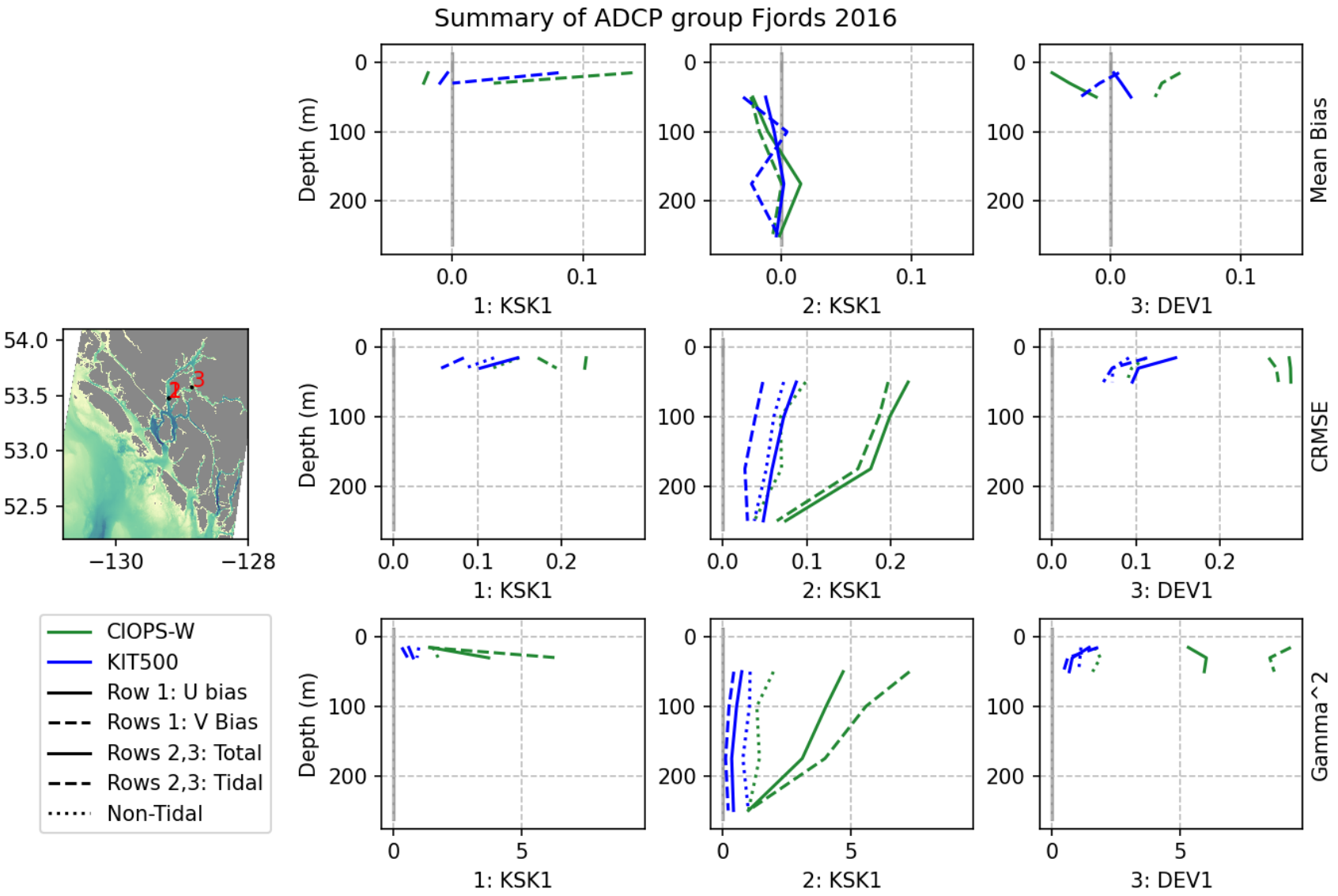

Figure 39. Summary of modelled current evaluation against ADCP data collected in the Kitimat fjord system, but outside of the 100 m port model domain, in 2016.

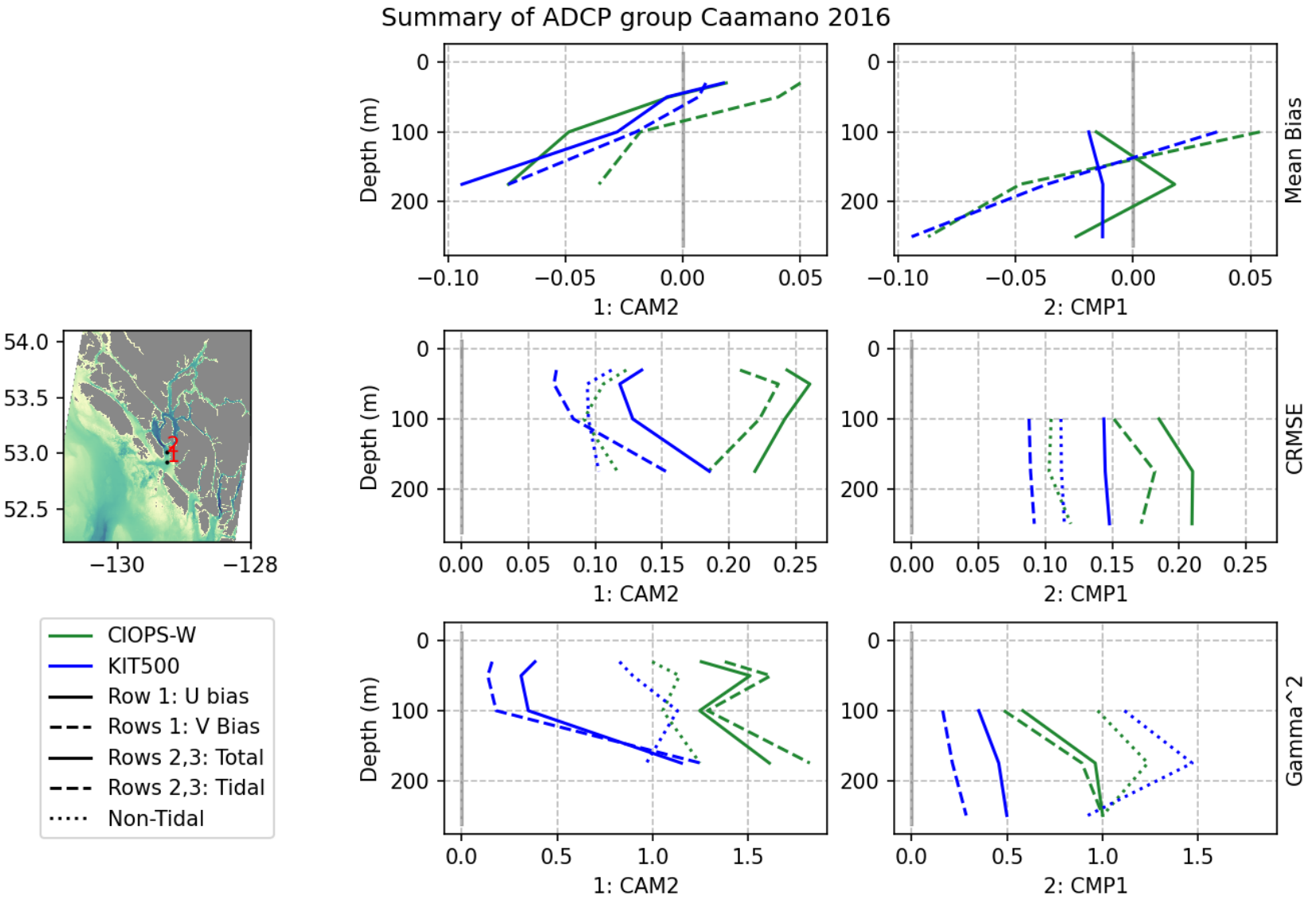

Figure 40. Summary of modelled current evaluation against ADCP data collected in Caamaño Sound in 2016.

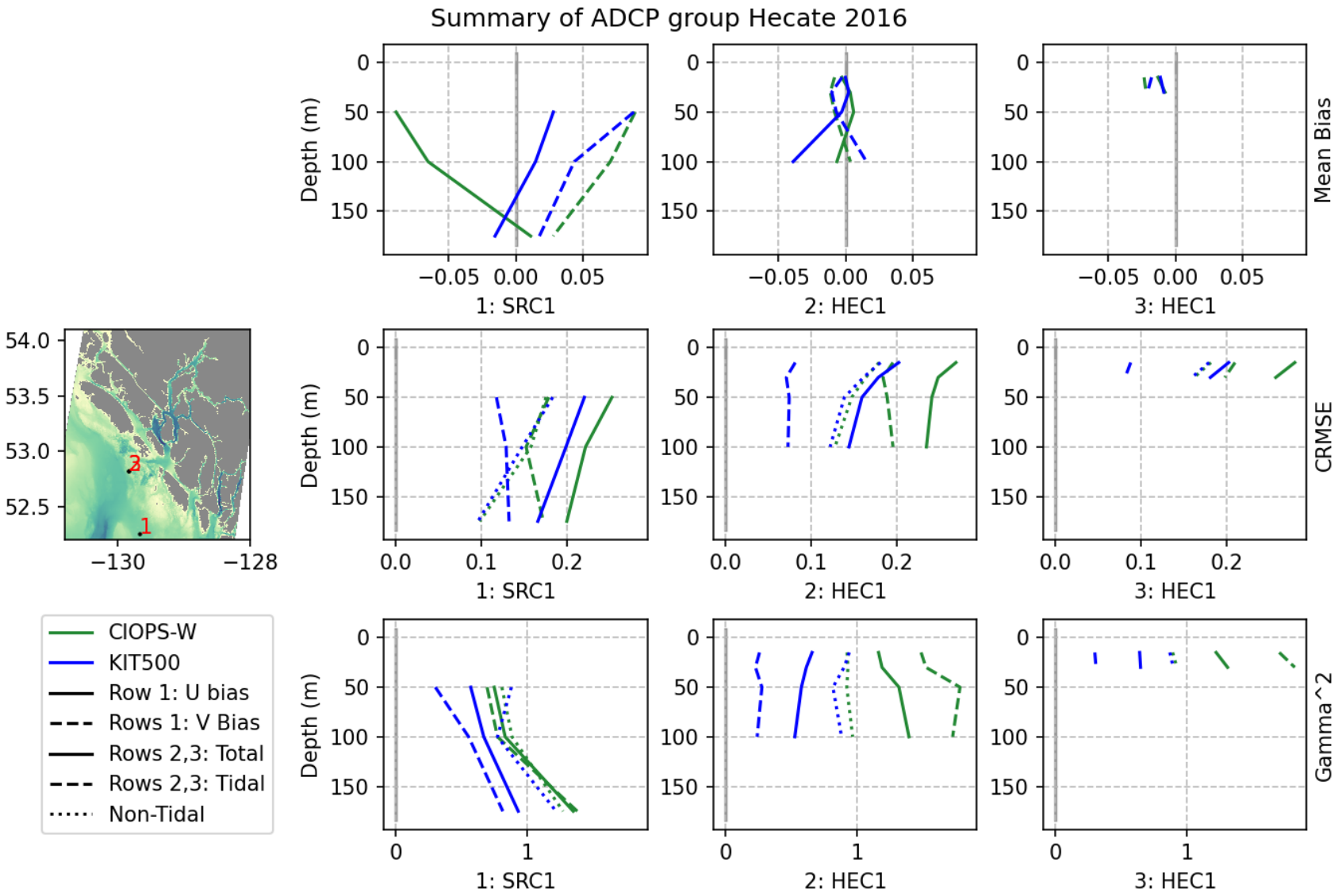

Figure 41. Summary of modelled current evaluation against ADCP data collected in Hecate Strait in 2016.

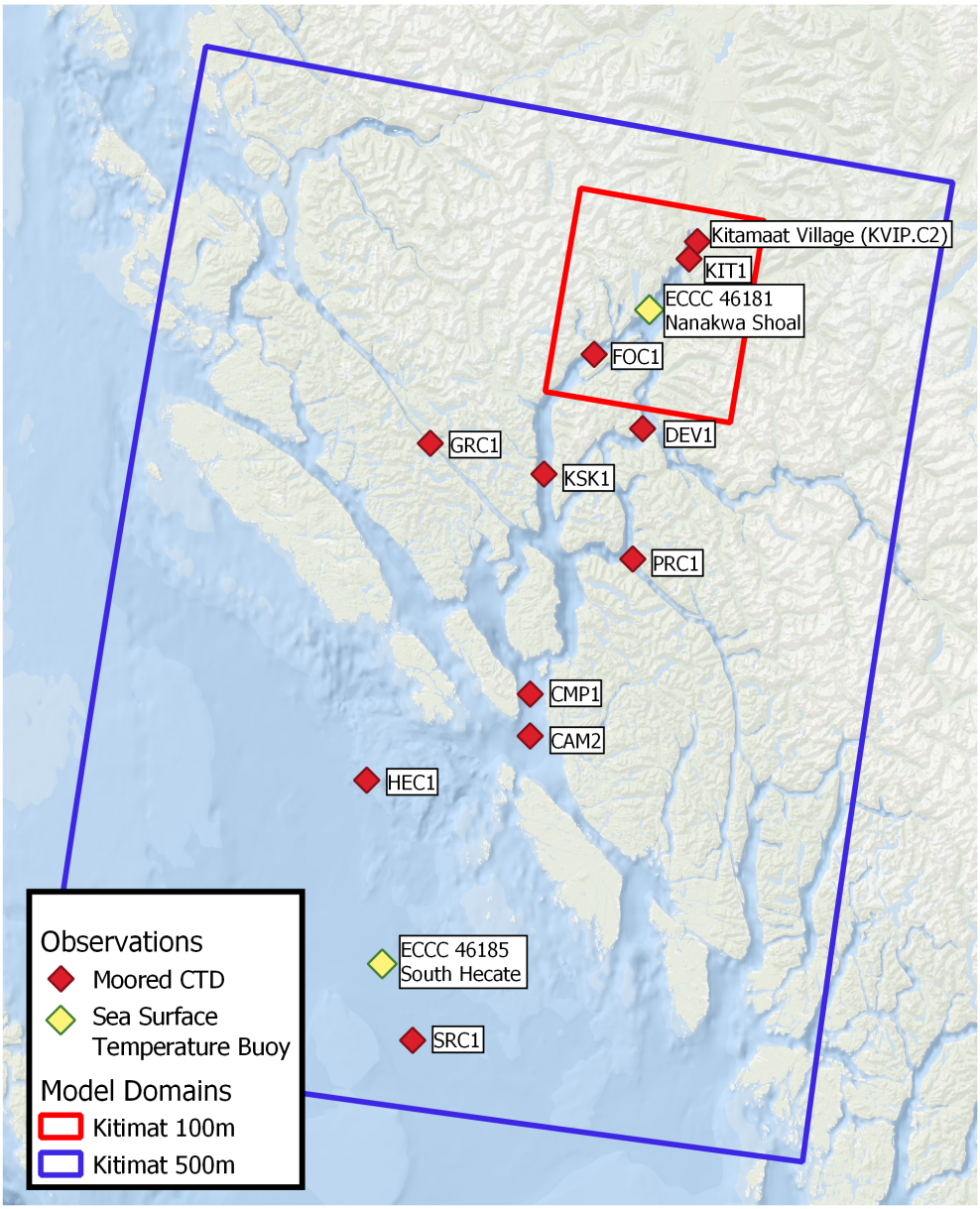

Figure 42. Key plot showing mooring locations with CTD, and buoys with SST sensors, active during the hindcast period.

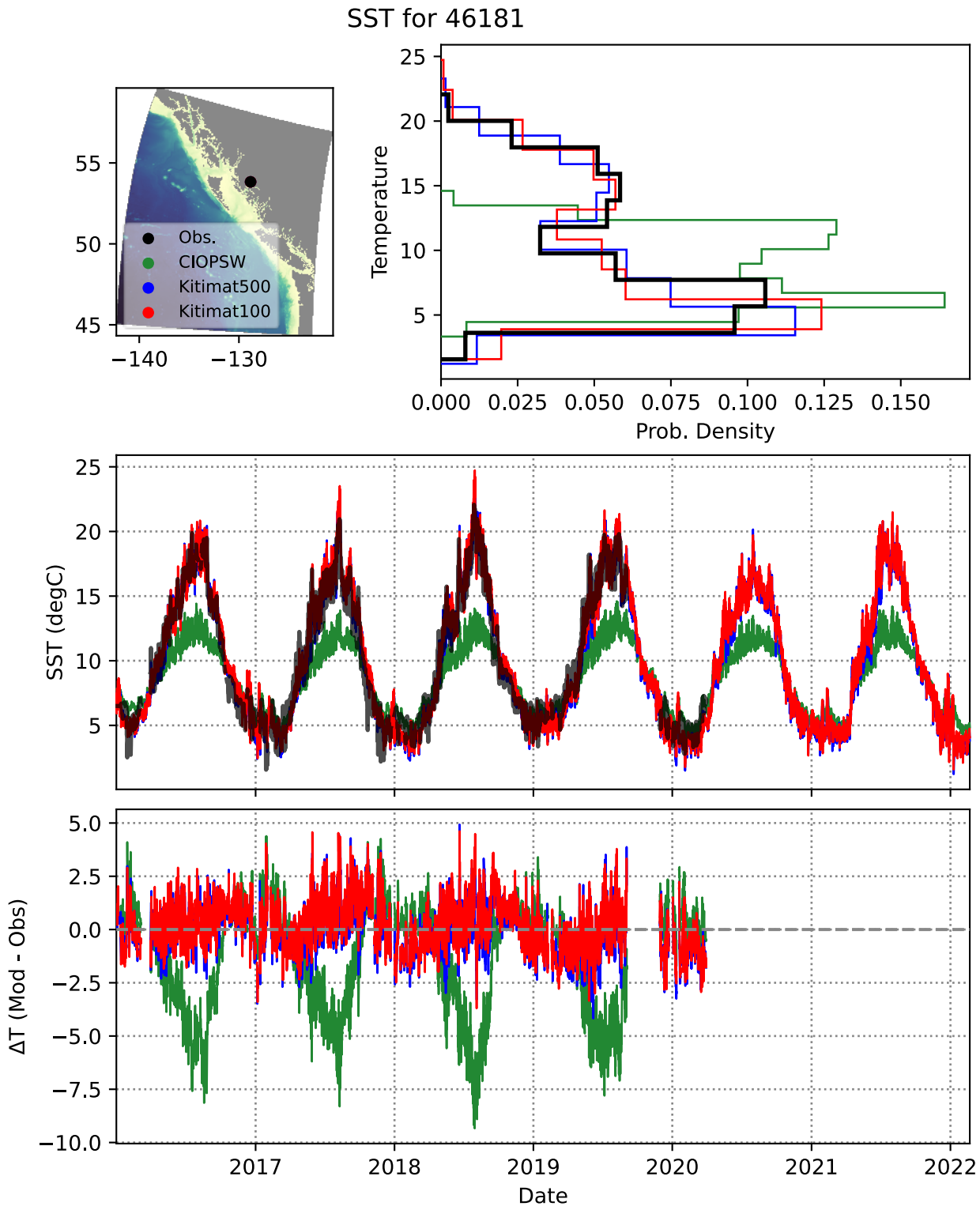

Figure 43. Comparison of sea surface temperature measured at ECCC station 46181 (Nanakwa Shoal, upper Douglas Channel) and model results from CIOPS-W and the Kitimat port model domains.

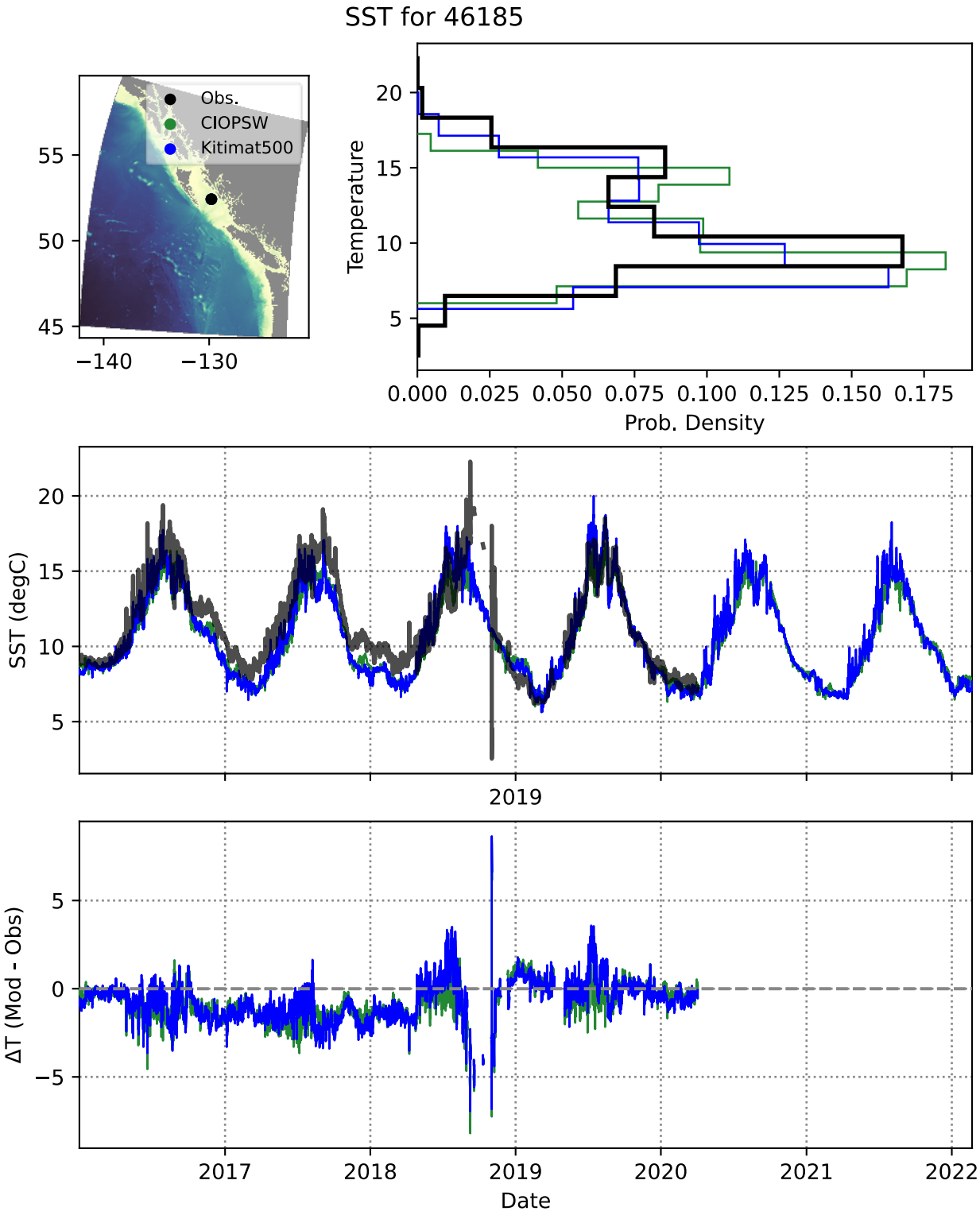

Figure 44. Comparison of sea surface temperature measured at ECCC station 46185 (South Hecate, Hecate Strait) and model results from CIOPS-W and the Kitimat 500 m port model domain.

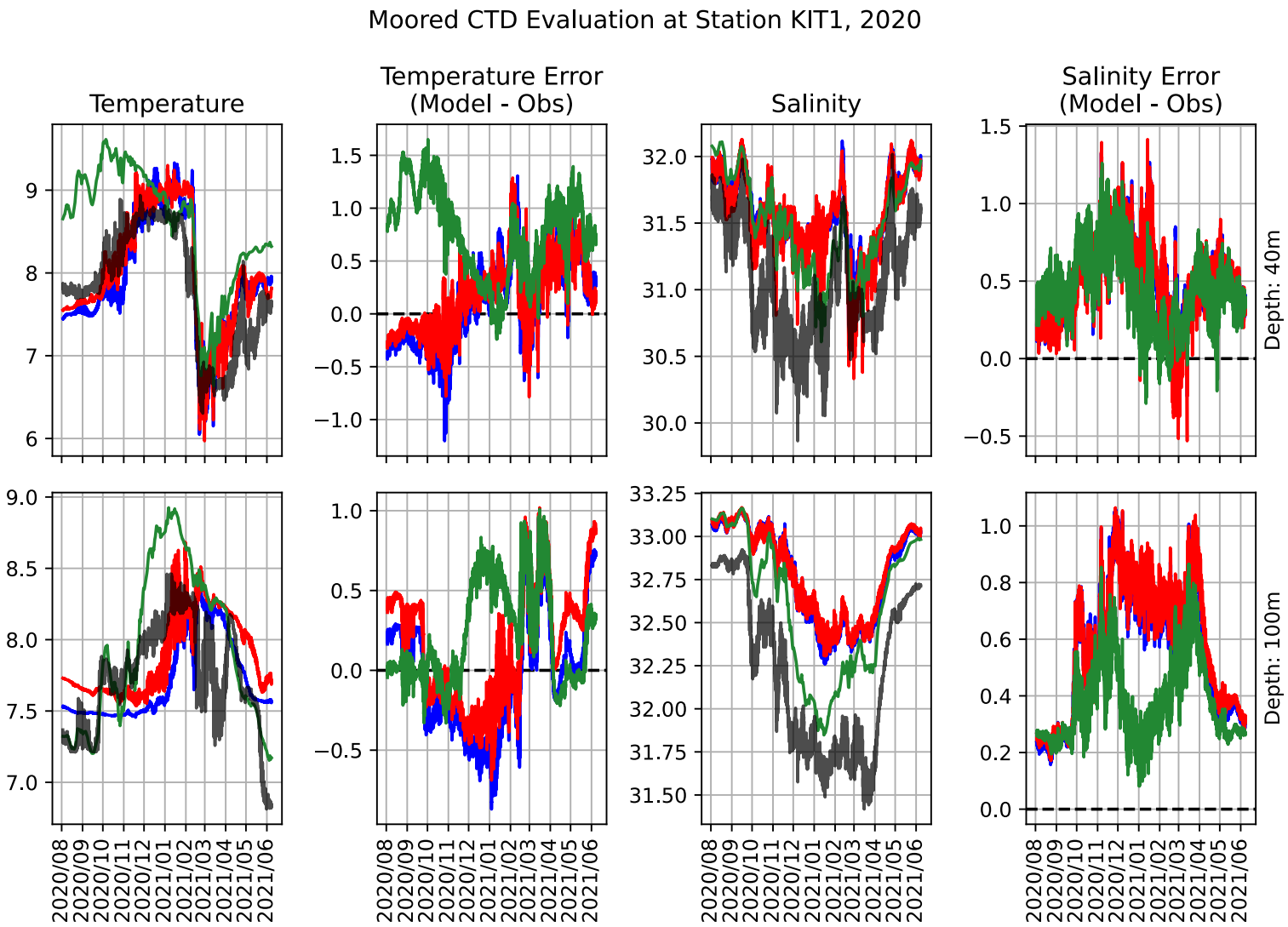

Figure 45. Summary of validation against temperature and salinity measurements from mooring KIT1, July 2020 - July 2021. Observations are shown in black and compared to model results from Kitimat 100 m (red), Kitimat 500 m (blue), and CIOPS-W (green).

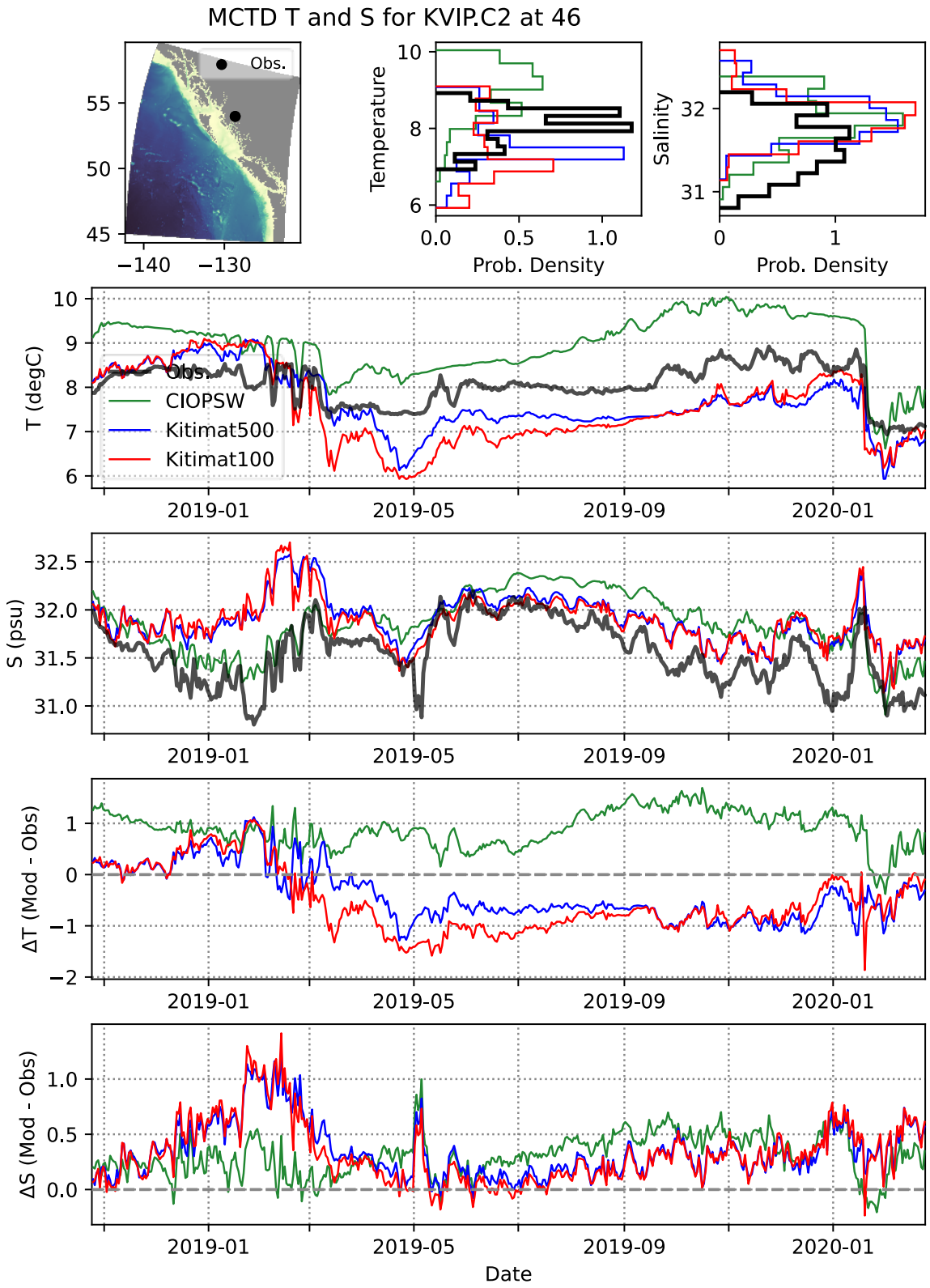

Figure 46. Comparison of temperature and salinity measured by a CTD moored at station Kitamaat Village (Kitimat Arm, 46 m depth) and model results from CIOPS-W and the Kitimat port model domains.

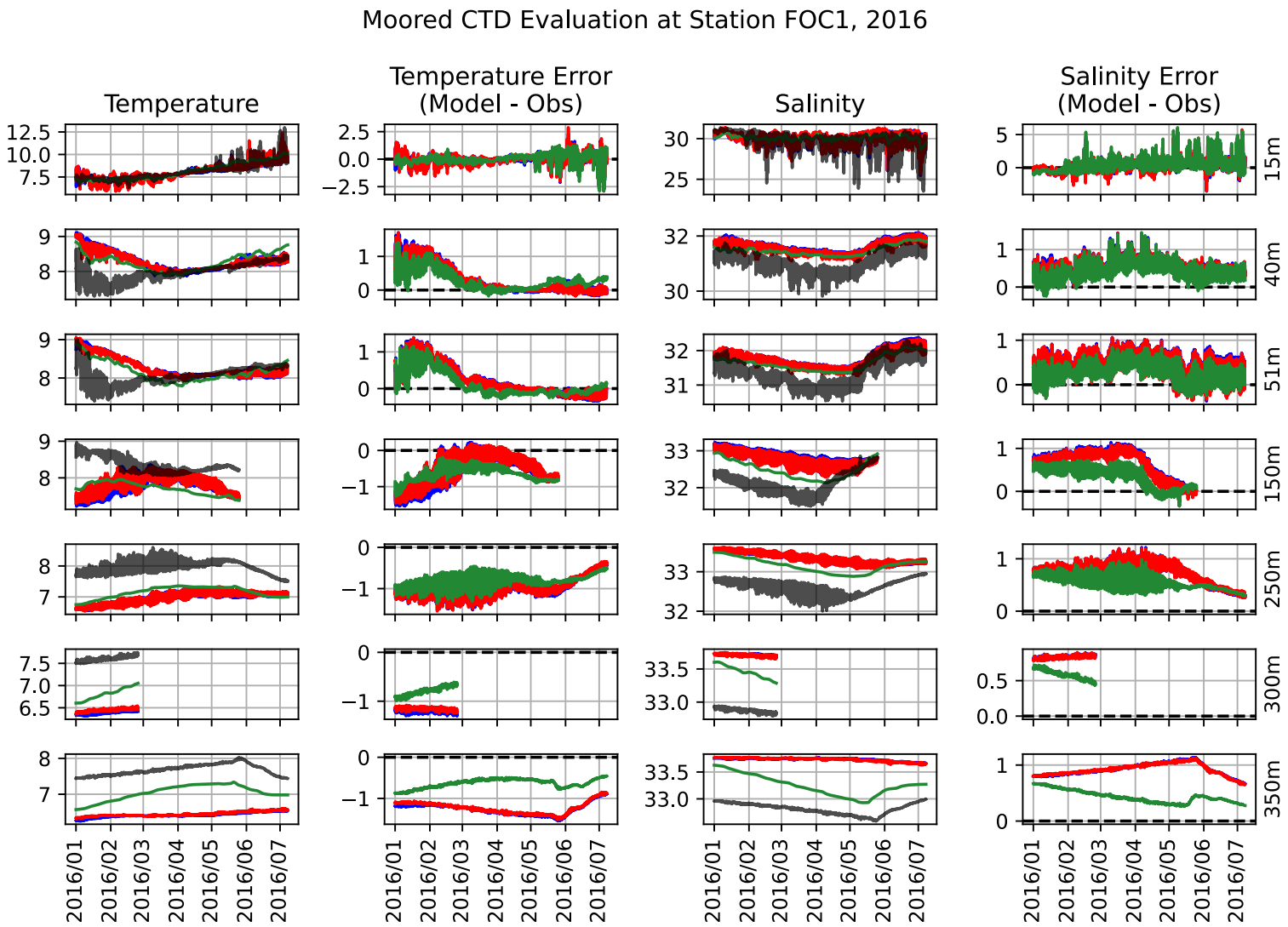

Figure 47. Summary of validation against temperature and salinity measurements from mooring FOC1, Jan – July 2016. Observations are shown in black and compared to model results from Kitimat 100 m (red), Kitimat 500 m (blue), and CIOPS-W (green).

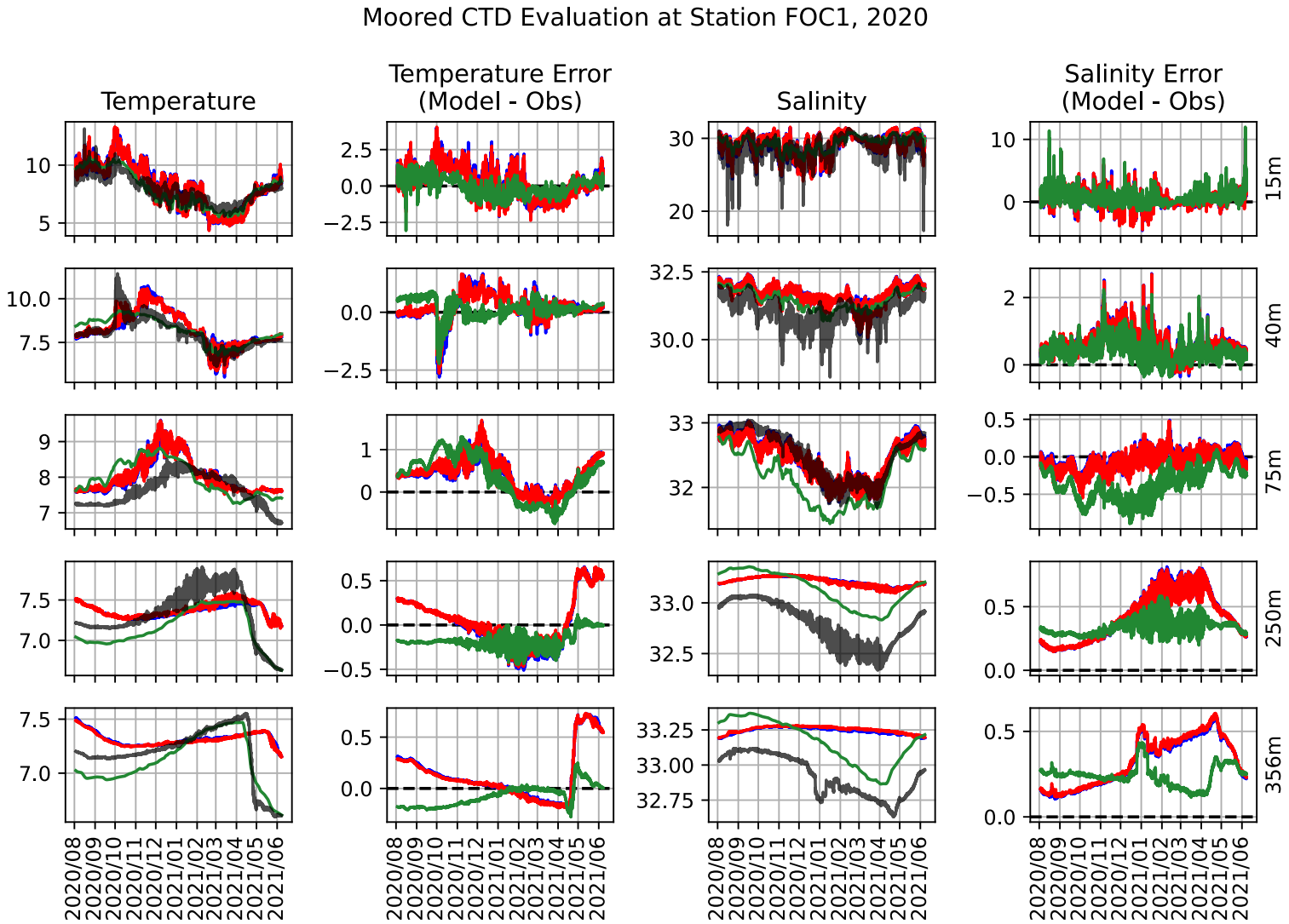

Figure 48. Summary of validation against temperature and salinity measurements from mooring FOC1, July 2020 - July 2021. Observations are shown in black and compared to model results from Kitimat 100 m (red), Kitimat 500 m (blue), and CIOPS-W (green).

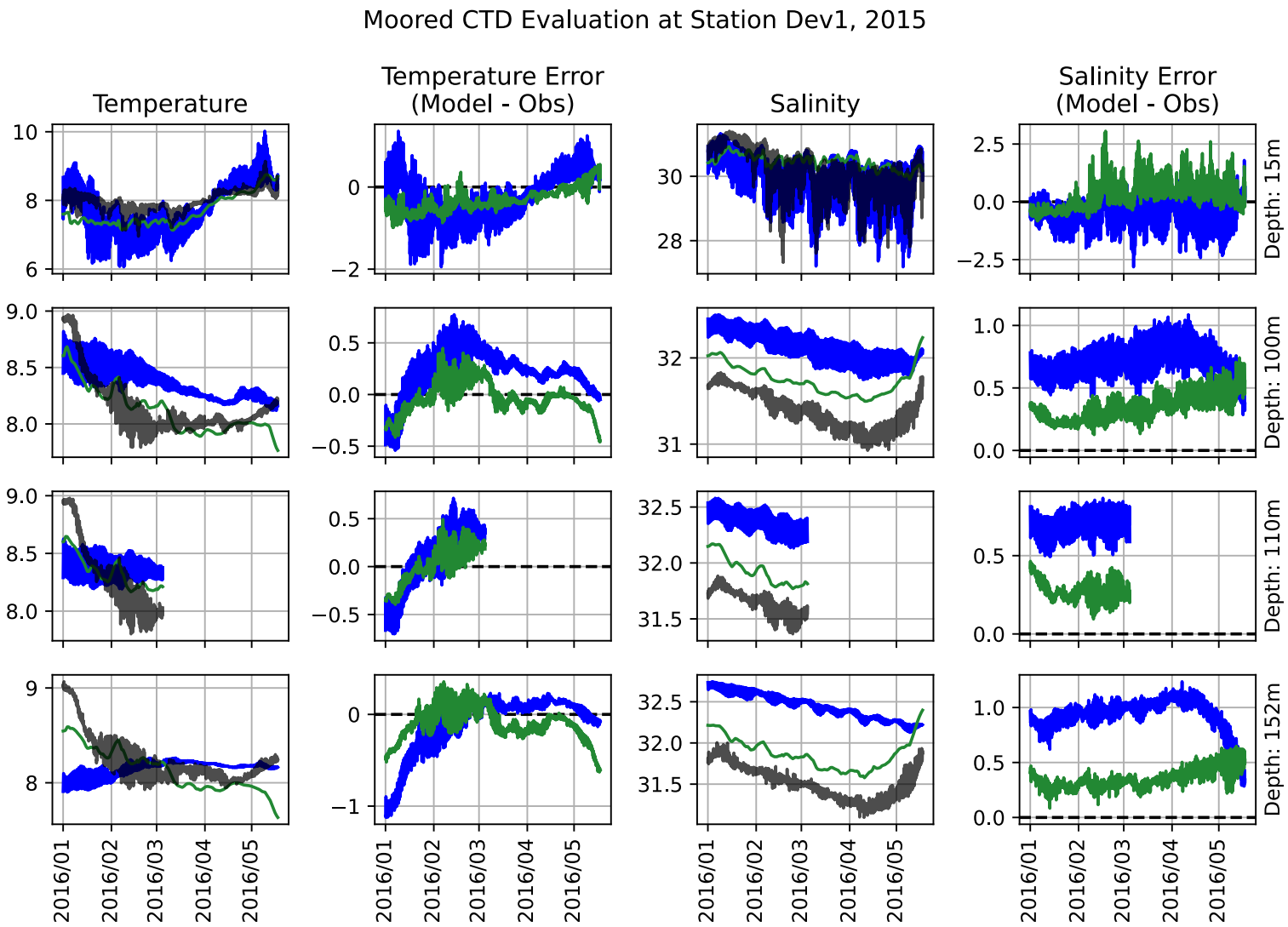

Figure 49. Summary of validation against temperature and salinity measurements from mooring DEV1, Jan – June 2016. Observations are shown in black and compared to model results from Kitimat 500 m (blue), and CIOPS-W (green).

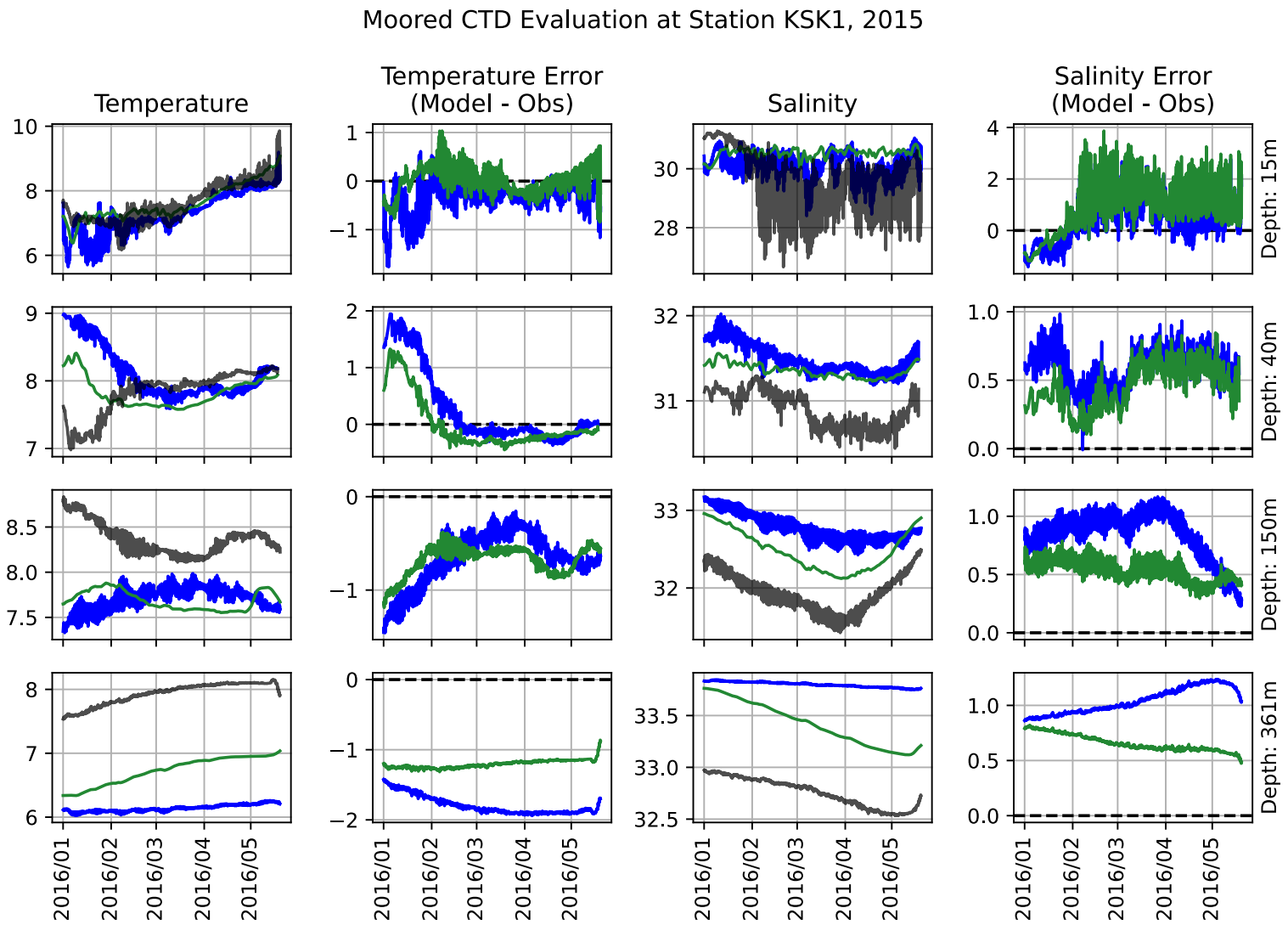

Figure 50. Summary of validation against temperature and salinity measurements from mooring KSK1, Jan – June 2016. Observations are shown in black and compared to model results from Kitimat 500 m (blue), and CIOPS-W (green).

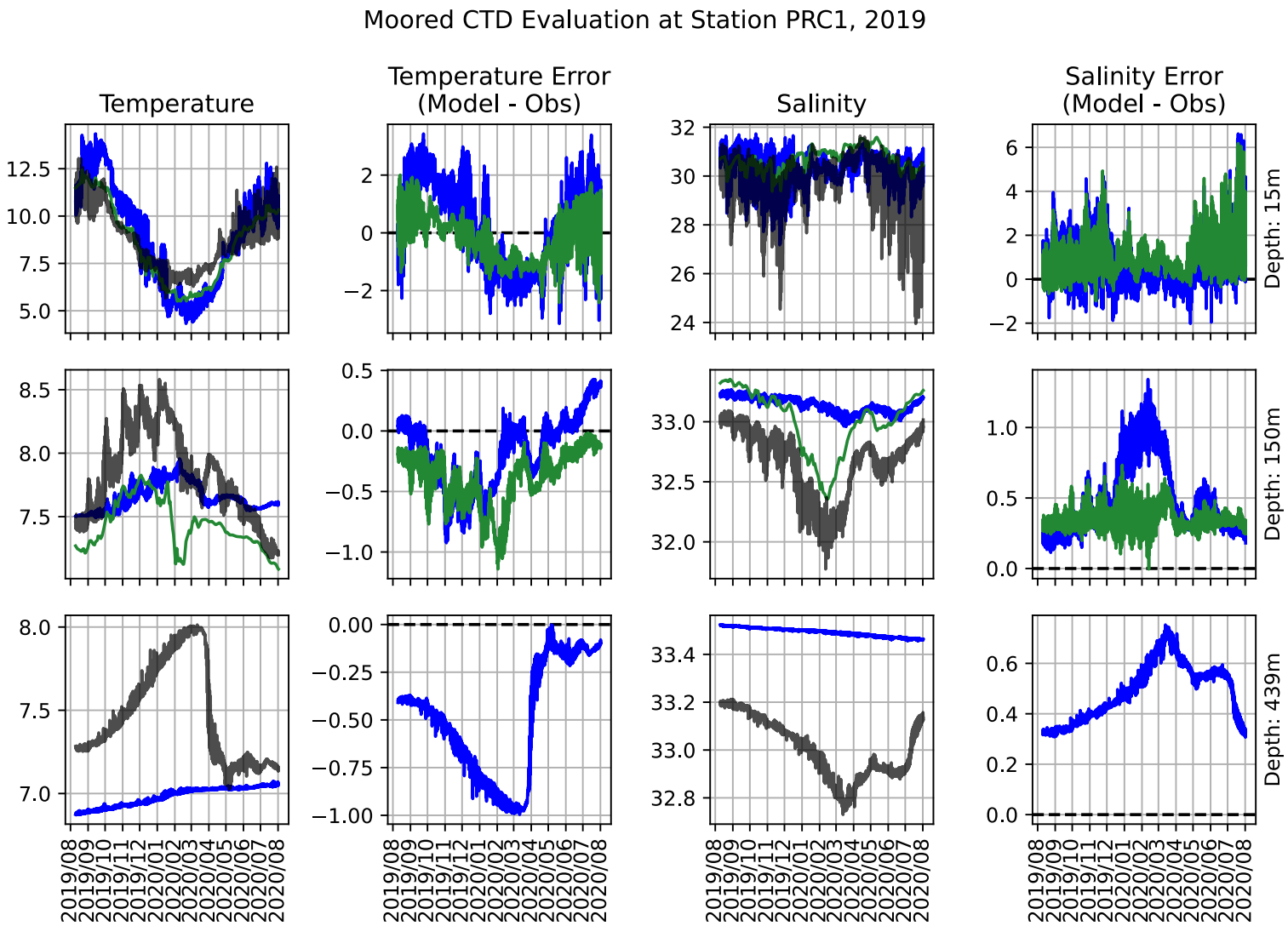

Figure 51. Summary of validation against temperature and salinity measurements from mooring PRC1, July 2019 – Aug 2020. Observations are shown in black and compared to model results from Kitimat 500 m (blue), and CIOPS-W (green).

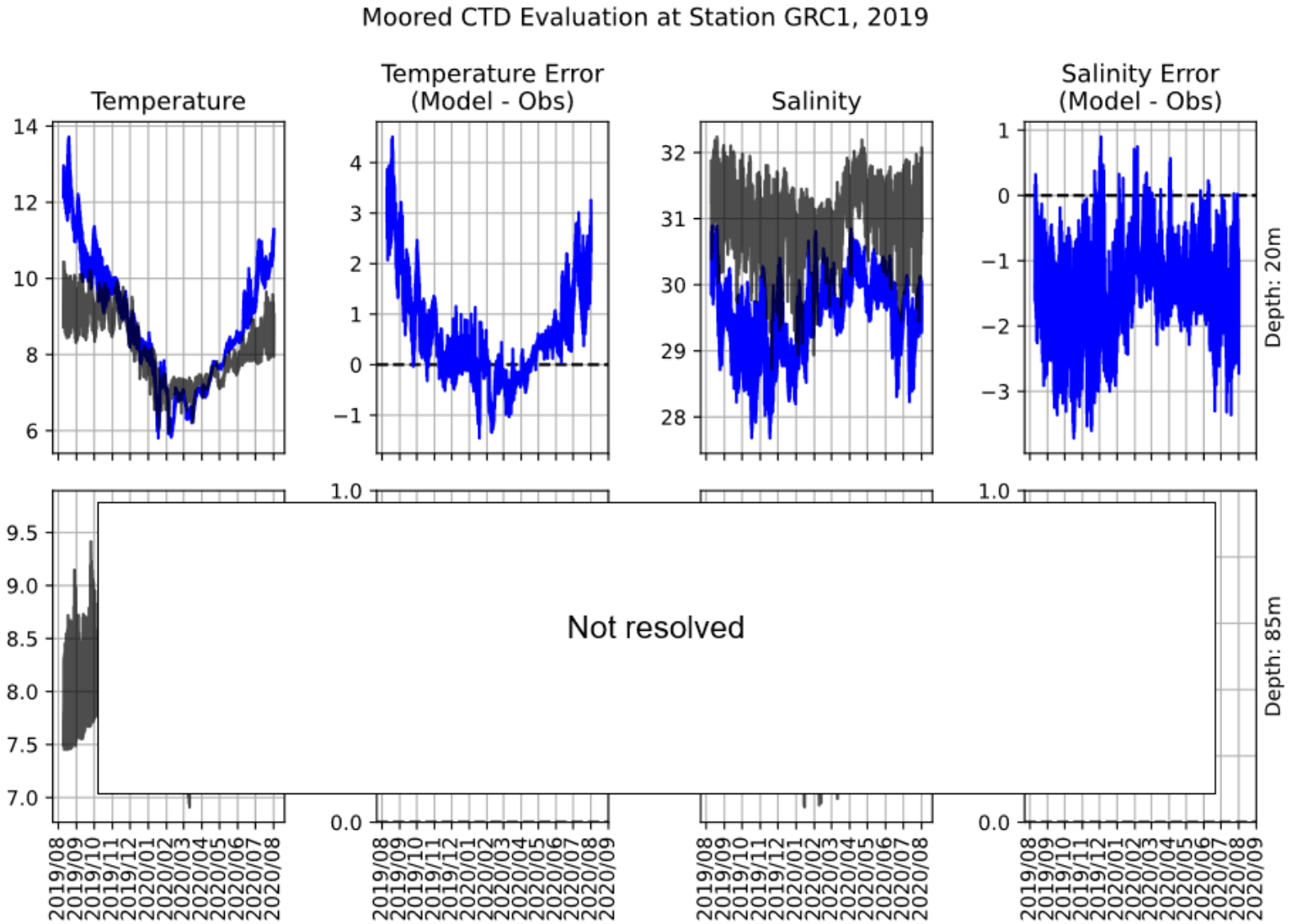

Figure 52. Summary of validation against temperature and salinity measurements from mooring GRC1, July 2019 – Aug 2020. Observations are shown in black and compared to model results from Kitimat 500 m (blue), and CIOPS-W (green). The instrument at 85m depth (bottom row) is not resolved in the model due to coarse resolution of the bathymetry in the vicinity of the mooring.

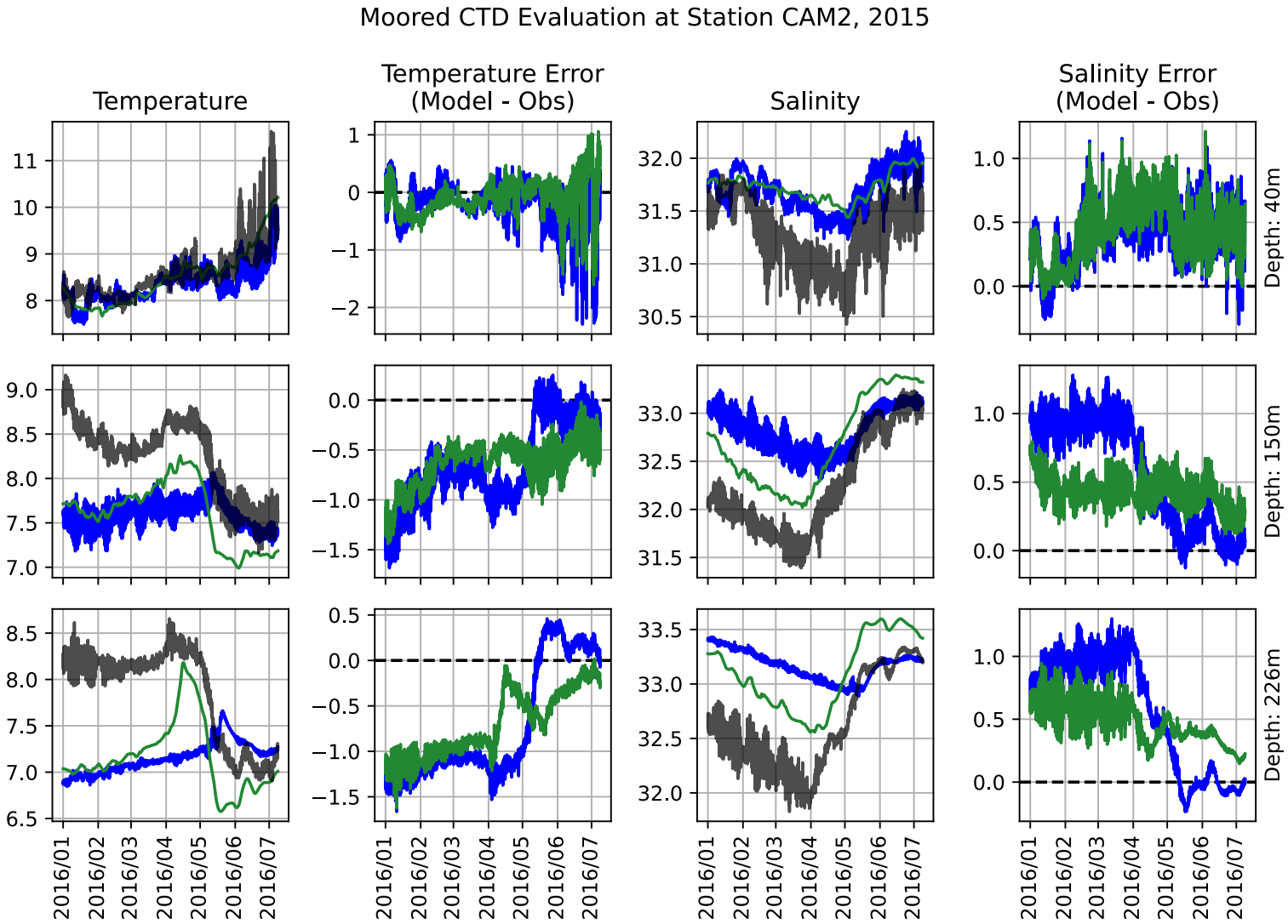

Figure 53. Summary of validation against temperature and salinity measurements from mooring CAM2, Jan – July 2016. Observations are shown in black and compared to model results from Kitimat 500 m (blue), and CIOPS-W (green).

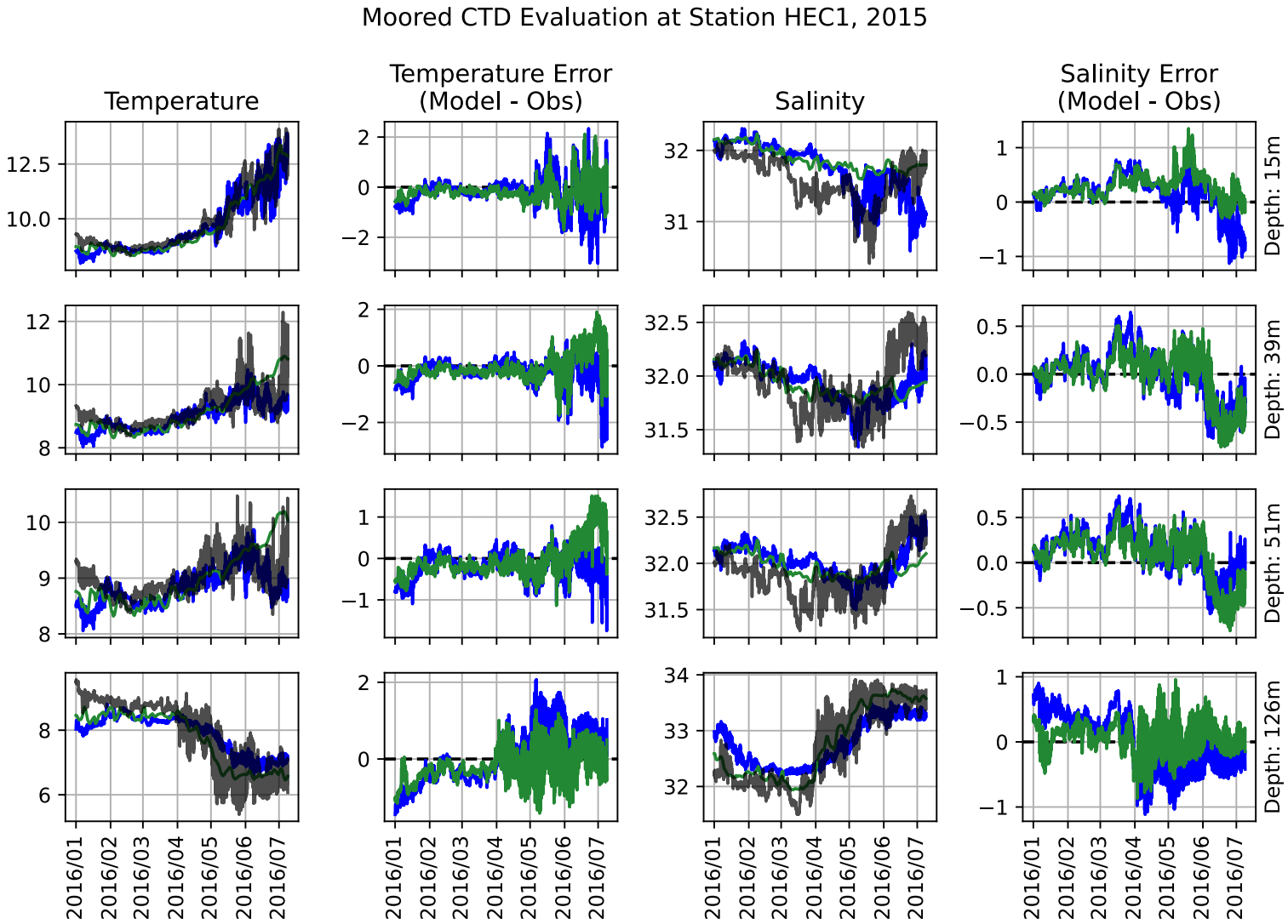

Figure 54. Summary of validation against temperature and salinity measurements from mooring HEC1, Jan – July 2016. Observations are shown in black and compared to model results from Kitimat 500 m (blue), and CIOPS-W (green).

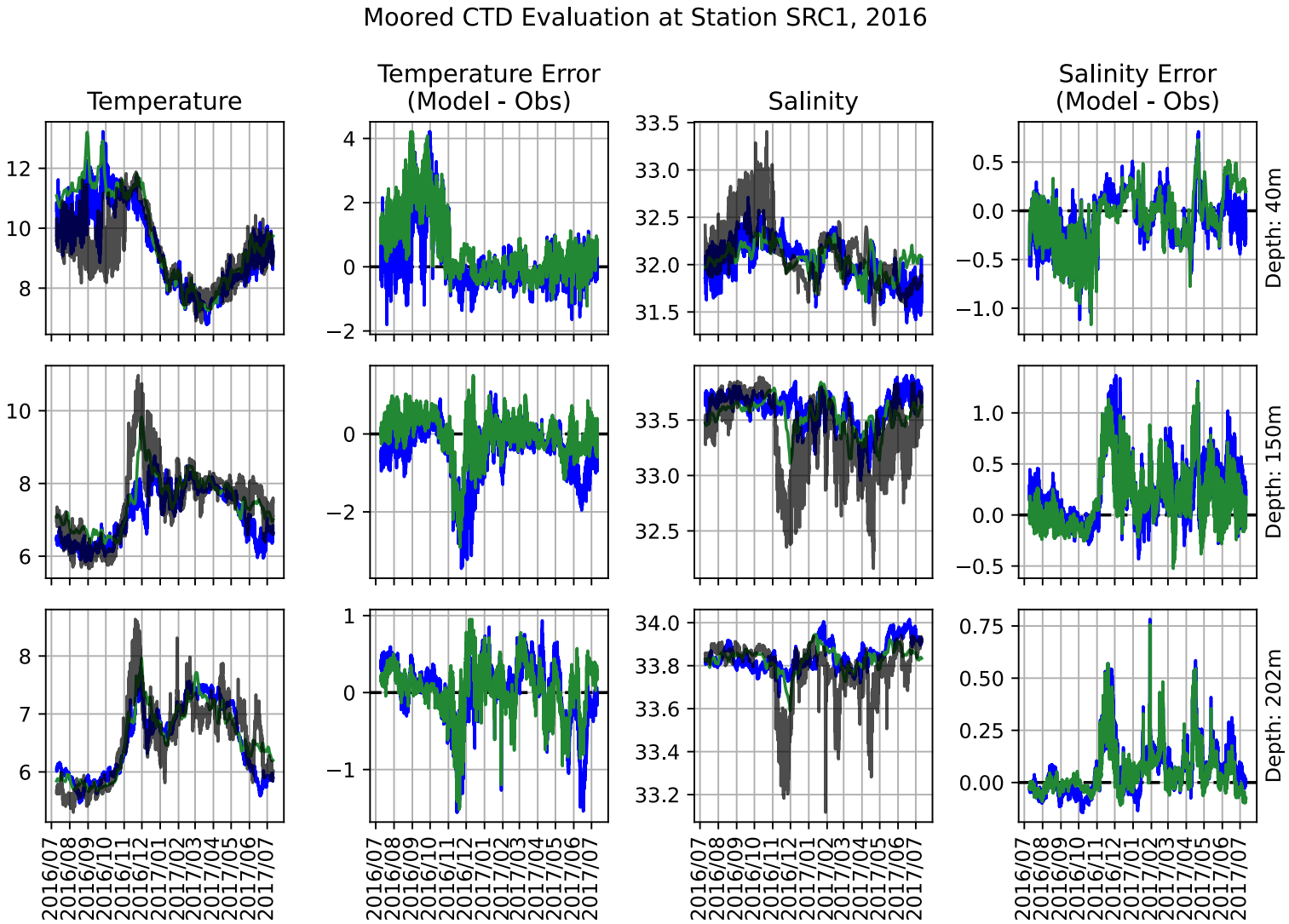

Figure 55. Summary of validation against temperature and salinity measurements from mooring SRC1, July 2016 – July 2017. Observations are shown in black and compared to model results from Kitimat 500 m (blue), and CIOPS-W (green).

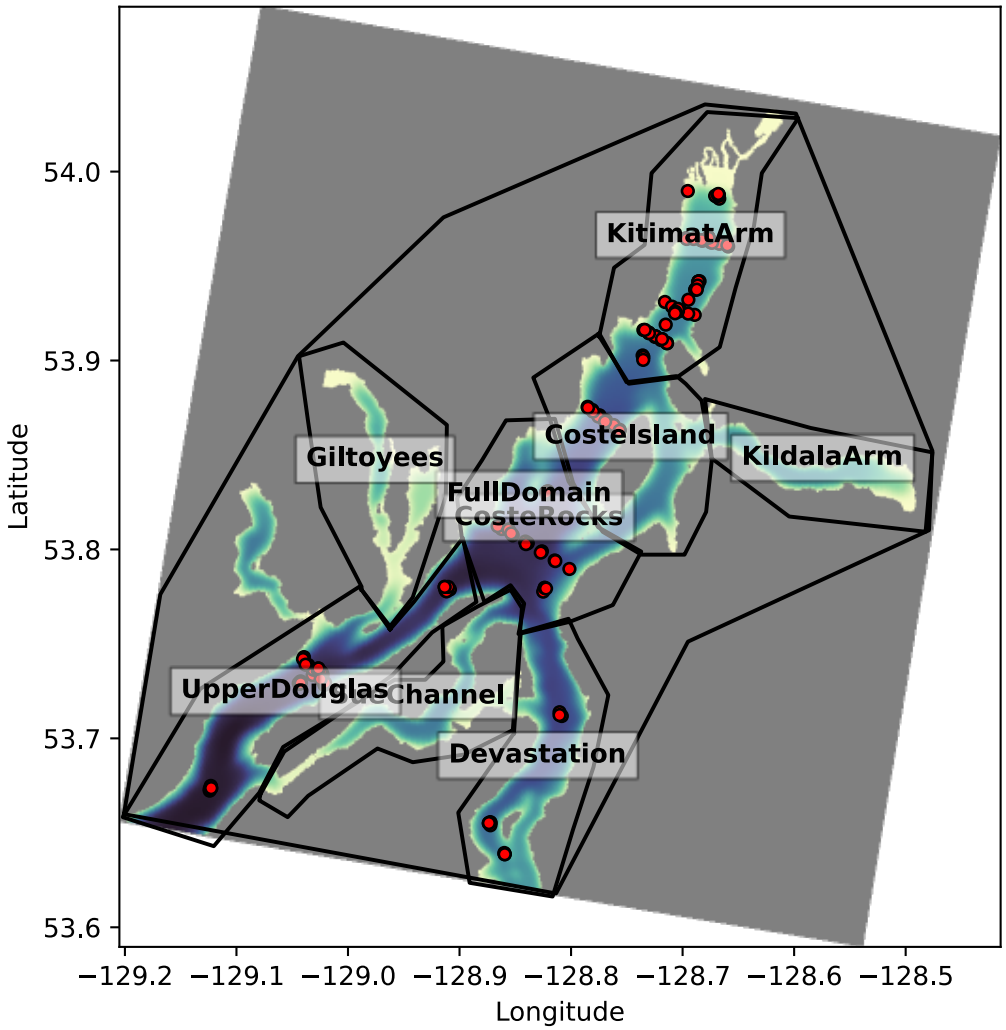

Figure 56. CTD casts (red plots) and sub-regions (outlined with solid black lines) used for the analysis in Kitimat 100 m domain.

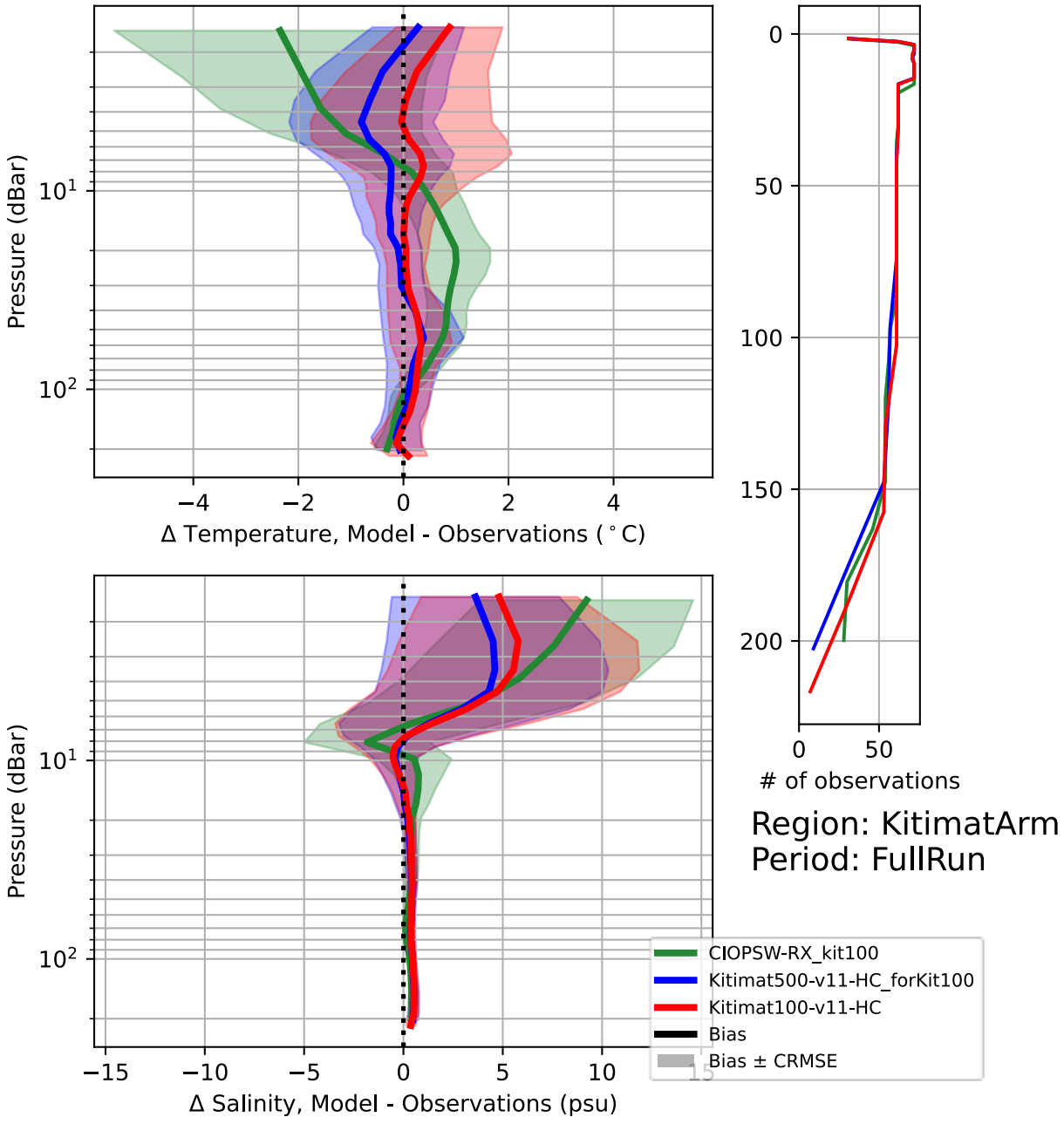

Figure 57. Comparison of temperature and salinity errors against CTD casts in Kitimat Arm sub-region of Kitimat 100 m domain.

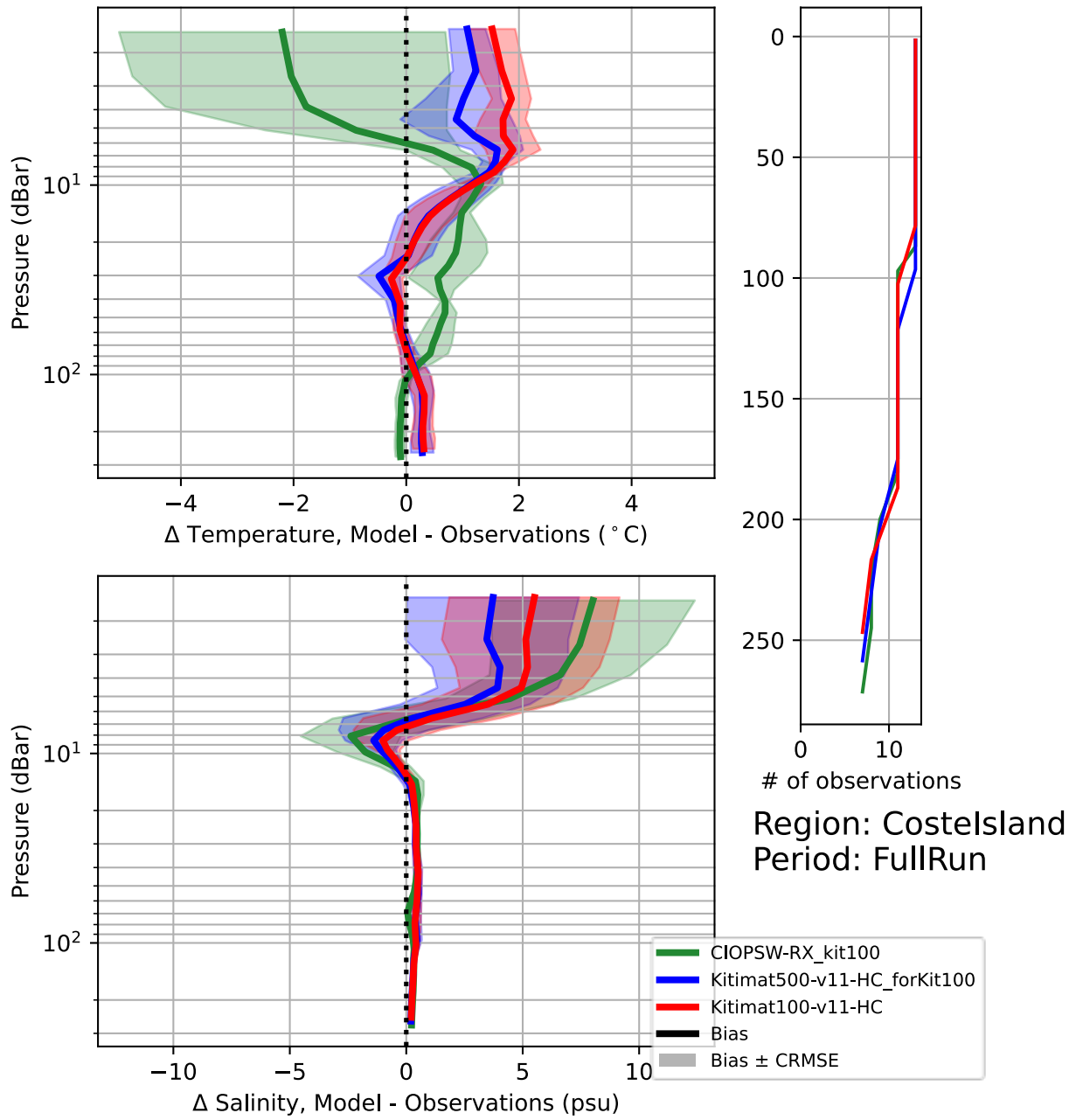

Figure 58. Comparison of temperature and salinity errors against CTD casts in Coste Island sub-region of Kitimat 100 m domain.

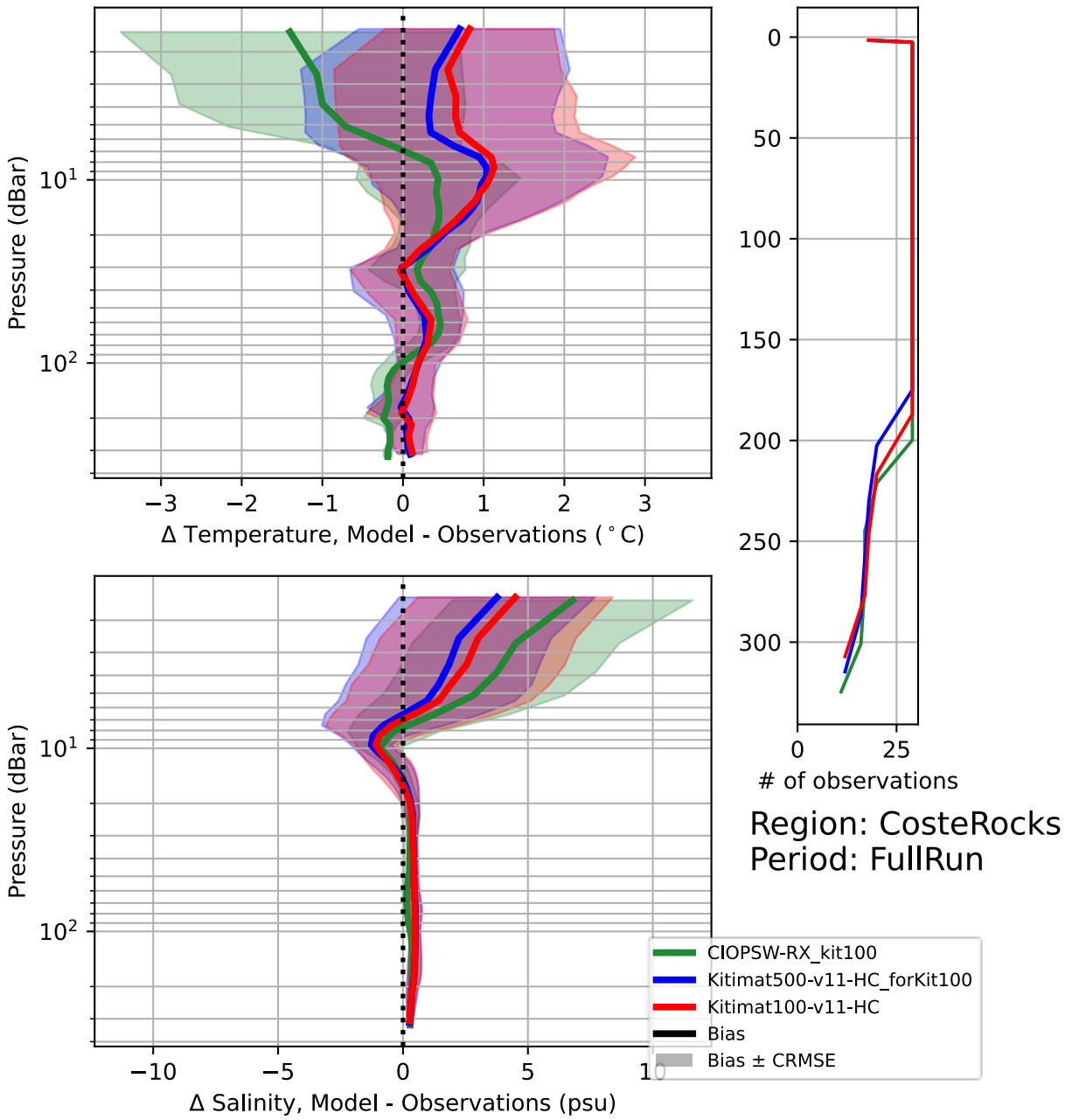

Figure 59. Comparison of temperature and salinity errors against CTD casts in Coste Rocks sub-region of Kitimat 100 m domain.

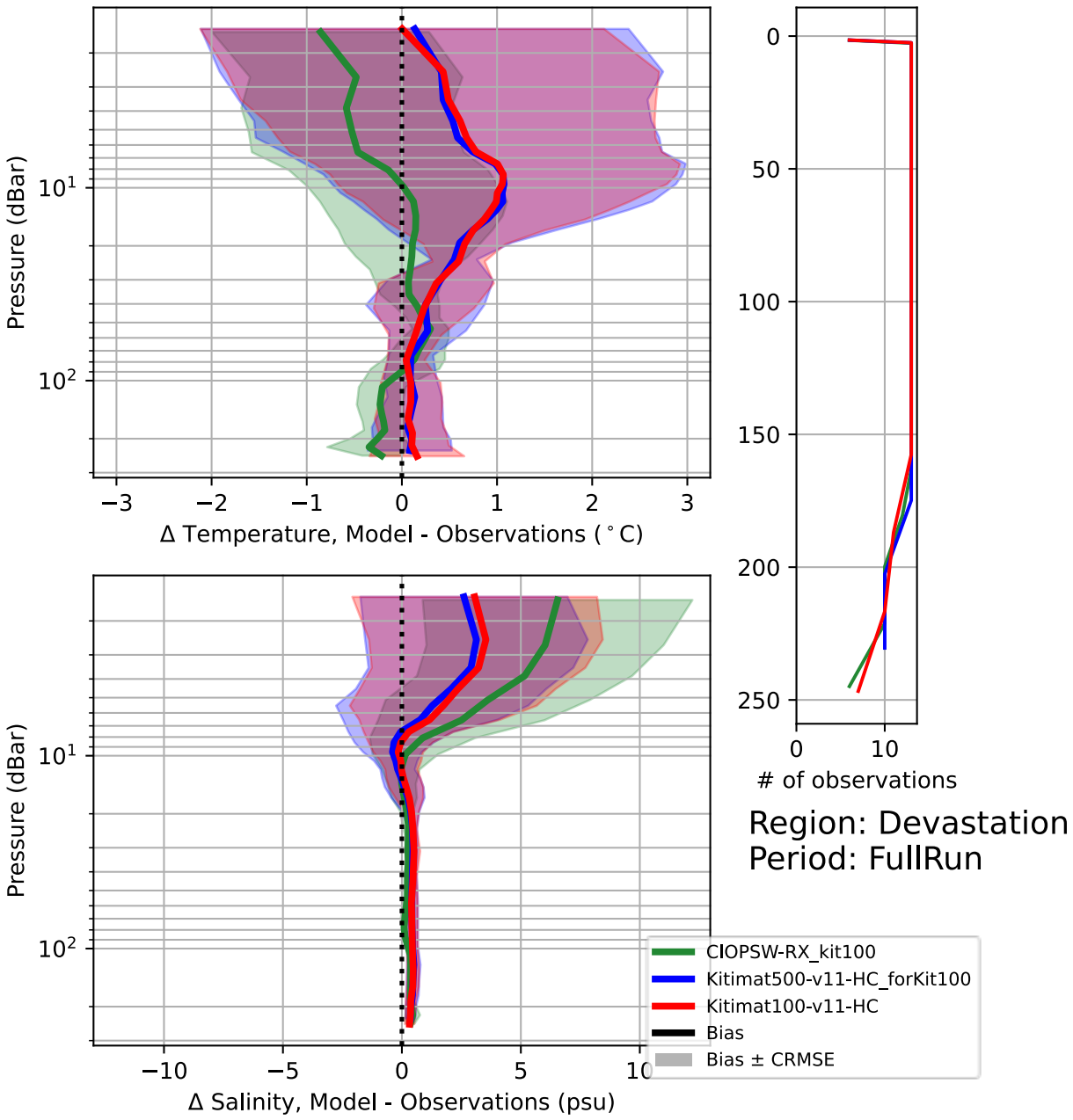

Figure 60. Comparison of temperature and salinity errors against CTD casts in Devastation Channel sub-region of Kitimat 100 m domain.

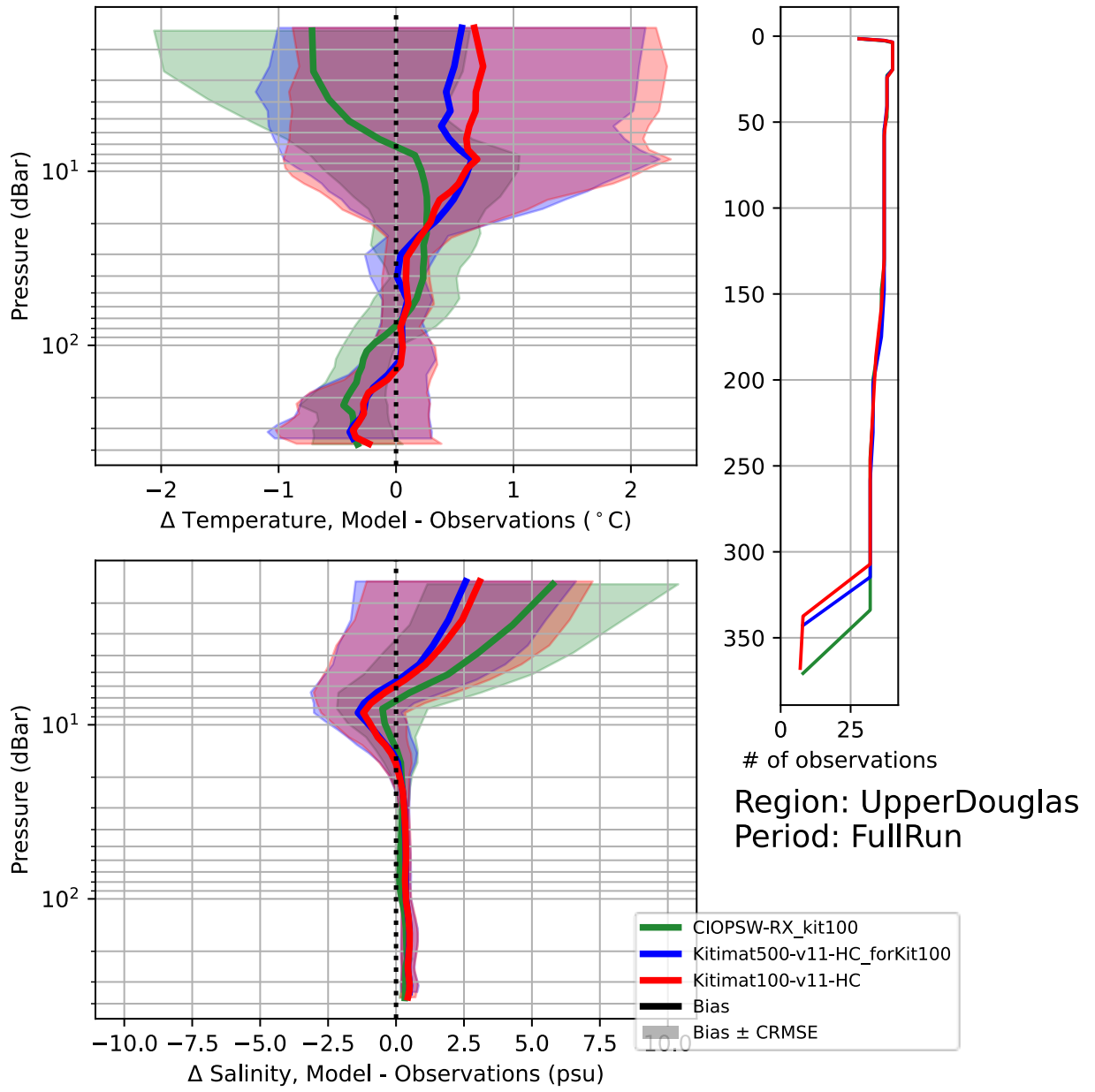

Figure 61. Comparison of temperature and salinity errors against CTD casts in upper Douglas Channel sub-region of Kitimat 100 m domain.

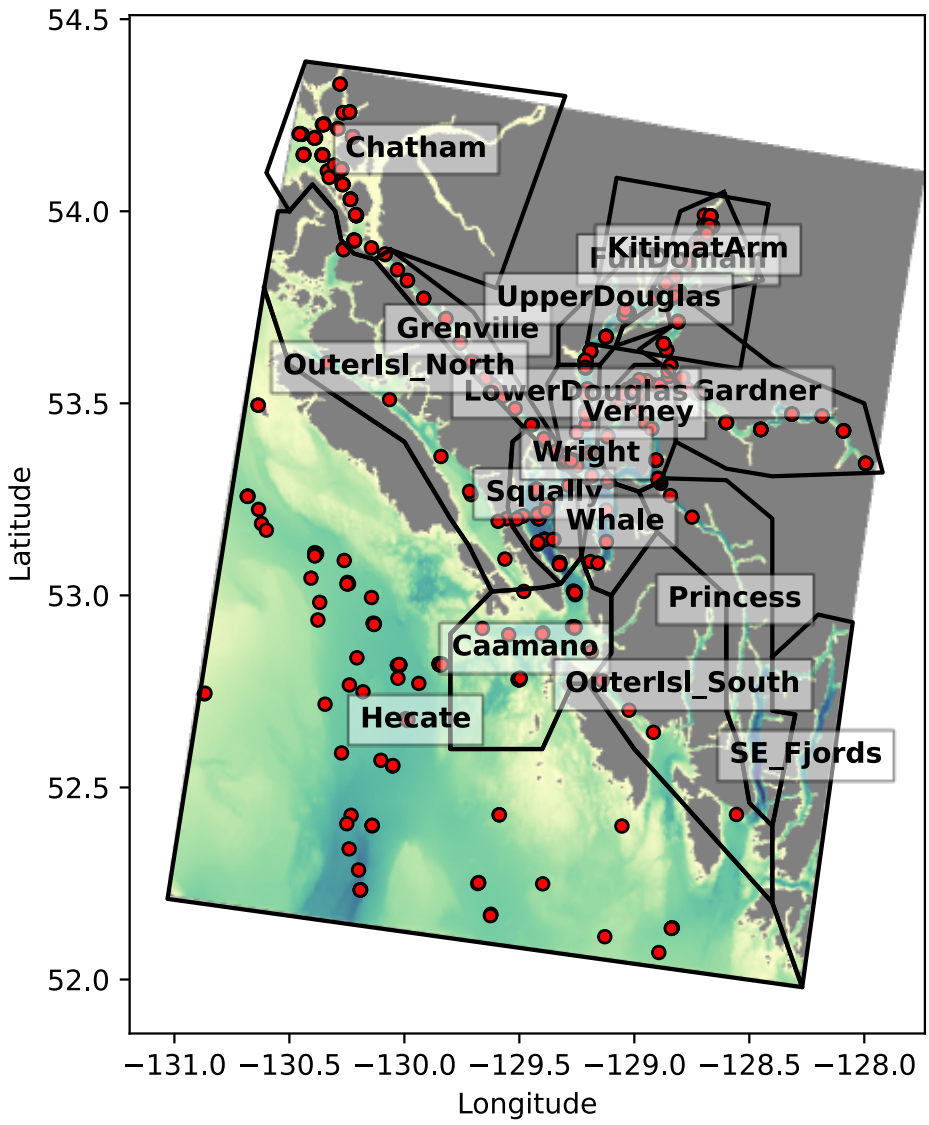

Figure 62. CTD casts (red plots) and sub-regions (outlined with solid black lines) used for the analysis in Kitimat 500 m domain.

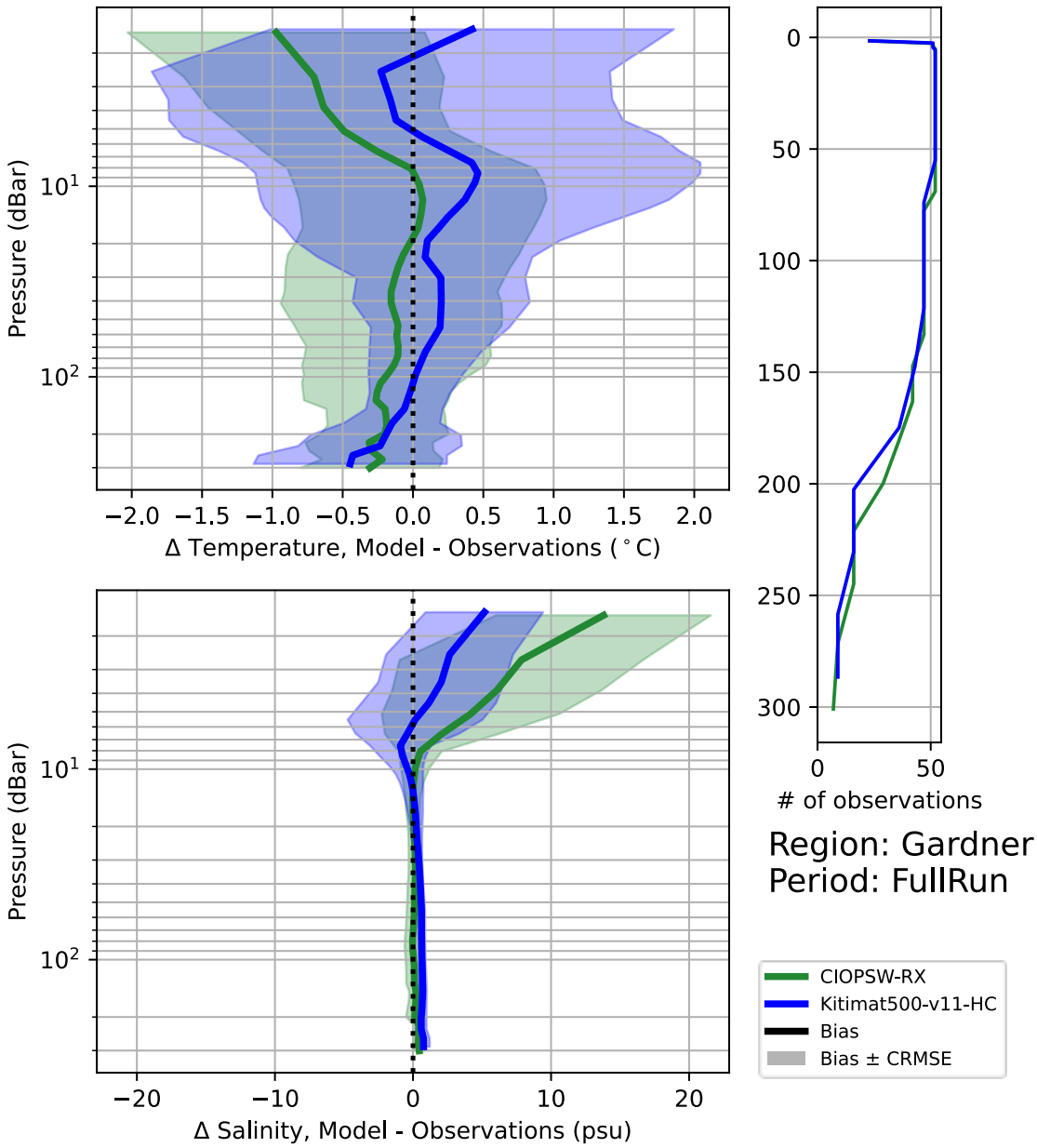

Figure 63. Comparison of temperature and salinity errors against CTD casts in Gardner Canal sub-region of Kitimat 500 m domain.

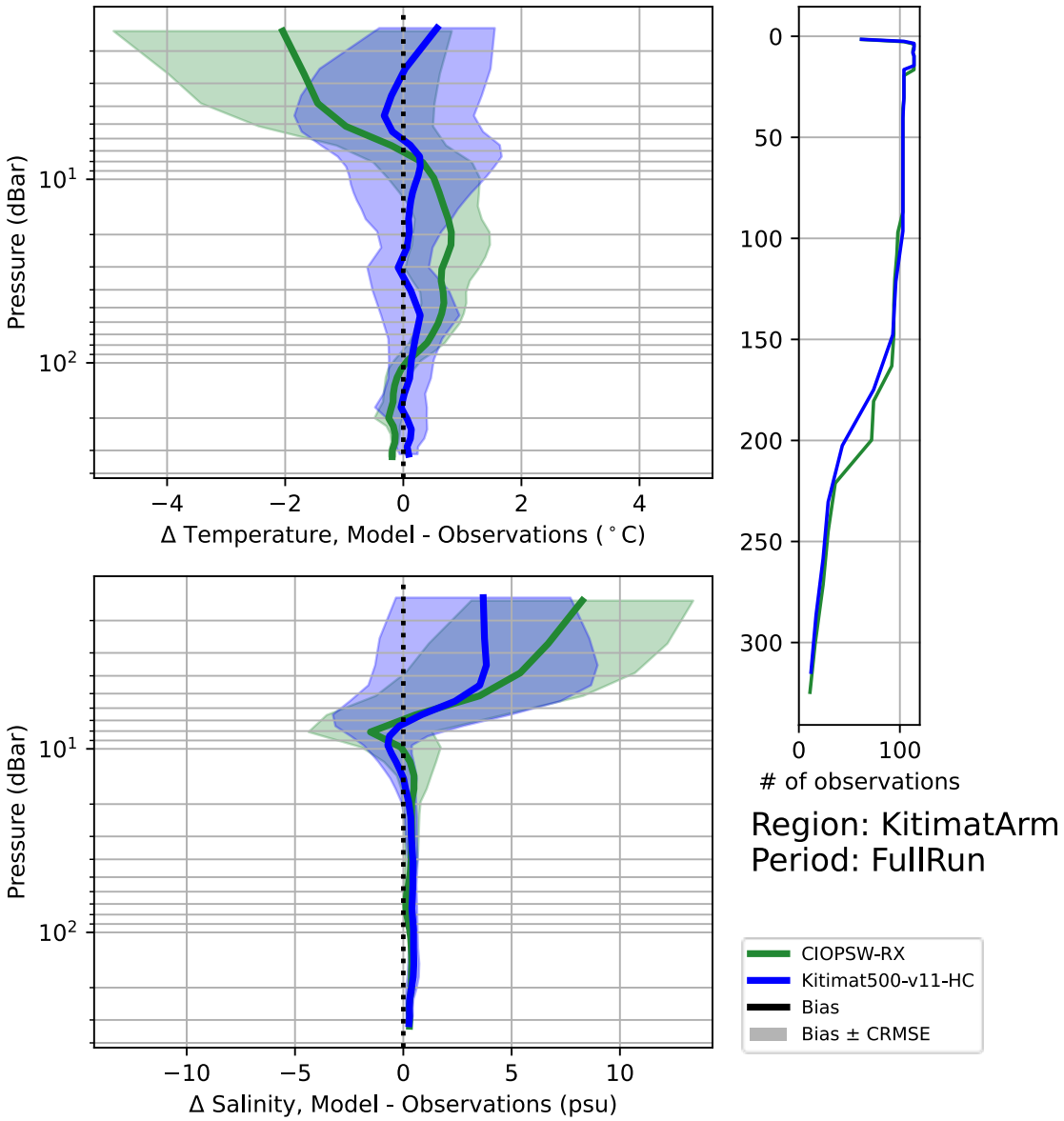

Figure 64. Comparison of temperature and salinity errors against CTD casts in Kitimat Arm sub-region of Kitimat 500 m domain.

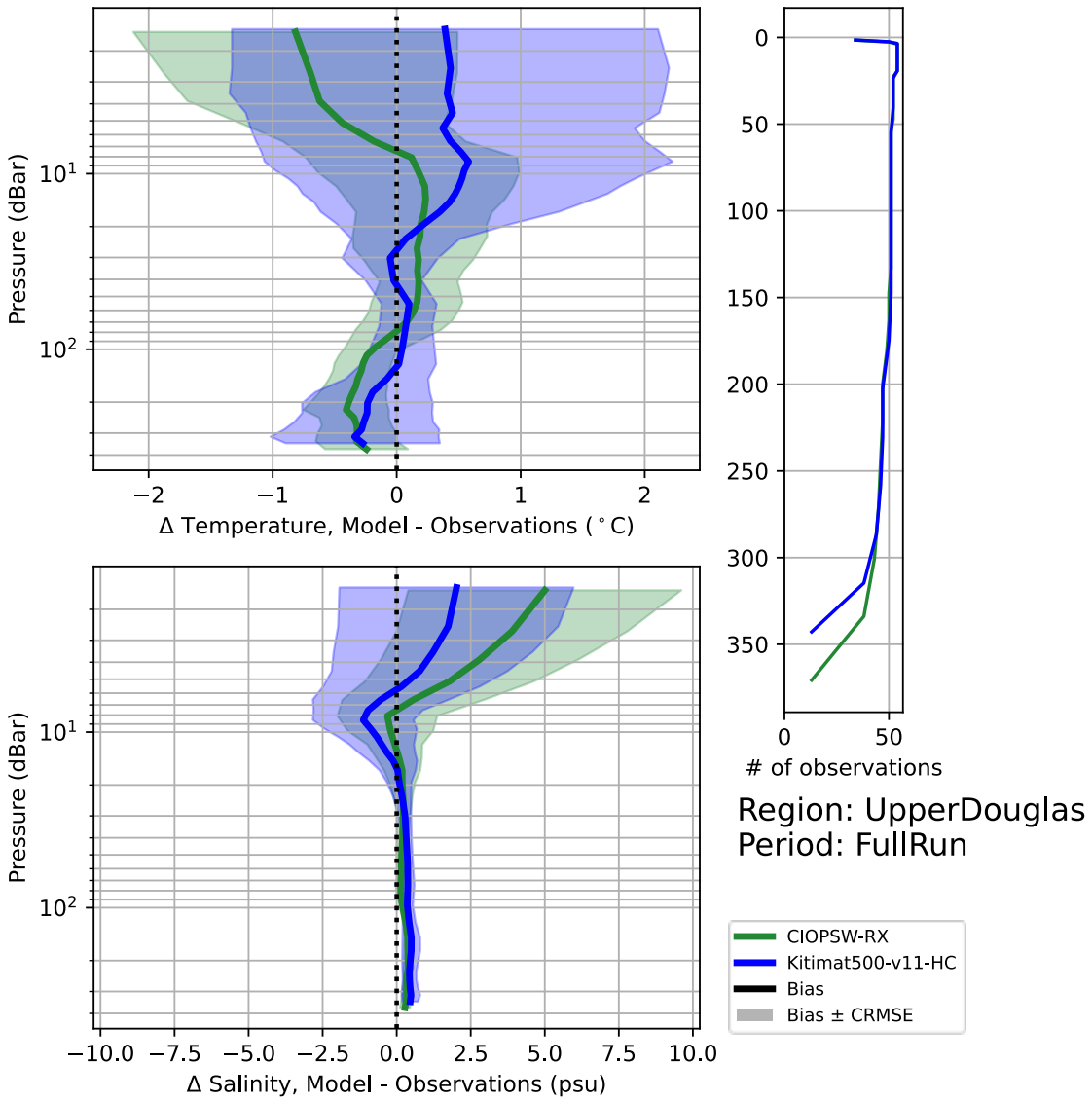

Figure 65. Comparison of temperature and salinity errors against CTD casts in upper Douglas Channel sub-region of Kitimat 500 m domain.

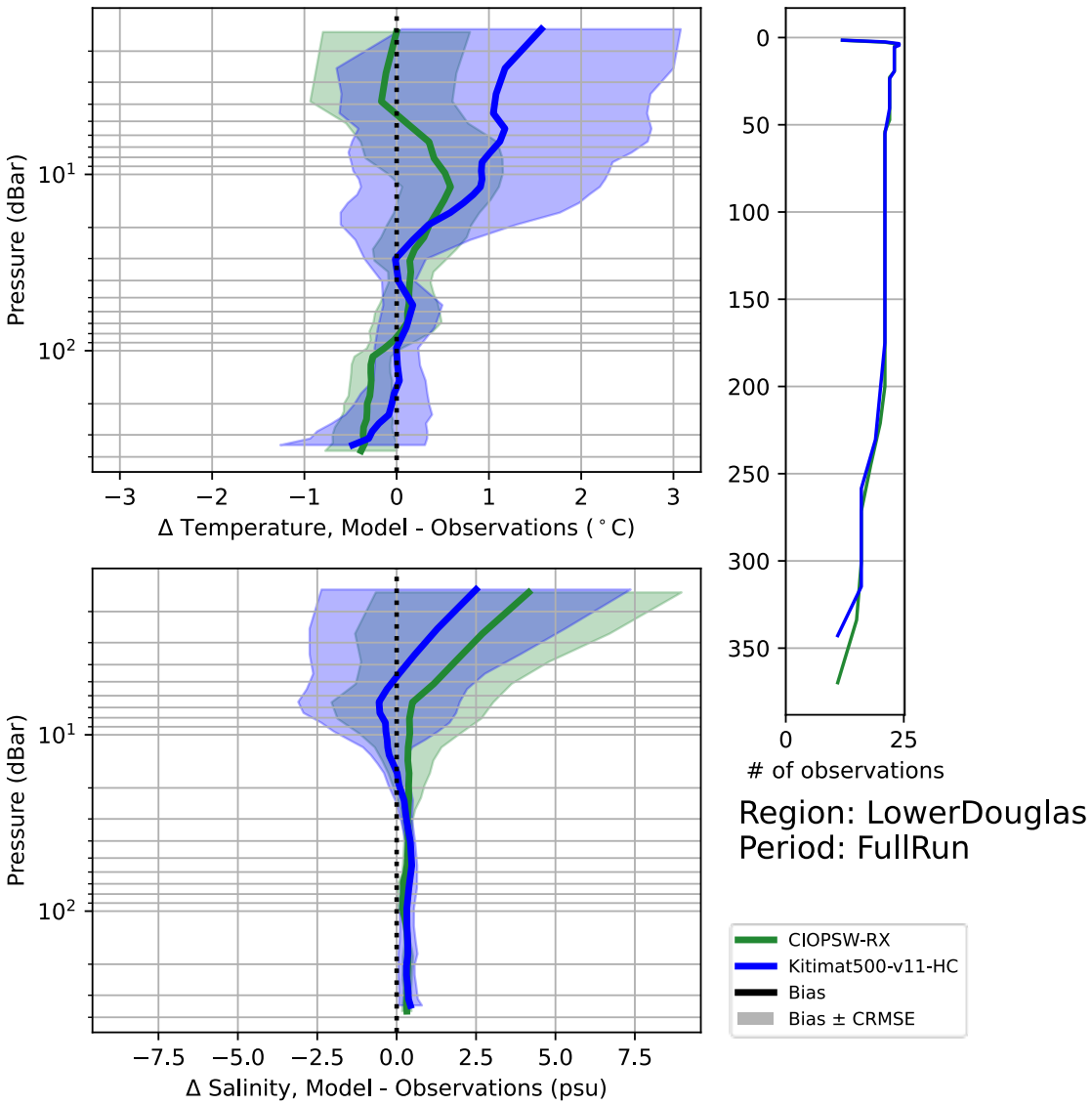

Figure 66. Comparison of temperature and salinity errors against CTD casts in lower Douglas Channel sub-region of Kitimat 500 m domain.

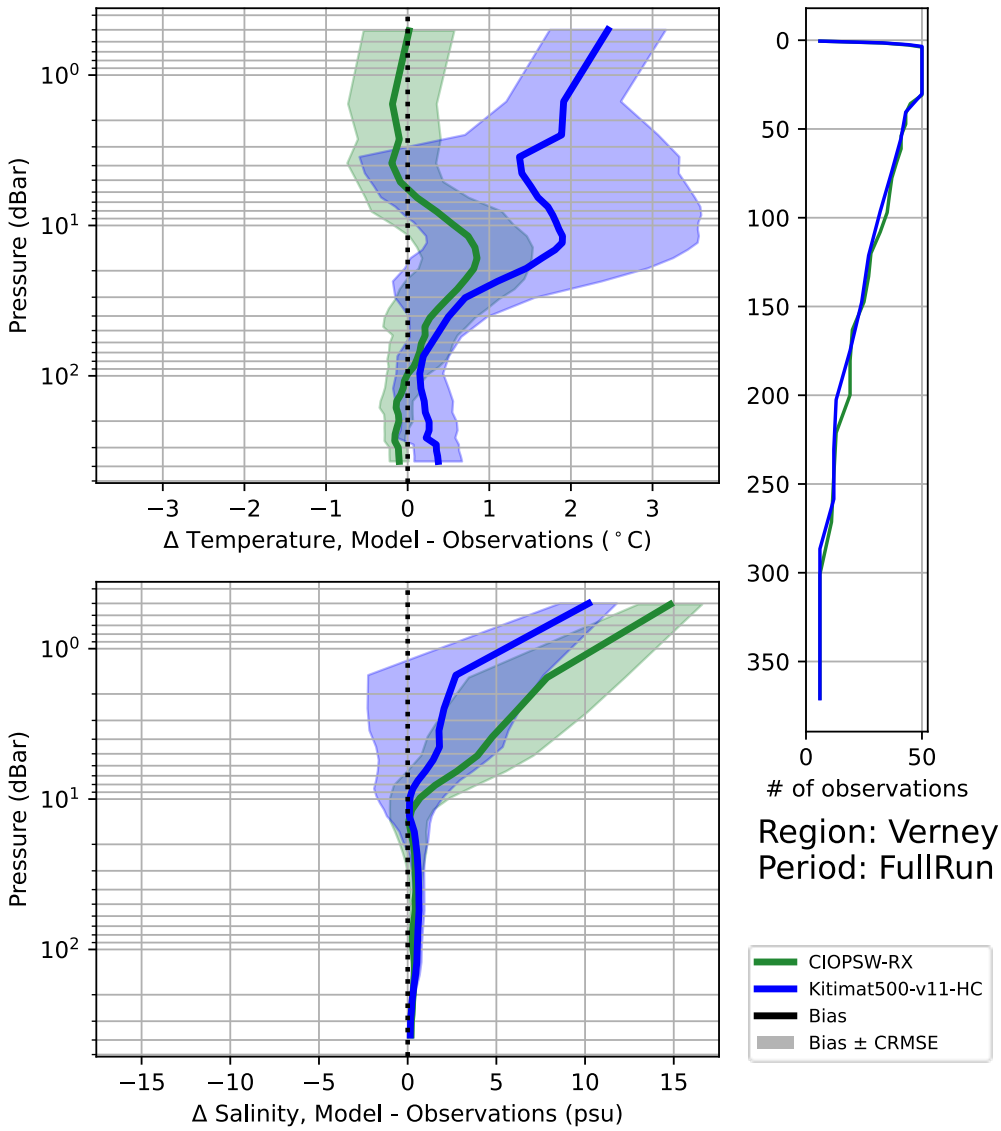

Figure 67. Comparison of temperature and salinity errors against CTD casts in Verney Passage sub-region of Kitimat 500 m domain.

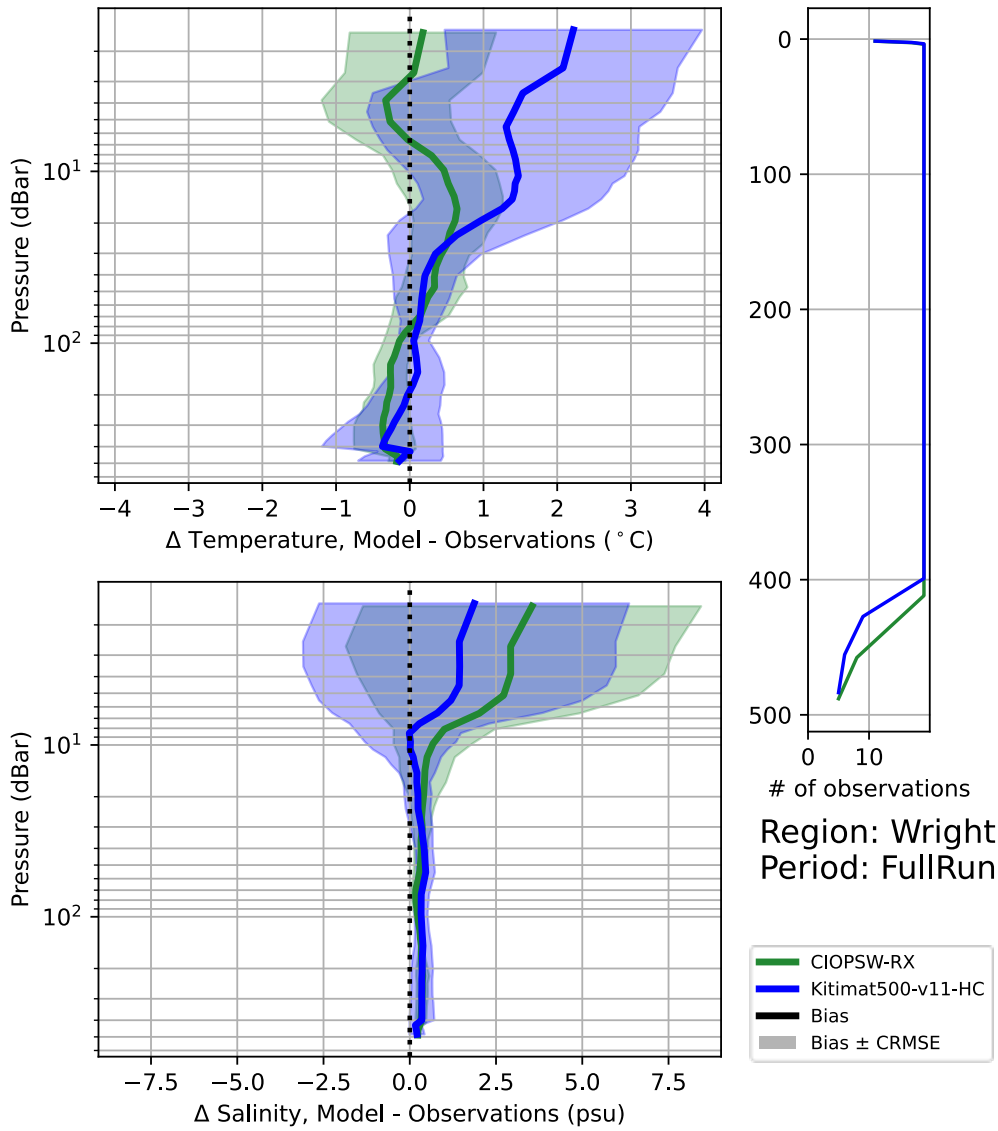

Figure 68. Comparison of temperature and salinity errors against CTD casts in Wright Sound sub-region of Kitimat 500 m domain.

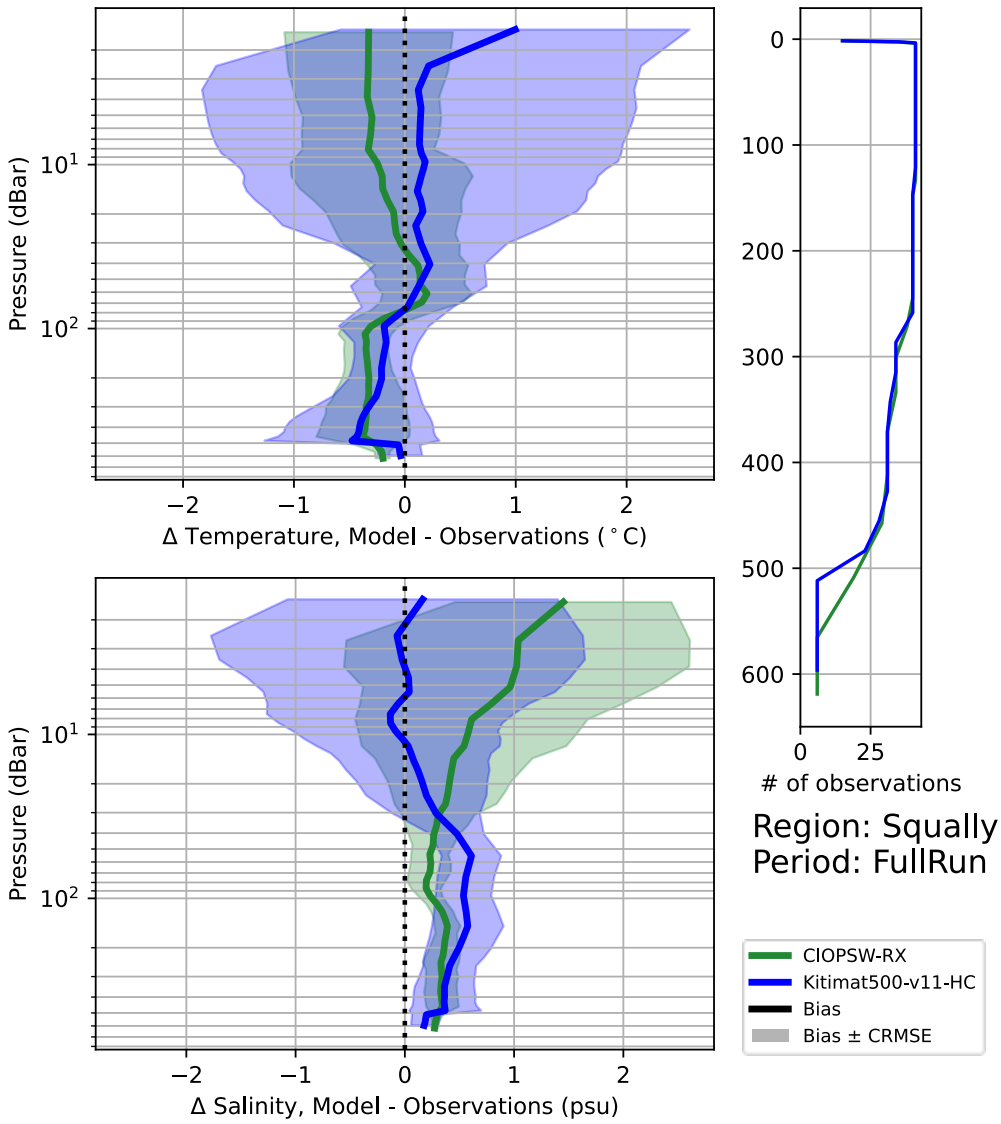

Figure 69. Comparison of temperature and salinity errors against CTD casts in Squally Channel sub-region of Kitimat 500 m domain.

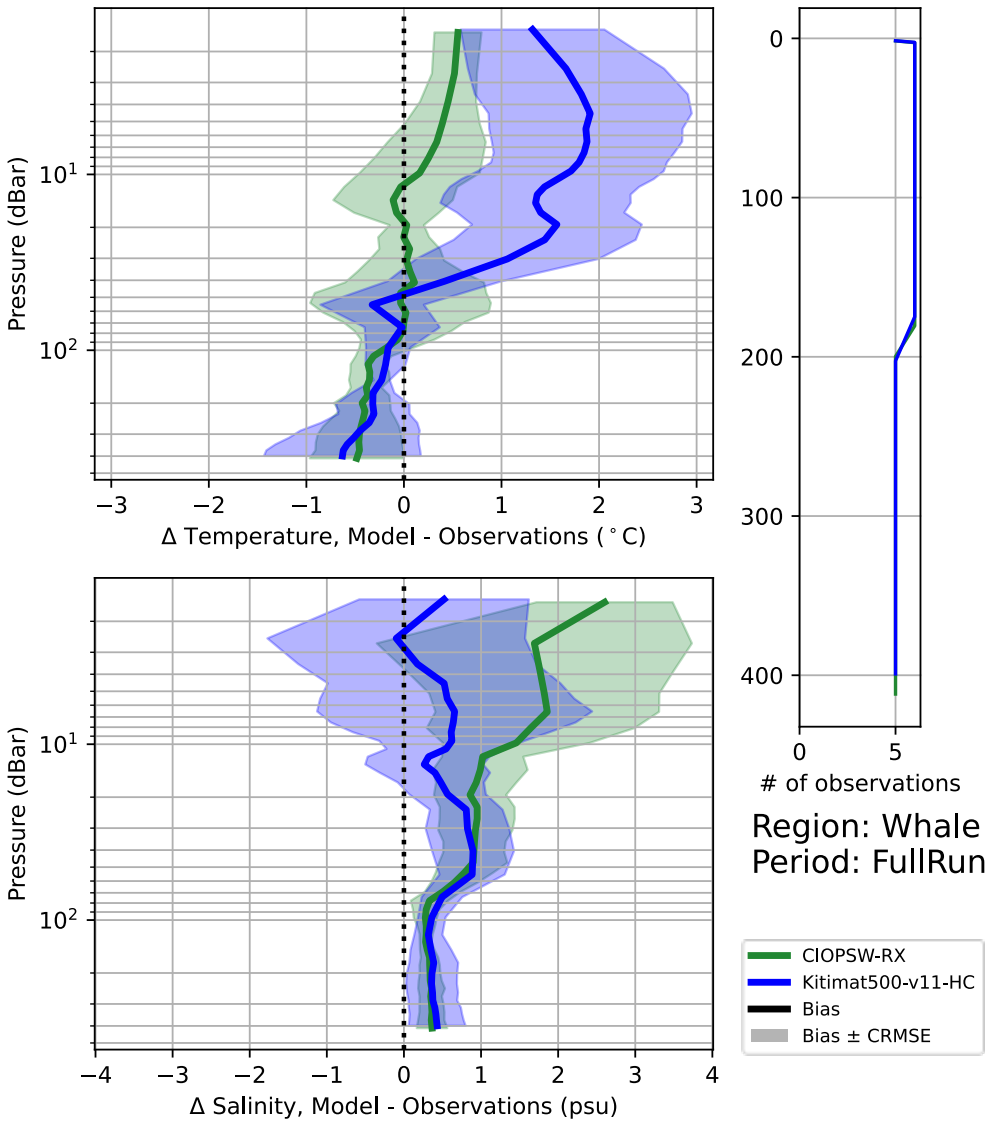

Figure 70. Comparison of temperature and salinity errors against CTD casts in Whale Channel sub-region of Kitimat 500 m domain.

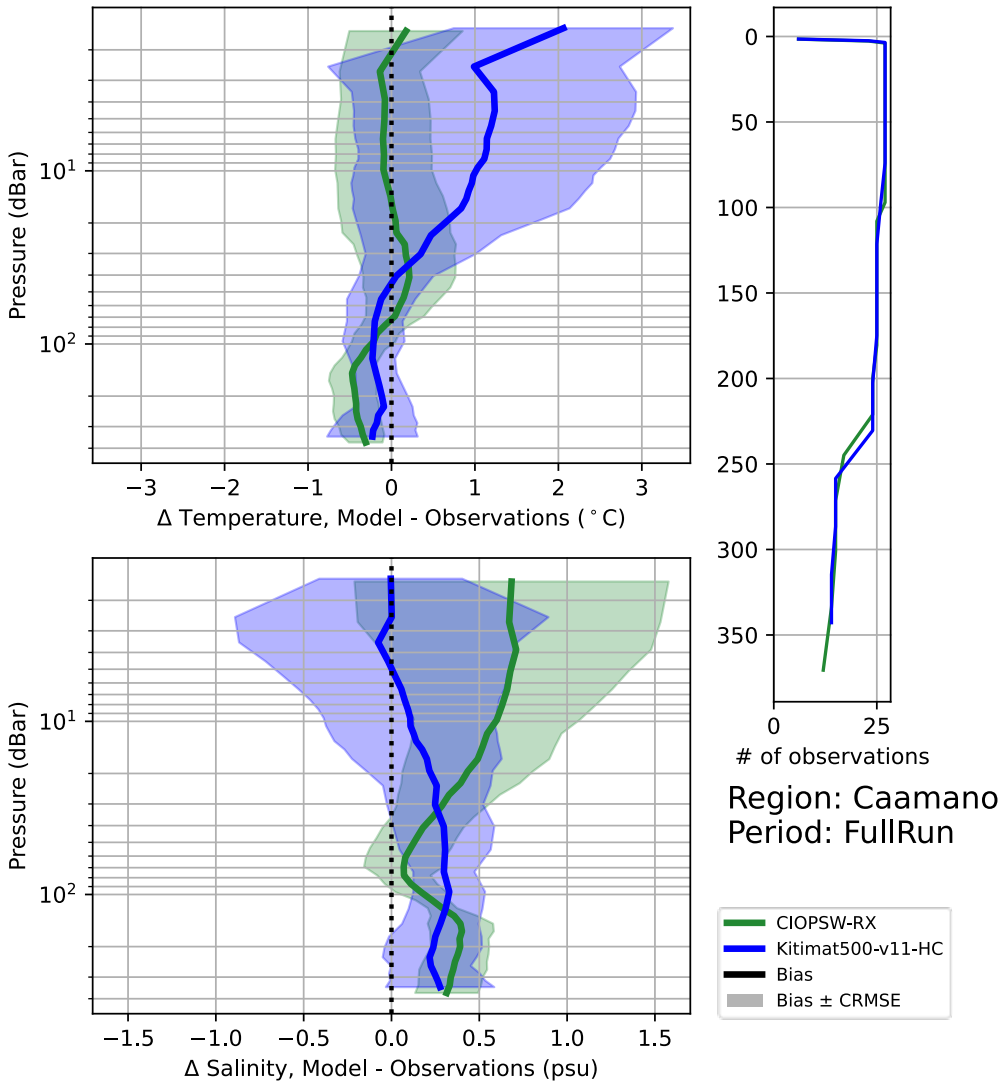

Figure 71. Comparison of temperature and salinity errors against CTD casts in Caamaño Sound sub-region of Kitimat 500 m domain.

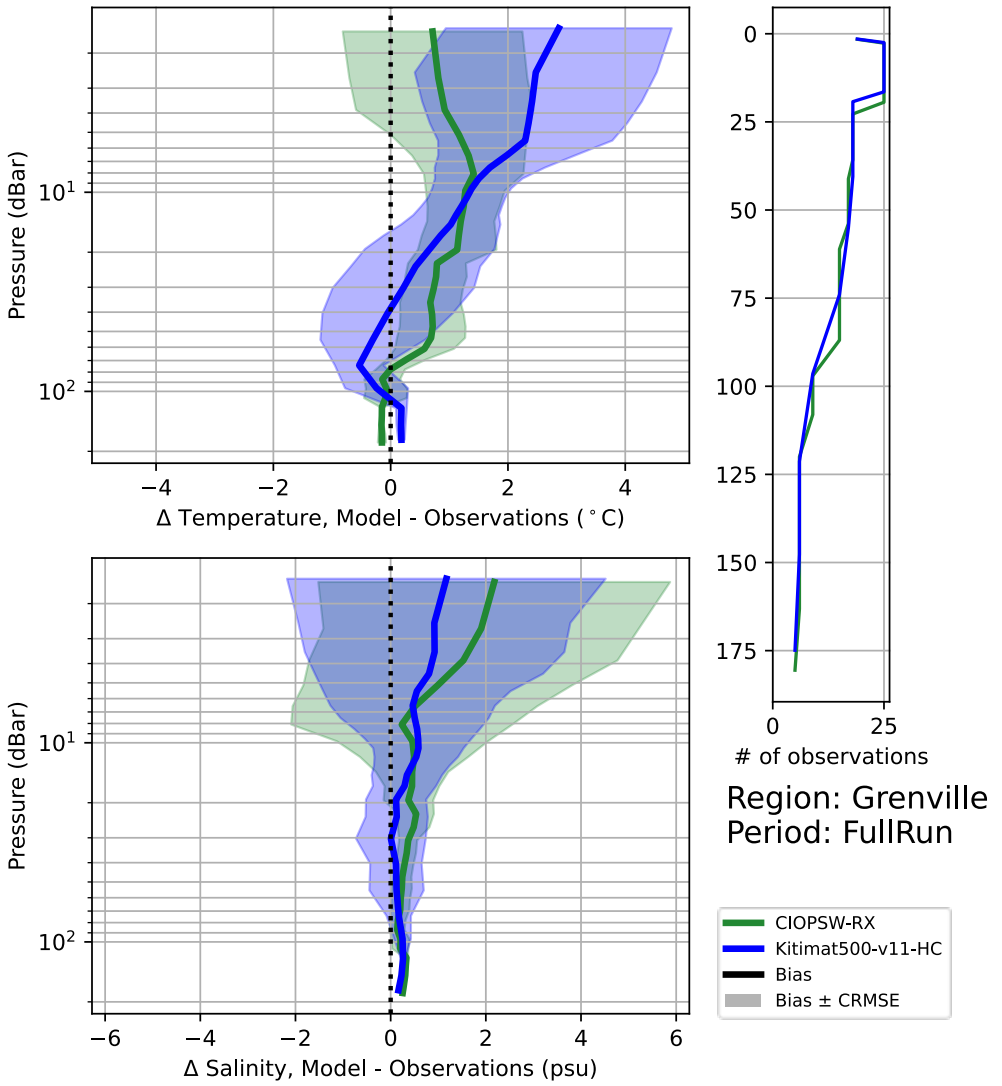

Figure 72. Comparison of temperature and salinity errors against CTD casts in Grenville Channel sub-region of Kitimat 500 m domain.

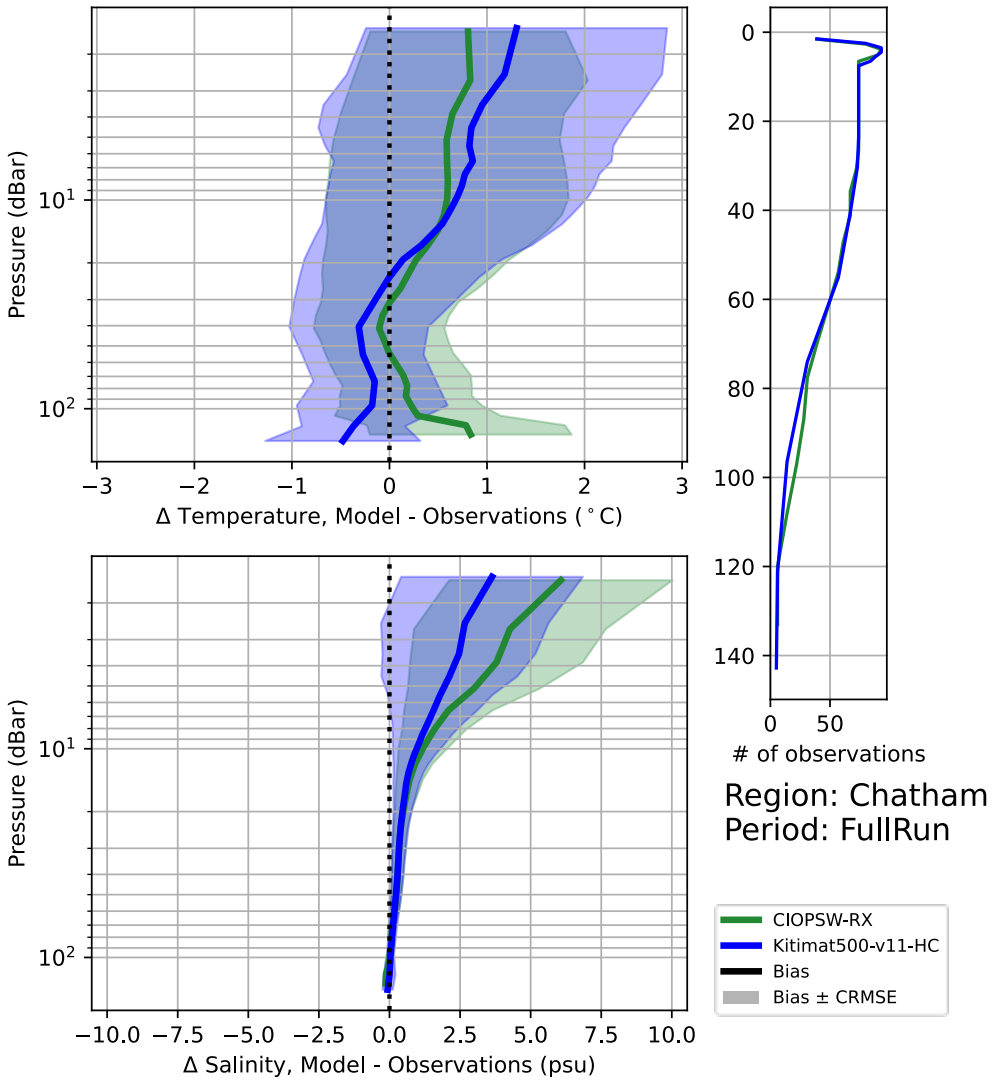

Figure 73. Comparison of temperature and salinity errors against CTD casts in Chatham Sound sub-region of Kitimat 500 m domain.

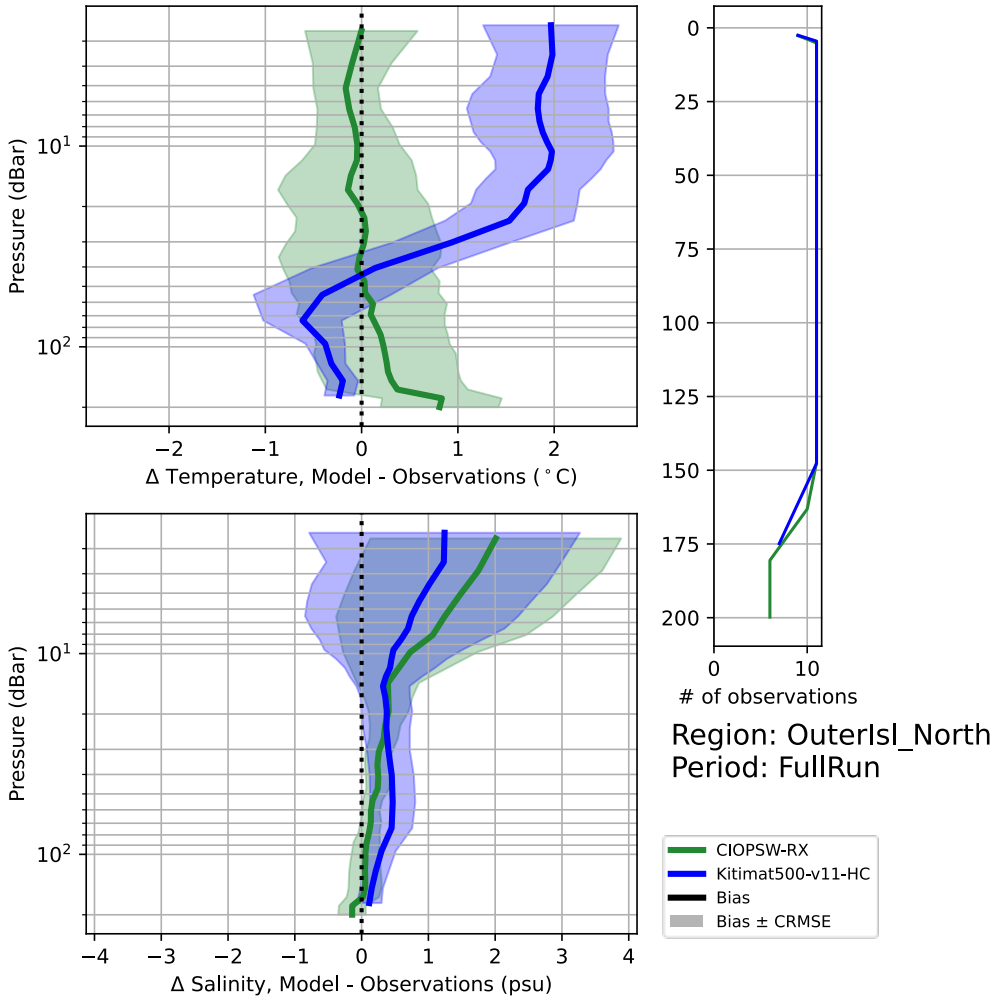

Figure 74. Comparison of temperature and salinity errors against CTD casts in northern Outer Islands sub-region of Kitimat 500 m domain.

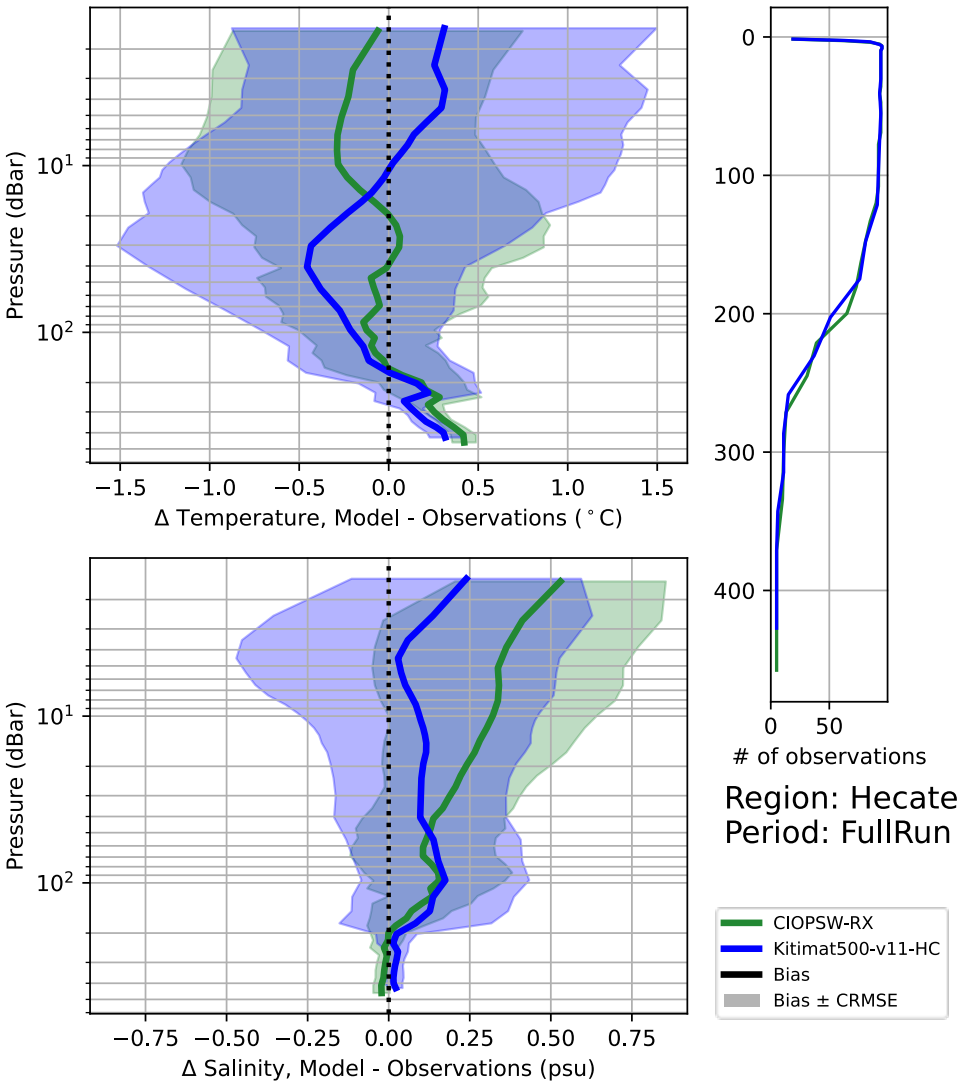

Figure 75. Comparison of temperature and salinity errors against CTD casts in Hecate Strait sub-region of Kitimat 500 m domain.

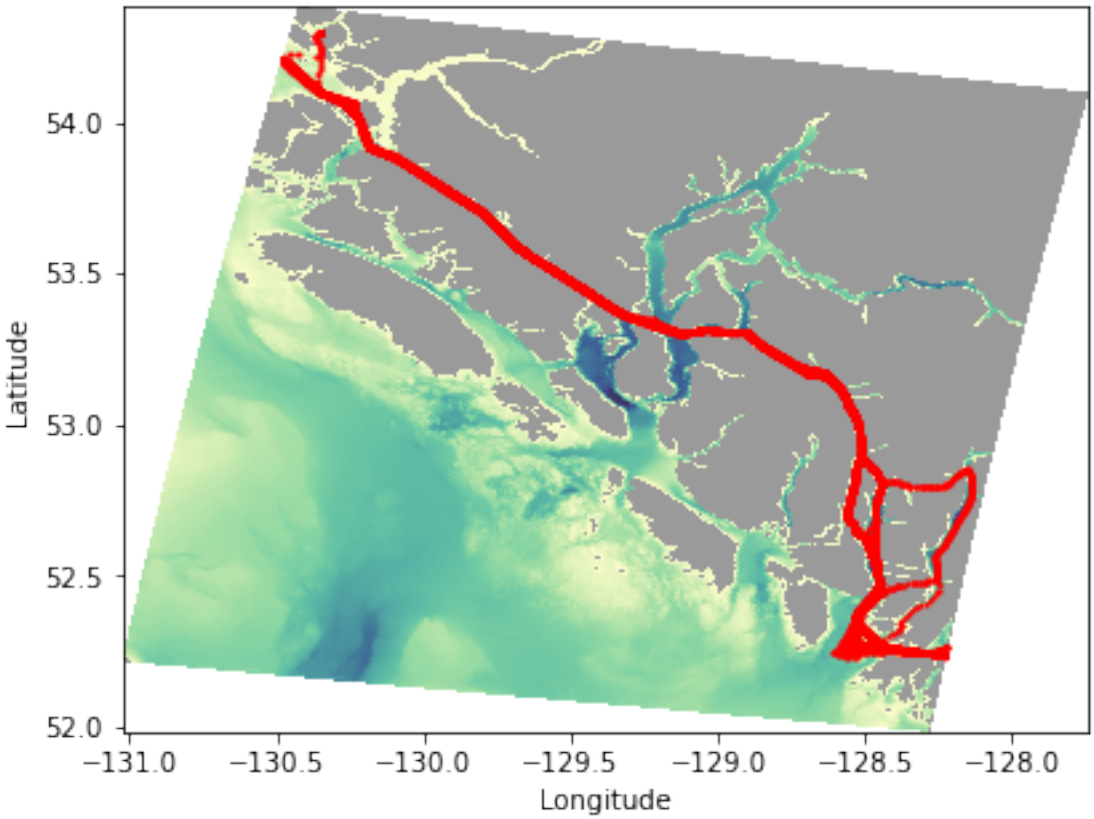

Figure 76. Key plot showing the route of the Bellingham - Alaska ferry through the Kitimat 500 m domain.

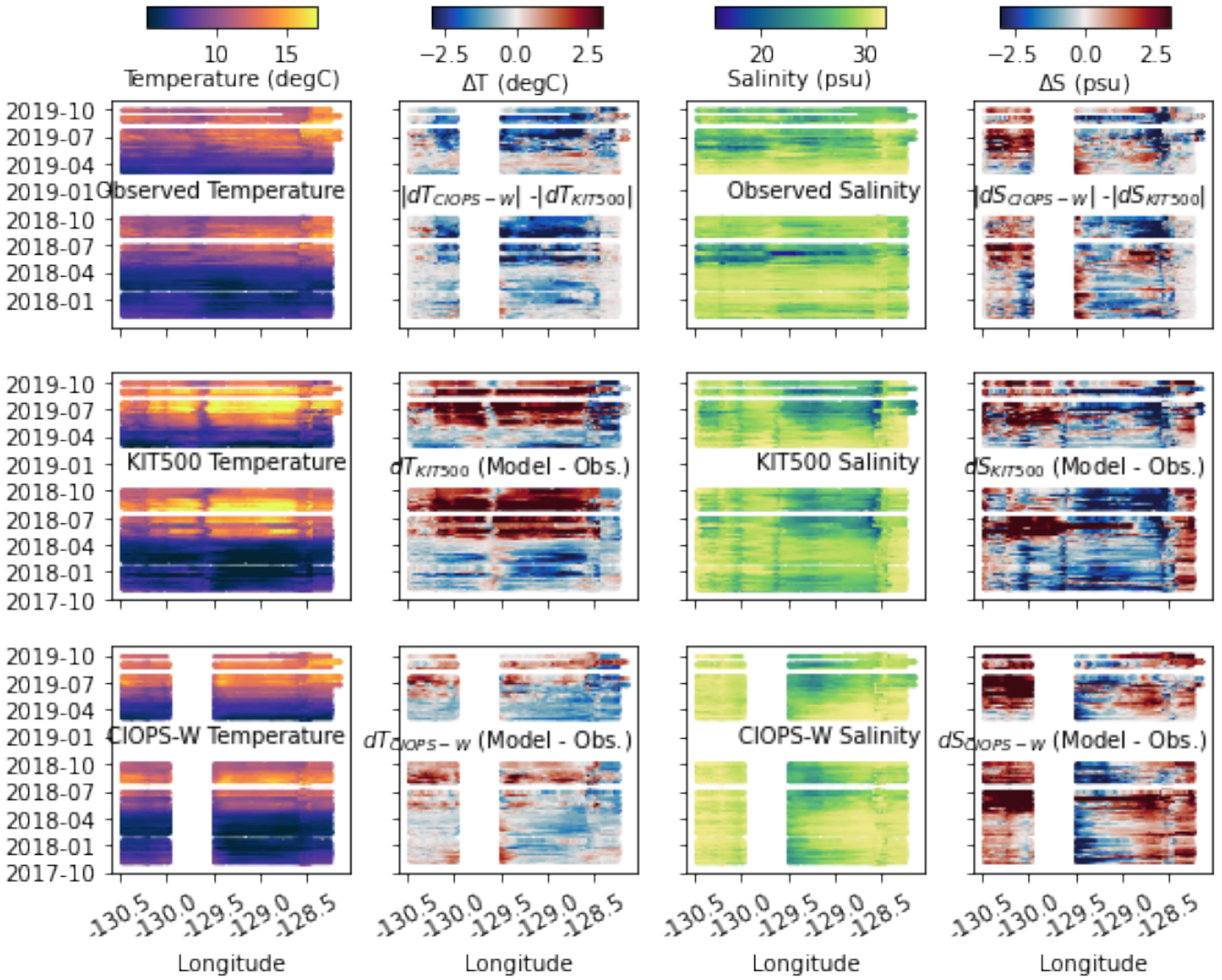

Figure 77. Comparison between sea surface temperature and salinity measured from the Bellingham - Alaska ferry (first and third panel top row) to modelled values from Kitimat 500 m and CIOPS-W (second and third rows). Differences between model results and observations are shown in the second and third row of the second and fourth column. In the top row, these columns show the differences between the models' absolute deviation from observations. Here red indicates that Kitimat 500 m is closer to observations, while blue indicates that CIOPS-W is closer.

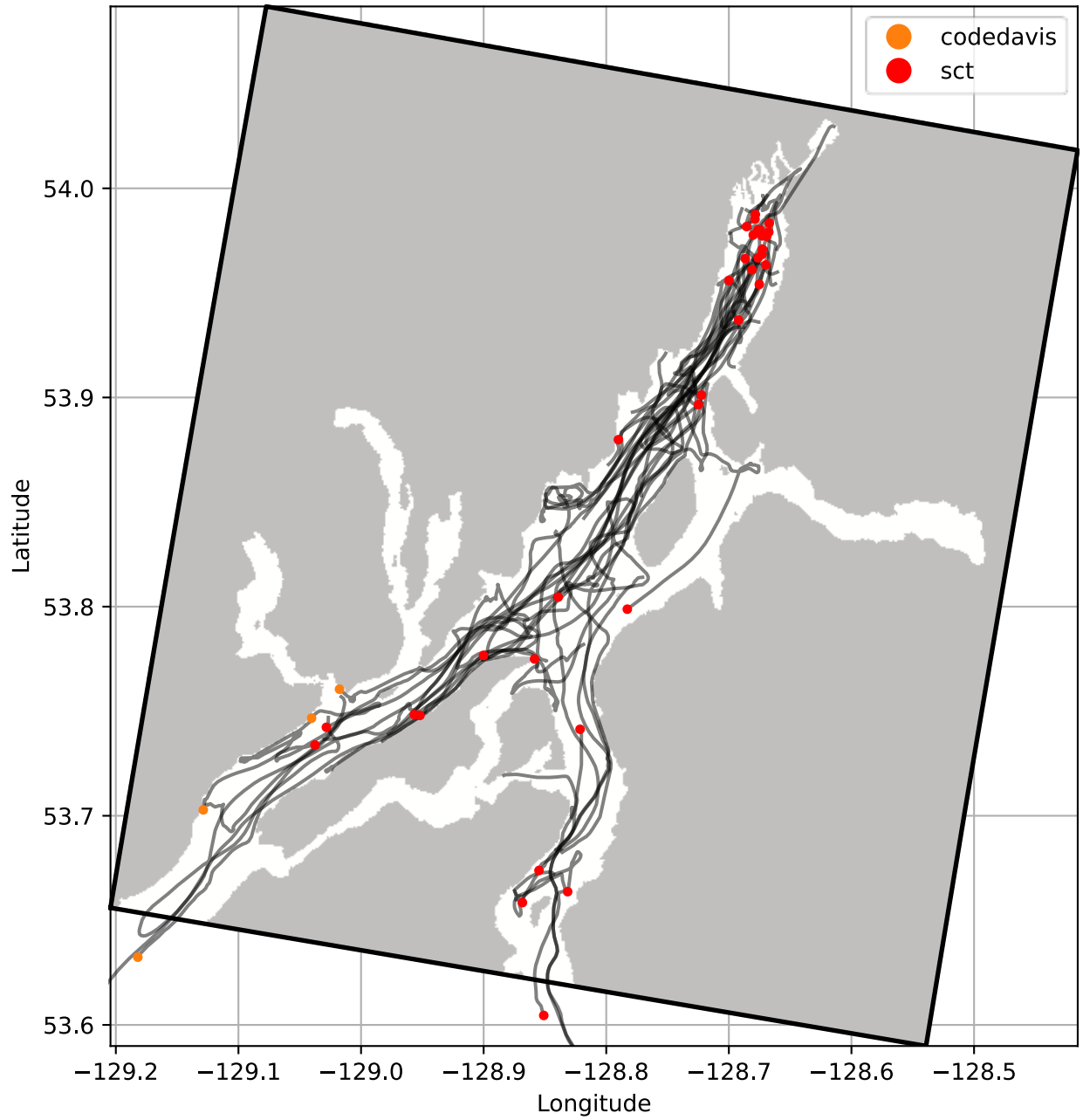

Figure 78. Map of drifter observations in the Kitimat 100 m port model domain.

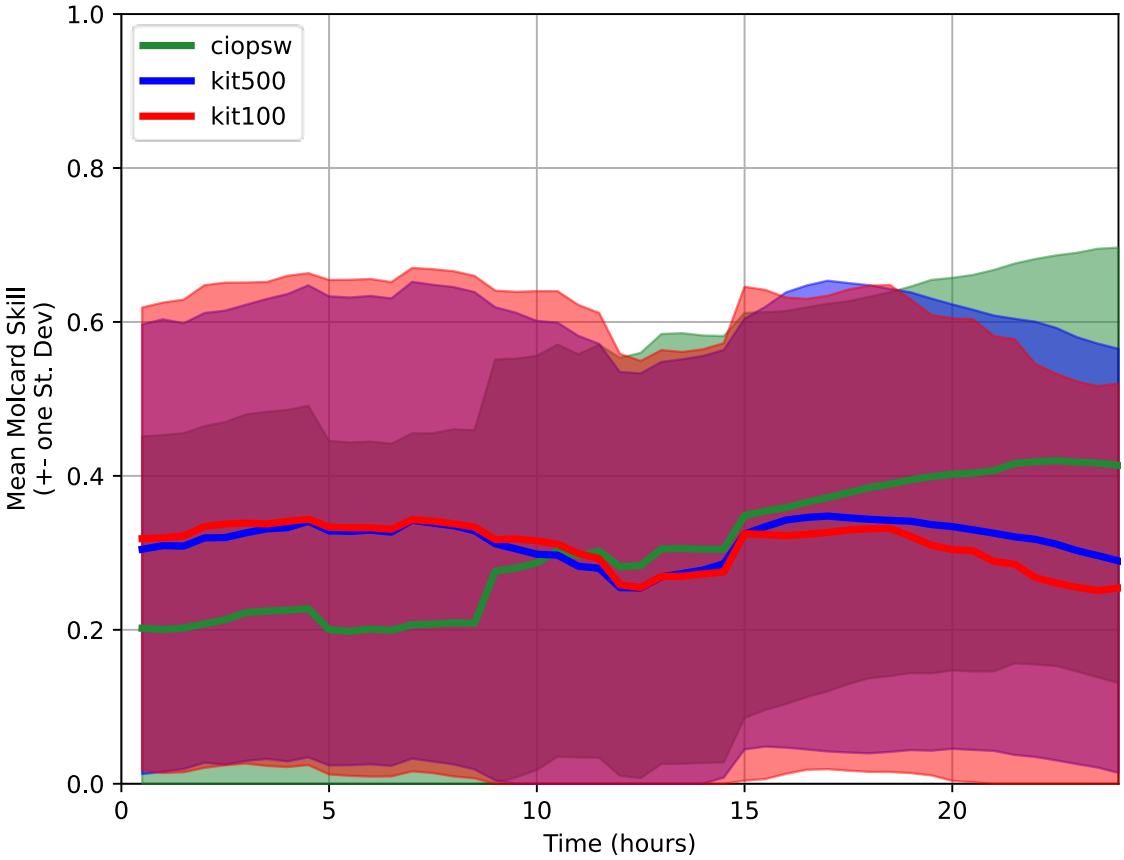

Figure 79. Evolution of Molcard drifter trajectory scores over 24 hours, in the Kitimat 100 m domain.

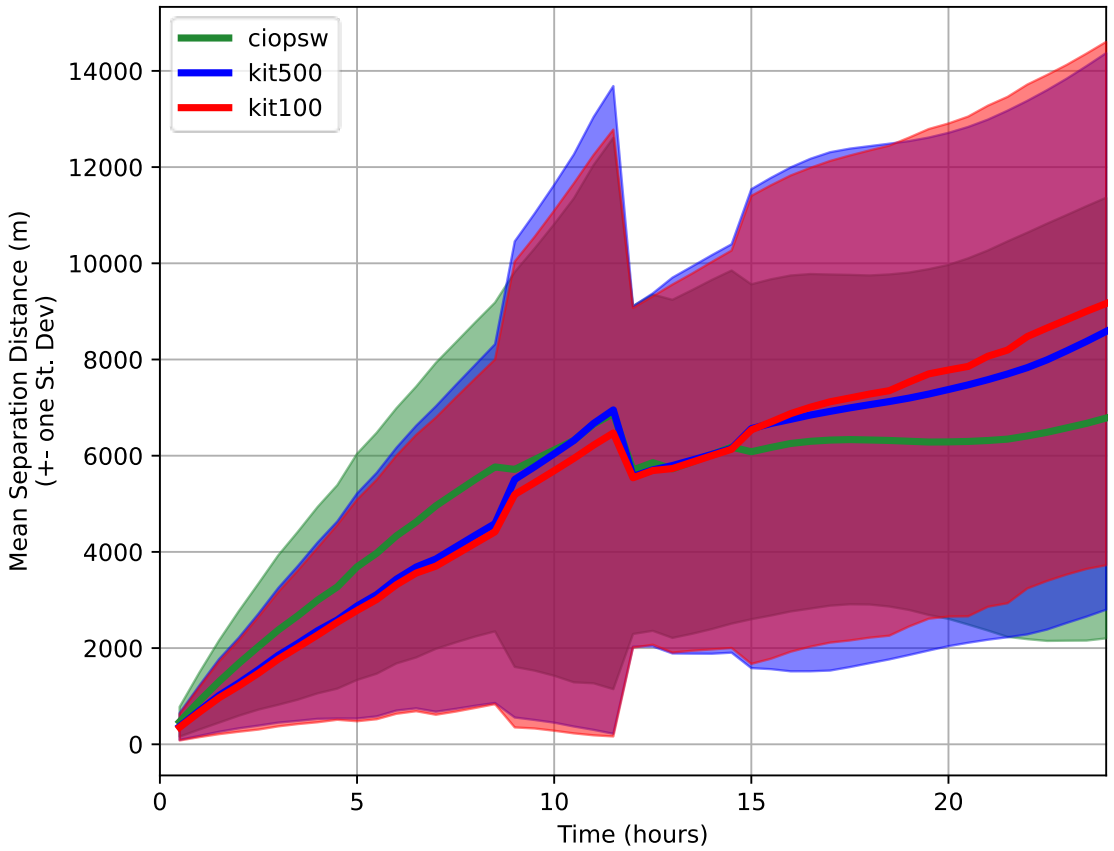

Figure 80. Evolution of separation distance between modelled and observed drifters over 24 hours, in the Kitimat 100 m domain.

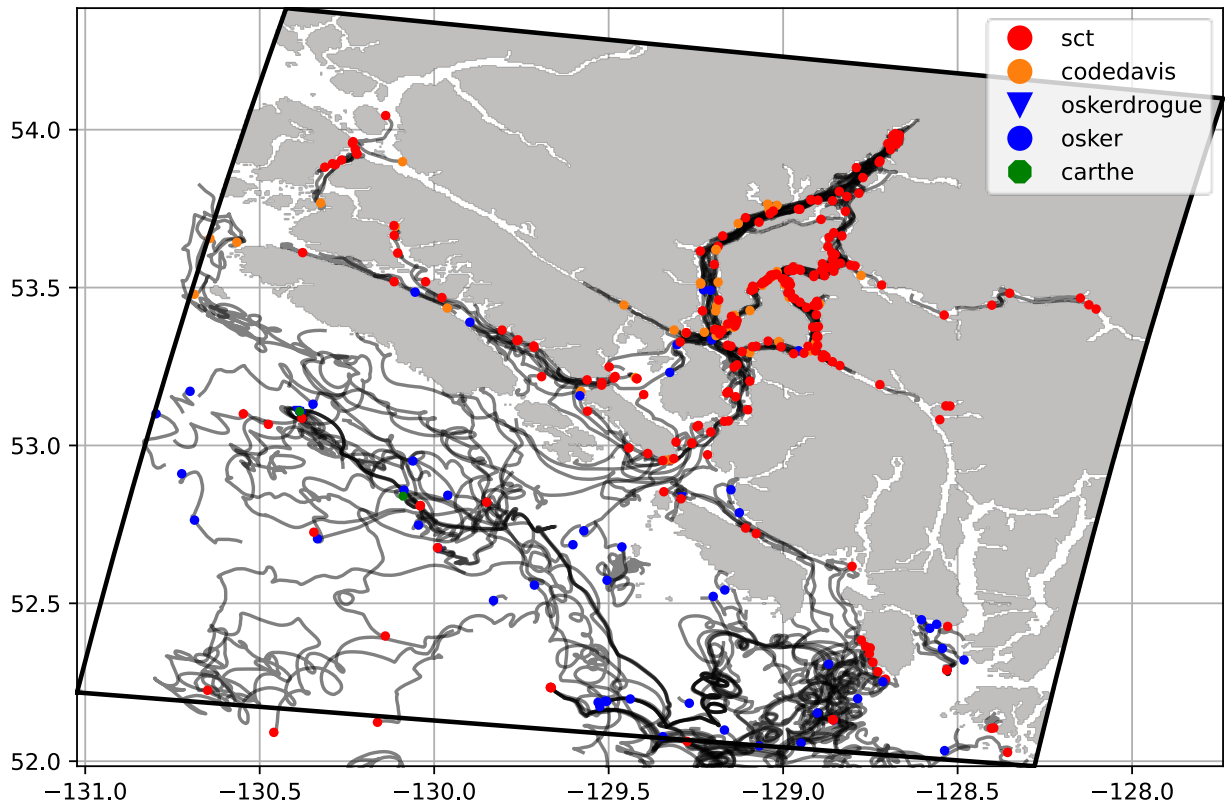

Figure 81. Map of drifter observations in the Kitimat 500 m port model domain.

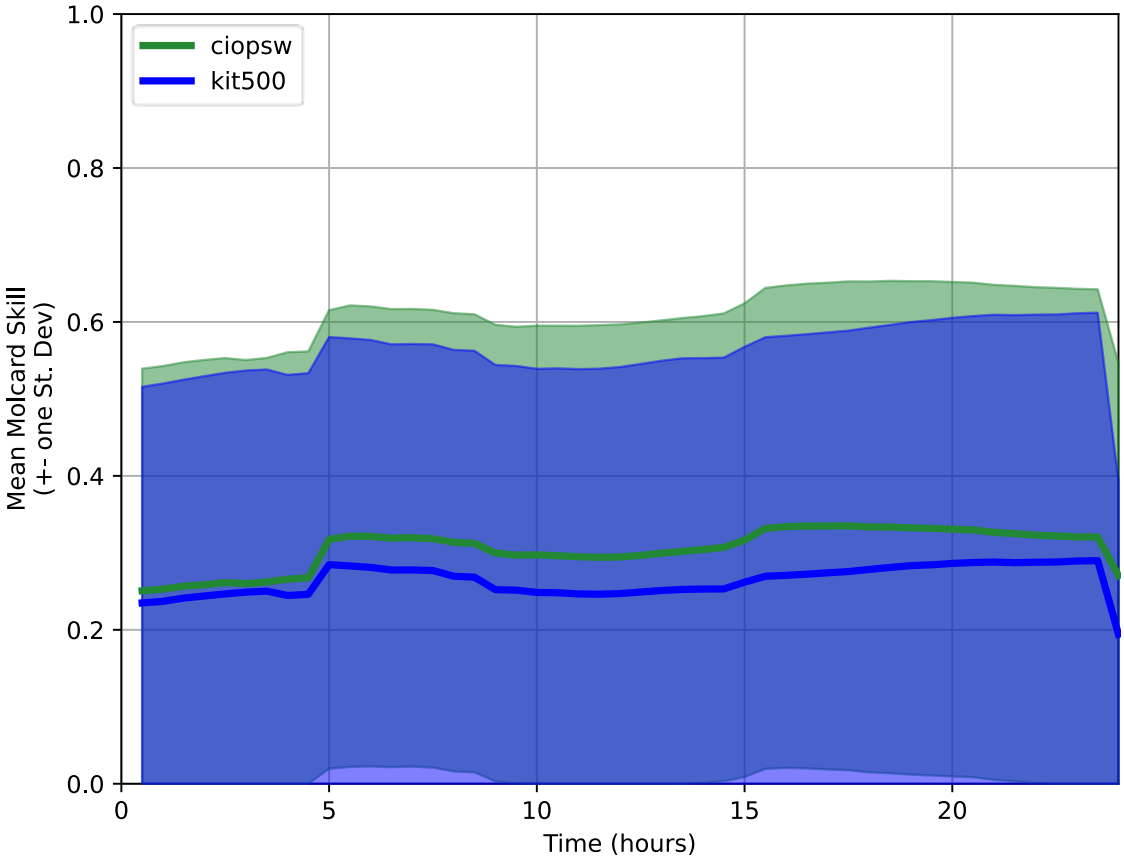

Figure 82. Evolution of Molcard drifter trajectory scores over 24 hours, in the Kitimat 500 m domain.

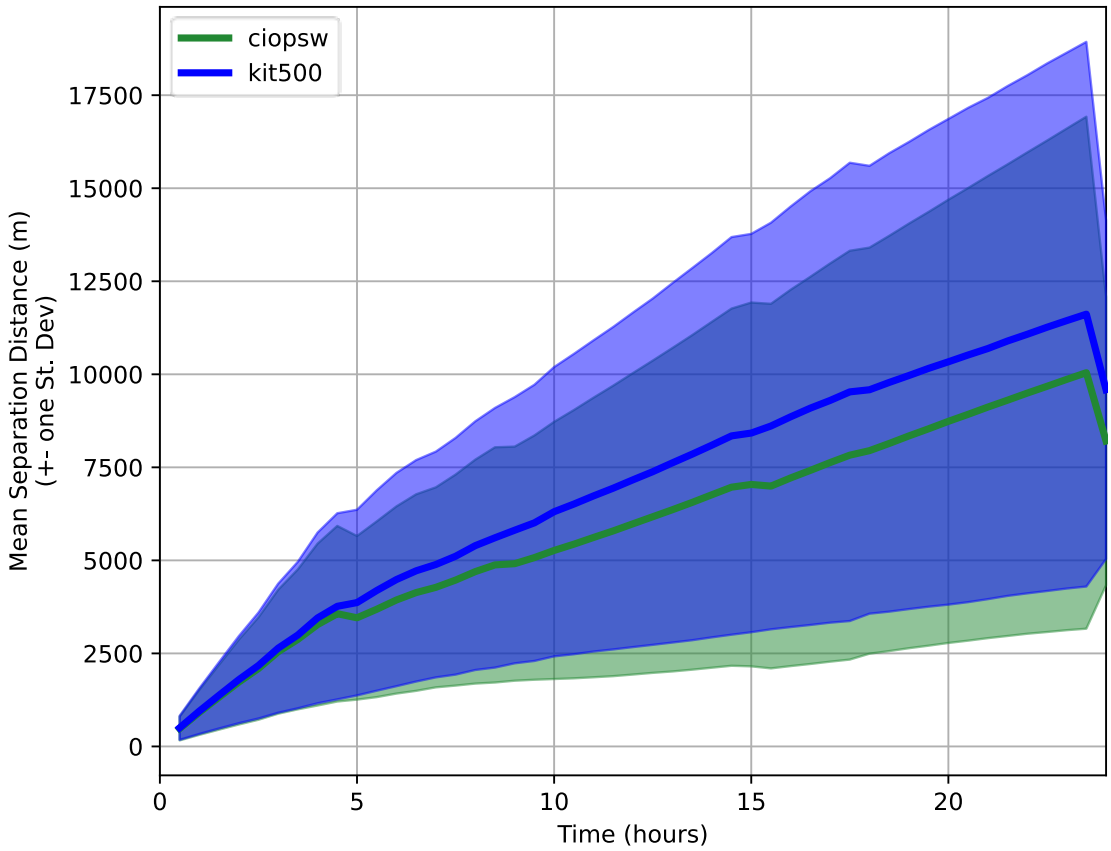

Figure 83. Evolution of separation distance between modelled and observed drifters over 24 hours, in the Kitimat 500 m domain.

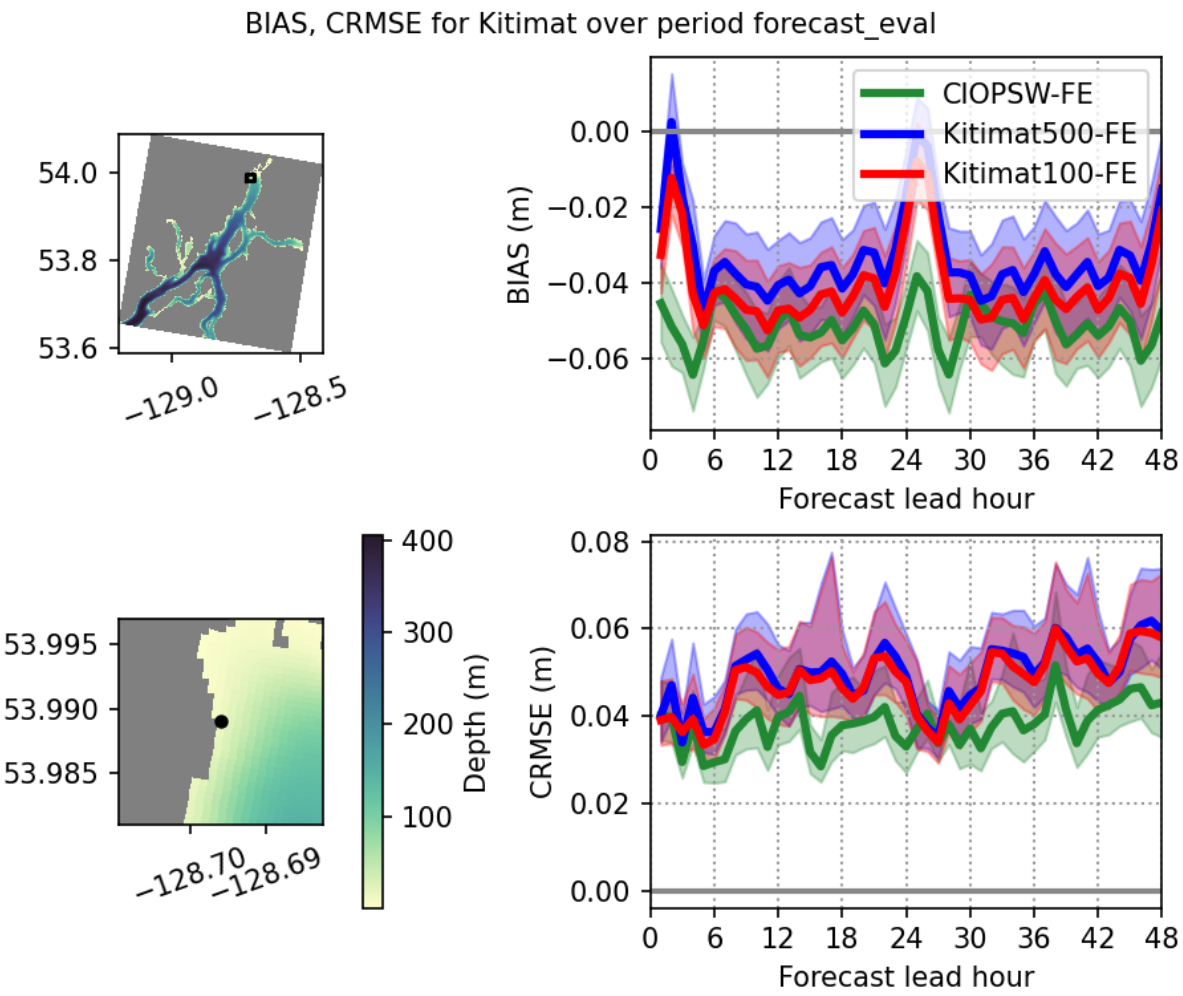

Figure 84. Evolution of non-tidal water level bias and CRMSE at Kitimat. Curves are shown for Kitimat 100 m (red), Kitimat 500 m (blue), and CIOPS-W (green).

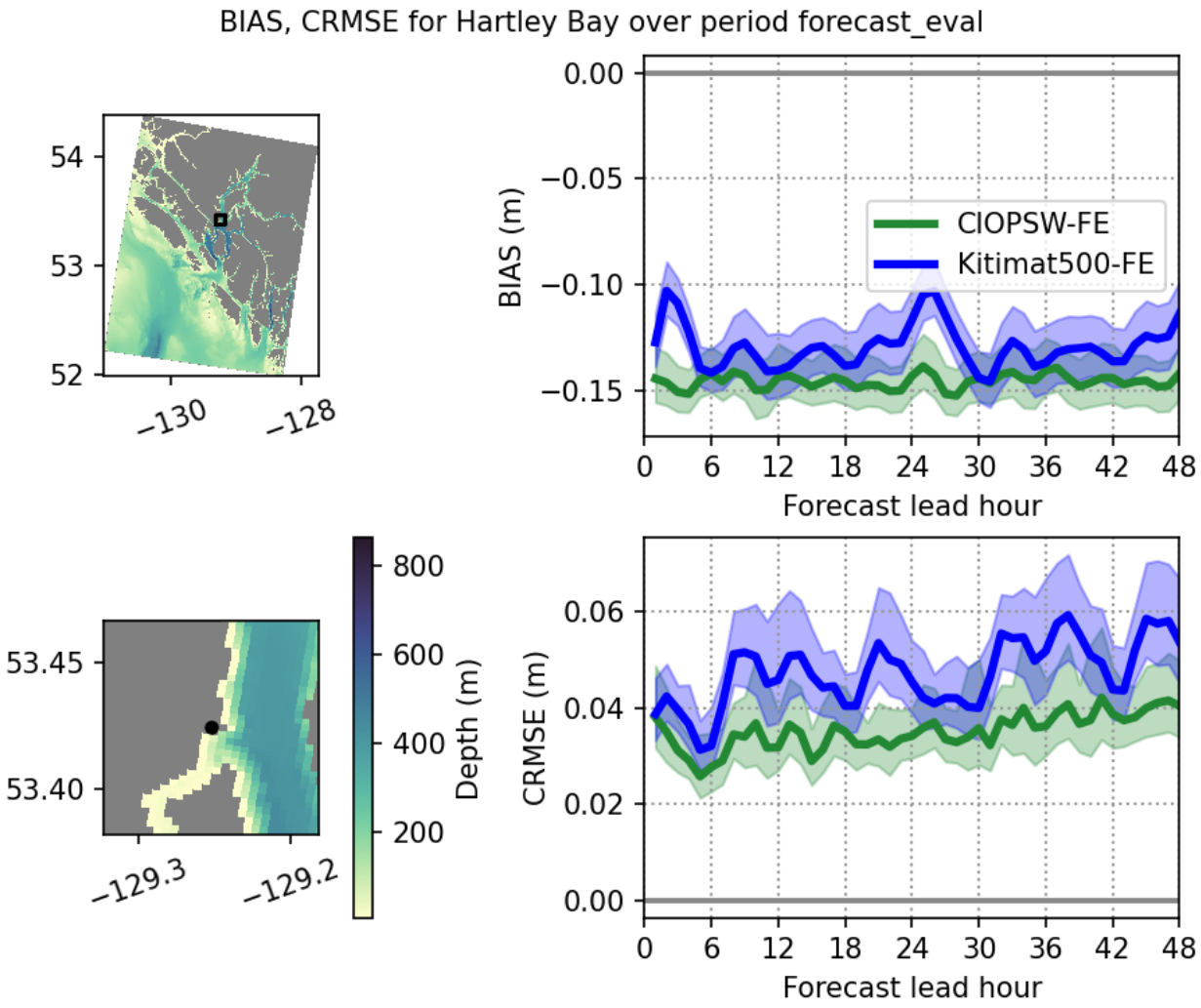

Figure 85. Evolution of non-tidal water level bias and CRMSE at Hartley Bay. Curves are shown for Kitimat 500 m (blue) and CIOPS-W (green).